



Copyright © 2017, Publication Division, Center of Technology (CoT)

Faculty of Engineering, Hasanuddin University

ISSN: 2615-5109

Reproduction in whole or in part by any means, is subject to the permission in writing by Publication Division, Center of Technology (CoT), Faculty of Engineering, Hasanuddin University. All Rights Reserved.

Publisher:

Center of Technology, Fakultas Teknik, Universitas Hasanuddin

Address:

Engineering Faculty Campus, Hasanuddin University

Jl. Poros Malino km. 6, Bontomarannu

Kabupaten Gowa, Sulawesi Selatan, Indonesia, 92171

Email : epi-ije@unhas.ac.id

Website : cot.unhas.ac.id/journals/index.php/epiije

Telp/Fax : +62-(0)411-586015

Congratulatory messages to EPI-IJE

I would like to congratulate Engineering Faculty, Hasanuddin University, especially Center of Technology and JICA C-BEST project for successful publication of the 1st edition of EPI International Journal of Engineering (EPI-IJE). This is surely a great achievement and a proof of Center of Technology skills and potentials in high-quality international journal publication and management. I believe publishing a high-quality journal will not be possible without hard work, perseverance, and dedication. Therefore, I commend your efforts to make this publication possible, congratulation!



Satryo Soemantri (Vice President, Indonesian Academy of Sciences)

I am pleased to hear that you (editorial members) are succeeding in launching a new technical journal, entitled "EPI International Journal of Engineering". That part of our world has few published technical journals. As one of my former, long-time Associate Editors of the international journal "Applied Mechanics Reviews", you (one of the associate editors in EPI-IJE) had good experience, and you have had much experience with other technical journals, as well. I look forward to seeing the first issue of your new journal.



Arthur W. Leissa (former Editor-in-Chief, Applied Mechanics Reviews, ASME)

I'm really delighted to know that you all have been able to start 'EPI International Journal of Engineering'. I'm sure that thanks to your experienced leadership this new international journal will contribute to sharing and the worldwide knowledge in the various engineering fields more and more. Furthermore, it will give opportunities to talented Indonesian scientists to publish their finding in an international forum. I'll be personally interested in reading papers from this new exciting journal.



Erasmo Carrera (Editor-in-Chief, Advances in Aircraft and Spacecraft Science, Mechanics of Advanced Materials and Structures, President of A.I.D.A.A. Associazione Italiana di Aeronautica ed Astronautica)

EPI International Journal of Engineering

Editor-in-Chief : **Dr. Muhammad Ramli**
Hasanuddin University, Indonesia

Associate Editors : **Dr. Faisal Mahmuddin**
Hasanuddin University, Indonesia
Prof. Yoshihiro Narita
Hokkaido University, Japan

Editorial Board :

- Indonesia

Dr. Wahyu H. Piarah, Hasanuddin University (Makassar, Indonesia)
Prof. Hammada Abbas, Hasanuddin University (Makassar, Indonesia)
Prof. M. Ramli Rahim, Hasanuddin University (Makassar, Indonesia)
Prof. Herman Parung, Hasanuddin University (Makassar, Indonesia)
Prof. Imran Umar, Hasanuddin University (Makassar, Indonesia)
Dr. Rhiza S. Sadjad, Hasanuddin University (Makassar, Indonesia)
Dr. Ganding Sitepu, Hasanuddin University (Makassar, Indonesia)
Prof. Satriyo Brodjonegoro, Bandung Institute of Technology (Bandung, Indonesia)
Prof. I Ketut Aria Pria Utama, Surabaya Institute of Technology (Surabaya, Indonesia)
Dr. Arifuddin Idrus, Gadjah Mada University (Yogyakarta, Indonesia)
Dr. Ngurah Nitya, Udayana University (Denpasar, Indonesia)
Dr. Putu Wijaya Sunu, Bali State Polytechnic (Denpasar, Indonesia)
Dr. Lukiyanto YB, Sanata Dharma University (Yogyakarta, Indonesia)

- Outside Indonesia

Prof. Erasmo Carrera, Polytechnic University of Turin (Torino, Italy)
Prof. Mark Ewing, University of Kansas (Lawrence, USA)
Prof. Danna Ganbat, Mongol University of Science and Technology (Ulaanbaatar, Mongolia)
Prof. Peter Hagedorn, Technical University of Darmstadt (Darmstadt, Germany)
Prof. S. Ilanko, University of Waikato (Hamilton, New Zealand)
Prof. David Kennedy, Cardiff University, (Cardiff, United Kingdom)
Prof. Woo Il Lee, Seoul National University (Seoul, Korea)
Prof. Vasaka Visoottiviseth, Mahidol University, (Bangkok, Thailand)
Dr. Jane Louie Fresco Zamora, Weathernews Inc. (Chiba, Japan)
Dr. Kazunori Abe, Akita University (Akita, Japan)
Prof. Jun Ando, Kyushu University (Fukuoka, Japan)
Prof. Shun Chiyonobu, Akita University (Akita, Japan)
Prof. Naohiro Hozumi, Toyohashi University of Technology (Toyohashi, Japan)
Prof. Shigeru Kashihara, Nara Institute of Science and Technology (Nara, Japan)
Prof. Akio Miyara, Saga University (Saga, Japan)
Prof. Prakash Bhandary Netra, Ehime Univ. (Matsuyama, Japan)
Prof. Tsubasa Otake, Hokkaido University (Sapporo, Japan)
Prof. Nobumasa Sekishita, Toyohashi University of Technology (Toyohashi, Japan)
Prof. Hideaki Yasuhara, Ehime University (Matsuyama, Japan)

Foreword

We are delighted that at this beginning of the year 2018, we could finally be able to launch an international journal titled “EPI International Journal of Engineering” (EPI-IJE). The term EPI (Eastern Part of Indonesia) was included as the journal name because we realized the importance of Engineering Faculty of Hasanuddin University roles and responsibility as the largest engineering faculty in EPI region. The journal is expected to be a media for Indonesian researchers as well researchers from outside Indonesia to publish their innovative and cutting-edge research results and findings. By publishing the high-quality research findings and results, we hope that it could give significant positive contributions and effects on improving research quality and academic publication of researchers in EPI region.

In this 1st edition, a total of 16 manuscripts is published which authored by researchers from various institutions in Indonesia and abroad. We realized that collecting papers and preparing the publication of these manuscripts certainly were not an easy matter. The publication would not be possible without hard work and high commitment from all staff involved. Therefore, we would like to express our sincere appreciation to all staff who already make the publication possible. Our sincere gratitude also to JICA C-BEST project team especially to Prof. Yoshihiro Narita for strong support and great effort in the publication of the journal. Our thanks also to all author who have contributed to the 1st edition of this journal. We hope that the journal quality will be improved over time.

Warm regards,

Dr. Muhammad Ramli

Editor-in-Chief of EPI-IJE

TABLE OF CONTENTS

Congratulatory Messages	i
Editorial Board	ii
Foreword	iii
Table of Contents	iv

<Civil and Environmental Engineering>

Inorganically Precipitated Phosphates and Carbonates to Improve Porous Material Properties	1-6
Debendra Neupane (Penta-Ocean Construction Co., Japan)	
Hideaki Yasuhara, Naoki Kinoshita (Ehime University, Japan)	
Heriansyah Putra (Bogor Agricultural University, Indonesia)	
Naoki Kinoshita (Ehime University, Japan)	

<Mechanical and Industrial Engineering>

Minimum Weight Design of Composite Panel under Aeroelastic Constraint	7-12
Shinya Honda, Gaku Yokoyama (Hokkaido University, Japan)	
Modelling of Thin Structural Polymer Composites for Use of Automobiles -Review-.....	13-20
Daisuke Narita (Hokkaido University of Science Junior College, Japan)	
Yoshihiro Narita (Hokkaido University, Japan)	
Role of Flow Simulation as a Tool for Failure Analysis Induced by Sulfate-Reducing Bacteria	21-24
Yudha Pratesa, Badrul Munir (Universitas Indonesia, Indonesia)	

<Naval Architecture, Ocean, and Marine System Engineering>

Analysis of Corrugated Bulkhead against Transverse Plane Bulkhead in a Tanker Ship	25-29
Hamzah, Ganding Sitepu, Muh. Hidayat Arif (Hasanuddin University, Indonesia)	
Fatigue Analysis of Catenary Mooring System due to Harsh Environment in Head Seas.....	30-38
Fuad Mahfud Assidiq, Daeng Paroka, Muhammad Zubair Muis Alie, Syerly Klara (Hasanuddin University, Indonesia)	
Study of Engine Propeller Matching for High-Speed Vessel with Gawn Series Propeller.....	39-42
Nurhadi, Hardi Zen, Sumarsono (BPPT, Indonesia)	
Identifying Model for Decision Making Process in a Collaborative Manufacturing Network Environment	43-53
Mohammad Rizal Firmansyah, Wihdat Djafar (Hasanuddin University, Indonesia)	

<Electrical and Informatics Engineering>

**Simulation of Partial Discharge Induced Electromagnetic Wave
in Power Transformer..... 54-59**

Nhet Ra, Tomohiro Kawashima, Naohiro Hozumi, Yoshinobu Murakami
(Toyohashi University of Technology, Japan)

Umar Khayam, Suwarno (Bandung Institute of Technology, Indonesia)

**Transmission Scheduling Method for Delivery of Large-Sized Data Object
based on Delay Constrained Request over Scheduled Transportation Vehicles 60-68**

Shigeru Kashihara (Nara Institute of Science and Technology, Japan)

**Support Vector Machine Method to Reduce The Execution Time
of Vehicle Plate Recognition System..... 69-75**

Muhammad Ismail, Indrabayu, Intan Sari (Hasanuddin University, Indonesia)

Partial Discharge Signal Denoising by Discrete Wavelet Transformation 76-82

Trinurkalid Sumarwoto, Arief Basuki, Umar Khayam (Bandung Institute of Technology, Indonesia)
Naohiro Hozumi (Toyohashi University of Technology, Japan)

<Architecture and Urban & Regional Development Engineering>

**Development of The Structure and Construction of Seaweed Farmer's Residence
in Bantaeng Regency..... 83-89**

Pratiwi Mushar, Victor Sampebulu' (Hasanuddin University, Indonesia)

**The Effect of Air Distribution System towards Indoor Air Quality
(Case Study: Auditorium of Phinisi Tower)..... 90-97**

Yetti Yunianti Ishak, Baharudding Hamzah, Rosady Mulyadi (Hasanuddin University, Indonesia)

<Multidisciplinary Engineering>

**Deformation Analysis of Self-Expanding Stent Considering Plaque
and a New Expanding Mechanism 98-106**

Katsuhiko Sasaki, Yukiko Tomooka, Ryo Takeda (Hokkaido University, Japan)

Achmad Syaifudin (Sepuluh Nopember Institute of Technology, Indonesia)

**Comparative Study on Search Performance between GA and PSO
for Stacking Optimization of Laminated Plates..... 107-116**

Michio Innami (Hokkaido Polytechnic College, Japan)

Yoshihiro Narita (Hokkaido University, Japan)

Inorganically Precipitated Phosphates and Carbonates to Improve Porous Material Properties

Debendra Neupane,^a Hideaki Yasuhara,^{b*}, Heriansyah Putra,^c Naoki Kinoshita,^d

^aPenta-Ocean Construction Co., LTD. Email: deben646@yahoo.com

^bDepartment of Civil and Environmental Engineering, Faculty of Engineering, Ehime University. Email: yasuhara.hideaki.me@ehime-u.ac.jp

^cDepartment of Civil and Environmental Engineering, Faculty of Agricultural Technology, Bogor Agricultural University.

Email: heriansyahptr@apps.ipb.ac.id

^dDepartment of Civil and Environmental Engineering, Faculty of Engineering, Ehime University. Email: kinoshita.naoki@ehime-u.ac.jp

Abstract

Inorganically precipitated metal phosphate and metal carbonates may improve the physical and mechanical properties of the porous materials. Two types of porous materials i.e., sand and concrete, are examined. The phosphate and carbonate minerals of calcium and magnesium are appraised. Two series of experiments are conducted. In the first series of experiments, the efficacy of the inorganic grout is examined to improve the mechanical properties of sandy soil. In the second series of experiments, the efficacy of the inorganic phosphate to reduce the permeability of concrete is evaluated. The potential of these combinations is also appraised to reduce the permeability through the concrete cracks. The results exhibit that the reduction of the permeability through the cracks up to 3 orders of magnitude is possible.

Keywords: Carbonate; crack sealing; phosphate; inorganic precipitation; soil improvement

1. Introduction

Soil is the foundation of almost all engineering projects. For the safe and proper functioning of the civil engineering structures, they should be founded on firm soil. The physical and mechanical properties of soil should meet certain requirements for the structures to be founded on it. The properties of soils may not always be adequate. Soil improvement is necessary in places where the soils do not meet the engineering requirements. Grouting should be one of the solutions, and the development of a new grouting technique is aimed in this work.

Chemical grouting has been studied for its various possible applications such as preservation of the limestone monuments [1], plugging up the pores of oil recovery reservoir rocks and removing the contaminants in groundwater systems [2], repairing the cracks in concrete [3], reducing the swelling potential of clayey soil, mitigation of the liquefaction potential of soil [4], [5], and soil permeability control and improvement [6]–[10].

Research on carbonate and phosphate precipitation and their solidification has been conducted as potential soil improvement and permeability control technique. The precipitation within the soil samples reduced the permeability significantly [8], [9]. Application of calcium phosphate compound (CPC-chem) have been reported as a promised method for as the soil improvement technique [5], [11], [12]. The CPC-chem has the two unique characteristics; its pH is dependent on its solubility and it exhibits a self-setting mechanism [13]. In addition, the CPC-chem is easy to obtain, safe to handle, non-toxic, and recyclable. Therefore, it may be one of the suitable materials for civil engineering applications [5].

Concrete is used as most popular construction materials all over the world. The maintenance of the constructed concrete is a main issue for our sustainable society. Novel methodology to repair the cracked concrete is required for this purpose. In this work, various chemicals which are expected to give carbonates and phosphate minerals of calcium and magnesium are examined. The combinations that produce hard crystals and that have considerable time before the precipitation begins are selected. Small scale sand samples are prepared and treated with the newer grout. The newer grout is also evaluated for its possible application in lowering the permeability through the cracked concrete.

*Corresponding author. Tel.: +81-89-927-9853
3, Bunkyo-cho, Matsuyama, Japan, 790-8577

2. Precipitation test

The main objective of the experiments presented in this work is to evaluate the methods of mineral precipitation. Mineralized phosphates and carbonates are produced by allowing soluble salts of calcium and magnesium to react with soluble carbonates, bicarbonates and phosphates. The chemicals utilized in this study are summarized in Table 1.

Table 1. Summary of the evaluated chemicals.

Soluble metal salts of		Soluble carbonate, bicarbonate and phosphate	pH controller
Calcium	Magnesium		
CaCl ₂	MgCl ₂	Na ₂ CO ₃	NaOH
Ca(NO ₃) ₂	Mg(NO ₃) ₂	NaHCO ₃	NH ₄ OH
	MgSO ₄	NaH ₂ PO ₄	

The precipitated materials are evaluated directly in the transparent PP (polypropylene) tubes. Several chemical combinations are appraised. The combinations that bring about an insoluble, crystalline material at the bottom of the tubes are shown in Table 2. The concentrations of reagents are selected by following the expected chemical equations in a way to obtain the final product concentration of 0.5 mol/L. Various combinations of chemicals, as shown in Table 1, are mixed thoroughly in PP tubes. The final volume of the mixed solution is 30 mL. The solution is allowed to react for two days in room temperature. After two days, the crystalline materials and the supernatant are separated. The crystalline materials are washed and dried in room temperature. Hard insoluble materials as shown in Fig. 1 are obtained. The precipitated materials may bind with soil particles to improve the mechanical properties of sandy soil. The precipitated material may plug the pore/cracks in concrete to reduce its permeability.

Table 2. Selected combinations for small cylinder experiment.

Exp. name	Chemical A [0.5 mol/L]	Chemical B [1.0 mol/L]	pH controller C	Expected precipitate [0.5 mol/L]
In24	Mg(NO ₃) ₂	NaHCO ₃	-	MgCO ₃
In25	Mg(NO ₃) ₂	NaHCO ₃	NaOH (0.10)	MgCO ₃
In28	MgSO ₄	NaHCO ₃	NaOH (0.10)	MgCO ₃
In29	MgSO ₄	NaHCO ₃	NH ₄ OH (0.15)	MgCO ₃
P-13	NaH ₂ PO ₄	Mg(NO ₃) ₂	NaOH (0.25)	Mg(H ₂ PO ₄) ₂
P-16	NaH ₂ PO ₄	MgCl ₂	NaOH (0.4)	Mg(H ₂ PO ₄) ₂

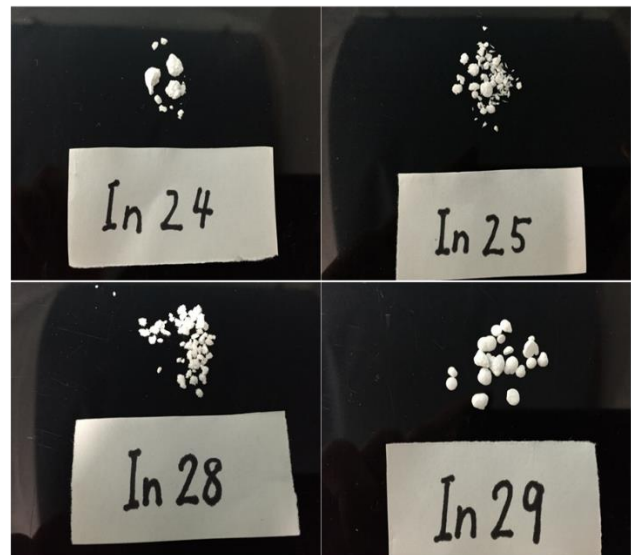


Figure 1. Precipitated materials of the selected combinations.

3. Small cylinder experiment

Cylindrical PVC (polyvinyl chloride) molds with a diameter of 50 mm and a height of 100 mm are utilized to prepare sand specimens. 300 g of silica sand (keisha #6) is carefully pluviated in air to acquire a relative density of 50 %. The grain size distribution of the sand used is shown in Fig. 2. Grout solutions A and B, and catalyst C as shown in Table 2 are blended together. One pore volume of the blended solution (i.e., grout) is poured into the dry sand specimens. Pouring is continued three times at an interval of 24 hours. After 24 hours of the final pouring, 150 mL of distilled water is poured to flush out the by-products. Distilled water is allowed to drain out for another 24 hours, and finally sand specimens are removed of the mold. The improvement in the treated soil specimens is observed. The specimens are capable to self-stand as shown in Fig. 3. Although hard and crystalline materials are obtained in the precipitation test, these materials are not found capable of improving the soil strength noticeably.

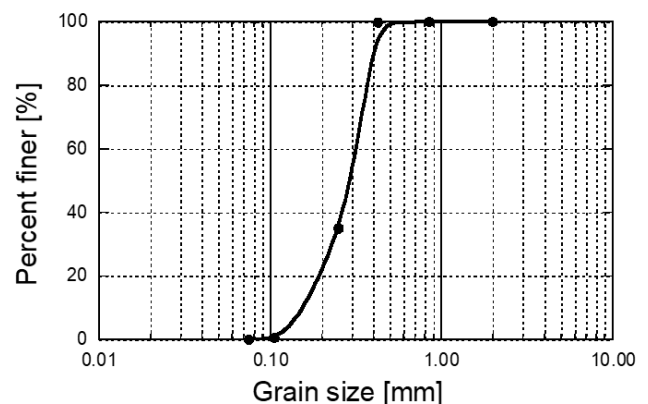


Figure 2. Grain size distribution of sand.

After conducting six experiments we came into conclusion that the precipitated materials, in spite of their hardness, in normal condition are poorly capable to adhere with or bind the grains of the silica sand utilized in this experiment. The SEM images shown in Fig. 4 show that a very small fraction of precipitated materials take part in making connections between the soil particles making anchors with each other. Further research is required to achieve a good bonding from the inorganically precipitated materials.

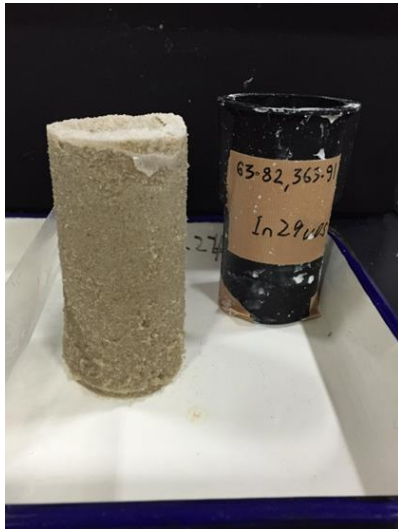


Figure 3. Self-standing treated specimen.

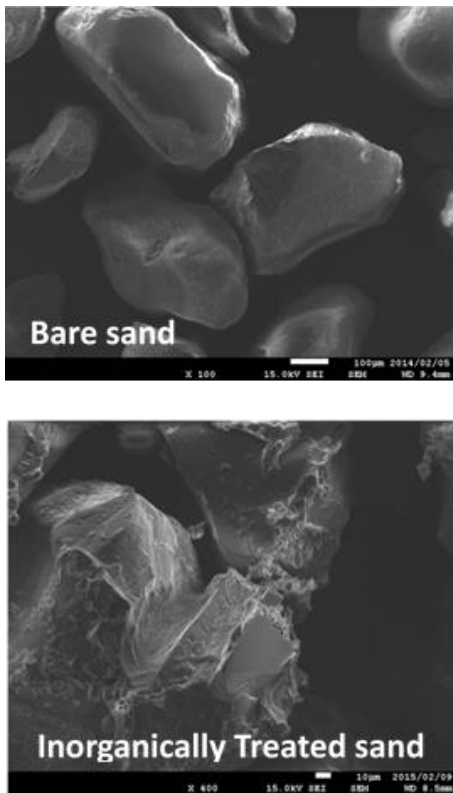


Figure 4. SEM image of bare sand and inorganically treated sand.

4. Concrete permeability test

Cracks in concrete act as pathways that allow water and other aggressive chemicals to penetrate through it, enabling its deterioration [14]. Highly permeable concrete cracks increase the risk of damage due to freezing and thawing. The permeability of the hydraulic structures should be well controlled to reduce seepage. The mineralized phosphate grout which may reduce the permeability of the cracked concrete by plugging the cracks and fractures is evaluated. The method of reducing permeability helps to improve the resistance to chemical problems, such as sulphate attack, chloride ion penetration.

The evaluated grout is composed of a mixture of NaH_2PO_4 and $\text{Mg}(\text{NO}_3)_2$. In this method, the rate of precipitation can be controlled by adding NaOH to NaH_2PO_4 solution before mixing with $\text{Mg}(\text{NO}_3)_2$. A concentration of 0.2 mol/L of NaOH is adjusted in this study in a way that the precipitation starts to occur after about 4 hours of mixing. The expected reaction is given in Eq. 1.



The permeability reduction method may be applicable in mass concrete where fast setting grouts and grouts with high viscosity cannot reach the required depth of concrete. Since the rate and time of precipitation can simply be controlled by adjusting the concentration of NaOH . This method may also be applicable to plug the fractured rock in the underground rock cavern for petroleum storage.

4.1. Experimental procedure

Concrete cylinders with a diameter of 10 cm and a height of 20 cm, in PVC pipes with an internal diameter of 10 cm and a height of 30 cm are utilized. The schematic of the prepared specimen is shown in Fig. 5.

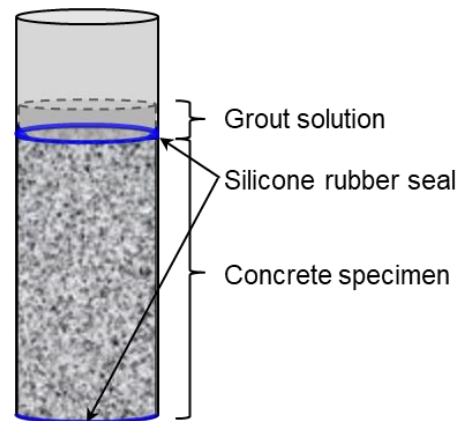


Figure 5. Schematic of the concrete specimen.

The specimens are cracked in splitting tensile testing machine (Brazilian Test machine) as shown in Fig. 6. The space in between the concrete specimen and the PVC pipe is sealed with silicone rubber as shown in Fig. 5. The silicone

rubber is allowed to set for 1 day. The specimen is immersed in water for 7 days to make it fully saturated. The initial permeability of the specimen is evaluated.

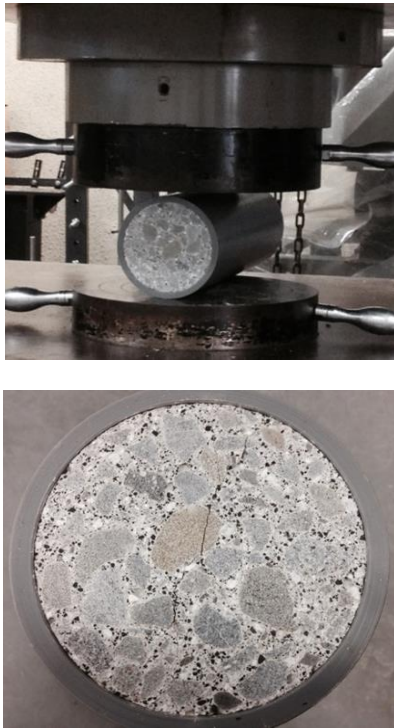


Figure 6. Preparation of the cracked concrete specimen.

The schematic for the permeability experiment is shown in Fig. 7. As illustrated in the figure, the PVC pipe with concrete specimen is set in an arrangement which allows to inject and drain the water. A water tank and adjustable pressure pump is mounted in the injection side. The drained water is collected in a beaker set on a weighing machine. The weighing machine is connected to a data logger which records the flow through the specimen at every 5 seconds. Different injection pressure is applied for different specimens. The injection pressure depends upon the flow rate through the specimens. If the flow rate is high, low pressure is maintained and if the flow rate is low relatively higher pressure is maintained. For a specimen with a wide crack, several centimetres pressure head was enough to maintain the flow. For the specimen with very low flow rate, such as treated specimens, the pressure required to maintain the flow should be several tens of kPa.

After the evaluation of the initial permeability, the specimen is removed from the permeability experiment set-up to inject the grout. 100 mL freshly prepared grout solution is poured from the surface of the specimen as shown in Fig. 5. The grout is freely allowed to permeate through the cracks for two days. Grout is injected three times at an interval of every two days. Before the application of second and the third grout, the solution retained above the specimen, and the precipitated material on the surface are removed. The top surface should be cleaned before the new injection,

otherwise the precipitated material restricts the fresh grout to flow into the cracks. Similarly, the older grout solution may affect the reaction rate of the newly injected grout solution which is not desirable. After completing the third grout application, the retained solution and the precipitated material at the concrete surface are removed. The specimen is arranged to permeability test set-up, and the final permeability test is conducted.

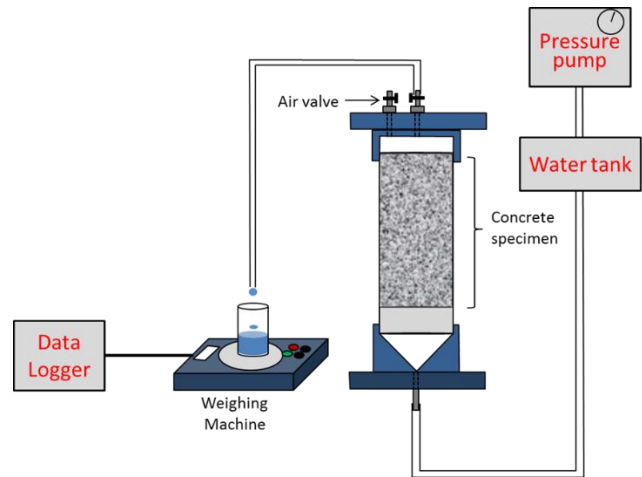


Figure 7. Schematic of the permeability experiment.

4.2. Results and discussion

Summary of the concrete specification, grout composition and grout application are given in Table 3. Altogether 6 specimens are experimented. Experiment P1 and P2 are conducted to examine the distribution of the grout inside the concrete along the major cracks. After the treatment, specimens are removed from the PVC mold and broken along one of the major cracks using split tensile test (Brazilian Test) machine. The distribution of the grout along one of the major cracks is shown in Fig. 8. As is apparent in Fig. 8, the grout is observed to distribute throughout the length of the specimen.

Table 3. Summary of the permeability test.

Specimen size	$\phi = 100 \text{ mm}$, $h = 195 \text{ mm}$
Immersed in water	for 7 days
Solution injection	100 mL each, 3 times at an interval of every 2 days
Grout content	NaH_2PO_4 [1.0 mol/L] + $\text{Mg}(\text{NO}_3)_2 \cdot 6\text{H}_2\text{O}$ [0.5 mol/L] + NaOH [0.2 mol/L]

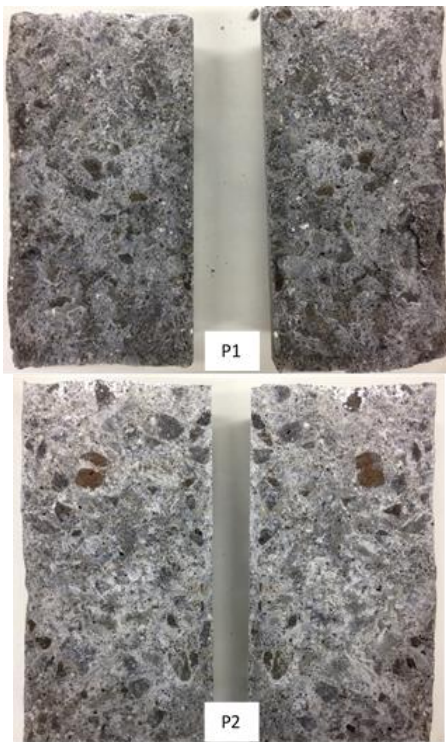


Figure 8. Treated specimens is cut along one of the major crack (white material is phosphate).

Experiment P3 and P4 are conducted to evaluate the evolution of permeability. The comparison of the flow rates through the concrete specimen before and after treatment are shown in Fig. 9. The flow rates are consistent for given water pressures which validates the permeability test results. The flow rate has been noticeably reduced after treatment. As shown in Fig. 9 (P3), flow occurs at low heads (15 cm) before the treatment. However, after the treatment, flow occurs only at high head (9 kPa). Moreover, discharge is very low after the treatment even at a relatively higher pressure (i.e., 82 kPa) in case of P4.

The change in permeability of the concrete specimens before and after the treatment is shown in Fig. 10. As is observed in the figure, remarkable reduction of permeability is obtained through the treated concrete specimens. The reduction of permeability is up to 3 orders of magnitude. The final hydraulic conductivity obtained in case of P4 is 5.99×10^{-6} cm/s. The equivalent permeability equals 6.11×10^{-15} . The permeability of the treated concrete is nearly equal to the permeability of the intact concrete. These results show that the method of phosphate grouting is capable of reducing the permeability of the concrete specimens considerably.

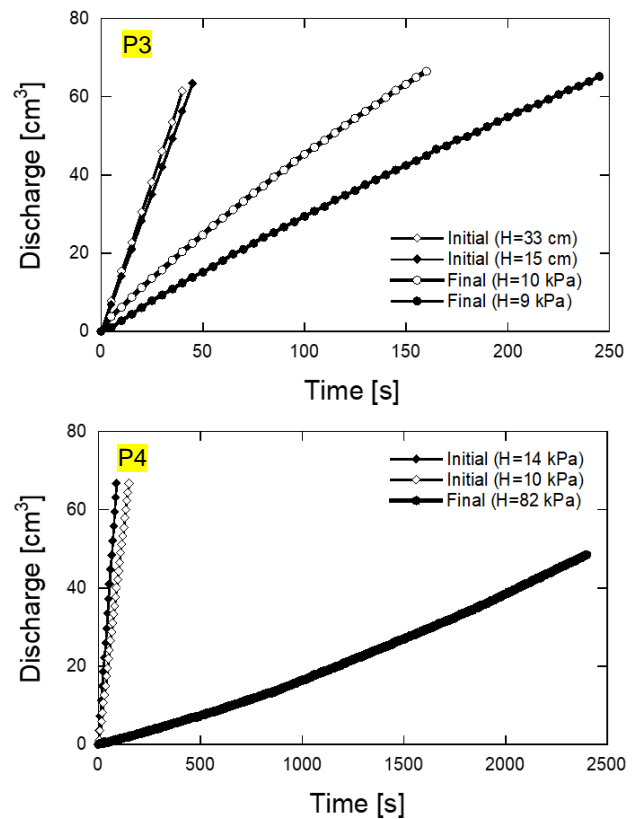


Figure 9. Initial and final flow rate through the concrete specimens (P3 and P4).

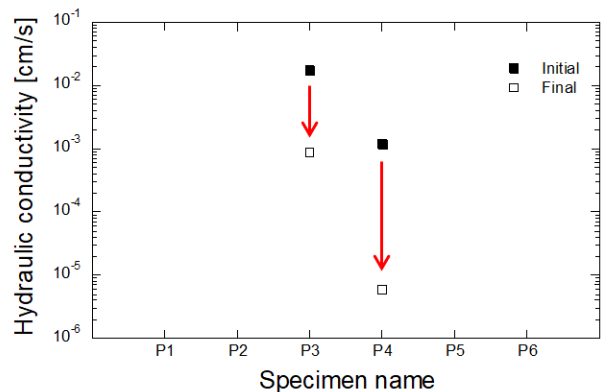


Figure 10. Initial and final permeabilites of the treated samples.

5. Conclusions

Inorganically precipitated minerals of phosphates and carbonates were appraised. The inorganic reactions were relatively simple and easy to control in comparison with the organic reactions. Inorganically precipitated materials were used to evaluate the mechanical properties of treated soil specimens. The soil specimens treated with inorganic grout were able to self-stand.

Afterwards, inorganic grout was utilized to reduce the permeability of the cracked concrete specimens. Cracked concrete specimens were treated three times with grout.

Permeability of the specimens before treatment and after treatment was measured. An appreciable reduction in permeability was achieved in the treated sample. The reduction in permeability was up to 3 orders of magnitude. The injected grout was also found to distribute uniformly along the cracked surface which showed the uniformity of this grouting technique. This method may be useful to plug the cracked concrete for enhancing its hydraulic performance.

Acknowledgements

This work has been partly supported by research grant from the Penta-Ocean Construction Co., LTD., Tokyo, Japan. This support is gratefully acknowledged.

References

- [1] S. M. Al-Thawadi, "Ureolytic Bacteria and Calcium Carbonate Formation as a Mechanism of Strength Enhancement of Sand," *J. Adv. Sci. Eng. Res.*, vol. 1, pp. 98–114, 2011.
- [2] M. Nemat, E. A. Greene, and G. Voordouw, "Permeability profile modification using bacterially formed calcium carbonate: comparison with enzymic option," *Process Biochem.*, vol. 40, no. 2, pp. 925–933, Feb. 2005.
- [3] W. De Muynck, D. Debrouwer, N. De Belie, and W. Verstraete, "Bacterial carbonate precipitation improves the durability of cementitious materials," *Cem. Concr. Res.*, vol. 38, no. 7, pp. 1005–1014, Jul. 2008.
- [4] V. Ivanov and J. Chu, "Applications of microorganisms to geotechnical engineering for bioclogging and biocementation of soil in situ," *Rev. Environ. Sci. Bio/Technology*, vol. 7, no. 2, pp. 139–153, Jun. 2008.
- [5] M. Akiyama and S. Kawasaki, "Novel grout material comprised of calcium phosphate compounds: In vitro evaluation of crystal precipitation and strength reinforcement," *Eng. Geol.*, vol. 125, pp. 119–128, Jan. 2012.
- [6] V. S. Whiffin, L. A. van Paassen, and M. P. Harkes, "Microbial Carbonate Precipitation as a Soil Improvement Technique," *Geomicrobiol. J.*, vol. 24, no. 5, pp. 417–423, Aug. 2007.
- [7] J. T. DeJong, B. M. Mortensen, B. C. Martinez, and D. C. Nelson, "Bio-mediated soil improvement," *Ecol. Eng.*, vol. 36, no. 2, pp. 197–210, Feb. 2010.
- [8] H. Yasuhara, D. Neupane, K. Hayashi, and M. Okamura, "Experiments and predictions of physical properties of sand cemented by enzymatically-induced carbonate precipitation," *Soils Found.*, vol. 52, no. 3, pp. 539–549, Jun. 2012.
- [9] H. Putra, H. Yasuhara, N. Kinoshita, and A. Hirata, "Application of magnesium to improve uniform distribution of precipitated minerals in 1-m column specimens," *Geomech. Eng.*, vol. 12, no. 5, pp. 803–813, 2017.
- [10] L. A. Van Paassen, M. P. Harkes, G. A. Van Zwieten, W. H. Van Der Zon, W. R. L. Van Der Star, and M. C. M. Van Loosdrecht, "Scale up of BioGrout: A biological ground reinforcement method," in *Proceedings of the 17th International Conference on Soil Mechanics and Geotechnical Engineering: The Academia and Practice of Geotechnical Engineering*, 2009.
- [11] E. Fernández, F. J. Gil, S. M. Best, M. P. Ginebra, F. C. M. Driessens, and J. A. Planell, "Improvement of the mechanical properties of new calcium phosphate bone cements in the CaHPO₄ · 2H₂O-Ca₃(PO₄)₂ system: Compressive strength and microstructural development," *J Biomed Mater Res*, vol. 41, pp. 560–567, 1998.
- [12] M. Akiyama and S. Kawasaki, "Microbially mediated sand solidification using calcium phosphate compounds," *Eng. Geol.*, vol. 137–138, pp. 29–39, Jun. 2012.
- [13] M. S. Tung, "Calcium Phosphates: Structure, Composition, Solubility, and Stability," in *Calcium Phosphates in Biological and Industrial Systems*, Z. Amjad, Ed. Boston, MA: Springer US, 1998, pp. 1–19.
- [14] C.-M. Aldea, S. P. Shah, and A. F. Karr, "Permeability of cracked concrete," *Mater. Struct.*, vol. 32, pp. 370–376, 1998.

Minimum Weight Design of Composite Panel under Aeroelastic Constraint

Shinya Honda,^{a,*} Gaku Yokoyama,^b

^aDepartment of Human Mechanical Systems & Design, Faculty of Engineering, Hokkaido University. Email: honda@eng.hokudai.ac.jp

^bDepartment of Human Mechanical Systems & Design, Faculty of Engineering, Hokkaido University.

Abstract

The present study minimizes the number of layers of wing shaped plates fabricated by laminated composite (CFRP) under aeroelastic constraint which keeps stable flutter speed. The finite element analysis (FEA) for the aeroelastic characteristics requires considerable calculation effort. Therefore, the response surface method (RSM) is utilized to reduce the computational time for optimization where an approximate expression uses bending rigidity of composite plates as input and flutter speed as output. Then, distributed genetic algorithm (DGA) is employed as an optimizer and minimizes numbers of layers of composite plates by designing fiber orientation angles. The optimum wing model shows large amount of weight reduction and enough flutter speed in less computational time than without RSM.

Keywords: Aeroelastic flutter; genetic algorithm; laminated composite; optimum design

1. Introduction

In aerospace industry, weight saving of airframes is the most important issue due to increasing fuel costs, and use of composite materials, especially carbon fiber reinforced plastics (CFRP), are mainstream of aircraft development. CFRP are utilized for structures by stacking orthotropic layers because they have high specific strength and stiffness [1]. Design of its lay-up configurations enables aeroelastic tailoring, which controls stiffness of wings to meet aeroelastic requirements. Aeroelasticity is a field of study focusing on interactions among aerodynamic force, elastic force and inertia force for airframes [2]. Weisshaar [3] showed that composite materials are superior in aeroelastic tailoring. In aeroelastic problems, flutter [4] is critical in particular. Kameyama and Fukunaga [5] observed flutter properties of composite plates by using lamination parameters. Guo [6] optimized composite wings to satisfy weight and flutter requirements. These reports conducted aeroelastic tailoring for composite wings, however, there are few publications that aim at weight minimization of

composite wings and search practical lay-up configurations in consideration of lay-up constraint.

The present paper proposes the practical optimization method for lightweight aircrafts. Distributed Genetic Algorithm (DGA) [7] is employed as an optimizer. In the optimization, fiber orientation angles of laminated composites are assigned to design variables, and the critical value of flutter speed is imposed as the constraint.

The optimization problem requires a lot of calculation effort for aerodynamic analyses of the wing shaped models by the finite element analysis (FEA). Therefore, Response Surface Method (RSM) is involved in the optimization. The RSM is available to various optimization problems in order to reduce computational cost. Todoroki and Ishikawa [8] studied the optimization of laminate stacking sequence for maximizing buckling load with Genetic Algorithm (GA) and the RSM. The optimum wing model obtained by the optimization in less computational time showed the effective weight reduction and enough resistance to the flutter. The present study employs MD. Nastran for aerodynamic analysis and MATLAB for other optimization process.

*Corresponding author. Tel.: +81-11-706-6415
Kita-13, Nishi-8, Kita-ku
Sapporo, Hokkaido, Japan, 060-8628

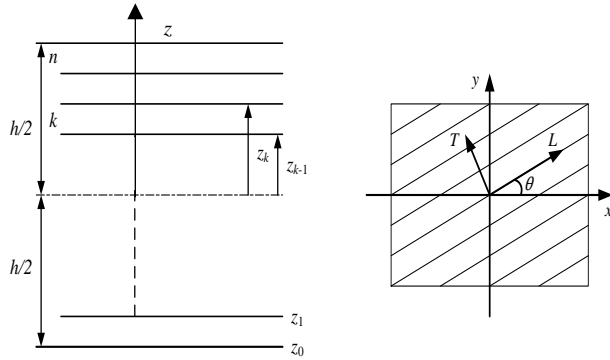


Figure 1. The coordinate systems of laminated plates.

and minor Poisson ratios, z_k is the distance from the plate middle surface to the upper surface of the k th layer, and θ is the fiber orientation angle in the k th layer.

2.2. Finite element analysis

The finite element model with four-node elements as shown in Fig. 2 is used for structural and aerodynamic finite element analyses (FEA) by MD. Nastran. In structural analysis, the lowest four vibration mode shapes and natural frequencies are calculated. In aerodynamic analysis, critical air speed leading to flutter V_F is evaluated with the $\Delta V_F = 1$ m/s. Dimensions of this model and material constants for CFRP are defined as

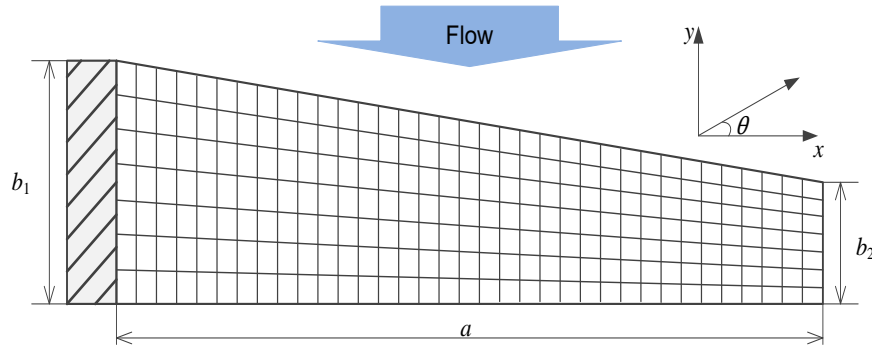


Figure 2. The finite element mesh model.

2. Analysis method

2.1. Bending stiffness of laminated plates

A symmetrically N -laminated plate is considered as shown in Fig. 1. The bending stiffness D_{ij} of this plate is given by

$$D_{ij} = \frac{1}{3} \sum_{k=1}^N (\bar{Q}_{ij})_k (z_k^3 - z_{k-1}^3), \quad (i, j = 1, 2, 6)$$

$$\begin{aligned} \bar{Q}_{11} &= Q_{11}l^4 + 2(Q_{12} + 2Q_{66})l^2m^2 + Q_{22}m^4 \\ \bar{Q}_{12} &= Q_{12}(l^4 + m^4) + (Q_{11} + Q_{22} - 4Q_{66})l^2m^2 \\ \bar{Q}_{22} &= Q_{11}m^4 + 2(Q_{12} + 2Q_{66})l^2m^2 + Q_{22}l^4 \\ \bar{Q}_{16} &= (Q_{11} - Q_{12} - 2Q_{66})l^3m - (Q_{22} - Q_{12} - 2Q_{66})lm^3 \\ \bar{Q}_{26} &= (Q_{11} - Q_{12} - 2Q_{66})lm^3 - (Q_{22} - Q_{12} - 2Q_{66})l^3m \\ \bar{Q}_{66} &= (Q_{11} + Q_{22} - 2Q_{12} - 2Q_{66})l^2m^2 + Q_{66}(l^4 + m^4) \end{aligned} \quad (1)$$

$$Q_{11} = \frac{E_L}{1 - \nu_{LT}\nu_{TL}}, \quad Q_{22} = \frac{E_T}{1 - \nu_{LT}\nu_{TL}},$$

$$Q_{12} = \frac{\nu_{TL}E_L}{1 - \nu_{LT}\nu_{TL}} = \frac{\nu_{LT}E_T}{1 - \nu_{LT}\nu_{TL}},$$

$$Q_{66} = G_{LT}, \quad l = \cos \theta, \quad m = \sin \theta$$

where E_L and E_T are the moduli of elasticity in the L and T directions, G_{LT} is the shear modulus, ν_{LT} and ν_{TL} are the major

$$\begin{aligned} a &= 1000 \text{ mm}, & b_1 &= 300 \text{ mm}, \\ b_2 &= 150 \text{ mm}, & t &= 0.19 \text{ mm} \\ E_L &= 152 \text{ GPa}, & E_T &= 8.00 \text{ GPa}, \\ G_{LT} &= 4.00 \text{ GPa} \\ \nu_{LT} &= 0.340, & \rho &= 1600 \text{ kg/m}^3 \end{aligned} \quad (2)$$

where the thickness of one ply is denoted by t .

In order to compare with optimized models, the benchmark model with $[45^\circ/0^\circ/-45^\circ/90^\circ]_{4s}$ lay-up is introduced here. As a result of aerodynamic analysis, V_F of the benchmark model is obtained as

$$V_{F \text{ required}} = 165 \text{ m/s} \quad (3)$$

3. Response surface method

RSM gives an approximate equation between responses y and predictor variables x . The present study employs the response surface equation written as

$$\begin{aligned} y &= \beta_0 + \beta_1x_1 + \beta_2x_2 + \beta_3x_3 + \beta_4x_4 \\ &+ \beta_5x_5 + \beta_6x_6 + \beta_7x_7 + \beta_8x_8 + \beta_9x_9 \\ &+ \beta_{10}x_{10} + \beta_{11}x_{11} + \beta_{12}x_{12} + \beta_{13}x_{13} \\ &+ \beta_{14}x_{14} + \beta_{15}x_{15} + \beta_{16}x_{16} + \beta_{17}x_{17} \\ &+ \beta_{18}x_{18} + \beta_{19}x_{19} + \beta_{20}x_{20} \end{aligned}$$

with

$$\begin{aligned}
 x_1 &= D_{11}, x_2 = D_{16}, x_3 = D_{22}, x_4 = D_{26}, \\
 x_5 &= D_{66}, x_6 = D_{11}^2, x_7 = D_{16}^2, x_8 = D_{22}^2, \\
 x_9 &= D_{26}^2, x_{10} = D_{66}^2, \\
 x_{11} &= D_{11} \times D_{16}, x_{12} = D_{11} \times D_{22}, \\
 x_{13} &= D_{11} \times D_{26}, x_{14} = D_{11} \times D_{66}, \\
 x_{15} &= D_{16} \times D_{22}, x_{16} = D_{16} \times D_{26}, \\
 x_{17} &= D_{16} \times D_{66}, x_{18} = D_{22} \times D_{26}, \\
 x_{19} &= D_{22} \times D_{66}, x_{20} = D_{26} \times D_{66}
 \end{aligned} \tag{4}$$

Table 1. Values and F-statistics of the coefficients.

	Values	F-statistics
b_0	154.0	1996270
b_1	20.01	7330
b_2	-40.41	7680
b_3	4.933	567.2
b_4	22.92	2869
b_5	49.51	21543
b_6	5.388	184.0
b_7	-168.8	26486
b_8	3.867	142.9
b_9	-72.15	6029
b_{10}	-8.355	155.7
b_{11}	-9.854	85.91
b_{12}	4.720	96.53
b_{13}	13.07	221.0
b_{14}	4.470	37.65
b_{15}	-13.58	225.2
b_{16}	112.6	7619
b_{17}	9.373	45.33
b_{18}	-2.947	9.587
b_{19}	-	0.02932
b_{20}	-5.311	16.86

where y , x and β represent flutter speed, bending stiffness and unknown coefficients respectively. Here, D_{12} is omitted due to linear relationship between D_{12} and D_{66} . The linear multiple regression model is expressed as

$$\mathbf{y} = \mathbf{X}\boldsymbol{\beta} + \boldsymbol{\varepsilon}$$

$$\mathbf{y} = \begin{Bmatrix} y_1 \\ y_2 \\ \vdots \\ y_n \end{Bmatrix}, \quad \mathbf{X} = \begin{bmatrix} 1 & x_{11} & x_{12} & \cdots & x_{1k} \\ 1 & x_{21} & x_{22} & \cdots & x_{2k} \\ \vdots & \vdots & \vdots & \ddots & \vdots \\ 1 & x_{n1} & x_{n2} & \cdots & x_{nk} \end{bmatrix} \tag{5}$$

$$\boldsymbol{\beta} = \begin{Bmatrix} \beta_0 \\ \beta_1 \\ \vdots \\ \beta_k \end{Bmatrix}, \quad \boldsymbol{\varepsilon} = \begin{Bmatrix} \varepsilon_1 \\ \varepsilon_2 \\ \vdots \\ \varepsilon_n \end{Bmatrix}$$

where n is the number of sampling point, k is the number of variables, and ε is an error vector. The unbiased estimator \mathbf{b} of β is obtained by the least square method as follows [8].

$$\mathbf{b} = (\mathbf{X}^T \mathbf{X})^{-1} \mathbf{X}^T \mathbf{y}$$

$$\mathbf{b} = \begin{Bmatrix} b_0 \\ b_1 \\ \vdots \\ b_k \end{Bmatrix} \tag{6}$$

The RSM equation is created along the following three steps.

1. The database of V_F derived random bending stiffness of the wing model shown in Fig. 2 is created by aerodynamic analysis. In order to create this database, 4500 times of FEA trials are conducted. Then, the data quantity is reduced to 3923 due to erasing of overlapped data, and the values of bending stiffness are normalized based on the maximum and minimum value.
2. The unbiased estimator \mathbf{b} is given by Eq. (6) for the database, where $k = 20$ and $n = 3923$.
3. F-test is performed to verify the validity of \mathbf{b} with significance level 0.01 as shown in Table 1. Finally, the response surface equation is written as follows.

$$\begin{aligned}
 y &= 154.0 + 20.01x_1 - 40.41x_2 + 4.933x_3 \\
 &+ 22.92x_4 + 49.51x_5 + 5.388x_6 - 168.8x_7 \\
 &+ 3.867x_8 - 72.15x_9 - 8.355x_{10} - 9.854x_{11} \\
 &+ 4.720x_{12} + 13.07x_{13} + 4.470x_{14} - 13.58x_{15} \\
 &+ 112.6x_{16} + 9.373x_{17} - 2.947x_{18} - 5.311x_{20}
 \end{aligned} \tag{7}$$

The adjusted determination coefficient is 0.8915 and indicates excellent accuracy of this equation.

4. Optimization method

Distributed Genetic Algorithm (DGA) [7] is adopted to solve the stacking sequence optimization problem as follows.

- [Objective function] Minimize n ($1 \leq n \leq 32$)
- [Subject to] $V_F \geq V_{F \text{ required}}$
- Symmetric lamination
- Less than 3 consecutive lamination of the same θ (8)
- [Design variable] θ_i ($i = 1, 2, \dots, n/2$)
- $-85 \leq \theta \leq 90$ ($\Delta\theta = 5^\circ$)

In this DGA, a large population is distributed to some islands labeled by each number of lamination. Thus, weight reduction is performed by selection of labeled islands as the number of lamination. At the same time, lay-up configurations in each island are optimized. Fitness H is evaluated independently in each islands as follows.

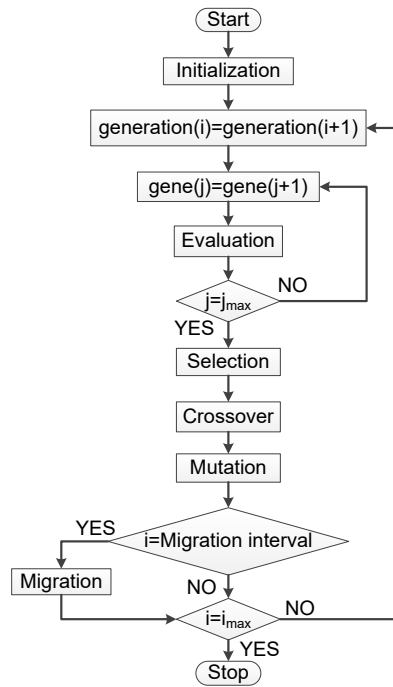


Figure 3. Flowchart of DGA

$$H = V_F \tag{9}$$

Moreover, DGA has the unique operation named as migration. This operation exchanges some individuals among some islands, and it contributes to keep diversity of populations. As DGA parameters, the number of generation is 100, total population is 150, crossover rate is 0.9, mutation rate is 0.1, the number of islands in one generation is two and migration interval is 10. This optimization adopts elitist strategy, roulette wheel selection and 2-point crossover. Fig. 3 illustrates flowchart of DGA. Table 2 represents decoding in DGA.

The optimization described above is performed in two cases Opt. A and Opt. B. In Opt. A, V_F is calculated by FEA in each time. On the other hand, estimated value y of Eq. (7) is substituted for V_F to reduce computational load in Opt. B.

5. Results and discussions

Table 3 shows the comparison of the benchmark model and two optimum models. The optimum solutions in Opt. A and B present 12.5 % reduced weight from the benchmark model and keep enough V_F . In Opt. B, $y = 179$ m/s is derived as the optimum solution with estimation equation. The calculated value by FEA for the obtained solution is 176 m/s, and the error is only 1.70 % in spite of 70 % reduction of FEA trials. Since the lay-up configurations of the optimum models contain the angles strong to torsion such as 45° , -45° , 40° and -40° , it is revealed that the optimum solutions have high D_{66} values, resulting in better resistance to flutter. Moreover, the values of D_{16} decrease compared to the benchmark model. These results indicate the importance of

Table 2. Decoding

Senary	Decimal	Phenotype (Fiber orientation angle)
00	0	0
01	1	5
11	7	10
10	6	15
12	8	20
02	2	25
22	14	30
21	13	35
20	12	40
23	15	45
13	9	50
03	3	55
33	21	60
32	20	65
31	19	70
30	18	75
34	22	80
24	16	85
14	10	90
04	4	-85
44	28	-80
43	27	-75
42	26	-70
41	25	-65
40	24	-60
45	29	-55
35	23	-50
25	17	-45
15	11	-40
05	5	-35
55	35	-30
54	34	-25
53	33	-20
52	32	-15
51	31	-10
50	30	-5

D_{66} and unimportance of D_{16} as observed from the F-statistics of b_5 and b_7 in Table 1.

Figures 4-6 show natural frequencies and vibration mode shapes for Bench mark model and both solutions of Opt. A and B. It is known from Figs. 4-6 that the natural frequencies for the bending modes decrease and torsional modes increase compared with the benchmark model since the lay-up configurations are strengthened against torsion.

6. Conclusions

The present study proposed the optimization method to reduce weight of wing shaped composite plates by using DGA and RSM. This method yielded the excellent optimum solution precisely in less computational time compared to the case without RSM. The obtained results revealed that assigning bending stiffness to predictor variables is effective to derive V_F as responses for RSM. In addition, the tested coefficients of the response surface equation showed the significant factors to keep enough V_F .

Table 3. Comparison between three models

	The benchmark model	Opt. A	Opt. B
Lay-up	[45/0/-45/90] _{4s}	[-40/45/45/-45/-30/40/-40/35/-65/-50/-5/-40/0/-65] _s	[-40/40/45/-40/-40/45/-40/30/-40/45/10/45/65/25] _s
V_F [m/s]	165	175	176
D_{11} [N·m]	1197	708.6	731.5
D_{12} [N·m]	385.5	441.0	452.1
D_{16} [N·m]	19.87	-56.13	-32.49
D_{22} [N·m]	1149	498.0	452.9
D_{26} [N·m]	19.87	-19.22	-1.610
D_{66} [N·m]	409.2	456.9	468.0
The number of layers	32	28	28
Weight [kg]	2.189	1.915	1.915
Reduced weight [%]	Reference value	12.5	12.5
aerodynamic FEA trials	-	15000	4500
Reduced FEA trials [%]	-	Reference value	70

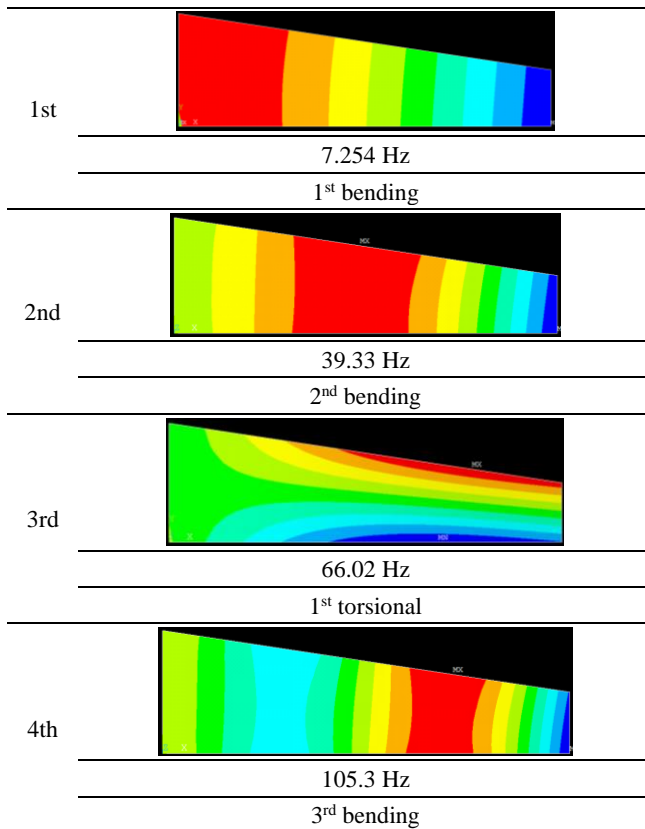


Figure 4. Vibration mode shapes and natural frequencies for benchmark model

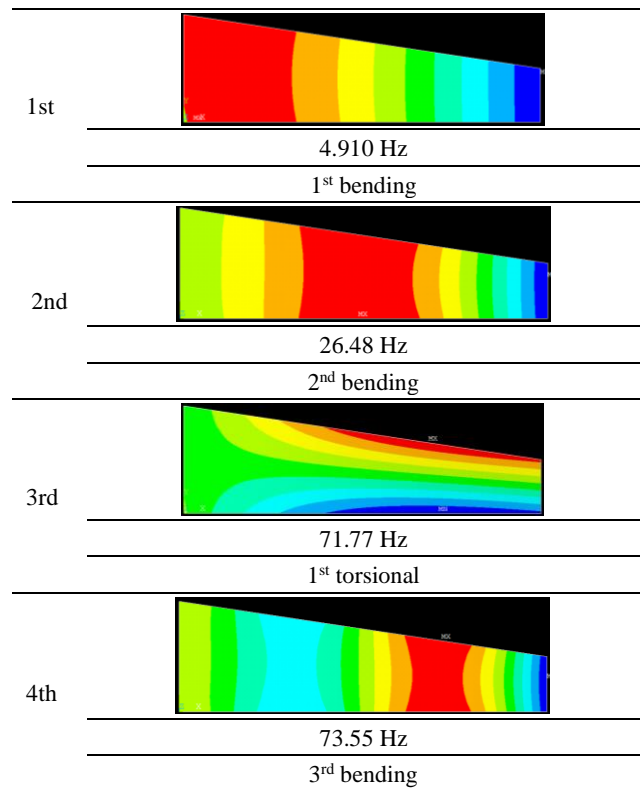


Figure 5. Vibration mode shapes and natural frequencies for Opt A

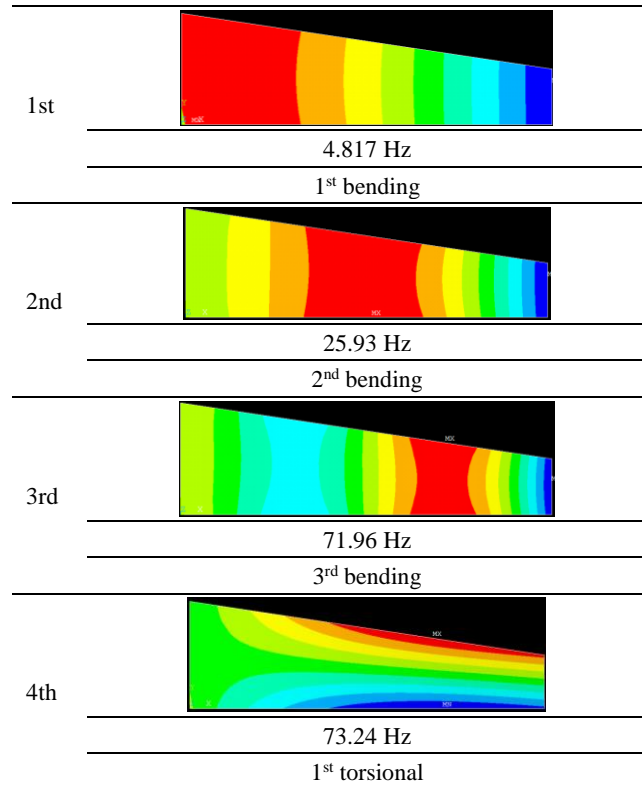


Figure 6. Vibration mode shapes and natural frequencies for Opt B

References

- [1]. Fukuda, H. and Ben, G. 1989. "Introduction of dynamics of composite materials," Kokonshoin (in Japanese).
- [2]. Washizu, K. 1957. "Aeroelastics," Kyoritsu (in Japanese).
- [3]. Weisshaar, T. A.. 1994. "Active Tailoring with Advanced Materials," *Journal of the Japan Society for Aeronautical and Space Sciences*, 42(487):455-461.
- [4]. Bisplinghoff, R. L., Ashley, H., and Halfman. R. L., 1996. "Aeroelasticity," Dover Publications.
- [5]. Kameyama, M. and Fukunaga, H. 2007. "Optimum Design of Composite Plate Wings for Aeroelastic Characteristics Using Lamination Parameters," *Computers & Structures*, 85:213-224.
- [6]. Guo, S.. 2007. "Aeroelastic Optimization of an Aerobatic Aircraft Wing Structure," *Aerospace Science and Technology*, 11:396-404.
- [7]. Hiroyasu, T., Miki, M. and Negami, M. 1999. "Distributed Genetic Algorithms with Randomized Migration Rate," in IEEE Proceedings of Systems, Man and Cybernetics Conference SMC'99, 1:689-694.
- [8]. Todoroki, A. and Ishikawa, T. 2004. "Design of Experiments for Stacking Sequence Optimizations with Genetic Algorithm Using Response Surface Approximation," *Composite Structures*, 64:349-357.

Modelling of Thin Structural Polymer Composites for Use of Automobiles -Review-

Daisuke Narita,^{a*} Yoshihiro Narita,^b

^aHokkaido University of Science Junior College, Teineku, Sapporo, Japan. Email: narita@hus.ac.jp

^bHokkaido University, C-BEST, Center of Technology, Faculty of Engineering, University of Hasanuddin, South Sulawesi, Indonesia.
Email: ynarita@eng.hokudai.ac.jp

Abstract

This review article introduces first a number of previous works and commercial examples on the use of fiber-reinforced polymer materials in the application to automobile structural components, and secondly considers the modeling for thin components of fiber-reinforced polymer composites with emphasis on the roofs and fenders of the automobiles. The need of this study seems obvious, since particularly in the sportive and high-grade automobiles, the composite materials have already replaced conventional metal materials resulting in the significant reduction of structural weight. In such application, laminated composite panels (shallow shells) are used for models of automotive panels. The structural components in the automobile are extensively exposed to vibration excitation and other external disturbances in practical use, and resonance phenomenon may cause disturbing effects such as noise and fatigue. One countermeasure for such negative effects is to make use of tailoring advantages for fiber reinforced laminated composites and the feasibility for optimization process is suggested.

Keywords: Automotive application; composite material; mechanical engineering; modeling; review

1. Introduction

Advanced composite materials are generally made of two or more material elements, namely fibers such as carbon or glass fibers, and matrix materials of thermoset or thermoplastic polymers. Particularly, carbon fiber is a flexible fabric-like soft material, but it has high strength and stiffness when it is under tension, almost equivalent to metal of equal size. The fiber is therefore used to act as reinforcing element in the base matrix material. Advantage of using polymer as the matrix material is that it can be molded into the shape of various parts that are stronger and lighter than today's steel and aluminum parts. For making a relatively large structural component with several different parts integrated, molding capability of the polymer composites become dominant by using the integrated molding.

The problem in using fiber-reinforced, polymer-based material for general industrial products is the high cost due to the high cost of fiber material itself, and therefore the use of composites has started mainly in less cost-sensitive aerospace and aeronautical industries. Another drawback is

to take longer production time due to molding and curing time, while metal thin parts are usually stamped in the order of seconds. In the present article, the use of polymer composite material reinforced by carbon fibers is considered in structural components of automobiles. The past progress is summarized through literature survey and practical applications found in commercial automobiles, and the analytical and numerical modeling approaches are presented for modeling of thin panels used in the automobile structure.

2. Literature review on application of composites in automobiles

When fiber-reinforced polymer composites are used in the structure of automobiles, they can yield significant reduction of vehicle weight due to their high strength-to-weight and stiffness-to-weight ratios. Many efforts of research and development have been done in the past few decades.

Das [1] examined the cost of automotive polymer composites in 2001 for the first time and assessed Doe Chemical's efforts to develop light weight materials in the automotive applications. This work addressed the use of composites extensively in automotive application, the unsolved issues for expanding the use, and the needs of

*Corresponding author. Tel.: +81-11-706-6415

Kita-13, Nishi-8, Kita-ku

Sapporo, Hokkaido, Japan, 060-8628

research for such challenges. As the title implied, the main focus was placed on studying the economic viability of these materials two decades ago. Some years later, a roadmap for future use of plastics and composites was shown [2] in 2007 for the safety of highly intensive automobiles. This work reported the approaches, activities and outcomes of the research to study advantages from the safety viewpoints of composites-intensive cars. The purpose of this report was therefore to review and examine the state of knowledge to identify the gaps, key research needs and potentials for safety enhancement.

In the year of 2012, two review papers were published. Andure and others [3] summarized basic knowledge of structural properties, mechanical properties and application examples of various type composites in automobiles. Mahajan and Aher [4] presented design method and vibration analysis of composite propeller shaft to discuss the advantage of replacing metal shaft with composite shaft. Rathnakar and Pandian [5] presented a comprehensive review on the use of polymer composites in automotive industry, and emphasized the promising technical possibilities for fabricating more automotive components with fiber composites. They concluded that the cost acts as the final arbitrator in the selection of particular composite material for a specific application. More recently, Pervaiz and others [6] reviewed situations of the main motives and current legislation, when the original equipment manufacturers (OEM) for automotive industries face for weight reduction. They also studied emerging effects in development of light-weighting materials on low-cost carbon economy. The most recent survey work was made by Masilamani and others [7] and they discussed in detail with the benefits of usage of carbon-fiber reinforced plastics (CFRP) in each part of car, i.e., bumper, hood or bonnet, roof and so on.

The review articles mentioned above dealt mostly with use of polymer composite materials with chemical fibers made from petroleum resource. From viewpoint of sustainability in natural resource, however, bio-composites (green-composites) may play more important role than before, and such materials deriving from renewable resources will be preferred as opposed to the exhaustible fossil products. Koronis and others [8] provided in 2013 a literature review in the broad field of bio (green) composites seeking for practical materials with a potential to be applied in the new future on automotive body panels. The literature [9] also provided in 2017 an overview of bio-composites application in the automotive, including the history and progressive steps that were taken to break into the production lines of some car-makers. This also offered an analysis of key factors that have motivated the research and practical adoption of bio-composites. The recent review by Fagorasi and Barbu [10] in 2017 considered a wide range of bio-composites issues with special reference to mechanical properties of fibers, interfacial adhesion and environmental implication.

The bumper, one of automotive structural elements, may be one of the most frequently applied targets of the advanced composites, since it contributes to vehicle crashworthiness and occupant protection at the time of front or rear collisions. Sapuan and others [11] presented a first review of polymer-based composite bumper system in 2002, and discussed proper bumper design, material selection and manufacturing process. After more than ten years in 2014, John and Alex [12] summarized the progress in various studies about the selection of composite materials for desirable production of bumpers. They specifically considered energy absorption, performance, cost, weight, service conditions, manufacturing process, availability of materials, and environment aspects. Similarly, Ezekwem [13] took up this problem by comparing two types of bumpers made from nylon composites and polyethylene with specific fillings. The mechanical properties of these materials showed superior characteristics on weight, cost and environment impact than conventional bumper, except for difficulty in mass production.

As compared to active research on bumper, analytical studies on mechanical design and material selection are limited on application of thin composites to bonnet and roof structure. They have been used in expensive automobiles such as sportive cars, and on-going examples are introduced in the next chapter. One of sparse literatures is the study on analysis and design of thermoplastic CFRP bonnet for pedestrian safety [14]. This study is one of the examples in the efforts to follow Japanese standard for pedestrian protection [15].

3. Practical examples in application of composites for automobiles

In recent years, the application of fiber reinforced polymer composite materials is expanding to not only to aeronautical and astronautical fields but also to commercial expensive vehicles. Such examples are found in the monocoque bodies of expensive sports cars as shown in Fig.1 and 2 for McLaren Automotive 720S [16] and Lamborghini Aventador [17], respectively. For thin panel structural components, such as bonnet and roof, some applications are seen for outer-surface panels in Fig.3 and Fig.4 for Lexus RCF [18] and Subaru WRXSTIS [19], respectively. These are not as considerably expensive as those shown in Fig. 1 and 2, but still belong to a class of luxurious cars. For inner-surface of bonnet and fender, the composites are already used for the panels where stiffening parts are included additionally. Those examples are seen in inner-surface of bonnet for Nissan GT- R in Fig. 5 [20] and in Fig. 6 for Toyota Prius [21]. In contrast to the applications above [16-21] to relatively thin panels, CFRP CFRP composites have been used in large production scale since in 1990's as propeller shafts, as shown in Fig. 7, to transmit torque from engine to wheels. The use for the propeller shafts brings significant effects on reduction of

vehicle weight by the design where no intermediate supports are necessary and the absorption of dynamic energy is made possible at the collision situation.



Figure 1. Monocoque body of McLaren 720S, [16].



Figure 2. Monocoque body of Lamborghini Aventador, [17]



Figure 3. Bonnet (outer surface) of Lexus RC F Carbon Exterior package, [18]



Figure 4. Bonnet (outer surface) of Subaru WRX STI S208 NBR, [19]



Figure 5. Bonnet (inner surface) of Nissan GT-R black edition, [20]



Figure 6. Bonnet (inner surface) of Toyota Prius PHV, [21]



Figure 7. Example of a propeller shaft made of CFRP material, [22]

In Europe, the nation-wide scale project started in 2000's under the title of TECABS (Technologies for Carbon fiber reinforced modular Automotive Body Structures). This project consisted of Volkswagen, Daimler Chrysler, material manufacturers and research institutes to develop lightweight cars and to improve fuel efficiency. Also in Japan, NEDO (New Energy and Industrial Technology Development Organization) started a nation-wide project titled "Research project for development of carbon-fiber reinforced composite material for reduction of automobile weight", and one of the outcomes was success in the fast production process of the combined structure of front-floor and front side member. Besides these works, recently one of production methods "RTM (Resin Transfer Molding)" has been successfully developed, and lower cost became possible to fabricate automotive structures, for example, a body of electric cars BMWi shown in Fig. 8.



Figure 8. Monocoque body of BMW i3, [23]

Next, some new regulation is explained here in connection to the bonnet design in Japan. This regulation introduced a new concept to protect heads of pedestrians encountered in traffic accidents, because the rate of serious injuries of pedestrians involved in accident is very high and most of them suffer heavy head injuries. For this problem, the design of bonnets and front surfaces is considered to mitigate the impact between bonnets and pedestrian heads. The impact is measured by assuming the case when the head model is hit against the car front in 40 km/h, as shown in Figs. 9 and 10. Some proposed counter-measures for design against impact include to unify the bending stiffness of bonnet, to set margins of movable range of bonnet and to keep distance to the hard part in the engine room, and also to design fenders being flexible enough.



Figure 9. Impact test for assumption of pedestrian head, [14]

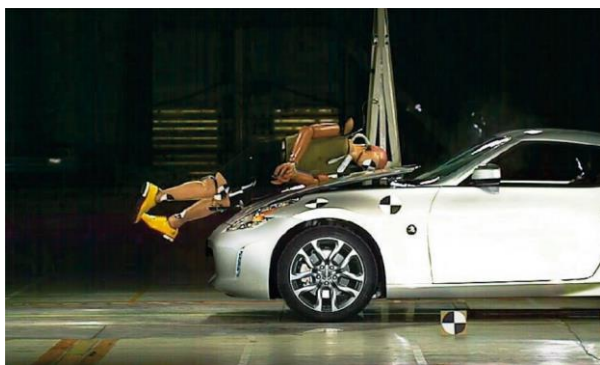


Figure 10. Collision test for assumption of a pedestrian, [23]

As previously mentioned, some examples already existed in application of CFRP composites to bonnet, their objectives are mostly for total weight reduction of the body, together with the function of energy absorption and global bending deformation not to break into the driver room at the time of collision. Kin and others [14] presented design of the bonnet made of CFTRP (carbon fiber thermoplastic plastics) to increase safety of pedestrians. The finite element analysis was made to follow the regulation for pedestrian safety, and the results showed that their designed CFTRP bonnet takes longer time to accept the impact, resulting in smaller damage to pedestrians' heads.

4. Modeling approaches to bonnet and roof of automobiles

This chapter overviews different modelling approaches to analyzed dynamic behaviors of thin panel structures. Some advantages and disadvantages of the approaches are summarized. The experimental modeling approach, such as the modal analysis technique [24], is not included in this work.

4.1. Analytical model of automobile panels

As shown in Fig.11, automobile panels may be modeled as shallow shell structure with non-uniform curvature. For this model, some works have been done by the present authors [25-30]. The dimension of the shell is assumed to be $a \times b$ as rectangular planform, and its z -coordinate ϕ measured from the mid-plane is defined by a cubic polynomial function of x and y in the coordinates shown in Fig.11, where c_{ij} ($i, j = 0, 1, 2, 3$) are shape coefficients to determine shell shapes, and they may be determined by the least square method to match with actual shell shapes of automobile panels.

$$\phi(x, y) = c_{00} + c_{10}x + c_{01}y + c_{20}x^2 + c_{11}xy + c_{02}y^2 + c_{30}x^3 + c_{21}x^2y + c_{12}xy^2 + c_{03}y^3 \quad (1)$$

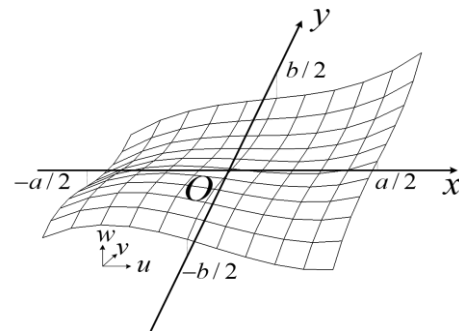


Figure 11. Coordinate system for analysis of doubly curved panel

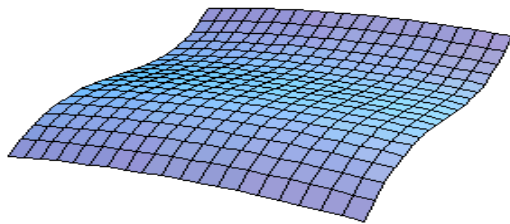


Figure 12. Fender models represented by a cubic function,

$$(a) \phi(x, y) = -0.1x^2 + y^3$$

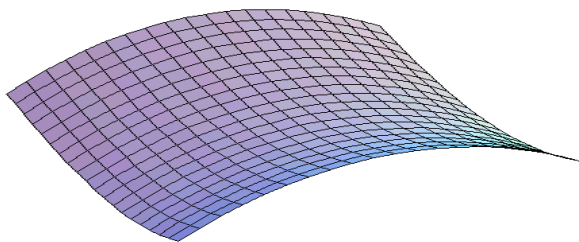


Figure 12. (b) $\phi(x, y) = 0.5x^2 - y^2 + 0.5x^2y$

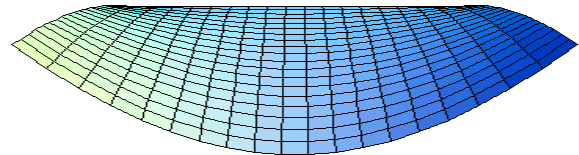


Figure 12. (c) $\phi(x, y) = 0.5x^2 - 0.1y^2 - x^2y$

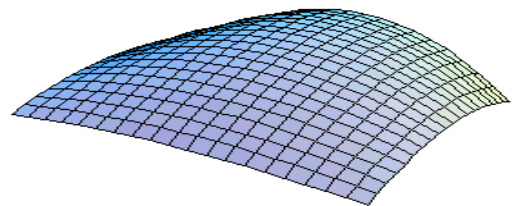


Figure 12. (d) $\phi(x, y) = -x^2 - 0.6y^2 - 1.5x^2y$

Four examples are presented in Fig. 11 to demonstrate the effectiveness of the present analytical model in practical situations. Fig. 12(a) is an example of a shell panel shape with both convex and concave curvature existing in one region and it is represented by $\phi(x, y) = -0.1x^2 + y^3$.

Figures 12(b)(c) and (d) are cases with only concave or convex curvature existing in the region, represented by the equations written in the figure captions.

Based on the Donnell-Mushtari theory, relation between displacements u , v and w and strains ϵ_x , ϵ_y and γ_{xy} is defined by

$$\begin{aligned} \epsilon_x &= \frac{\partial u}{\partial x} + \frac{w}{R_x}, \quad \epsilon_y = \frac{\partial v}{\partial y} + \frac{w}{R_y}, \\ \gamma_{xy} &= \frac{\partial v}{\partial x} + \frac{\partial u}{\partial y} + \frac{2w}{R_{xy}} \end{aligned} \quad (2)$$

In the Ritz method, vibration of composite shells with non-uniform curvatures may be analyzed, and the method is useful for the parametric study in varying boundary conditions, aspect ratios and shell shapes.

The Ritz method is a kind of energy method, and it evaluates strain and kinetic energies to derive mechanical responses, for example, natural frequencies. The strain energy is given by

$$U = U_s + U_{bs} + U_b \quad (3)$$

where U_s , U_{bs} and U_b are the energy due to in-plane deformation, coupling between in-plane and out-of-plane

and out-of-plane deformation, respectively, and they are given by

$$\begin{aligned}
 U_b &= \frac{1}{2} \iint \{\varepsilon\}^T [A] \{\varepsilon\} dx dy, \\
 U_{bs} &= \frac{1}{2} \iint (\{\kappa\}^T [B] \{\varepsilon\} + \{\varepsilon\}^T [B] \{\kappa\}) dx dy, \\
 U_b &= \frac{1}{2} \iint \{\kappa\}^T [D] \{\kappa\} dx dy
 \end{aligned}
 \tag{4}$$

where $\{\varepsilon\}$ is the strain vector and $\{\kappa\}$ is the curvature vector in the plate mid-plane. Matrixes $[A]$, $[B]$ and $[D]$ are stiffness matrixes [31-33] of extension, extension-bending coupling and bending, respectively. The kinetic energy is given by

$$T = \frac{\rho h}{2} \iint \left[\left(\frac{\partial u}{\partial t} \right)^2 + \left(\frac{\partial v}{\partial t} \right)^2 + \left(\frac{\partial w}{\partial t} \right)^2 \right] dx dy \tag{5}$$

where ρ is the mass density and h is the thickness.

To make the analysis simple, non-dimensional coordinates $\xi = 2x/a$ and $\eta = 2y/b$ are introduced to above equations. Then, the displacement u in the x direction is defined by

$$u(\xi, \eta, t) = \sum_{i=0}^{I-1} \sum_{j=0}^{J-1} P_{ij} X_i(\xi) Y_j(\eta) \sin \omega t \tag{6}$$

where P_{ij} are unknown coefficients, and $X_i(\xi)$ and $Y_j(\eta)$ are functions that satisfy the geometric boundary conditions at each edge of the shell. They are defined by

$$\begin{aligned}
 X_i(\xi) &= \xi^i (1-\xi)^{BC11} (1+\xi)^{BC31}, \\
 Y_j(\eta) &= \eta^j (1-\eta)^{BC21} (1+\eta)^{BC41}
 \end{aligned}
 \tag{7}$$

where BC_{pq} ($p = 1, 2, 3$ and 4 , $q = 1, 2$ and 3) are boundary indexes. The subscript p denotes each edge of the shell in counterclockwise direction from left edge of the shell, and q is the degree-of-freedom to be constrained. The numbers 1, 2, and 3 means u , v and w . The indices $BC_{pq} = 0$ and 1 indicates free and simply supported edges for $q = 1$ and 2, and $BC_{pq} = 2$ indicates clamped edges for $q = 3$. Displacements v and w are defined in the similar way with Eqs. (6) and (7). The functional F defined by the difference of maximum strain energy U_{max} and maximum kinetic energy T_{max} is minimized with respect to unknown coefficients P_{ij} , Q_{kl} and R_{mn} , and then frequency equation is derived to be solved numerically.

$$\left(\begin{bmatrix} k_{11} & k_{12} & k_{13} \\ k_{21} & k_{22} & k_{23} \\ k_{31} & k_{32} & k_{33} \end{bmatrix} - \Omega^2 \begin{bmatrix} m_{11} & 0 & 0 \\ 0 & m_{22} & 0 \\ 0 & 0 & m_{33} \end{bmatrix} \right) \begin{Bmatrix} P_{ij} \\ Q_{kl} \\ R_{mn} \end{Bmatrix} = 0 \tag{8}$$

4.2. FEM models of automobile panels

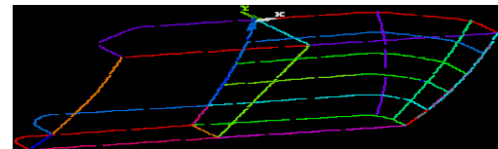
The analytical models introduced in section 4.1 are computationally very efficient, but they have some limitations on the geometric expression. For more accurate geometric modeling, the use of the finite element method (FEM) is more suitable. Particularly, sophisticated modeling technology is available in commercial FEM software [34-35].

Figure 13 shows the modeling process of thin composite structural part of automobile panel. In the modeling, first, a few lines are modeled as a basis. The first idea was to model simple areas and to realize area fillet between them to give the curved shape of the hood. This appeared quickly uneasy with ANSYS commands. Therefore, some key-points were placed on the skeleton to model lines all along the surface of the hood. Line fillets allowed modeling the curvature of the panel. The area was then created by skinning.

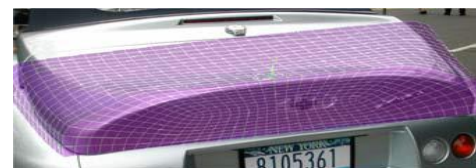
Similarly, Figure 14 shows a fender part panel of the hood, where dimensions are approximated with respect for the proportions but are inspired from real technical data. Also shown here in this figure are examples of accurate shape modeling in the FEM code. Similarly, in the pre-processor, key-points are chosen on the skeleton and set model lines all along the surface. Line fillets allowed modeling the curvature of the panel. The area was then created by skinning to derive the mesh. The design here is lead by using ANSYS, with Element Shell99 [36].



(a)Rear panel

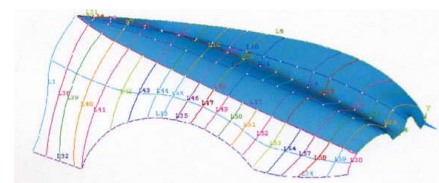


(b) Skelton model by using keypoint and surface

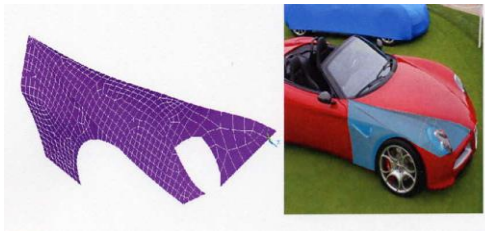


(c) Meshed model

Figure 13. Modeling process of a rear panel.



Example (a)



Example (b)

Figure 14. FEM modeling of fender

5. Conclusions

The present review-type work made efforts to cover the recent development found in the literature and to introduce practical applications in the last decade. Some other approach for pedestrian safety in Japan was also given. The application of fiber polymer composites, most likely CFRP, is promising in automotive industries worldwide, since the materials provide with higher specific strength/stiffness ratios and also the energy absorbing capability. The recent research also covers quality control of the materials, and efficient molding strategy. The cost, however, still acts as a decisive player in further extensive use of the material. As for thin panel modeling, two approaches are introduced here, one based on the cubic expression of curved surfaces, and the other more flexible surface shape modeler, that is the use of commercial finite element analysis code. The former has a limit in shape presentation, but the computation time is very short, therefore giving wider usability for time-consuming computation, i.e., optimum design of the composite panels for automobile bonnets and roofs. Finally, it is important to consider the optimization in the design process, but due to space limitation here, the topic will be presented in the next work.

References

[1] Das, S., The cost of automotive polymer composites: a review and assessment of DoE's lightweight materials composites research., US Department of Energy, 2001, ORNL/TM-2000/283.

[2] Brecher, A, A safety roadmap for future plastics and composites intensive vehicles, U.S. Department of Transportation, DOT HS 810863, 2007, www.nhtsa.gov.

[3] Andure, M.W., Jirapure, S.C., Dhamande, L.P., Advance automobile material for light weight future-a review, International Conference on Benchmarks in Engineering Science and Technology, Proceedings IJCA, 2012, pp.15-21.

[4] Mahajan, G.V., Aher, V.S., Composite material: a review over current development and automotive application, International Journal of Scientific and Research Publications, 2, 2012, pp.1-5.

[5] Rathnakar, G., Pandian, P., A review on the use and application of polymer composites in automotive industries, International Journal for Research in Applied Science & Engineering Technology, 3, 2015, pp.898-903.

[6] Pervaiz, M., Panthapulakkal, S., Birat, K.C., Sain, M., Tjong, J., Emerging trends in automotive lightweighting through novel composite materials, Materials Sciences and Applications, 7, 2016, pp.26-38.

[7] Masilamani, R., Dhandapani, N.V., Kumar, K.V., Mani, K.T., A review on usage of carbon fiber reinforced plastics in automobiles, International Journal of Pure and Applied Mathematics, 117, 2017, pp.537-544.

[8] Koronis, G., Silva A., Fontul M., A review of adequate materials for automotive applications, Composites Part.B., 44, 2013, pp.120-127.

[9] Akampumuza, O., Wambua, P.M., Ahmed, A., Li, W., Qin, X., Review of the applications of biocomposites in the automotive industry, Polymer Composites, 38, 2017, pp.2553-2569.

[10] Fogorasi, M.S., Barbu, I., The potential of natural fibres for automotive sector -review-, IOP Conference Series: Materials Science and Engineering, 252, 2017, pp.1-11.

[11] Sapuan, S.M., Suddin, N., Maleque, M.A., A critical review of polymer-based composite automotive bumper systems, Engineering Review, 10, 2002, pp.627-628.

[12] John A., Alex, S., A review on the composite materials used for automotive bumper in passenger vehicle, International Journal of Engineering and Management Research, 4, 2014, pp.98-101.

[13] Ezekwem, L., Composite materials literature review for car bumper, ResearchGate, <https://www.researchgate.net/publication/305775906>, pp.1-11.

[14] Kin, T., Koyama, H., Uzawa, K., Takahashi, J., Morit, A., Structural optimization of CFRTP bonnet for pedestrian safety (in Japanese), 34th Symposium of Japan Society of Composite Materials, 2009, pp.135-136, ResearchGate, <https://www.researchgate.net/publication/283087938>

[15] National Agency for Automotive Safety & Victim's Aid, Pedestrian head protection performance tests, http://www.nasva.go.jp/mamoru/en/assessment_car/head_protection_test.html.

[16] McLaren720S, referred from <http://jp.cars.mclaren.com/>

[17] Lamborghini Aventador, referred from <http://www.lamborghini.com/>

[18] Lexus RC F, Carbon Exterior package, referred from <http://lexus.jp/>

[19] Subaru WRX STI S208 NBR Challenge Package, referred from <http://www.honda.co.jp/>

[20] Nissan GT-R black edition, Track edition engineered by nismo, referred from <http://www.nissan.co.jp/>

[21] Toyota Purius PHV, referred from <http://monoist.atmarket.co.jp/>

[22] CFRP propeller shaft, referred from <http://nissan.co.jp/>

[23] BMW i3, referred from <https://clicccar.com/>

[24] Bruel & Kjar, Structural testing, part.2 modal analysis and simulation, 1988, <https://www.bksv.com/media/doc/br0507.pdf>.

[25] Narita, D., Narita, Y., Vibration analysis of laminated shallow shells with non-uniform curvature (in Japanese), Transaction of JSME, 72, 2006, pp.3743-3750.

[26] Narita, D., Narita, Y., Vibration optimization of laminated shallow shells with non-uniform curvature, 16th Proceedings of International Conference on Composite Materials, 2007, pp.1-8.

[27] Narita, D., Narita, Y., Analysis for vibration of laminated shallow shells with non-uniform curvature, Key Engineering Materials, Vol.334-335, (2007), pp.85-88.

- [28] Narita, D., Narita, Y., Analysis and design of curved laminated composite panels under external pressure, *Key Engineering Materials*, 353-358, 2007, pp.1271-1274.
- [29] Narita, D., Narita, Y., Vibration analysis of shallow shells with general surfaces expressed by cubic polynomial function, *Journal of System Design and Dynamics*, 2, 2008, pp.105-116.
- [30] Honda, S., Kato, T., Narita, Y., Narita, D., Multidisciplinary design optimization of surface shapes and lay-up configurations for composite laminated shells (in Japanese), *Transaction of JSME*, 77, 2011, pp. 1793-1802.
- [31] Vinson, J.R., Sierakowski, R.L., *The Behavior of Structures Composed of Composite Materials*, Martinus Nijhoff, Dordrecht, 1986.
- [32] Reddy, J.N., *Mechanics of laminated composite plates theory and analysis*, CRC Press, Inc., 1997.
- [33] Jones, R.M., *Mechanics of Composite Materials*, 2nd ed., Taylor & Francis, 1999.
- [34] Couppie, C., Honda, S., Narita, Y., Layerwise optimization for vibration of automobile panels, *Proceedings of The First Japan-Korea Joint Symposium on Dynamics and Control*, 2009, pp.37-38.
- [35] Narita, Y., Honda, S., Couppie, C., Layerwise optimization for vibration of automobile composite panels, *Proceedings of 17th International Congress on Sound and Vibration*, 2010, (CD-ROM), pp.1-6.
- [36] SHELL99, http://www.ansys.stuba.sk/html/elem_55 /chapter4/ES4-99.htm.

Role of Flow Simulation as A Tool for Failure Analysis Induced By Sulfate-Reducing Bacteria

Yudha Pratesa,^{a,*} Badrul Munir,^b

^aDepartment of Metallurgy and Materials Engineering, Universitas Indonesia. Email: yudha.pratesa@gmail.com

^bDepartment of Metallurgy and Materials Engineering, Universitas Indonesia. Email: munir@metal.ui.ac.id

Abstract

Sulphate Reducing Bacteria (SRB) is one of the challenging problems in oil and gas. It could attack the metals to form a pit. The SRB usually left a colony as the indication of corrosion attack. One of the main problems to prevent the corrosion attack is the ability to mapping the possibility of attacking area. However, this study offers a method to simulate the bacterial growth area based on the differential flow rate in the pipe. The flow simulation shows the ability to be used as the analytical tool for the bacterial growth mappings. Scanning Electron Microscope (SEM) and Energy Dispersive Spectroscopy were also conducted for confirmation of the SRB presence in the system

Keywords: Corrosion; flow; simulation; sulphate reducing bacterial

1. Introduction

One of an offshore platform in java area had a leakage incident. A Leakage incident occurred at 2” elbow pipe at discharge line of gas production. This event repeatedly happened at the elbow on the same line area. Both of leakages occurred adjacent to welding line of pipe body and elbow. This pipe was classified as low carbon steel grade material. It was used to transport mixed fluid which consists of saline water and oil. Fluid analysis indicated the presence of colonies of Sulphate Reducing Bacteria (SRB). Biocide has been given into the material two months before the leak (June to August), and the applied dosages below the recommended level. The fluid flowed intermittently every 30 minutes.

There are several failure analysis studies that are related to microbial induced corrosion (MIC) for example sulfide reducing bacteria (SRB). MIC was found able to attack several types of metals such as stainless steel, steel, copper, and aluminum. Steel is prone to MIC attack compared to the stainless steel due to lower nickel and chromium contents. Surface protection approach that used galvanizing did not give sufficient protection for the SRB attack.

Galvanized steel will suffer local corrosion attack due to selective zinc released [1]. Stainless steel was found corroded by bacterial oxidizing *Pseudomonas aeruginosa*.

Pseudomonas Aeruginosa (*P.Aeruginosa*) biofilm could oxidize the passive film of duplex stainless steel from Cr₂O₃ to CrO₃, which highly soluble compound [2]. Another study in stainless steel also found microbial induced corrosion activity increase when bacterial activity is highest, it will minimize the amount of carbohydrate and protein during the process. This microbial corrosion was activated by thermophilic bacterial [3].

Microbial induced corrosion in carbon steel is usually associated with Sulphate Reducing Bacterial (SRB) activity. SRB can form a colony which later forms a biofilm. Biofilms can present the phenomenon of the electrolyte diffuse into the biofilm. This condition is evidenced by the Warburg constant and appearances of phase elements indicates the evolution of the cover films well-formed and the impedance of the layers with time [4].

The system of SRB attack commonly involving at least four components in an environment that is (1) gas, liquid bulk (2), (3) fouling deposits, and (4) substratum. The reaction between the four components using convection and diffusion [5].

As a living being, the SRB requires an ideal condition to create a colony. A colony can be formed at a flow rate of 0.2 m/s up to 1.0 m/s. When flow velocities above 1 m/s biofilm layer would be broken, and the SRB is difficult to establish the colony [6]. Besides the velocity, many bacteria can survive at the ambient temperature, but they could not survive at a temperature above 149 F [7].

*Corresponding author. Tel.: +62-21-786-3510

Kampus Baru Universitas Indonesia, Depok, Indonesia, 16424

Many approaches had been proposed for detection and prevention of sulfate-reducing bacteria. J. Starosvetsky [8] used several methods to detect the presence of SRB in the industrial system. He used Energy Dispersive Spectroscopy to analyze the corrosion product and also conduct microbial analysis test to find a number of the microbial in the system. This method had been claimed as a successful method for failure analysis in industrial practice to find out the bacterial absences.

However, this method did not give a better analysis of the location of the sulfate-reducing bacterial where it will attack in the system and why they tend to attack one location than another location. This study will use velocity gradient that showed by finite element methods to find the reason of the preferred location of SRB attack.

2. Materials and Methods

This study used low carbon steel with industrial specification API 5L grade B. The methodology was separated into two parts. The first parts are failure analysis methods and the second parts are flow simulation. Both of them will be matched together to find out the correlation between both methods.

The sample was cut using wire cut machine to prevent phase changing. Both of test was conducted after surface preparation with grinding until mesh 600# to remove the oxide layer. Scanning Electron Microscope and Energy Dispersive Spectroscopy (EDS) analysis were carried out on the surface of material especially an area that covered with white rust.



Figure 1. (a) Visual condition of the corroded tubing, (b) section of failed tubing, (c) corrosion at the weldment and straight pipe, (d) condition of the elbow pipe before cleaning, and (e) pit revealed after cleaning

Finite element analysis was conducted using operational parameter as shown in Table 1.

Table 1. Operational parameter for finite element analysis

Velocity m/s	Temp (F)	Press (psig)
0.15	90	15

3. Discussion

3.1. Laboratory

3.1.1. Visual Examination

The first step in the examination is a visual examination. As the received sample is a part of tubing pipe that consists of tee pipe, straight pipe, and elbow pipe. (Fig. 2A) The leakage is found near welding area. After internal observation, the leakage was initiated from internal of the pipe (Fig. 2B). It propagated at HAZ area through the welding area. In the internal tubing, a white layer covered the tubing. (Fig. 2C) The denser white layer area is always found together with the corrosion attack at the adjacent area. The exciting findings are the pitting that is found precisely below the white layer. It is revealed after the removing of the white layer (Figs. 1D and 1E). Moreover, if we make a comparison between the elbow and straight pipe, it is found that the elbow had less density of white scale if compared with straight pipe (Figs. 1C and D).

3.1.2. Microstructure

The microstructure was taken from several areas, weld area, Heat Affected Zone (HAZ), Base metal of straight pipe. The results of the microstructure test between pipe A and pipe B showed similar phase that consists of ferrite and pearlite phase. It showed that there is no issue of microstructure effect on corrosion in the weldment. Acicular ferrite was shown at the weld area, which is typical of fast solidification.

The microstructure of base metal consists of pearlite and ferrite. Based on Fig. 2, corrosion propagated from weld and Heat Affected Zone (HAZ) area. Fig 2. showed leak located at the HAZ 1 while HAZ 2 is in normal condition. It showed the area after the welding cap is a “dead zone area.” At this area, the velocity will lower than the other area. This phenomena is the effect of vortex zone area. The leak formed a shallow pit which is indication effect of flow.

Walsh et al.. found the microstructure in weldment could contribute to the rapid microbial induced corrosion attack [9]. Sreekumari et al. also showed the similar result in carbon steel [10]. It showed that weldment microstructure would attack faster than the other area.

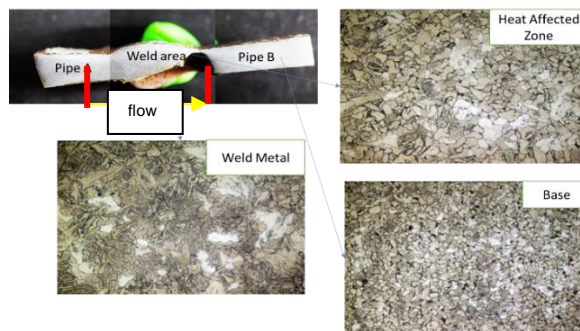


Figure 2. Microstructure of weld area that was attacked by SRB corrosion

However, our result showed the different result with Sreekumari et al. We found that the microstructure of weldment did not give a significant effect on microbial induced corrosion as shown in Fig. 3. We concluded that the microbial induced corrosion was more affected by the flow pattern in the weldment than the microstructure.

3.1.3. Scanning Electron Microscope

Scanning Electron Microscope (SEM) examination was performed at leak area. The results showed microbial activities, indicated by the presence of tubercle and extra polymeric substance (EPS). EPS could accelerate corrosion by binding with metal ions or accelerate iron oxidizing [11]. This EPS will be easier to form in the low velocity area. Fig. 1C showed that the white area consisted of EPS and the colony. The white area covered area around the pit area.

3.1.4. Energy Dispersive Spectroscopy

Energy dispersive spectroscopy (EDS) was performed to analyze chemical composition of the Extra Polymeric Substance (EPS). Based on the result, the EPS consisted of Sulphur, carbon, oxygen, and iron. It indicated the activity of bacterial. Calcium and Natrium are not detected in this area. It conforms that the white layer is not a salt precipitation or carbonate scale. On the other hand, the black scale area consists of carbon, oxygen, and iron with small percentage of Sulphur. It showed the black area is an oxide area which did not have any bacterial growth.

Table 2. Energy Dispersive Spectroscopy of SRB

	Element (%)							
	C	S	O	Ca	Na	Si	Cl	Fe
EPS	38.1	24.9	9.25	n.d	n.d	n.d	n.d	27.9
Black scale	47.6	0.48	28.7	3.14	2.38	0.73	n.d	17.0

3.2. Flow simulation

Flow simulation analysis was performed using a finite element software. Operational data such as flow velocity, temperature and pressure were used to run this simulation. The flow velocity (V) is taken from the conversion of the production fluid number (Q) that passed through the leaking pipe using Eq. 1.

$$v(m/s) = \frac{Q(m^3/s)}{A(m^2)} \tag{1}$$

Excessive root weld was simulated as a semicircular dimension with a diameter of 3 mm. The results of this simulation show some areas have a different flow velocity inside the pipe. Those areas were the area that is exposed to the effects vortex phenomenon.

Flow vortices are rotating flow and usually turbulent. Any spiral motion with the direction of flow is called

vortices flow. The speed of rotational vortices is zero at the center of vortices flow and increases proportionally according to the distance from its center. This vortex also has a minimum pressure at the center.

Based on the simulation result, it can be seen that the Sulphate Reducing Bacterial (SRB) spread widely around the areas that affected by the vortices especially at the center of the vortices, where the velocity is very low.

The results can be seen in Fig. 3 that showed a significant thinning rate caused by corrosion that is faster than other areas.

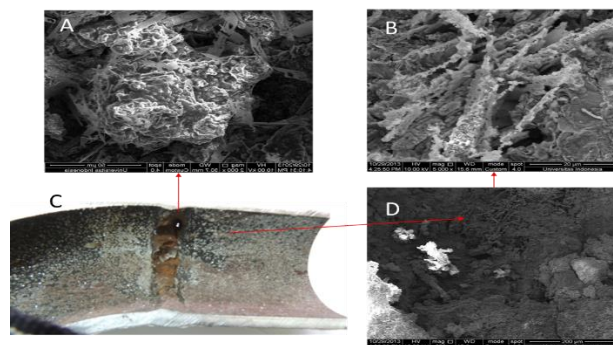


Figure 3. Scanning electron microscope (SEM) analysis at leak position (C) showed Extra Polymeric Substance threads with (B and D) that bind the colony (A)

The reason of occurrence of such mechanisms is the stability of the Sulphate Reducing Bacterial growth rate. The Simulation results also showed that both of these areas had a flow rate below 0.5 m/s. The value is quite ideal for the growth of bacteria.

Javaherdasti, 2008 also said that the bacteria need a slow velocity for they growing process. The maximum speed is about 0.5 m/s so that the colony is stable and Extra Polymeric Substance can be formed

4. Conclusion

Flow simulation could help mapping process of Sulphate Reducing Bacterial growth. The laboratory testing confirms the presence of sulfate-reducing bacterial attack as showed by Sulphur and Iron in scale composition. This element is the important substance for Iron Sulphide scale. The flow simulation showed a differences flow rate even in the laminar flow. Differences in flow pattern could help the the colony growth easier in the lower flow rate regime.

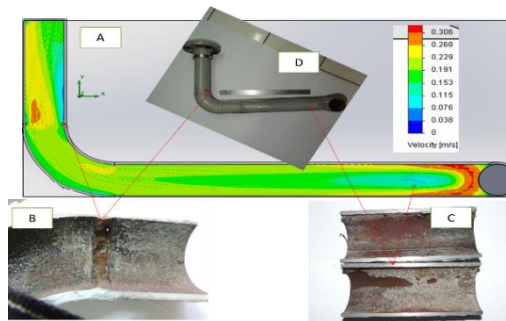


Figure 4. Simulation result showed similar result with the failure area

References

- [1] N. Bolton, M. Critchley, R. Fabien, N. Cromar, and H. Fallowfield, "Microbially influenced corrosion of galvanized steel pipes in aerobic water systems," *J. Appl. Microbiol.*, vol. 109, no. 1, pp. 239–247, 2010.
- [2] E. Zhou *et al.*, "Accelerated corrosion of 2304 duplex stainless steel by marine *Pseudomonas aeruginosa* biofilm," *Int. Biodeterior. Biodegradation*, vol. 127, no. November 2017, pp. 1–9, 2018.
- [3] S. Lata, C. Sharma, and A. K. Singh, "Microbial influenced corrosion by thermophilic bacteria," *Cent. Eur. J. Eng.*, vol. 2, no. 1, pp. 113–122, 2012.
- [4] H. Castaneda and X. D. Benetton, "SRB-biofilm influence in active corrosion sites formed at the steel-electrolyte interface when exposed to artificial seawater conditions," *Corros. Sci.*, vol. 50, no. 4, pp. 1169–1183, 2008.
- [5] W. Lee, Z. Lewandowski, P. H. Nielsen, and W. A. Hamilton, "Biofouling: The Journal of Bioadhesion and Biofilm Research Role of sulfate-reducing bacteria in corrosion of mild steel: A review," no. April 2015, pp. 37–41, 2009.
- [6] T. Liu, Y. F. Cheng, M. Sharma, and G. Voordouw, "Effect of fluid flow on biofilm formation and microbiologically influenced corrosion of pipelines in oilfield produced water," *J. Pet. Sci. Eng.*, vol. 156, pp. 451–459, 2017.
- [7] Javaherdashti R, *Microbiological Influenced Corrosion Handbook*. Springer, 2008.
- [8] J. Starosvetsky, D. Starosvetsky, and R. Armon, "Identification of microbiologically influenced corrosion (MIC) in industrial equipment failures," *Eng. Fail. Anal.*, vol. 14, no. 8 SPEC. ISS., pp. 1500–1511, 2007.
- [9] D. Walsh, D. Pope, M. Danford, and T. Huff, "The effect of microstructure on microbiologically influenced corrosion," *JOM*, vol. 45, no. 9, pp. 22–30, Sep. 1993.
- [10] K. r. sreekumar., "Microbially Influenced Corrosion and Biodeterioration of Structural Metals," *Tetsu-to-Hagane*, vol. 88, pp. 620–628, 2002.
- [11] K. Y. Chan, L. C. Xu, and H. H. P. Fang, "Anaerobic electrochemical corrosion of mild steel in the presence of extracellular polymeric substances produced by a culture enriched in sulfate-reducing bacteria," *Environ. Sci. Technol.*, vol. 36, no. 8, pp. 1720–1727, 2002.

Analysis of Corrugated Bulkhead against Transverse Plane Bulkhead in a Tanker Ship

Hamzah,^{a,*} Ganding Sitepu,^b Muh. Hidayat Arif,^c

^aDepartment of Naval Engineering, Faculty of Engineering, Hasanuddin University. Email: anca_naval99@yahoo.com

^bDepartment of Naval Engineering, Faculty of Engineering, Hasanuddin University. Email: sitepu.unhas@gmail.com

^cDepartment of Naval Engineering, Faculty of Engineering, Hasanuddin University.

Abstract

Ship is built from thousands of integrated construction materials. The selection of a strong and efficient construction material is significant since it directly affects the weight of the ship. For a watertight bulkhead in a tanker ship, there are two kinds of bulkhead construction which are transverse plane bulkhead and corrugated bulkhead. The selection of these two bulkhead constructions for watertight bulkhead is based on the bulkhead strength analysis as well as bulkhead weight. The analysis was conducted using an engineering structural analysis software by comparing the bulkhead structural configurations which has the same von Misses tension. For corrugated bulkhead, corrugation angle was simulated between 45° - 90° while for transverse plane bulkhead, the range of stiffener distances was simulated between 400-1400 mm. The result shows that minimum corrugated bulkhead weight which is 41.18 ton can be obtained on the corrugation angle of 60° with the structural efficiency ratio of 1.79% - 30.91% while for transverse plane bulkhead, minimum weight of bulkhead which is 71.175 ton can be obtained on the stiffeners distance of 600 mm with structural efficiency ratio of 2.62% - 60.25%. It can be seen that for the same von Misses tension, corrugated bulkhead construction is more efficient in terms of bulkhead weight and cost with the difference weights of almost 30 ton.

Keywords: Corrugated bulkhead; tanker ship; transverse plane bulkhead; von Misses tension

1. Introduction

The construction configuration and material must be carefully selected when designing ship construction. The common selection criteria are the construction strength to fulfil the ship strength requirements as well as the construction weight to reduce the ship building cost. One example of the selection of construction configuration is the selection of watertight bulkhead construction configuration for a tanker ship. Watertight bulkhead is a bulkhead constructed in a ship to divide ship into compartments. It has to be watertight to prevent water to flow to the nearest compartments. In a tanker cargo tank, the watertight bulkhead is constructed to prevent one liquid cargo to mix up with other different liquid cargo especially with different density and viscosity. The watertight bulkhead is constructed transversally and longitudinally in the tanker cargo tank. There are two kinds of watertight bulkheads

which are being used in a tanker ship namely transverse plane bulkhead and corrugated bulkhead.

The selection of the design watertight bulkhead construction is based on the cargo hold capacity maximization as well as for easy and reduced cargo tank cleaning process time. In addition to the parameters, the bulkhead selection is also considered the ease of tank operational process, construction structural strength and the economic aspect of the selected bulkhead.

In the ship construction rules, the use of transverse plane bulkhead or corrugated bulkhead as transversal bulkhead is not regulated. Furthermore, for corrugated bulkhead, the plate geometry is not fully regulated in the construction rules. The rules only regulate the corrugation depth, angle and the radius between corrugations. Even, for some classification bureaus, the rules for corrugation angle are different. Therefore, there is no exact rule for determining a good geometry form of corrugated bulkhead.

In the construction application, both types of the bulkhead are being used interchangeably or being used together on the same ship. As in a tanker ship which is being the case study for this research, the watertight bulkhead to

*Corresponding author. Tel.: +62-812-4420-9266
Jalan Poros Malino km. 6, Bontomarannu
Gowa, Sulawesi Selatan, Indonesia, 92171

separate between cargo hold are constructed using both types of the bulkheads. Transversal bulkhead uses corrugated bulkhead with the plate thickness of 14 mm while longitudinal bulkhead uses transverse plane bulkhead with the same thickness. An analysis for comparing the two forms of the watertight bulkhead in a tanker ship is conducted in order to identify the most efficient use of those two bulkheads in terms of some criteria as explained previously.

The tanker ship which is under investigation is owned by one of the oil company in Indonesia which is still under construction in a shipyard. Material used for cargo hold tank is Steel Grade A while the ship itself is 17,500 LTDWT.

2. Theoretical background

2.1. Transverse plane bulkhead

This type of watertight bulkhead construction is the most common bulkhead construction being used in a ship. This bulkhead is constructed by installing a plane plate with a required plate thickness in a longitudinal or transversal position in a ship. This plate then be strengthened with stiffeners using angle bar, T bar and bulb plate (Fig. 1). Based on Indonesian Bureau Classification (BKI) Vol. II, Rules for Hull, Section 9/A.1.1 [1], the distance between stiffeners is no less than the distance between ship frames or no less than 600 mm.

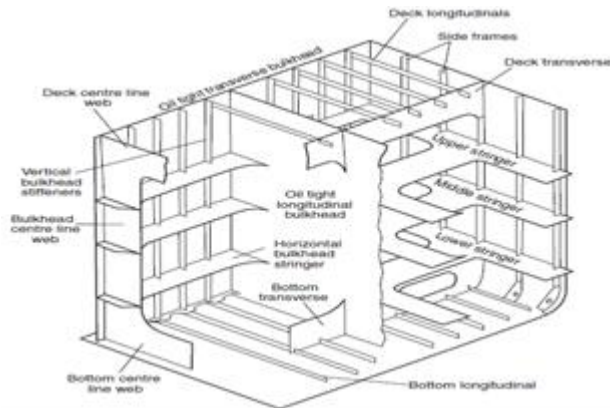


Figure 1. Transversal watertight bulkhead using transverse plane bulkhead [2]

2.2. Corrugated Bulkhead

Different cargo will require different packaging and cargo hold shape. For liquid cargo such as oil in a tanker ship, the separation of cargo hold is compulsory. Corrugated watertight bulkhead is commonly used to separate between tanks. The main reason for selecting this bulkhead is for maintenance reason as it is relatively easy to clean up the tank. This type of bulkhead does not use stiffeners as the corrugation form replaces the stiffener tasks. The corrugation in this bulkhead is made vertically (Fig. 2) in order to increase the bulkhead effectivity in maintaining liquid density as well as supporting structural strength [3].

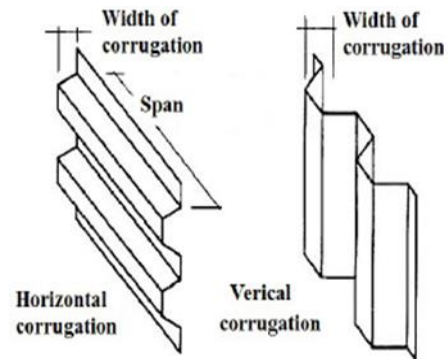


Figure 2. Horizontal and vertical corrugated bulkhead [4]

In a corrugation plate, the main parameter for determining bulkhead structural strength is the value of bulkhead corrugation angle. The construction of corrugated bulkhead can be seen in Fig. 3.

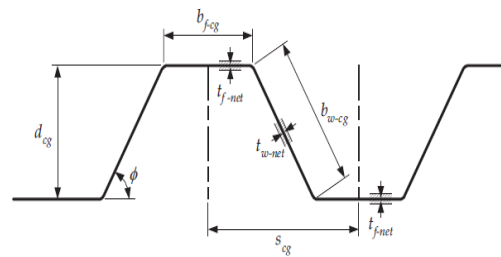


Figure 3. Element of the corrugated bulkhead [5]

where:

- s_{cg} = length of the half wave, in mm
- b_{w-cg} = width of the web plate, in mm
- b_{f-cg} = width of the face plate, in mm
- d_{cg} = depth of the corrugated bulkhead, in mm
= $b_{w-cg} \sin \theta$
- t_{f-net} = thickness of the face plate, in mm
- t_{w-net} = thickness of the web plate, in mm
- θ = angle of the bulkhead corrugation ($\geq 55^\circ$)

2.3. Optimization theory

There are three parameters in optimization theory which are [6]:

1. Design variable, the values are changing during optimization process.
2. Constraints, the values are constant during the optimization process.
3. Objectives, contains criteria for the optimization process.

3. Research methodology

The analysis consists of three main steps. The first step is determining variables and their values for optimization. The variables will be based on the parameters which have been explained in the previous section. The second step is determining sloshing pressure in the tank. The main purpose of this step is to determine pressure as a result of longitudinal

liquid motion in the tank. The last step is determining additional load of construction and equipment weight.

3.1. Variables for optimization

The main variable for the optimization process in corrugated bulkhead is the corrugation angle. As the asymmetry principle, the other bulkhead dimension will be changed as well. The optimization variables for corrugated bulkhead in this research can be seen in Table 1.

Table 1. Variable for optimization of corrugated bulkhead structure

No	Optimization variables	Description
1	Design variables	1 Angle of the corrugation bulkhead (θ)
		2 Length of the half wave (s_{cg})
		3 Width of the web plate (b_{w-cg})
		4 Width of the plate (b_{f-cg})
		5 Thickness of the corrugated bulkhead (t)
2	Constraints	1 Depth of the corrugated bulkhead (d_{cg})
		2 Working load on the corrugated bulkhead
		3 Working stress
3	Objectives	1 Minimum bulkhead weight

In transverse plane bulkhead, the main variable for the optimization process is the distance between stiffeners. The other variables for this bulkhead can be seen in Table 2.

For corrugated bulkhead, the existing angle of corrugation is 64° . Based on this initial value, the

corrugation angle then is varied in order to find the optimum angle. Hence, the design variables values for the corrugated bulkhead can be seen in Table 3.

While for transverse plane bulkhead, the design variable values can be seen in Table 4.

Table 2. Variable for optimization of transverse plane bulkhead

No	Optimization variables	Description
1	Design variables	1 Transverse plane bulkhead plate thickness
		2 The distance between stiffeners
		3 Bulkhead construction
2	Constraints	1 Depth of the corrugated bulkhead (d_{cg})
		2 Working load on the corrugated bulkhead
		3 Working stress
3	Objectives	1 Minimum bulkhead weight

Table 3. Design variable values for corrugated bulkhead with varied corrugated angles

θ (deg)	b_{f-cg} (mm)	b_{w-cg} (mm)	s_{cg} (mm)
45°	68.02	1055.74	777.04
55°	508.95	916.88	1036.36
60°	680.12	868.65	1120.36
64°	840	830.32	1200
65°	870	826.48	1217.84
75°	1158.08	776.46	1364.12
85°	1458.00	752.87	1499.00
90°	1560	750	1560

Table 4. Design variable values for transverse plane bulkhead with varied stiffeners distance

Bulkhead number	Construction types	Distance between stiffeners (mm)									
		400	500	600	700	800	900	1000	1200	1400	
Bulkhead no. 1	Direct welding	400	500	600	700	800	900	1000	1200	1400	
Bulkhead no. 2	Tied by Bracket	400	500	600	700	800	900	1000	1200	1400	

3.2. Sloshing pressure in the tank

According to NK Rules, 2016, Part CSR-T, Section 7/4.2.2.1 [5], the sloshing pressure on the ship longitudinal bulkhead as a result of longitudinal liquid motion can be calculated using Eq. 1 below:

$$\int P_{slg-lng} = \rho \cdot g \cdot l_{slh} \cdot f_{slh} \left[0.4 - \left(0.39 - \frac{1.7l_{slh}}{L_{CSR-T}} \right) \frac{L_{CSR-T}}{350} \right] \quad (1)$$

where:

- ρ = fluid density in the tank = 0.797 ton/m³
- g = gravitational force = 9.81 m/s²
- h_{fill} = height of cargo, maximum height of the cargo for sloshing is 95 % of maximum height of tank = 95 % \times 10.15 m = 9.642 m
- h_{max} = maximum height of tank = 10.15 m
- f_{slh} = sloshing coefficient (Eq. 2)

$$= 1 - 2 \left(0.7 - \frac{h_{fill}}{h_{max}} \right)^2 \quad (2)$$

$$= 1 - 2 \left(0.7 - \frac{9.6425}{10.15} \right)^2 = 0.875$$

- L_{CSR-T} = LWL on scantling draught position = 152.295 m
- n_{wash-t} = number of wash bulkhead in tank which is none
- n_{wf} = number of web frame in tank which is 7
- a_{wash-t} = 0, because no wash bulkhead
- a_{wf} = coefficient of web frame in tank which is 0.572
- f_{wf} = factor of sum of web frame and wash bulkhead in tank = $n_{wf} (1 + n_{wash-t}) = 7 (1 + 0) = 7$
- $ltk-h$ = length of tank = 21.75 m
- $lslh$ = effective length of sloshing in tank (can be calculated using Eq. 3)

$$= \left(\frac{(1 + n_{wash-t} \times a_{wash-t})(1 + f_{wf} \times a_{wf}) l_{tk-h}}{(1 + n_{wash-t})(1 + f_{wf})} \right) \quad (3)$$

$$= \left(\frac{(1+0 \times 0)(1+7 \times 0.572) 21.75}{(1+0)(1+7)} \right)$$

$$= 13.604 \text{ m}$$

Hence, sloshing pressure in tank is:

$$P_{s\lg\text{-}l\text{ng}} = 0.797 \times 9.81 \times 13.604 \times 0.875 \times$$

$$\left[0.4 - \left(0.39 - \frac{1.71 \times 13.604}{152.195} \right) \frac{152.195}{350} \right]$$

$$= 25.62 \text{ kN/m}^2$$

Based on the rules from Nippon Kaiji Kyokai classification bureau, minimum value for sloshing pressure in tank is 20 kN/m². Sloshing pressure value to be used is the result value from calculation which is 25.62 kN/m². The sloshing pressure will be evenly distributed on the whole surface of the corrugated bulkhead.

3.3. Additional load of construction and equipment weight

Apart from sloshing pressure, the bulkhead structure gets an additional load of construction and equipment weight. The additional weight can be calculated using Eq. 4 from Nippon Kaiji Koyokai (NK) Rules, 2016, Part CSR-T, Section 7/2.2.5.1 [5] as follows:

$$F_{stat} = m_{un} \times g \tag{4}$$

where:

- m_{un} = weight of unit
- g = gravitational acceleration

Referring to the Nippon Kaiji Koyokai classification bureau rules, minimum construction weight and equipment working on the bulkhead is 20 ton. Accordingly, the additional weight working on the bulkhead construction is:

$$F_{stat} = 20 \text{ ton} \times 9.81 \text{ m/s}^2$$

$$= 196.2 \text{ kN or } 196200 \text{ N}$$

The above weight is a concentrated load. The average load which is working on the plate surface is varying according to the length of the corrugated plate as well as the corrugation angle.

4. Result and discussion

4.1. The weight of the corrugated bulkhead

The determination of the optimum corrugated bulkhead form must be based on the weight of the bulkhead structure with varied corrugation angle. The optimum bulkhead weight can be obtained by varying the bulkhead thickness which have the same stress on every corrugation angle. The stress indicator value in this analysis is the von Misses stress

of 150 N/mm². Von Misses stress is a resultant stress of two different forces which is working on a structure in different direction. In the corrugated bulkhead structure, the two forces are sloshing pressure in z-axis direction and the additional load of construction and equipment weight in y-axis direction.

Once the optimum bulkhead thickness is known, the bulkhead weight can be calculated as well by multiplying the bulkhead volume with steel density which is 7.85 ton/m³ for common steel. Stools weight (upper and lower stool) is then added to the bulkhead weight as an integrated component of the bulkhead.

The result shows that for 45° of corrugation angle, the bulkhead weight is 52.85 ton. If the corrugation angle was increased to 55°, the bulkhead weight is reduced into 41.93 ton (20.67% of weight reduction). If the corrugation angle was increased to 60°, the bulkhead weight only reduced to 41.18 ton (1.79% of weight reduction). This corrugation angle is the maximum angle for the corrugated weight reduction because from 65° to 90° of corrugation angles, the corrugated weight is increased with the percentage of 3.79% - 16.45%.

Hence, minimum weight of corrugated bulkhead can be achieved if the corrugation angle is 60° while maximum weight on the corrugation angle is 90°. Minimum weight of corrugated bulkhead on 60° of corrugation angle can be obtained as the plate thickness to hold the same stress on each corrugation angle variation is the smallest. On 60° of corrugation angle, the stress concentration on the corner of face plate and web plate of the corrugated plate geometry can be minimized. The effect of stress concentration can be clearly seen on the 45°, 85°, and 90° of corrugation angles as it requires more plate thickness to hold the same stress as on the 60° of corrugation angle. On these angles, the corner of the face plate and web plate is almost broken to hold the stress.

In general, for the same stress value, the changing of corrugation angles has changed the corrugation bulkhead weight significantly (Fig. 4).

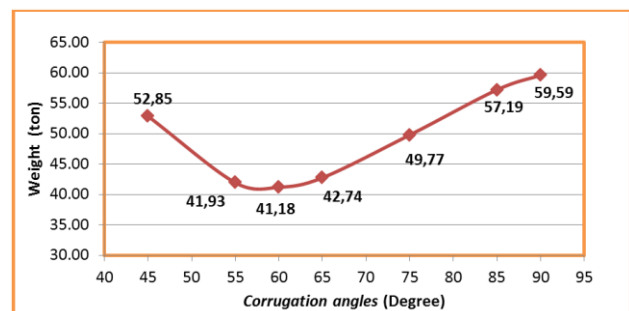


Figure 4. The relationship between corrugation angles and corrugation bulkhead weight

The difference weight between the minimum weight of corrugation bulkhead on 60° of corrugation angle with other corrugation angles is in the range of 0.75 – 18.42 ton. The weight reduction value is only for 1 (one) bulkhead. For

some bulkheads application in a ship such as tanker ship which requires more bulkheads for its cargo hold, the careful bulkhead selection will give a significant reduction in terms of cost as well the weight reduction.

4.2. The weight of the transverse plane bulkhead

For transverse plane bulkhead, two alternatives of bulkhead constructions have been tried out. The first type is transverse plane bulkhead with direct welding while the second type is the transverse plane bulkhead tied by some brackets. The difference between those two alternatives is laying on the integration method of the bulkhead and its stiffeners to the inner bottom plate and deck plate. For direct welding, the bulkhead and its stiffeners are directly welded into inner bottom plate and deck plate. While on the other alternative, stiffeners and brackets is first welded together. The brackets and the bulkhead plate are then welded into inner bottom plate and deck plate.

The stiffeners and brackets dimension are all the same with angle bar or profile L for stiffeners. The bulkhead analysis was done with nine variations of stiffeners distances. Hence, the number of stiffeners on each variation is different.

With the same von Misses stress of 150 N/mm^2 applications as an indicator, the bulkhead thickness has been simulated on each stiffeners distance variation. Based on the simulation, the minimum bulkhead thickness for certain stiffeners distance can be obtained. Hence, the bulkhead weight can be calculated as well by multiplying it with steel density of 7.85 ton/m^3 . Fig. 5 shows the relationship between stiffeners distance and the bulkhead weight.

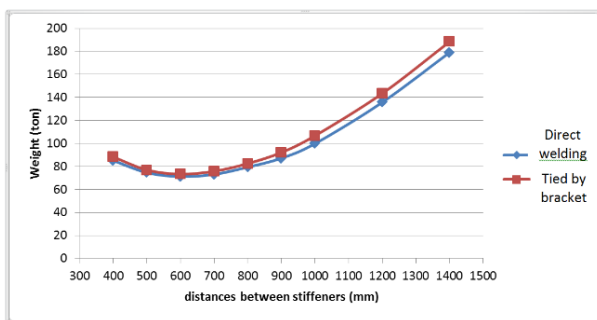


Figure 5. The relationship between stiffeners distance and the bulkhead weight

In Fig. 5, it can be seen that from 400-600 mm of the distance between stiffeners, the bulkhead weight is decreasing but when the distance between stiffeners is increasing, the bulkhead weight increases as well. The increasing tendency of bulkhead weight from 700 mm distance between stiffeners was caused by the increasing

plate thickness to hold the von Misses stress. From Fig. 5, the optimum distance between stiffeners for minimum weight of the bulkhead is 600 mm.

From the same figure, the total weight value of bulkhead with direct welding is 71.175 ton. This value is smaller 3.03% if compared with the total weight value of bulkhead tied by brackets of 73.336 ton.

4.3. The comparison results of corrugated bulkhead with transverse plane bulkhead

Minimum weight of corrugated bulkhead was obtained when the corrugation angle is 60° while for transverse plane bulkhead, the minimum weight of the bulkhead was obtained when the distance between stiffeners is 600 mm with direct welding.

The total minimum weight of the corrugated bulkhead is 41.18 ton while for transverse plane bulkhead with direct welding, the total minimum weight is 71.175 ton. The corrugated bulkhead weight is 29.095 ton or 57.86% smaller than the transverse plane bulkhead weight. This number is for one bulkhead. In the tanker ship, there are 4 (four) cargo holds. If the corrugated bulkhead is used instead of transverse plane bulkhead in the ship, the total weight reduction of the used material plate is significant.

5. Conclusion

Based on the analysis, some conclusions can be drawn as follows:

- With the same strength, the minimum weight of corrugated bulkhead can be obtained on 60° of corrugation angle while for transverse plane bulkhead, minimum weight can be obtained when the distance between stiffeners is 600 mm.
- Corrugated bulkhead weight is smaller for about 57.86% of the transverse plane bulkhead weight.

References

- [1] Biro Klasifikasi Indonesia. 2014. Volume II. Rules for the Classification and Construction Seagoing Steel Ship. Jakarta: Indonesia.
- [2] Eyres, David J. 2001. Ship Construction, University of Plymouth: India.
- [3] Taggart, Robert. 1980. Ship Design and Construction. The Society of Naval Architects and Marine Engineers: New York.
- [4] Shama, Mohamed. 2013. Buckling of Ship Structures. Alexandria University: Egypt.
- [5] Nippon Kaiji Kyokai (NK) Rules. 2016. Rules for The Survey and Construction of Steel Ship: Part CSR-T Common Structural Rules For Double Hull Oil Tankers: Japan.
- [6] Rigo, Ph and J-D. Caprase. 2016. Optimization of Ship Structures. University of Liege: Belgium.

Fatigue Analysis of Catenary Mooring System due to Harsh Environment in Head Seas

Fuad Mahfud Assidiq^{a,*}, Daeng Paroka^b, Muhammad Zubair Muis Alie^c, Syerly Klara^d

^aOcean Engineering, Faculty of Engineering, Hasanuddin University. Email:fuadassidiq9@gmail.com

^bOcean Engineering, Faculty of Engineering, Hasanuddin University. Email: dparoka@eng.unhas.ac.id

^cOcean Engineering, Faculty of Engineering, Hasanuddin University. Email: zubair.m@eng.unhas.ac.id

^dMarine Engineering, Faculty of Engineering, Hasanuddin University. Email: elikapal83@gmail.com

Abstract

The Floating Production Unit (FPU) is a floating gas production barge that is moored by catenary mooring system to the seabed. In the operation, FPU will be impacted by dynamic loads such as ocean waves, ocean currents, and winds on the mooring line structure periodically. This may cause damage to the mooring line structures which effect the operational structure performance. The aim of the present study is to investigate fatigue life on catenary mooring system. The model studied refers to the comparison of with and without using the Single Line Freestanding Riser (SLFR), the operational design and installation conditions are located in the Makassar Strait. The dimensions of mooring line type six-strand wire rope are 0.115 meters of outer diameter and 1,200 meters of length then it will be analyzed of fatigue life. The FPU motion observation in head seas shows the highest Response Amplitude Operator (RAO) of surge, sway, heave, roll, pitch, and yaw motion due to harsh environments with $H_s = 4.0$ meters and $T = 7.7$ sec are obtained 0.615 m/m, 9.354×10^{-7} m/m, 1.048 m/m, 18.423×10^{-6} /m, 2.225 /m, and 12.671×10^{-8} /m. It means that the response amplitude will always be smaller than the wave incident amplitude. The using SLFR has longer frequency about 0.207 rad/sec than without using SLFR. Taking into RAO motion calculation, the fatigue life on catenary mooring systems for head seas using SLFR is 412 years in mooring line 4 and 5. the fatigue life on catenary mooring systems for head seas without using SLFR is 6,636 years in mooring line 5. The structure is still in safe condition because of the design safety factor is about 300 years.

Keywords: Catenary; fatigue life; head seas; response amplitude operator; single line freestanding riser

1. Introduction

The Floating Production Unit (FPU) Gendalo-Gehem Chevron Indonesia Company, which is Indonesian Deepwater Development (IDD) mega project, is located in the Makassar Strait about 6.000 feet depths as shown in Fig. 1. The project will include two development hubs, FPU with subsea drilling center, and condensate pipelines and onshore facilities. The natural gas will be used domestically and converted to LNG in Bontang, East Kalimantan. The maximum daily production is expected to 1.1 billion cubic feet of natural gas and 31,000 barrels of condensate.

In this gas production phase, FPU will be impact by ocean waves, ocean currents and winds due to highest FPU motions and the highest stress responses of the catenary

mooring system while gas production process can damage these structures and other operational load factors. Consequently, it gets more critical conditions.

Moreover, the fatigue analysis is the most important effect in the FPU construction and production development. This research will discuss the fatigue analysis of the catenary mooring system to determine the fatigue life with SLFR and without SLFR in head seas for six degrees of freedom (surge, sway, heave, roll, pitch, and yaw motion).

*Corresponding author. Tel.: +62-856-9652-0325
Jalan Poros Malino km. 6, Bontomarannu
Gowa, Sulawesi Selatan, Indonesia, 92171

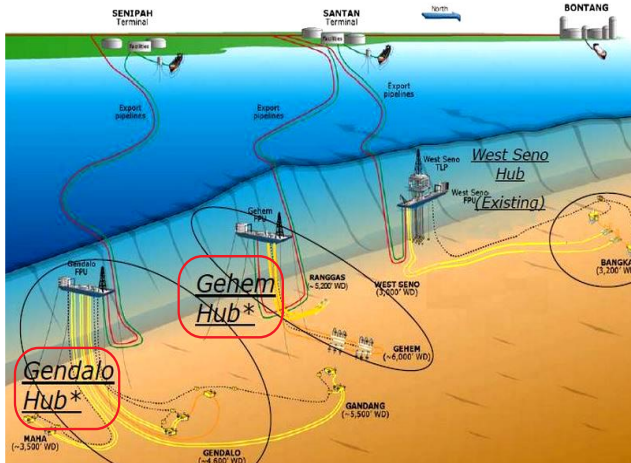


Figure 1. Gendalo–Gehem field

2. Literature Review

2.1. Ship Theory

Basically, floating objects have six degrees of freedom which are divided into two groups which are first, three translational modes (surge: X-axis transversal direction, sway: Y-axis transversal direction, and heave: Z-axis transversal direction) and three rotational modes (roll: X-axis rotational direction, pitch: Y-axis rotational direction, and yaw: Z-axis rotational direction). By using right hand axis system, the definition of six degrees of freedom mode can be explained in Fig. 2 [1]. The current study discusses surge motion. The surge motion system does not have stiffness element. As an illustration when the ship is moving then the added mass due to fluid particles movement around it.

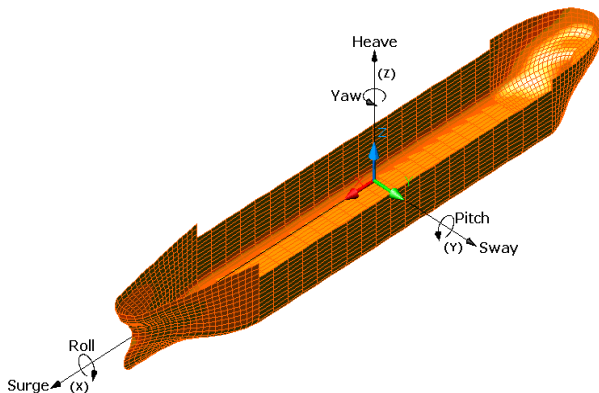


Figure 2. Six degrees of freedom on floating unit

The motion direction is affected the wave heading angle (μ), which is the angle between the direction of wave propagation and the ship direction rate. The angle setting of wave heading can be seen in Fig. 3, and Table 1 [2].

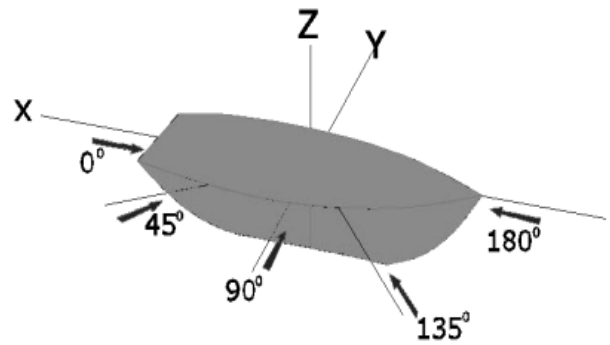


Figure 3. Heading direction in Ansys software

Table 1. Main heading on floating unit

Heading	Description
0°	Following Seas
45°	Stern Quartering Seas
90°	Beam Seas
135°	Bow Quartering Seas
180°	Head Seas

Response Amplitude Operator (RAO) is a tool to the wave forces transfer into the dynamic response of structures. RAO equation can be expressed as [3]:

$$RAO(\omega) = \frac{X_p(\omega)}{\eta(\omega)} \quad (1)$$

where:

$X_p(\omega)$ = Structure amplitude (meter)

$\eta(\omega)$ = Wave amplitude (meter)

2.2. Mooring System

Mooring systems typically have 8 to 16 mooring lines consist of the heavy chain, steel wire rope and polyester materials that connect anchor toward the seabed [4]. The catenary system paths arrive at the seabed horizontally, although taut mooring tethered to an angle formed [5]. Another important difference is that the strength of the recovery on the catenary mooring generated by the weight of the components while the taut mooring strength comes from the elasticity of the mooring lines.

When oil and gas extraction takes place from shallow water into deep water, the catenary mooring system is more popular but when identification of deep water production into ultra-deep water, mooring system becomes the limit factor. To solve this problem, a new solution was developed as taut leg mooring system. In Fig. 4 shows the mooring system configurations [6].

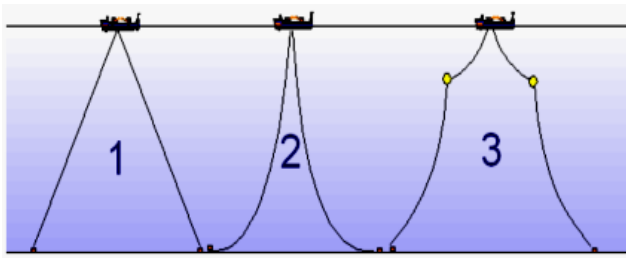


Figure 4. Mooring system configurations; (1) taut mooring; (2) catenary mooring and (3) catenary mooring with buoyancy

Tension which happens to the mooring line can be divided into two: the mean and maximum tensions. Mean tension is tension on the mooring line related to the mean offset of the vessel while the tension is the mean maximum tension under the combination effect of wave frequency and low- tension frequency [7].

The tension limit on the mooring line and safety factor recommended by American Petroleum Institute are as follows [8]:

Table 2. Criteria and tension limit safety factor mooring

Case	Analysis Method	Tension Limit (Percent of MBS)	Equivalent Factor of Safety
Intact (ULS)	Dynamic	60	1,67

2.3. Fatigue Analysis

The fatigue analysis is defined as research that includes global dynamic motion and local stress of catenary mooring tension. The existing methodology does not have the consistency and transparency level necessary to independently demonstrate the safety level and conservatism in the design of the catenary [9].

The basis of the S-N curve is mentioned between the plot of stress (*S*) and the number of cycles (*N*). This curve is used to express the characteristics of fatigue in materials due to cycle loads at a constant magnitude [10]. The accuracy level is affected by the determination of S-N curve slope parameter and interception, the analytical expression of the S-N curve is [11]:

$$Ni(s) = aD \cdot s^{-m} \tag{2}$$

where:

- Ni(s) = Cycle of failure
- s = Stress range (N/mm²)
- aD = Intercept parameter in S-N curve
- m = S-N curve slope

Meanwhile, *aD* and *m* parameters explanation are given in Table 3 and S-N curve is shown in Fig. 5.

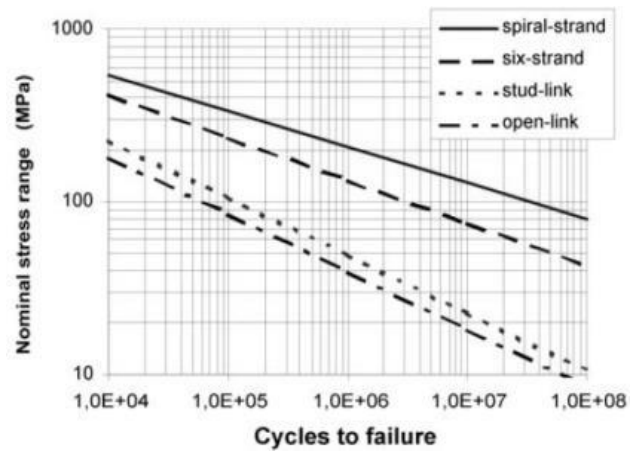


Figure 5. S-N curve

Table 3. S-N curve parameter

Mooring Types	<i>aD</i>	<i>m</i>
Stud Chain	1.2 x 10 ¹¹	3.0
Studless Chain (Open Link)	6.0 x 10 ¹⁰	3.0
Six-Strand Wire Rope	3.4 x 10 ¹⁴	4.0
Spiral Strand Wire Rope	1.7 x 10 ¹⁷	4.8

Each mooring lines take the fatigue life further process between the number of cycles-stress range and mooring line characteristics [12]. This fatigue life review when the condition of the surge, sway, heave, roll, pitch and yaw motion by heading 180⁰ (head seas) were calculated as follows [9]:

$$n = \frac{T}{Ta} \tag{3}$$

$$D = \sum_{i=1}^n \frac{n}{Ni} \tag{4}$$

where:

- n = Number of cycle
- D = Fatigue damage ratio
- T = Design life period (sec)
- Ta = Stress range period (sec)
- Ni = Cycles of failure

While the fatigue life calculations (in years) are from the total fatigue damage, and the safety factor at least about 10 [13], and additional safety between 0 and 1.

$$\text{Fatigue Life} = \frac{1}{Ni \times (10 + \text{additional safety})} \tag{5}$$

As well as the fatigue life in safety design criteria for mooring lines as follows [14]:

$$\text{Fatigue Life} > \text{Design Life}$$

3. Research Methods

The research was conducted by literature review and FPU supporting data as in Table 4, Table 5, and Table 6. The FPU simulation with and without using SLFR in head seas investigate the fatigue life on catenary mooring system. The FPU-SLFR design and wave heading direction indicated in Figs. 6 and 7.

Analyzing motion response FPU using Ansys AQWA obtain the stress range each mooring lines. Stress range of each mooring lines obtained from the time domain analysis to the catenary mooring system based FPU motion responses in the heading direction 180^0 so that resulting from the tensions due to each mooring lines affected when using SLFR and without using SLFR. Each mooring lines take the fatigue life process further between the stress range-failure and characteristics of the mooring line used against loading period head the DNV (Det Norske Veritas) and the API (American Petroleum Institute) criteria and then get the conclusion.

Table 4. FPU main dimension

Barge Hull Gas FPU	
LOA	160.5 m
B	50.0 m
H	17.0 m
T	8.40 m
Cb	0.98

Table 5. FPU mooring data

Mooring Properties	
Mass / Unit Length	140 kg/m
Outer Diameter	0.115 m
Section Length	1,200 m
Stiffness, EA	1.0×10^9 N
Maximum Tension	8.0×10^6 N

Table 6. Makassar strait wave scatter data

Hs/Tp	2-3	3-4	4-5	5-6	6-7	7-8	Total
0.00-0.25	5.64	7.44	2.42	2.50	2.01	0.68	20.69
0.25-0.50	4.77	13.42	7.19	6.06	5.77	1.36	38.57
0.50-0.75	1.07	6.64	6.66	3.10	3.10	0.78	21.35
0.75-1.00	0.27	2.93	3.32	2.45	1.48	0.29	10.74
1.00-1.25	0.05	1.07	1.55	1.02	0.73	0.07	4.49
1.25-1.50	0.00	0.19	1.04	0.68	0.53	0.02	2.46
1.50-1.75	0.00	0.17	0.46	0.29	0.29	0.02	1.23
1.75-2.00	0.00	0.00	0.17	0.19	0.07	0.00	0.43
2.00-2.25	0.00	0.00	0.02	0.02	0.00	0.00	0.04
Total	11.80	31.86	22.83	16.31	13.98	3.22	100

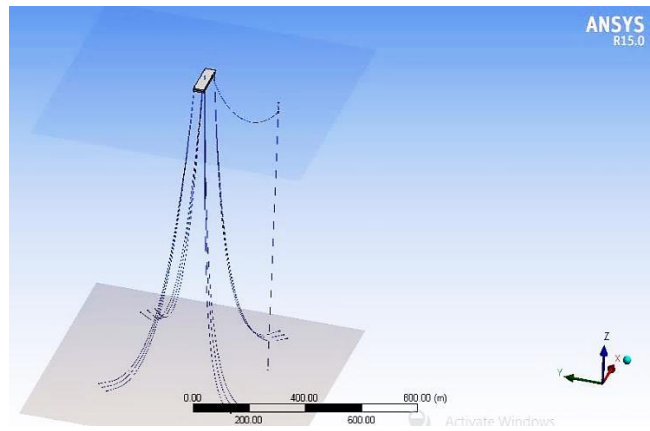


Figure 6. FPU and SLFR

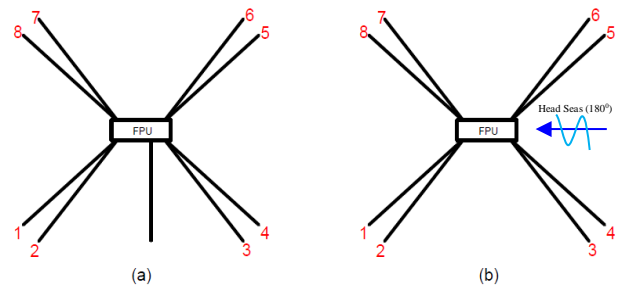


Figure 7. Mooring line numbering; (a) with SLFR and (b) without using SLFR

4. Results and Discussions

4.1. Hydrostatic Analysis

The hydrostatics FPU Gendalo-Gehem analysis results obtained from the hydrodynamic diffraction that considered the heave, roll and pitch motions. The hydrostatics generated from the FPU geometrical characteristics.

The FPU in Ansys Aqwa with and without using SLFR are very influential volumetric displacement, center of buoyancy position, distance COG to COB and metacentric height due to the the vertical motion modes (heave, roll and pitch motion). It has stiffness factor that may affect the damping factor becomes be smaller, so it will produce the highest characteristics result as shown in Table 7.

The FPU in horizontal motion mode (surge, sway, yaw motion) are also strongly important influential the stiffness of damping factor that do not rise up hydrostatic characteristics significantly.

4.2. Response Amplitude Operator Analysis

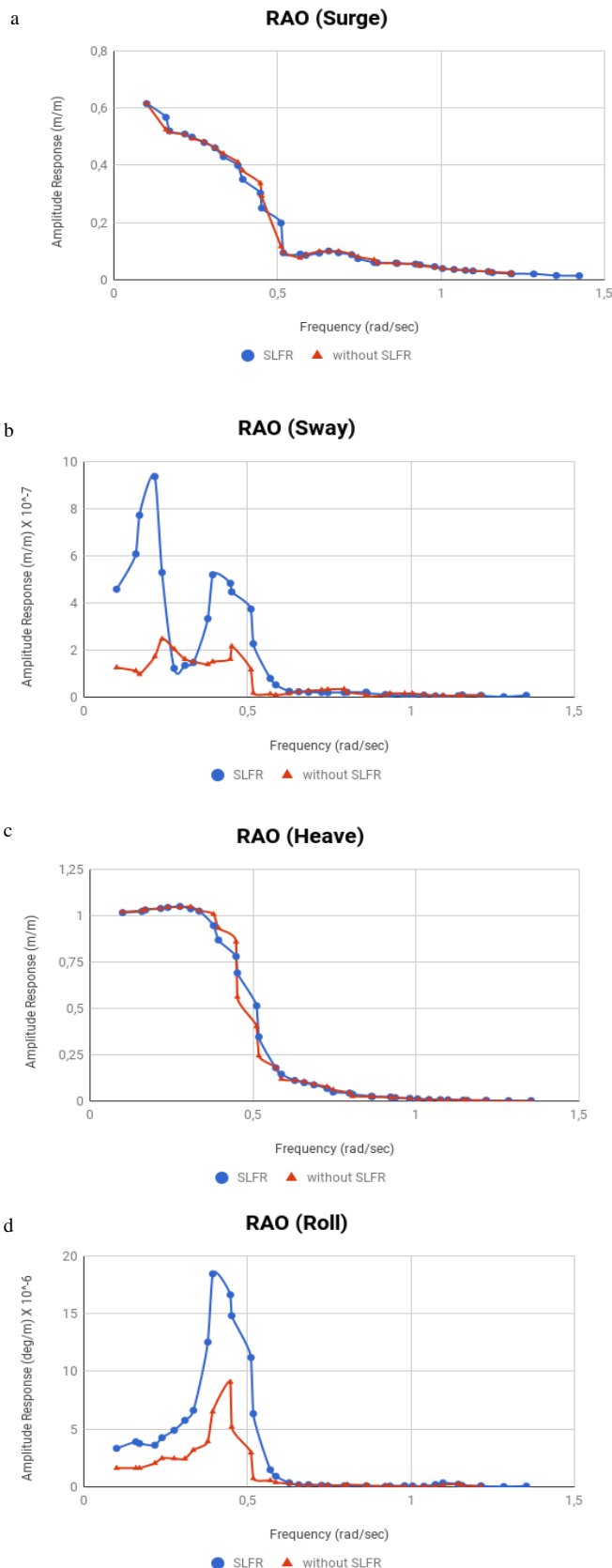
The results of RAO analysis with and without SLFR in head seas can be seen in Fig. 8. The response amplitude change over with and without SLFR condition. It proves that the mooring lines can reduce the FPU motion in harsh environment with $H_s = 4.0$ meters and $T = 7.7$ sec.

Table 7. Hydrostatic result using SLFR and without SLFR in Ansys AQWA

Item	with SLFR	without SLFR
Centre of Gravity Position		
X:	80.25 m	80.25 m
Y:	25.00 m	25.00 m
Z:	0.00 m	0.00 m
Heave(Z)	80,665,544 N/m	80,666,000 N/m
Roll(RX)	1.940E+08 N.m/°	1.940E+08 N.m/°
Pitch(RY)	2.923E+09 N.m/°	2.923E+09 N.m/°
Actual Volumetric Displacement		
Displacement	134,819.970 m ³	134,819.91 m ³
Equivalent Volumetric Displacement		
Displacement	134,819.520 m ³	134,819.52 m ³
Centre of Buoyancy Position		
X:	80.25 m	80.25 m
Y:	25.000002 m	25.00 m
Z:	-4.1999927 m	-4.2000031 m
Cut Water Plane Area	8,024.972 m ²	8,025.018 m ²
C.O.G. to C.O.B.(BG)	4.1999927 m	4.2000031 m
Metacentric Heights		
GMX:	8.2007885 m	8.2008057 m
GMY:	123.57906 m	123.57912 m
COB to Metacentre		
BMX:	12.400781 m	12.400809 m
BMY:	127.77905 m	127.77913 m
Restoring Moments		
MX:	3,385,393 N.m/°	3,385,399 N.m/°
MY:	51,015,060 N.m/°	51,015,060 N.m/°

When using SLFR, FPU motion characteristics do not exceed the maximum high waves well. It means that the RAO's amplitude responses are always smaller than the wave incident amplitude. In the surge, heave and pitch motions are shown in Figs. 8(a), 8(c) and 8(e). It shows that with and without using SLFR in head seas get the similar RAO. The maximum surge motion occurs when without using SLFR is 0.615 m/m and the maximum heave motion occurs when using SLFR in 1.048 m/m. The maximum pitch motion occurs when without using SLFR is 2.225 °/m. In Fig. 8(d) shows that the maximum roll when using SLFR is 18.423x10⁻⁶ °/m. The response amplitude using SLFR are greater than without using SLFR too. It occurs while using SLFR is 0.207 rad/sec longer frequency duration than without using SLFR.

Meanwhile, sway, and yaw motion show that both are the different trend as shown in Figs. 8(b) and 8(f). The maximum sway motion when using SLFR is 9.354x10⁻⁷ m/m and the RAO significant difference occurs are from 0.1 to 0.657 rad/sec. The maximum yaw motion occurs when using SLFR which is 12.671x10⁻⁸ °/m and on the early frequency, 0.239 rad/sec occur the significant difference response because SLFR position is not centering of the mid ship so RAO when using SLFR duration occurs sooner.



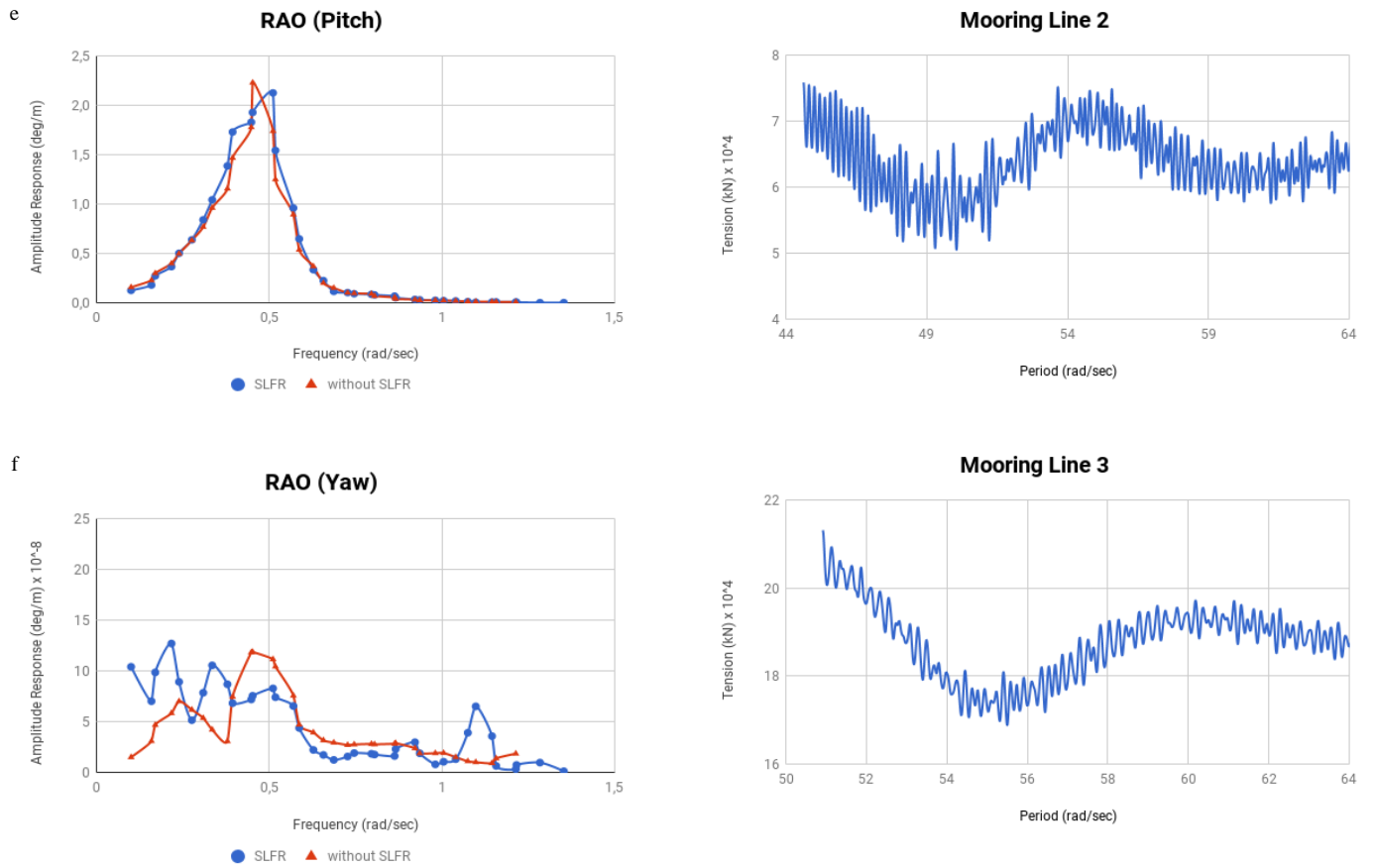
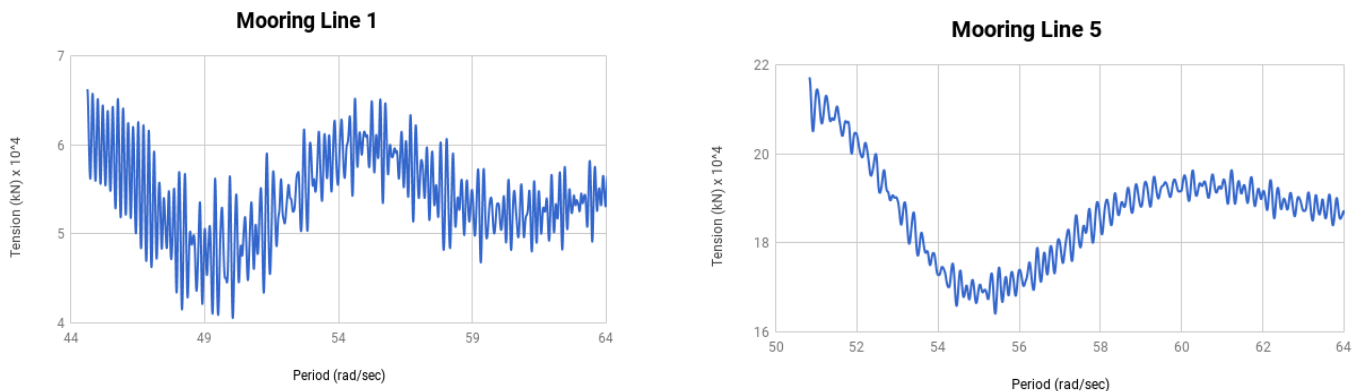


Figure 8. Comparison of RAO using SLFR and without SLFR; (a) surge motion; (b) sway motion; (c) heave motion; (d) roll motion; (e) pitch motion; and (f) yaw motion

4.3. Stress Range Results

After obtaining the RAO, then stress range can be determined by the maximum and minimum mooring lines tension within difference wave periods. In Fig. 9, the FPU mooring line tension occurs when using SLFR in head seas. From all mooring line tensions, tension trend generated is almost the same response. The maximum tension occurs in mooring line 4 worth 230,586.125 kN in 9.22 sec, and the minimum tension occurs in mooring line 1 is 40,560.648 kN in 11.12 sec as shown in Table 8.



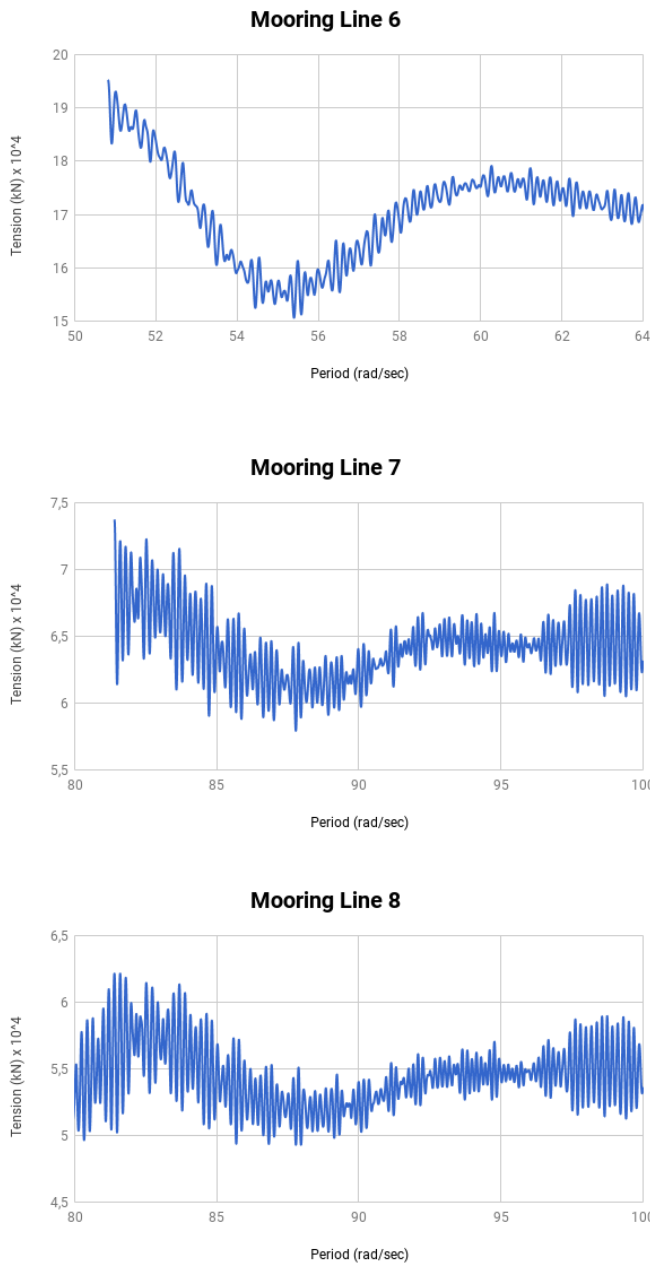
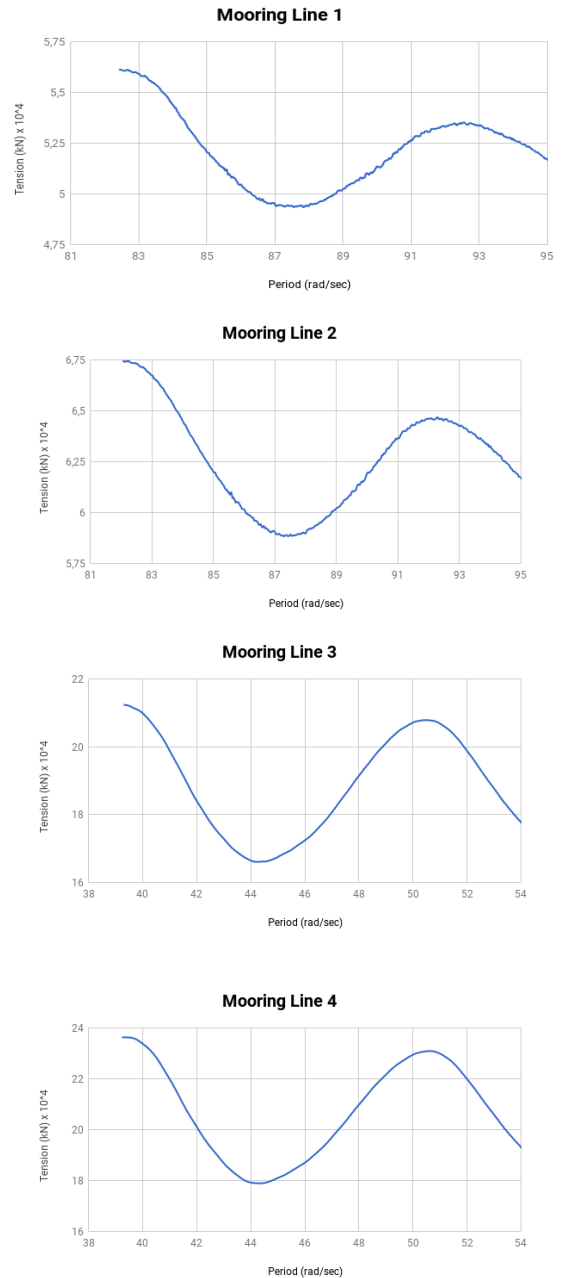


Figure 9. Tension of mooring line using SLFR

Table 8. Summary of mooring line tension using SLFR

Mooring Line	Tension [kN]			Period [Sec]
	Maximum	Minimum	Range	
1	66,249.992	40,560.648	25,689.344	11.12
2	75,845.055	50,511.129	25,333.926	10.46
3	213,124.094	168,838.700	44,285.394	9.72
4	230,586.125	182,490.890	48,095.235	9.22
5	217,183.172	167,975.230	49,207.942	9.32
6	195,280.516	150,674.780	44,605.736	9.53
7	73,744.500	57,945.961	15,798.539	12.42
8	63,594.832	45,602.555	17,992.277	10.40

In Figure 10, the FPU mooring line tension occurs when without using SLFR in head seas. From all mooring line tensions, tension trend is very similar responses because no SLFR load affects. The maximum tension occurs in mooring line 5 is 236,337.797 kN in 11.46 sec, and the minimum tension occurs in mooring line 8 is 49,361.270 kN in 10.31 sec. Meanwhile, the maximum tension range in mooring line 5 is 57,418.188 kN and the minimum tension range in mooring line 8 is 6,743.628 kN. For more information about summary mooring line tension when without using SLFR see Table 9.



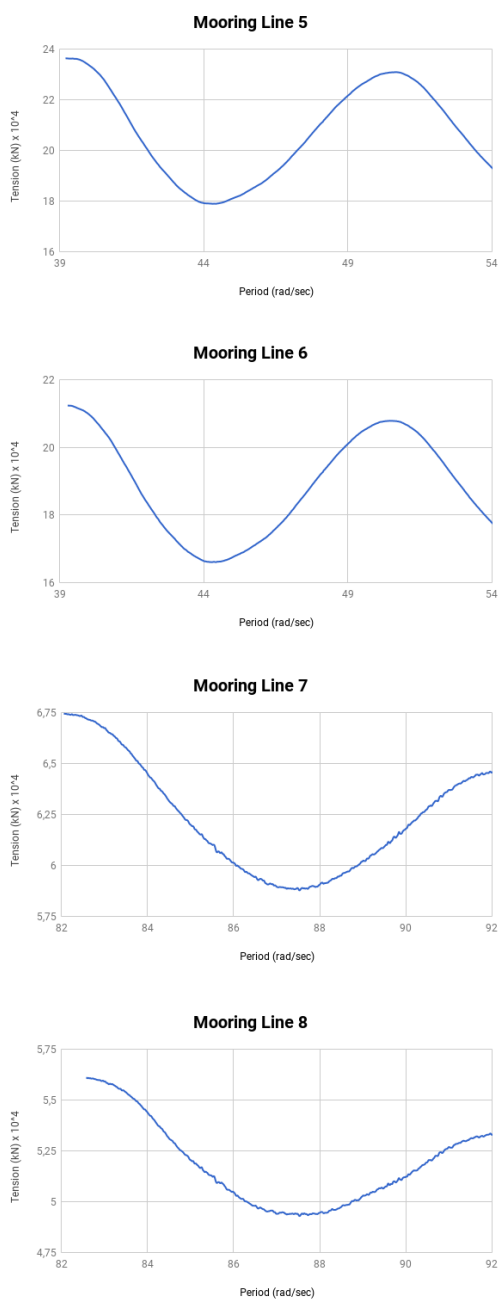


Figure 10. Tension of mooring line without using SLFR

Table 9. Summary of mooring line tension without using SLFR

Mooring Line	Tension [kN]			Period [Sec]
	Maximum	Minimum	Range	
1	56,131.527	49,355.484	6,776.043	10.41
2	67,466.961	58,837.230	8,629.731	10.30
3	212,374.688	166,064.969	46,309.719	11.28
4	236,306.781	178,893.109	57,413.672	11.44
5	236,337.797	178,919.609	57,418.188	11.46
6	212,346.016	166,055.531	46,290.485	11.29
7	67,454.625	58,784.664	8,669.961	10.34
8	56,104.898	49,361.270	6,743.628	10.31



Figure 11. Comparison of stress range using SLFR and without SLFR

After obtaining the tension range in Table 9 and Table 10, the stress range of each mooring lines can be determined by calculating the six-strand wire rope of mooring line cross-sectional area [15]. The cross-sectional area is $10.382 \times 10^{-6} \text{ m}^2$.

The stress range of mooring lines using SLFR is differently received by each mooring lines as in Fig. 11. The maximum and minimum stress range of mooring line using SLFR are 4.740 MPa with 9.32 sec and 1.522 MPa with 12.42 sec. While the stress range of mooring lines without using SLFR get the similar trend for each mooring lines. The maximum and minimum stress range is 5.531 MPa in 11.46 sec and 0.650 MPa in 10.31 sec.

4.4. Fatigue Life Analysis Results

From the stress range results, it is obtained the fatigue life of mooring lines. Then, it is determined by the number of cycles (n), fatigue damage (D) and fatigue life where the additional safety range about 0.67 [8].

Based on Fig. 12, the comparison of fatigue life of mooring lines with or without SLFR takes effect in the stress range and its period that get difference significantly in the mooring line 1 which is about 182.540×10^4 years because the SLFR located in midship area nearby the bow as in Fig. 7(a). When the wave incident in head seas happened, the mooring line 7 and 8 with SLFR get major structural responses as same as the mooring line 1 and 8 without SLFR. It is smaller tensions than other mooring lines. Consequently, the fatigue life using SLFR is smaller than without using SLFR.

At the same time, the fatigue life result using SLFR is 412 years on mooring line 4 and 5. The fatigue life result without using SLFR is 6,636 years on mooring line 5.

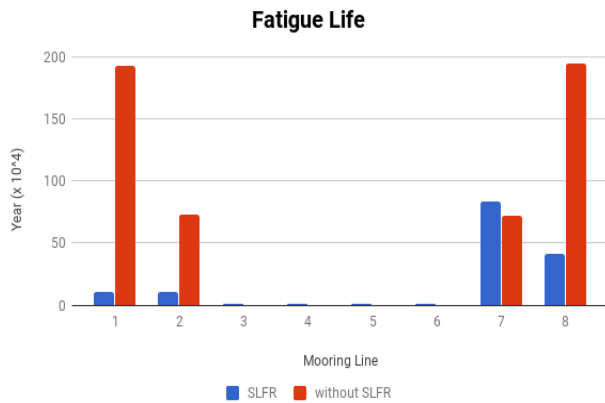


Figure 12. Comparison of fatigue life using SLFR and without SLFR

5. Conclusion

The fatigue analysis of catenary mooring system due to harsh environment in head seas have been performed using SLFR and without using SLFR. The general conditions can be drawn quite well because maximum RAO is less than the wave height. It means that the response amplitude always be smaller than wave incident amplitude, so that the maximum RAO due to the head seas in harsh environment with $H_s = 4.0$ meters and $T = 7.7$ sec in the highest surge motion without using SLFR is 0.615 m/m, the highest heave motion when using SLFR is 1.048 m/m while the highest pitch motion without using SLFR is 2.23 $^{\circ}$ /m. Another thing happened when using SLFR is about 0.207 rad/sec longer frequency than without using SLFR.

By catenary mooring system design accordingly and using SLFR calculated by head seas, the fatigue life result on catenary mooring systems in the harsh environment by using SLFR is 412 years on mooring line 4 and 5. Another the fatigue life result without using SLFR is 6,636 years on mooring line 5. The structure is still in safe condition because of the API design safety factor is about 300 years.

Acknowledgements

The authors would like to convey a great appreciation to PT. Chevron Indonesia Company, Balikpapan, East Kalimantan, Indonesia for supporting this research data.

References

- [1] Faltinsen OM. Hydrodynamics of High-Speed Marine Vehicles. New York: Cambridge University Press; 2005. p. 421-426.
- [2] Sun JW, Wang SQ. Study on Motion Performance of Deepwater Spar Platform under Different Mooring Methods. China: Period of Ocean University of China; 2010. p. 135-137.
- [3] Chakrabarti SK. Hydrodynamic of Offshore Structures. USA: Computational Mechanic Publication Southampton; 1987. p. 380-381.
- [4] Saidee MH. Fatigue Analysis and Design of Mooring Systems: Assessment and Comparison of Different Methods. Master of Science Thesis. Norway: NTNU; 2015. p. 3-4.
- [5] Vryh of Anchors BV. Anchor Manual: The Guide Anchoring. Netherlands: Capelle a/d Yssel; 2010. p. 7-8.
- [6] Larsen K. Lecture Note: Mooring and Station Keeping of Floating Structures. Norway: NTNU; 2014. p. 10-13.
- [7] Chrolenko MO. Dynamic Analysis and Design of Mooring Lines. Norway: NTNU; 2013. p. 3-4.
- [8] API RP 2 SK. Recommended Practice for Design and Analysis of Station Keeping Systems for Floating Structures. USA: American Petroleum Institute; 2005. p. 30-31.
- [9] Nugteren F. Flexible Riser Fatigue Analysis: Studying Conservatism in Flexible Riser Fatigue Analysis and Development of an Engineering Model to Study Influencing Parameters of Local Wire Stress. Master of Science Thesis. Netherlands: TU Delft; 2015. p. 10-12.
- [10] Bannantine AJ, Comer JJ, Handrock LJ. Fundamental of Metal Fatigue Analysis. USA: Prentice Hall; 1990. p. 1-10.
- [11] DNV OS E301. Position Mooring. Norway: Det Norske Veritas; 2004. p. 35-37.
- [12] Nallayarasu. Offshore Structures Analysis and Design. India: Indian Institute of Technology; 2015. p. 99-100.
- [13] API RP 2 RD. Design of Risers for Floating Production Systems (FPSs) and Tension-Leg Platforms (TLPs). USA: American Petroleum Institute; 1998. p. 55-56.
- [14] Larsen CM, Svein S, Jacob Q. Handbook on Design and Operation of Flexible Pipes; B1 Design Analysis. Norway: MARINTEK - NTNU - 4Subsea; 2014. p. 184-190.
- [15] DNV OS E304. Offshore Mooring Steel Wire Ropes. Norway: Det Norske Veritas; 2015. p. 26-27.

Study of Engine Propeller Matching for High-Speed Vessel with Gawn Series Propeller

Nurhadi,^{a,*} Hardi Zen,^b Sumarsono,^c

^aBalai Teknologi Hidrodinamika, BPPT. Email: nrhadi@gmail.com

^bBalai Teknologi Hidrodinamika, BPPT.

^cBalai Teknologi Hidrodinamika, BPPT.

Abstract

At the design stage, model testing is required to verify the results of the numerical calculation, such as resistance test, open water test, and self-propulsion test, which associated to the powering of the ship. Besides, engine propeller matching is required to determine the engine load characteristics. In this study, a high-speed vessel with Gawn series propeller type is used. Based on Engine Propeller Matching (EPM) results, it is known that at 28 knots of speed, the propeller has a high enough efficiency which is around 0.56 in rough hull condition. By using the CAT 280-8 engine, at 1000 rpm, ship speeds can reach about 30.5 knots and power requirements are 2400 kW.

Keywords: Engine matching; Gawn series propeller; high-speed vessel

1. Background

The development of ship design has progressed very rapidly. Some ship design software emerges with many features and advantages that are very useful for the designers to design ships.

At the design stage, model testing is required to verify the results of the numerical calculation, such as resistance test, open water test, and self-propulsion test, which is related to the ship powering [1].

From the model test results, it is important to calculate the matching point between the propeller load and the engine which will use the ship. The optimal operational and optimal load engine will know also the efficiency of propeller used. Engine propeller machine graph will facilitate the ship operation based on the desired engine load and speed of the ship [2].

Desired ship speed cannot be achieved in some cases because there is no matching between the propeller and the engine, not cause of the design of propeller or engine that used is to low [3].

Given the importance of engine propeller matching (EPM), this paper will discuss EPM on a high-speed vessel that uses Gawn series propeller type. The selection and use of Gawn series propeller are due to its high-rotary propeller

design to get high thrust and torque to achieve the desired service speed.

2. Literature review

The ship design is expected to be able to maintain the speed of service (V_s) on the operation. The design of drive system that can overcome the total resistance at such speed is necessary.

One of the stages of ship design evaluation is EPM (engine propeller matching). Matching point is an operating point of the engine rotation speed that matches the character of the propeller load. The operating point of rotation where the engine power is absorbed by the propeller is equal to the power that is generated by the engine. It produces the speed of the vessel corresponding to the planned speed of the shipping vessel.

In general, ships that move in water media with a certain speed will experience opposite resistance to the direction of motion of the ship. The amount of resistance that occurs should be able to be overcome by thrust that is generated by the propulsion system. Delivered Power (DP) is the power of the ship that drove from the Shaft Power (SP). The shaft power is getting from Brake Power (BP) that come from ship engine [4].

The forces and moments generated by the propeller can describe in terms of the principal quantities, which is presented in a series of nondimensional characteristics. These characteristics are used to describe in general the performance of a propeller [5]. These characteristics are:

*Corresponding author. Tel.: +62811328567
*Jl. Hidrodinamika, Kompleks ITS, Sukolilo
Surabaya, 60111*

Thrust Coefficient:

$$K_T = \frac{T}{\rho n^2 D^4} \quad (1)$$

Torque Coefficient:

$$K_Q = \frac{Q}{\rho n^2 D^5} \quad (2)$$

Coefficient Advance:

$$J = \frac{Va}{nD} \quad (3)$$

Where, D (propeller diameter), Va (advance velocity), n (propeller rotational velocity), ρ (fluid density).

The hull and propeller interaction is obtained from calculation to gain propeller performance characteristics when propeller operated as a propulsor of the ship [6]. The calculation method uses the following formula:

From the ship, it is known that:

$$R_T = 0.5 \rho C_T S V_S^2 \quad \text{with} \quad \alpha = 0.5 \rho C_T S \quad (4)$$

The ships thrust can be calculated by the formula:

$$T = \frac{R}{(1-t)}, \quad T = \frac{\alpha V_S^2}{(1-t)} \quad \text{with} \quad w = 1 - (Va/Vs) \quad (5)$$

$$T_{ship} = \frac{\alpha Va^2}{(1-t)(1-w)^2} \quad (6)$$

$$K_T = \frac{\alpha Va^2}{(1-t)(1-w)^2 \rho x n^2 x D^4} \quad (7)$$

$$\text{So, } K_T = \frac{\alpha V_A^2}{(1-t)(1-w)^2 \rho n^2 D^4} \quad \text{if } \beta = \frac{\alpha}{(1-t)(1-w)^2 \rho D^2} \quad (8)$$

$$K_T = \beta \frac{V_A^2}{n^2 D^2}, \quad K_T = \beta J^2 \quad (9)$$

Where, t (thrust deduction factor), w (wake factor), C_T (total resistance coefficient), S (ship wetted surface area).

3. Methodology

The research will use data analysis based on the obtained model test results. From the data model test, it will calculate the interaction between propeller load and the propulsion engine to know how many matches of them. For more details, it can be seen in the following diagram at Fig. 1.

4. Results and Discussion

When designing a ship, the propulsion engine is predicted from the value of the resistance of the ship. The values can be obtained through numerical approaches or ship model test in the towing tank [7].

This study uses a high-speed vessel with L_{pp} (55.35 m), B (8.10 m), T (2.6 m), block coefficient (0.395), midship section coefficient (0.567), prismatic coefficient (0.696), wetted surface area (457.3 m²). The propeller used is Gawn series type with a diameter (1.5 m), P/D at 0.7R (0.954), A_e/A_o (1.1), with a number of blade 3, as shown in Fig. 2.

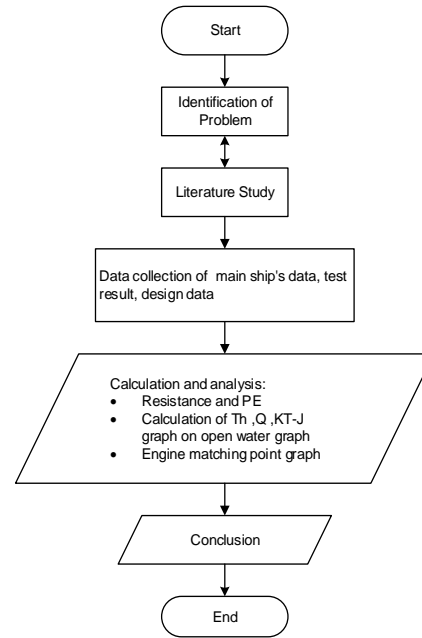


Figure 1. Diagram of the test methodology.

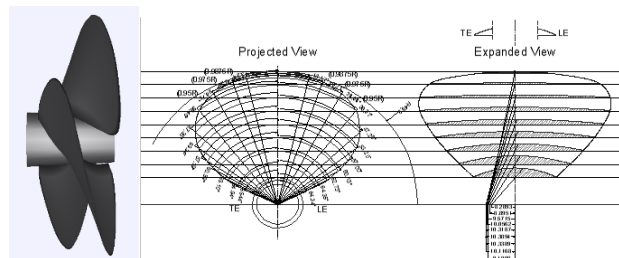


Figure 2. Used Gawn series propeller geometry.

Based on the results of the resistance test of a high-speed vessel model, the obtained of the effective power value are listed in Table 1.

Table 1. High-speed vessel resistance and PE prediction values

Vs Knots	Fn	RT kN	PE kW
27.07	0.6038	294.63	4102.9
28.09	0.6265	307.35	4440.9
29.07	0.6484	317.82	4752.3

For open water diagrams, they are obtained from open water test shown in Fig. 3.

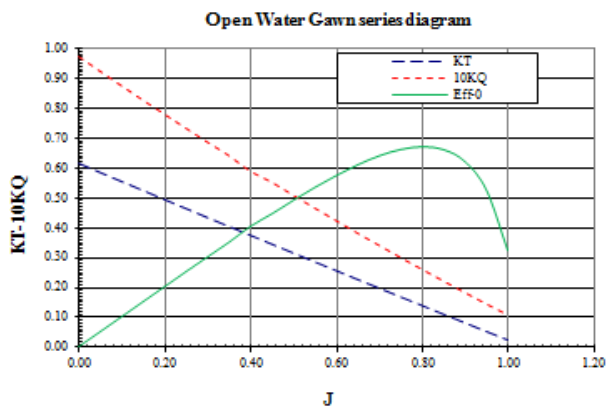


Figure 3. Gawn series open water test chart

With resistance and open water data, the KT-J value of the ship propeller load can be calculated to obtain the open water graph. For calculation of α , β with the existing formulas, the results obtained according to Table 2.

Table 2. α and β calculation of speed

VS Knots	RT/2 kN	α RTs/Vs ²	β	
			Clean	Rough hull-15%
27.07	147.3	759.640	0.698	0.803
28.09	153.7	736.076	0.676	0.778
29.07	158.9	710.705	0.653	0.751

The RT is divided by two, according to the twin-screw ship (two propeller movers), so for the calculation of one propeller, the total load resistance of the vessel is divided equally into 2. By varying the value of J from 0 – 1, the KT-J diagram can be calculated on clean hull condition and rough hull condition that a margin by 15%, it gets result according to Table 3.

The result of plotting propeller loads on open water propeller diagram shown in Fig. 4 is called KT-J graph.

Table 3. Calculation results of KT in Clean Hull and Rough Hull conditions

No	J	KT Clean Hull			KT Rough hull-15%		
		27 knots	28 knots	29 knots	27 knots	28 knots	29 knots
1	0.1	0.007	0.007	0.007	0.008	0.008	0.008
2	0.2	0.028	0.027	0.026	0.032	0.031	0.030
3	0.3	0.063	0.061	0.059	0.072	0.070	0.068
4	0.4	0.112	0.108	0.105	0.129	0.125	0.120
5	0.5	0.175	0.169	0.163	0.201	0.195	0.188
6	0.6	0.251	0.244	0.235	0.289	0.280	0.271
7	0.7	0.342	0.332	0.320	0.394	0.381	0.368
8	0.8	0.447	0.433	0.418	0.514	0.498	0.481
9	0.9	0.566	0.548	0.529	0.651	0.630	0.609
10	1	0.699	0.677	0.654	0.803	0.778	0.752

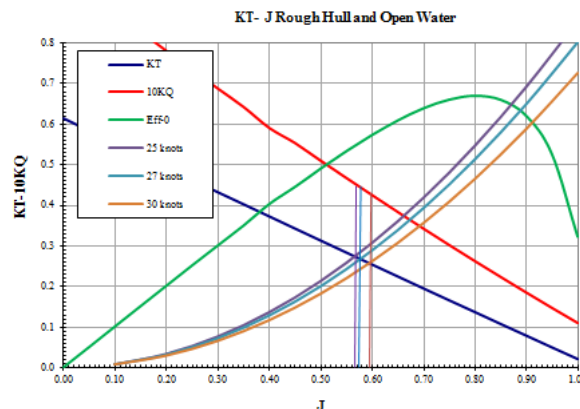


Figure 4. KT- J propeller load of rough hull conditions.

The KT-J on Fig. 4 at rough hull condition:

- At 28 knots of the KT-J and open water charts, it is known that the intersection of KT-J lines with open water graph is intersected by the KT line at the value of $J = 0.585$ where the value of KT is 0.265 and the value of 10KQ at the value of 0.44
- By knowing the value of J, the optimum rotation of the propeller can be calculated

where $J = \frac{V_A}{nD}$ or $n = \frac{V_A}{J.D}$ so Q can be calculated with the formula $the K_Q = \frac{Q}{\rho n^2 D^5}$ and $Q = K_Q \rho n^2 D^5$

4.1. Calculation of DHP and BHP

In developing the propeller load characteristics, the variables involved are propeller torque and propeller speed. Propellers torque are calculated from the graphical processing of hull and propeller interaction which get by self-propulsion test. While the calculation of Power required is calculated by the formula $P = 2. \pi. Q. n$ Calculation results for each speed in clean hull condition is shown in Table 4 and rough conditions in Table 5.

4.2. Engine Propeller Matching

From the calculation, it is known that for the condition of Rough Hull, at 28 knots the required power of 2074 kW so that if the speed is at 85% MCR then the required engine power is $2074 \times 1.15 = 2440$ kW. From the existing engine specifications, obtained Caterpillar engine, Cat 280-8 type of propulsion engine which 2460 kW power [8]. The engine is working at 1000 rpm, so the reduction gearbox with a ratio of 1.28: 1 is needed.

Based on the results, a graph of propeller load, speed, and power is made to see the characteristics of the engine when loaded as shown in Fig. 5. This figure shows the propeller load power requirement is still below the maximum power generated by the engine and coincide with propeller load.

Table 4. DHP and BHP rotation on speed variation of clean hull condition

Speed	KT-J			Va	n-prop		Q- clean hull	DHP- clean hull	BHP- clean hull
Knots	J	KT	10KQ	m/s	rps	rpm	kN	kW	HP
27.07	0.602	0.252	0.4250	10.42	11.5	692	22.03	1597	1646
28.09	0.605	0.250	0.4200	10.81	11.9	715	23.21	1736	1790
29.07	0.612	0.248	0.4150	11.19	12.2	731	24.00	1837	1894

Table 5. DHP and BHP rotation on speed variation of Rough hull condition

Speed	KT-J			Va	n-prop		Q- Rough hull	DHP- Rough hull	BHP- Rough hull
Knots	J	KT	10KQ	m/s	rps	rpm	kN	kW	HP
27.07	0.602	0.27	0.442	10.42	12.0	719	24.68	1857	1914
28.09	0.605	0.265	0.44	10.81	12.3	739	26.00	2012	2074
29.07	0.612	0.26	0.435	11.19	12.6	759	27.07	2149	2215

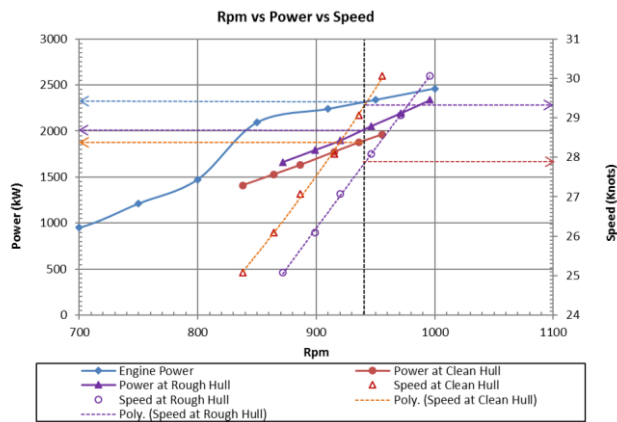


Figure 5. CAT engine matching C280-8 with propeller load on rough condition

In addition, the relationship between RPM, power, and speed are shown in Fig. 5. At 940 rpm engine speed (black dash line) will intersect with the line of speed at rough hull conditions (purple dash line). It is known the speed is 27.8 knots (the right y-axis), intersecting with the speed at clean hull (orange dash line) known that the speed is 29.3 knots. The line intersects with the clean hull (orange line) power line, so it is known that the power requirement is 1900 kW and the rough hull condition is 2050 kW. At 940 rpm. The black dash line cut the engine power curve, it is known that engine can generate power up to 2350 kW.

5. Conclusion

From the discussion and calculation of Engine-Propeller Matching on the high-speed vessel using propeller Gawn series and 280-8 Cat engines known that:

- From the calculations, it is known that to achieve 28 knots at Clean Hull condition the required power is 1736 kW (DHP) and at Rough Hull condition power requirement is 2012 kW (DHP).
- The propeller efficiency at 28 knots rough hull condition, is relatively good enough that is around 0.56.
- From EPM diagram at 1000 rpm, the obtained speed is about 30.5 knots with a power requirement of 2400 kW in rough hull conditions.
- From the calculations performed, engines and propellers are properly used to high-speed vessel type.

References

- [1] ITTC. Testing and Extrapolation Methods Propulsion, Propulsor Open Water Test, (Revision 01); 2002. p. 7.5-02-03-02.1.
- [2] Habibi, Nurhadi. Analisa Pemilihan Propeller Tipe B- Series Pada Kapal Feri Ro-Ro 600 GT Dengan Menggunakan Aplikasi Matchpro. Jurnal Ilmiah Teknologi Maritim Wave. Vol. 10 No.02; 2016. p. 75–81.
- [3] Setyo Leksono. Sinkronisasi Propeller Dengan Mesin Induk Pada Kapal Ikan Untuk Meningkatkan Efisiensi dan Kinerja. Jurnal Ilmiah Teknologi Maritim Wave. Vol. 9 No.02; 2015. p. 19–24.
- [4] Abidin M. Z., Adji S. W, Arief I. S. Analisa Performance Propeller B-Series dengan Pendekatan Structure dan Unstructure Meshing. Jurnal Teknik ITS, 1(1); 2012. p. 241–246.
- [5] Kristensen, Lützen M. Prediction of resistance and propulsion power of ships, Project no. 2010-56, Report 4 - Resistance and Propulsion Power; 2012.
- [6] Carlton J. Marine Propellers and Propulsion, second edition. Elsevier. Oxford; 2012.
- [7] Specialist Committee of 23rd ITTC. Testing and Extrapolation Methods Resistance Uncertainty Analysis, Example for Resistance Test. (Revision 01), p. 7.5-02-02-02; 2002; page1-18.
- [8] <http://s7d2.scene7.com/is/content/Caterpillar/LEHM7096-01> accessed on February 10th; 2018.

Identifying Model for Decision Making Process in a Collaborative Manufacturing Network Environment

Mohammad Rizal Firmansyah,^{a,*} Wihdat Djafar,^b

^aDepartment of Naval Architecture, Engineering Faculty, Hasanuddin University, Makassar. Email: mr.firmansyah@unhas.ac.id

^bDepartment of Naval Architecture, Engineering Faculty, Hasanuddin University, Makassar.

Abstract

In order to be competitive through globalisation and free trade agreements, Small Manufacturing Enterprises must provide a high quality products at a competitive price at the right time. But inadequate resources of the enterprises have prevented them to remain competitive. Therefore they need to innovate and find new ways to overcome these challenges. Collaborative Manufacturing Network (CMN) is a way forward to address these challenges. However, the process of collaboration is not a simple process. Instead, it is a complex and very dynamic process since there are many factors involved that need to be considered for the establishment of a successful collaboration. Many researches have been conducted in this area of CMN, but there are still numerous unsolved problems identified. Decision making issues and formulating business collaboration model in a context of CMN are two such issues. This research tries to identify the problems faced in a CMN environment, stress on the importance of building a model based on the consideration of aspects involved in a CMN and then identifying model for decision making process in a CMN Environment.

Keywords: Collaborative manufacturing network; decision making process; small manufacturing enterprises

1. Introduction

In this global business environment, manufacturing companies are facing competitive strength even greater than before [1]. Manufacturers are forced to provide products with high quality as well as low prices in the right time [2]. Challenges for a manufacturer in today global environment includes short product life cycle, product varieties, minimal inventories, concurrent processing of different products, short delivery times [3], well informed and demanding customer [1], mass customization, and short lived market opportunities [4]. That is why manufacturing companies need to continuously make an innovation and adapt their business to survive and meet the fast changing market environment. This has influenced the way of business operates and interoperates with other enterprises [5].

There are several solution have been offered by some researchers for above challenges which are improving product cycles, reducing cost, communicate and work

concurrently in the enterprise network [1], working together and establishing partner in a collaboration network [3], internationalisation, operate in different country or develop global strategies for operation coordination [2]. It seems that coordination of activities in a network become urgent to respond the fast changing environment [6, 7]. Clarke [8] state that knowledge and expertise held by others is often required in order to operate effectively in this fast changing environment.

Collaboration is a way forward for manufacturing enterprises to solve their constraints. There are several reasons for companies to conduct business collaboration and the most important ones identified by Hansson in [9] which are; 1) Collaboration as strategic positioning, 2) Learning and exchange of experiences, 3) Possibility to develop and deliver more complex products, 4) Synergy factors in technology and product development, and 5) Economic factors, such as risk sharing, investments, etc.

The driving force for collaboration is stated by Noori and Lee [10] as digitization, the internet development, and high speed data networks. This can be used for addressing many issues from design to distribution. The collaboration is expected to gain a competitive edge [11, 12] of manufacturing enterprises through increasing their skills, capabilities and capacities [13], and focus on their core

*Corresponding author. Tel.: +62-812-3745-4156
Jalan Poros Malino km. 6, Bontomarannu
Gowa, Sulawesi Selatan, Indonesia, 92171

competencies and sharing their resources [10, 13]. It is needed to sustain in this environment [14, 15]. Companies now tend to engage in a partnership [13]. For some relatively small manufacturing companies, it is important for them to collaborate to increase their scale.

Collaboration could facilitate the company's growth through [16] fostering networking among vary manufacturing industries, developing business activities into national levels, facilitating industry participation, facilitating industry collaboration with Research Centre's and building industry capacity.

Collaborative manufacturing network (CMN) is an approach that can be used to solve those challenges. Johansen, Comstock and Winroth [17] see CMN as an "extended enterprises consisting of several companies that cooperate in a project resulting in a manufactured product, where each company has expert competencies in one or several areas". It can be seen that companies joined in a CMN have bigger opportunities to increase their market niche [18]. However, the process for collaboration is not a simple process. Instead, it is a complex and very dynamic process since there are many factors involved that need to be considered for the establishment of a successful collaboration. Besides, the interaction and relationship among participants in CMN is very complex as well.

The establishment of interconnection among enterprises become requirements of a CMN in order to [5]: 1) learn from each other and exchange experience, 2) strive towards mutual objectives and developed complementary products and services, 3) explore development of complex products and services that are beyond the capability of a single company, 4) identify synergies in capabilities such as technology and product development and 5) share risk and investment. However, there are some other requirements for manufacturing enterprises in order to build a successful integration of activities [10] which are 1) addressing multi plant organization, 2) handling supply chain and distribution, 3) integrating financial analysis, 4) providing real time forecasting, 5) supporting manufacturing execution systems and finite scheduling, and 6) providing executive information and decision-making tools.

To fulfil the requirements, many companies have built a complex system that facilitate the decision making process but most of the system are integrated vertically. In the decision making process connection among all decision components need to be integrated horizontally and vertically. This connection needs a very complex structure as well as requires large investment for the establishment. Unfortunately, most of the small manufacturing companies have limited financial resources and do not have such technical abilities to establish such a complex structure.

In order to build a supportive model that can be used by small manufacturing companies, several issues need to be considered. The production distribution among companies involves in a collaborative manufacturing [9], information and communication technology [19], the selection of

partners, the expansion capabilities of the respective participating companies for managing collaboration [5], [20], the worldwide distribution of the participant companies, the virtuality of the participating companies [21], the different uses of software tool of respective companies and understanding of the pattern of communication and information flow across different participants [19].

Trust among companies involved in collaboration need to be enhanced as well since the collaborative arrangements are based on identified competencies [22]. Many of the business process should be open to all participants without being fear of being taken advantage by others. This can be achieved if the participating companies understand the comprehensive aspect of their contribution, appreciate how their business information is to be used and understand how this risk is managed in respectful manner.

There are many factors and issues involved on the decision making process in a CMN. A range of production, managerial and economic decision confront a CMN including [23]: 1) where to manufacture, 2) sharing of design and engineering aspects among members of CMN, 3) optimal scheduling logistics of CMN, 4) dependency versus independency of manufacturing in a CMN, 5) how to perform business forecasting for the network, 6) who receives an order and how is it entered into shared systems, 7) purchasing issues among partners, 8) conflict resolution and risk management, 9) sharing confidential information among partners and 10) fostering trust across diverse organisational culture.

Most of these fragmented information and decision processes are controlled by various members in a CMN. Making a holistic decision model in this complex decision making environment increases the difficulty for the participants in a CMN to provide a complete solution to the customers. Coordination in a CMN which is includes a complex myriad of partners spanning several countries and even continents, is not understood yet [17].

The understanding of such factors is essential for the establishment of a comprehensive model of decision making process. Further, the relationships of dependent as well as independent participants in collaboration need to be mapped in order to model the business collaborations in the context of CMN. This is very significant for manufacturing companies since there are tendency for them to make collaboration without a clear understanding of the issues and constraints which could lead to increased risk on business failure.

2. Dependent and Independent Participants in a CMN

Basically, participants in a collaboration manufacturing network can be divided into internal and external participants. Internal participants are participants who exist within a company while external participants are participant from external company. The relationship among

participants can be dependent or independent to each other, within company (internal participants) and/or among external company (external participants) [24, 25]. Dependency of the participant relationship depends upon the type of collaborations they have involved [2].

There are several forms of collaborations and each form consists of different participant. Generally the most common form of collaboration is between system integrator (SI) and supplier [9]. Danilovic and Winroth [9] explain that the relationship of SI and supplier can be formed in three models which are the traditional model, the Japanese model and the advanced model. Each model is differentiated based on the involvement level of the supplier in the system integrator.

The traditional model, where suppliers are involved after the design is completed, and technical specifications determined. In this model, system integrator restricts access to the information design. In the Japanese model, the involvement of suppliers are in the early stage of the concept phase before design is determined while in the advanced model, the supplier involvement is balance between the benefits of the Japanese model with access to new technical ideas until the final definition is determined. In the SI and supplier relationship, Danilovic and Winroth [9] describe external participant relationship as a system integrator (usually big company) and several suppliers. The relationship among participants is dependent each other.

Different form of collaboration is proposed by Montreuil, Frayret, and D'Amours [26] which includes more detail different participants. They describe the collaboration form into network manufacturing (NetMan) which consists of several manufacturing centres. Each of these manufacturing centres can be in the form of external business or internal business. External business can be external supplier or subcontractor while internal centre can be manufacturing cell, a process centre, a department or a maintenance centre. Each of these internal businesses acts and operates as a manufacturing business but still in coordination with their parent business. In this NetMan model, there are internal and external participants involved. External business can be regarded as external participants while internal business can be regarded as internal participants.

Similarly, Mesa International [27] describes the types of participants involve in the collaborative manufacturing as external and internal participants. External participants include customer, distributor and channel partners, material and sub-product supplier, outsourced or contract manufacturers, logistics partners for distribution, warehousing and transportation and service provider. While internal participants within each company includes multiple departments and division supported the manufacturing process. The agility to deliver accurately of product (customized or new product) requires synchronization among manufacturing activities in the network [27]. This synchronization performed by internal participants consists

of design section which is working together with other sections (marketing, sales, etc) including partner design, production groups and customer.

Montreuil, Frayret, and D'Amours [26] describe three version of network manufacturing which is highly distributed manufacturing network, manufacturing network with bus realization centre, and manufacturing network with bus realization centre and centralized supply centre. Each alternative involves dependent and independent participants. Several centres in each alternative act as an independent participant while the other as dependent participants. ARC [28] explains the model of collaborative manufacturing management. In this model, it is described internal participants (functional area in a company) and external participants (external company entities). It emphasises the importance of internal participants to collaborate internally which mean that the relationship among internal participants need to be considered. The relationships between internal and external participants are also recognised.

2.1. Relationship of dependent and independent participants

The importance of relationship of dependent and independent, external and internal participants in a CMN has been described by several researchers. Firstly, it is need to define participants relationship in a collaboration network [24, 25, 29, 30, 31, 32]. Then trust and commitment in this relationship are required to link their activities and resource ties and to describe interdependency of internal and external participants, determine performance network and identify additional opportunities for joint project [8, 11, 25, 33, 34]. This also can be used to gain competitive advantages in cost savings, technological innovation, shorter lead times, joint marketing program and shortened response time [35] under the competitive pressures. This is important in determining long term relationship [26, 31, 36].

This long term relationship need strong business interdependencies which is relies on information exchange, collaborative planning and operation management and business rules of the game [11, 30, 35]. In managing the relationship, there are key successes factors need to be considered [11] which include; quality, reliability, flexibility, transparency, and process intervention, co-operative practices, learning from problems and commitment to quality and regular meetings concerned with strategic planning and development, and included quality evaluation, costing, forecasting and scheduling.

Kanter in [11] argues that the most productive relationship will achieve five types of integration which are; strategic integration – enable discussion among top leaders regarding respective company goal and economic change, tactical integration – enable middle managers to work together to develop plans for specific projects, operational integration – enable solution to carry out daily

work, interpersonal integration – enable building necessary foundation for sustaining the future of the relationship, and cultural integration – enable people involved in the relationship to have the communication skills and cultural awareness to bridge inter-organisational and interpersonal differences.

Choy, Lee, and Lo [1] described two forms of the relationship of participants in a collaboration which are customer relationship management (CRM) and supplier relationship management (SRM). CRM is “a process by which a company maximizes customer information in an effort to increase loyalty and retain customers’ business over their lifetimes”. This CRM is about finding, getting and retaining customers to build long term and profitable relationship. SRM is a relationship that can be used in supplier selection for increasing the competitiveness of a manufacturer through three establish mechanisms which are; 1) Support of improved business processes across the supply chain, 2) a next-generation architecture that can handle multi-enterprise processes, and 3) facilitation of rapid product cycles and new product introduction.

Johansen, Comstock and Winroth [17] divides relationship in a collaboration network into four categories which are upstream vertical relations (each company has suppliers), downstream vertical relations (relationship with customer or buyer), direct horizontal relations (relationship between the company and/or organization and other industry players), and indirect horizontal relations (relationship with industry outside its own industry segment). The relationship is different from the Palakshappa and Gordon [37] views. They categorised relationship into high or low technology use, cumulative or complementary resource contributions, international or domestic partners and above or below average performance.

The simpler categorization of relationship is stated by Valespir and Kleinhans [38]. They differentiate the relationship among participants as make or buy relationship. Palakshappa and Gordon [37] explained that the relationship in collaborative network may differ in terms of their legal structures, governance arrangements and the number of participating organisations which may include many other participants in research and development, production and manufacturing, sales and marketing, or a number of other activities.

Montreuil, Frayret, and D’Amours [26] explain the other form of relationship among participants in a network manufacturing (NetMan) centres. They said that all relationship must be built on a mutually agreed conventions and agreements. The convention arranges coordination as well as the information flows from each centre respectively. The contents of the conventions are deal with the rules of how to perform and modify order among center.

Perrin et al. [5] described a Synchronization Point (SP) model which can be used for supporting collaboration and

cooperation for multi enterprises processes. The model takes advantages of workflow management systems and groupware systems. With this model participants can work together by only need to agree cooperation rules according to contract specification and the SP model will provide all information needed for the cooperation. The advantages of this SP model is its ability to be updated during work progress as well as to evaluate the process against a given specific criteria.

2.2. Issues in the relationship of independent and dependent participant

Anumba et al. [19] has introduced a concept of a multi agent system (MAS). The MAS can support the interaction among different participants that usually conducted in a collaborative design. They argued that the system can be used for facilitating collaborative design in a distributed construction environment. The concept can also be used for ease multidisciplinary perspective, tool and techniques. However, the systems still need to be developed as some issues in the relationship between participants are not covered yet. Issues include is mechanism for the integration of agents with legacy CAD and IT systems.

Issues regarding distances in a relationship are stated by Miralles in [9]. He said that there are four types of distances in which companies can have in their relationship. They are social distance, cultural distance, technological distance, and time distance. Further, they explain that social distance is whether the companies familiar each other with their way of thinking, cultural distance is whether they are different in term of values and norms, technological distance is whether they are different in terms of technological development while time distance refers to whether time for make product delivery as well as payment. These distances can be reduced by increasing social interaction among companies.

2.3. Map of the relationship in the dependent and independent participants

Relationships between buyers and suppliers in manufacturing industries have changed substantially over the past few decades [35]. The successful collaboration among participants in a CMN depends on the degree of closeness in the relationship (Prasad in [9]). There are many participants involved in collaboration and each participant with their production characteristic need to relate with other in order to get optimum benefit of such collaboration. Besides, there are many types of collaboration with their respective relationship among participants. In order to have successful integration, all components involve in a collaboration have to be considered and managed [39]. Coordination aspect is seen as important factor to be considered in the mapping of relationship as it relate interdependency among business process [33].

Palakshappa and Gordon [37] stressed the importance of how the relationship is conducted. The purpose of collaboration need to be analysed as it determined the successful collaboration. Further, they said that it needs to differentiate whether a company's conduct in collaboration on their own or as a result of public policy initiatives as they will result on a different benefit. Participants in collaboration manufacturing network consist of manufacturing nodes which are connected by material, information and process flow. This relationship need to be mapped as it determines the success implementation of collaboration [5, 28].

It can be said that for the successful of collaboration, there are some aspects need to be understood. First of all, types of collaboration, then how many participants involved in the collaboration and how they connected each other in terms of their production characteristics. The relationship among participant is important to understand. Hence the identification of all participants to be joint in a CMN needs to be known as well as their respective relationship [40]. Further they said that the understanding of supplier and customers must also include the customers' customers and the suppliers' suppliers.

According to Shi and Gregory [41], coordination between market requirements and corporate strategies influence all aspects in the collaboration including manufacturing network and internal participants. Pattern of coordination must be decided before collaborative network is designed. This pattern and other aspects are important for designing collaborative manufacturing network [41]. Further, Yam, Chan and Chung [40] said that it is very important to understand that all participants to get involved in a manufacturing network.

The successful collaboration among participants in a CMN depends on the strength relationship among them. Mapping the relationship among participants involved in a CMN is crucial in order to better understand the connection of each participant. Huff in [37] described that mapping technique have been used to develop a visual representation of elements which influence performance in the relationship. Further they explained that mapping provides a good trigger for memory and will help reveals gaps in information. In a mapping of relationship, there are three things need to be considered which are information, material and process flow [28]. Palakshappa and Gordon [37] said that mapping will allows us to assess participants' relationship and their performance in the collaboration.

2.4. Classification of participants and their relationship

There are some possibilities regarding participants and their relationship. Participants both can have dependent and independent relationships. In the describing the relationship, it is much easier if the relationships among participants are being put in the house of relationship (Fig. 1).

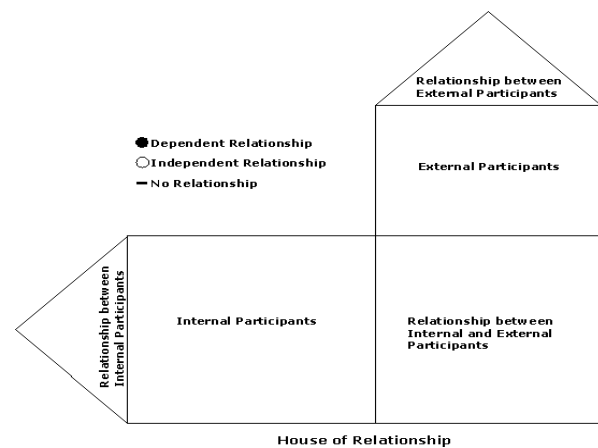


Figure 1. House of relationship (adapted from Evans and Lindsay [42])

The idea of this house of relationship is adapted from the house of quality [42]. In this house, a set of matrixes is used to relate the internal participants and external participants and between external and internal itself. Building the house consists of five basic steps which are 1) identify internal participants, 2) identify external participants, 3) relate internal participant to the external participants, 4) relate participant in the internal participants and 5) relate participants in the external participants.

The development of this house of relationship can be illustrated below.

Step 1. Identify internal participants. Internal participants are participants who exist within a company that relate directly and indirectly with external participants in the collaboration. Participants who relate directly with external participant are called dependent participants while participants who relate indirectly with external participants are called independent participants. These kinds of participants can be system integrator (the company itself), manufacturing cell, a process centre, a department, a maintenance centre or any functional area in a company. Beside the relationship with external participants, internal participants also can have relationship among them.

Step 2. Identify external participants. External participants are participants external company that relate directly or indirectly with internal participants. These kinds of participants can be supplier, customer, distributor and channel partner, material and sub-product supplier, outsourced or sub-contractor, logistics partners for distribution, warehousing and transportation and service provider. Similarly, the relationship is not only with internal participants in a company but also among the external participants itself.

Step 3. Develop a relationship matrix between internal participants to the external participants. Internal participants are listed down the left column while external participants are written across the top. In the matrix itself, symbol indicates the relationship. The purposed of the relationship matrix is to show whether the relationship

between external participants and internal participants are dependent, independent or no relationship.

Step 4. Relate participants in the internal participants. In this step, relationship between internal participants is showed. The relationship is also represented in a symbol which show whether the relationship is dependent, independent or no relationship.

Step 5. Relate participants in the external participants. This step is conducted in the same way in step 4. Only that it relate between external participants itself.

There are several types of collaborations and each type involves different participants. Several relationship models are described to show the use of this house of relationship. Danilovic and Winroth [9] describe participants in his model as external and internal. Internal participant is described as system integrator (SI), usually a big company which has several suppliers which act as external participants. The relationship among these participants is dependent between SI and supplier but independent and possibly dependent among suppliers. The relationship among these participants can be described in the house of relationship below (Fig. 2);

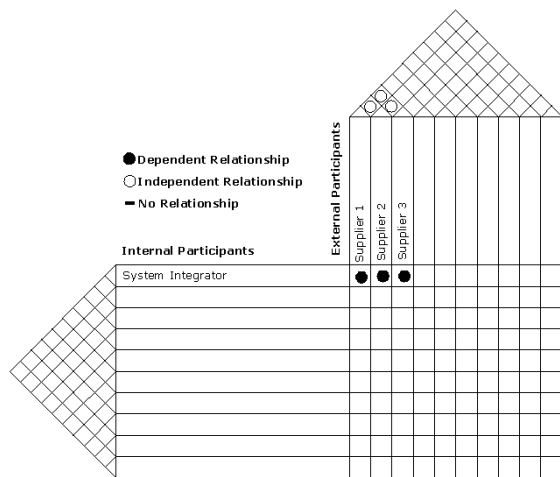


Figure 2. Mapping of relationship for Danilovic and Winroth model [9]

The relationship between suppliers can be dependent or independent depend on whether between one supplier and other supplier has direct relationship among them. If they have direct relationship, it means that they have dependent relationship and vice versa.

Different form of collaboration is proposed by Montreuil, Frayret, and D'Amours [26] who includes more detail of participants compare to Danilovic and Winroth [9] model. They described the collaboration form into network manufacturing (NetMan) which consists of several manufacturing centres. Each of these manufacturing centres can be in the form of external business or internal business. External business can be regarded as external participants which includes external supplier or subcontractor while internal centre which can be as internal participants includes manufacturing cell, a process centre, a department

or a maintenance centre. The relationship among these participants are described in the house of relationship below (Fig. 3);

The more complete description of external participants is explained in Technology Partnerz [43] which includes supplier, customer, media, shareholder, employees, creditors, unions, governments, regulators, and market analysis. For internal participants, the most complete description is discussed by Timings [44] which includes marketing, design, procurement, material preparation, processing, assembly, finishing, packaging, quality control. Not all identified participants here are important and used in the collaborative manufacturing process. For examples, in the external participants, media, employee, creditors and unions are not too important in the manufacturing process.

These participants are regarded not important as from the author point of view, they are not directly and indirectly involve in the manufacturing process. In fact, they have no any relationship with manufacturing process activities.

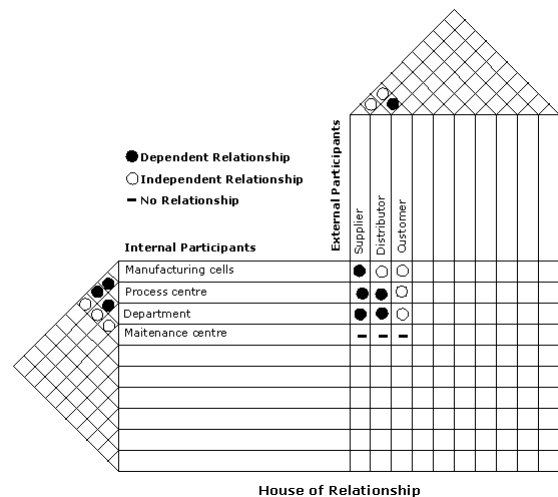


Figure 3. Mapping of relationship for Montreuil, Frayret and D'Amours (2000) model [26]

The more comprehensive identification of external and internal participants which is involved in the collaborative manufacturing network can be described as follows; external participants includes supplier, customer, distributor, subcontractor, regulator and government while internal participants includes marketing, design, procurement, material preparation, processing, assembly, finishing, packaging, quality control.

Mapping of these relationships can be conducted using the house of relationship as follows (Fig. 4);

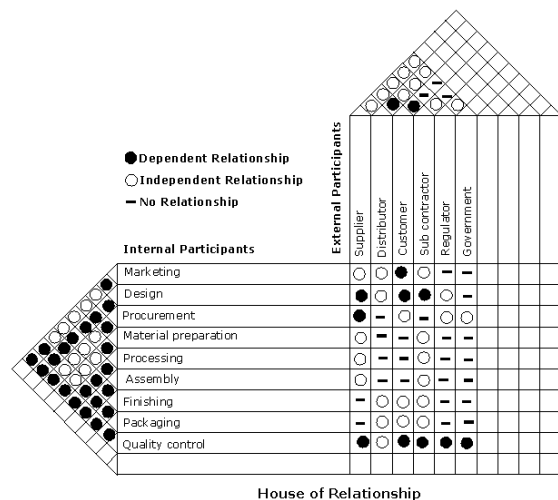


Figure 4. Mapping of relationship for proposed CMN model

It can be seen from these cases of participants and their relationship that as long as all participants (internal or external) which involve in the collaboration manufacturing network can be identified, then analysis regarding their relationship can be easily conducted using the house of relationship. Although the more complete identified participants, the more complex their relationship matrix is. Any issues regarding the relationship must be considered in this mapping process.

3. Issues in decision making process

The decision made to be involve in a globally network collaboration will determine the competitiveness of a company. Factors that need to be considered in this decision-making process are production, marketing, design and development. Cil, Alpturk, and Yazgan [20] includes social, environment and economic concerns in the consideration for decision making process. Forecasting demand is one other factor that influences the decision making [45]. There are several systems have been developed in order to facilitate the decision making process in a collaborative environment.

Courtney [46] described the flow of conventional decision making process as follows. First is problem recognised and defined. After that alternatives of solution are generated and by using model development, alternatives of solution being analysed. Then the best solution can be selected and implemented. This process keep continued in a loop of decision making process. Based on this simple decision making process, Courtney [46] developed group decision support systems (GDSS). The development is forced by the change in the collaboration network where production unit which is previously operated separately become an integrated production and by the changes of participant number and size from dispersed area. This is also influenced by the behaviour change in collaboration network. This new system enables

brainstorming, idea evaluation and communication to support team problem solving. The establishment of executive information systems extend the possibility of this system to include corporate level decision making process [46]. For making decision making smarter support, Courtney [46] included a model management system and knowledge based decision support system which is based on artificial intelligence and expert systems into GDSS. The process of decision making in this new approach is start from the recognition and definition of problems but instead of analysing technical perspective, the process consists of developing multiple perspectives. Perspective then synthesized and translated it into actions as a result of decision making [46].

Further, Courtney [46] described several form of organization in decision making. This organization can be in the form of units within an enterprises or temporary groups to solve decision problems. They categorized the organization into four which are;

- The Leibnizian organization. This organization can creates knowledge to make inferences about cause and effect of a relationship.
- The Hegelian organization. The decision making is based on conflict. Decision makers encourage the development of alternative points to solve a decision problem. The solution is chosen for solving the problems.
- The Kantian organization. The decision making is made from selection of many alternatives which is generated by organization. The problems is analysed from a technical perspectives. This approach requires knowledge management which are capable of maintaining problem data and support the development alternatives for explaining the data.
- Singerian organizations. This organization views the world as a holistic system, in which everything is connected each other. Assumption should be made by identifying group or anyone affected by the decision as well as 'true' assumption which will be based on the decision actions.

Courtney decision making then developed into group decision support system (GDSS) by Cil, Alpturk and Yazgan [20]. This development was conducted in order to cover the complexity of social function in decision choice. This social function consists of cultural, organizational, personal, ethical and aesthetical. This system consists of web technology, a group decision making (GDM) process, a large number of multi-criteria decision making methods and social function. The need for GDM currently is even greater than before. This is because the tendency of company to involve in collaboration which is result in the complexity of business relationship. The complex relationship adds the number of organization and decision makers that involve in the decision process. This situation become more complex as there is greater online access to multiple external information sources besides the decreasing time needed to make a decision [20]. This GDSS system supports a group working in an unstructured

problem and can support discussion oriented task in a group decision making [20].

Another system of decision making in a collaborative environment is proposed by Lee and Lau [47]. They designed a multi-agent modelling which can be used in a distributed information system applications. Further, they explained that this system can be used for modelling dispersed manufacturing network which can connect variety of manufacturing company on a global basis. Companies involve could be geographically separated in terms of allocation, coordination and monitoring of administration tasks. This model has an ability to facilitate the efficient performance of task allocation to the most appropriate company. Intelligent agents are used in this model to monitor the information flow and the allocation of task among participants in a network. The authors argue that the model developed can be used for various purposes, including decomposing jobs into fundamental tasks and design and creation of intelligent agents to optimize task sequence across distributed network.

An agent based systems are also suggested which can be used for make a decision locally according to local knowledge [19]. While the importance of understanding the factors involved in the decision making process is stressed by Danilovic and Winroth [9]. They composed four big questions into of ‘what’ is integrated, ‘who’ participating in the network, ‘when’ such participation and integration needed and ‘how’ the integration securely in a mechanism.

The decision making process issues in collaborative network environment involves on how to design an approach that can facilitate the decision making process while considering all factors of decision making. Lee and Lau [47] said that in their developed model which is multi-agent approach for handling administration matters among companies in the network, factors for refining central management systems still need to developed in supporting the fully integration of the system. On the other hand, the importance of community and collaboration was emphasized by Courtney [46] though conflict can emerge in any part in the network. This conflict must be managed and dealt with it so that new decision making environment are needed as the expansion of current decision making system and knowledge management [46].

4. Business model collaboration in the CMN context

The extension of complexity of collaborative network which is varying in the degree of integration is not described yet. The most important reasons identified behind this [9] which are 1) creation of procedures and organizational routines enabling a high degree and high intensity of integration, and 2) design of a supportive decision-making structure. They further explained that it is very important to understand the characteristics of organization behavior in order to better design network setting in term of what is integrated, who is participating in networks, when such participation and integration is

needed and how desired integration is to be secured. The other factors that influence the difficulty in designing a comprehensive framework for collaborative network are the lack of definition of complex business model collaboration which considered the levels of integration. Therefore it is important to define first the complete business model of collaboration before designing the framework for such comprehensive collaborative network.

Model of CMN proposed by Lin [48] will be suitable for development by considering relationship mapping in the previous section. In his model, collaborative partners of small manufacturing enterprises are categorised into three groups which are customer, suppliers and contractors. In this new proposed model, partners of SMMEs consist of four groups which are customer, suppliers, subcontractor and distributor. In addition, there are four collaboration network identified in the CMN itself which are collaborative marketing, collaborative design, collaborative procurement and collaborative production. Each of these four collaborations conducted only for their designated goal and CMN combine all these four into one single of collaboration. All these collaboration can be conducted by two or more participants companies.

The design of business collaboration in CMN context is showed in Fig. 5. It can be seen from this figure that group of customers have relationship with group of sub-contractor, group distributor, collaborative design and collaborative marketing. While group of sub-contractor have relationship with collaborative design beside with group of customer. Group of distributor have relationship with customer and CMN itself while group of supplier have relationship with collaborative design, collaborative production and collaborative procurement.

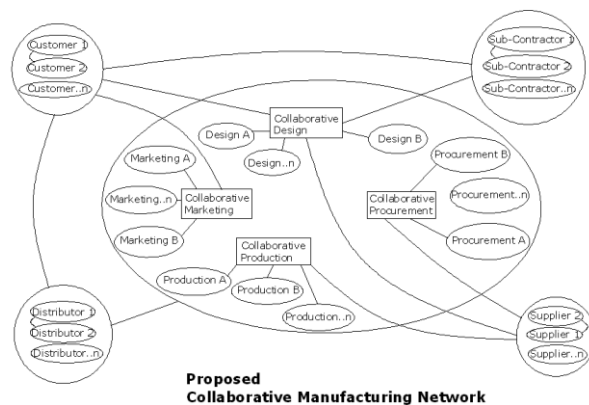


Figure 5. Business collaboration model in the context of CMN

5. Identification of an integrated model of decision making process in CMN

It has been discussed that there are several issues regarding decision making process in collaborative manufacturing. Many factors are need to be considered in order to facilitate the decision making process. Several approaches have been developed but there are still factors need to be included in the process. Factors that need to

considered in the design of decision making for CMN are manufacturing, logistics and servicing process should be planned on the basis of massive, real time and quality information, participants should be able to make their own decision and taking their own initiative, interaction among centre should be supported by electronic forms of data interchange and by using new information technologies and information coordination needed for massive and complex exchanges of data.

A complete model of decision making process in collaborative manufacturing environment has been developed by Courtney in Lin [48]. This decision model was developed based on Simon's four phase decision making model in Lin [48]. In the Courtney model, there are four stages for the systematic decision-making process which are; collect intelligence, develop perspective preference and mental model, design decision model and evaluate choices and implement decision outcome [48]. This decision making model is depicted in Fig. 6.

Further, Lin [48] discusses the stages in this model. First is intelligence collection. This intelligence scans the manufacturing environment within the CMN and identifies deviation between actual performance and the respective goal. Any deviation means an indication of a problems and decision is needed. The main function of intelligence are setting business and manufacturing performance goal, identifying decision problems, establishing decision problem ownership and constructing formal problem statements.

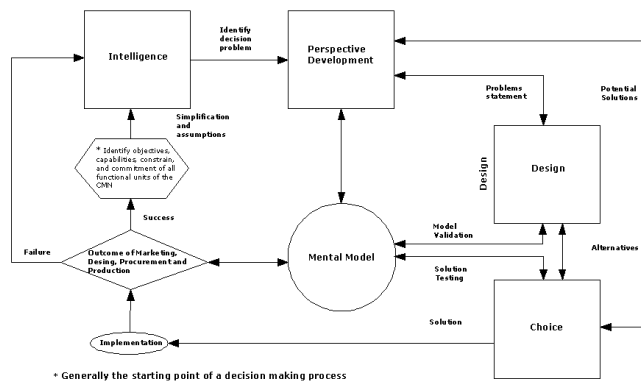


Figure 6. Systematic decision making process for GDSS. Adapted from Lin [48]

Next stage is development of perspective preference and mental model. The development is based on the expertise contributions of each manufacturing entities and these contribution bring new perspective to the creation of goals, alternatives and constraints. The understanding of manufacturing problems and participants perspectives on the problems form a complete mental model that suggest what kind of information and data should be analysed, to what extend and with which method. This mental model is evolved as more perspectives developed. After that, stage of design decision model and evaluate choice is discussed.

In this stage, design phase focus on the simplification of manufacturing environment in CMN and conceptualising decision problems in order to developing model that can analyse alternatives for decision solution. The choice phase in the mean time, compares all potential solution based on the decision model and justifies organizational resources for implementation recommended solution. The stage discuss is implementation of decision outcome. In this stage, implementation means to physically execute manufacturing activities in accordance to the recommended outcomes.

The identification of comprehensive decision model of CMN which consider all participants in the network is based on the Courtney in Lin [48] decision model. From the definition of proposed collaborative manufacturing network model in the previous section, it can be described that the CMN model consists of several collaboration which are collaborative marketing, collaborative design, collaborative procurement and collaborative production and CMN it self (Fig. 7). All this collaboration is involved in the new decision making model for collaborative manufacturing network.

In this extended decision making model, it also consist of four stages for the systematic decision-making process which are; collect intelligence, develop perspective preference and mental model, design decision model and evaluate choices and implement decision outcome. The differences with Courtney model are in the extended model, each stage consist of four collaborative items which is marketing, design, procurement and production. The differences influence the decision making process in each stage.

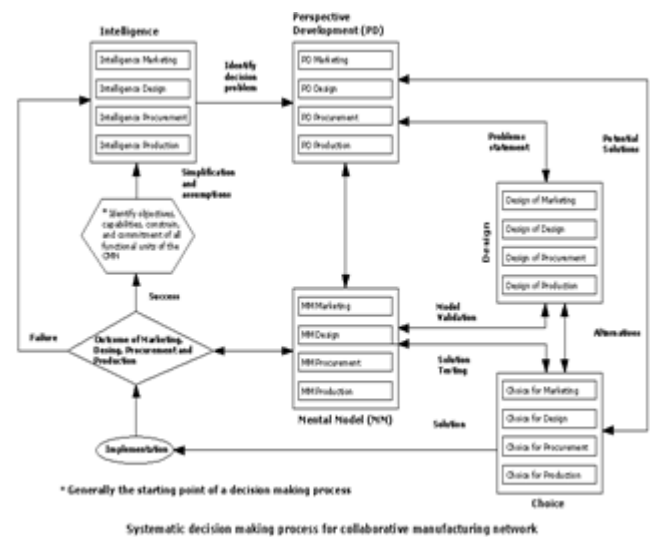


Figure 7. Extended systematic decision making model for collaborative manufacturing network. (Adapted from Lin [48])

First is in the intelligence collection. In this intelligence stage, scanning the manufacturing environment within the CMN are conducted four times which is in marketing, design, procurement and production environments.

Identification of deviations are also conducted four times between actual performance and the respective goal which indicates the problems and hence decision is needed. As four different specific environments are scanning, then setting business and manufacturing performance goal, identifying decision problems, establishing decision problems ownership and constructing formal problem statements are become more complex and complete.

In the next stages which are development of perspective preference and mental model, design decision model and evaluate choice, and the implementation of decision stage, all have the same procedure as stage 1. In each stage, instead of only consider one environment, it consider four environments.

The second stage is development of perspective preference and mental model. In this stage, the development is based on the expertise contributions of each manufacturing entities from four different environments and these contributions bring four new perspectives to the creation of goals, alternatives and constraints. The understanding of more manufacturing problems and participants perspectives which includes all environment on the problems form a more complete mental model that suggest what kind of information and data should be analysed, to what extend and with which method in each environment. This mental model is evolved as more perspectives developed.

After that, stage of design decision model and evaluate choice is discussed. In this stage, design phase focus on the simplification of all manufacturing environment in CMN and conceptualising decision problems in order to developing models that can be analyse alternatives for decision solution. The choice phase in the mean time compares all potential solution from four environments based on the decision models and justifies organizational resources for implementation recommended solution.

The last stage discussed is implementation of decision outcome. In this stage, implementation means to physically execute manufacturing activities in accordance to the recommended outcomes.

6. Conclusion

It has been discussed the formation of relationship mapping among participants in collaborative manufacturing network. This mapping is used as a basis to define new comprehensive business model in CMN context. The last part of this paper is the development of decision making process for the new CMN model which is previously defined.

References

[1] Choy KL, Lee WB, Lo V. An enterprise Collaborative management system – a case study of supplier relationship management. The Journal of Enterprise Information Management. 2004; 17(3): 191-207.

[2] D'Amours S, Lefrancois P, Montreuil B, Ramudhin A. Unquality costing sampling plans by variables and their implications on supply relationships. International Journal of Production Economics. 1993; 32: 315-326.

[3] Bareduan SA, Hasan S, Ariffin S. Finite scheduling of collaborative design and manufacturing activity: a Petri net approach. 2008; 19(2): 274-288.

[4] Wang Q. Artificial neural networks as cost engineering methods in a collaborative manufacturing environment. International Journal of Production Economics. 2007; 109: 53-64.

[5] Perrin O, Wynen F, Bitcheva J, Godart C. A Model to Support Collaborative Work in Virtual Enterprises. in Proceedings of the International Conference of business Process management. Eindhoven. The Netherlands: Springer-Verlag. 2003.

[6] Chan HK, Chan FTS, Samaranyake P. Adaptive Make-to-Order Strategy in Distributed Manufacturing Supply Chains. in Proceedings of the 3rd IEEE International Conference on Industrial Informatics. (INDIN). 2005.

[7] Rudberg M, West BM. Global operations strategy: Coordinating manufacturing networks. The International Journal of Management Science. 2008; 36: 91-106.

[8] Clarke N. The relationships between network commitment, its antecedents and network performance. Management Decision. 2006; 44(9): 1183-1205.

[9] Danilovic M, Winroth M. A tentative framework for analysing integration in collaborative manufacturing network settings: a case study. Journal of Engineering and Technology Management. 2005; 22: 141-158.

[10] Noori H, Lee WB. Dispersed network manufacturing: adapting SMEs to compete on the global scale. Journal of Manufacturing Technology Management. 2006; 17(8): 1022-1041.

[11] Coughlan P, Coghlan D, Lombard F, Brennan L, McNichols T, Nolan R. Managing collaborative relationships in a period of discontinuity. International Journal of Operations & Production Management. 2003; 23(10): 1246-1259.

[12] Shi YJ, Gregory M. Winning a Faster Global Business Growth on a New Entrepreneurial Collaborative Network. IEEE. 2004.

[13] Ren Z, Hassan TM, Anumba CJ. The engineering services of a universal e-Engineering Hub: Application to the construction industry. Advances in Engineering Software. 2008; 39: 545-557.

[14] Bititci US, Martinez V, Albores P, Parung J. Creating and managing value in collaborative networks. International Journal of Physical Distribution & Logistics Management. 2004; 34(3/4): 251-268.

[15] Ito T. Whiteboard-based interface for collaboration in e-manufacturing environment. Journal of Manufacturing Technology Management. 2007; 18(1): 25-35.

[16] Australian Government, Department of Industry, Tourism and Resources. Making It Globally: Advanced Manufacturing Action Agenda. viewed 2 March 2009, <<http://www.industry.gov.au/amaa>>. 2006.

[17] Johansen K, Comstock M, Winroth M. Coordination in collaborative manufacturing mega-networks: A case study. 2005; 22: 226-244.

[18] Winroth M, Danilovic M. Linking Manufacturing Strategies to Design of Production Systems in Collaborative Manufacturing Networks. in Proceedings of the 14th Annual Conference of the Production and Operations Management Society. Savanna. Georgia. USA. 2003.

[19] Anumba CJ, Ugwu OO, Newnham L, Thorpe A. A multi-agent system, for distributed collaborative design. Logistics Information Management. 2001; 14(5/6): 355-366.

[20] Cil I, Alpturk O, Yazgan HR. A new collaborative system framework based on a multiple perspective approach: InteliTeam. Decision Support Systems. 2005; 39: 619- 641.

[21] Wang D, Nagalingam SV, Lin GCI. Development of an agent-based Virtual CIM architecture for small to medium manufacturers. Robotics and Computer-Integrated Manufacturing. 2007; 23: 1-16.

- [22] McClellan, M. Collaborative manufacturing: A strategy built on trust and cooperation. 2003; 12. Control Solutions International.
- [23] Nagalingam S. A Holistic Model for a Collaborative Manufacturing Network. Internal Document. University of South Australia. Australia. 2008.
- [24] Freeman S, Cray D, Sandwell M. Networks and Australian professional services in newly emerging markets of Asia. *International Journal of Service Industry Management*. 2007; 18(2): 152-166.
- [25] Jack S L. Approaches to studying networks: Implications and outcomes, *Journal of Business Venturing*. 2008.
- [26] Montreuil B, Frayret JM, D'Amours S. A strategic framework for networked manufacturing. *Computers in Industry*. 2000; 42: 299-317.
- [27] Mesa International. Collaborative Manufacturing Explained. www.mesa.org. 2004.
- [28] ARC Advisory Group. Collaborative Manufacturing Management Strategies. Thought Leaders for Manufacturing & Supply Chain. 2002.
- [29] Ramudhin A, Montreuil B, Lefrancois P. Scheduling project activities in a distributed environment. *European Journal of Operational Research*. 1994; 78: 242-251.
- [30] Frayret JM, D'Amours S, Montreuil B, Cloutier L. A network approach to operate agile manufacturing systems. *International Journal of Production Economics*. 2001; 74: 239-259.
- [31] Fujimoto H. Collaborative networking in a multi-stage industrial channel. *International Journal of Physical Distribution & Logistics Management*. 2003; 33(3): 229-235.
- [32] Bolduc MC, Renaud J, Montreuil B. Synchronized Routing of Seasonal Products through a Production/Distribution Network. *CEJOR*. 2006; 14: 209-228.
- [33] Cloutier L, Frayret JM, D'amours S, Espinasse B, Montreuil, BT. A commitment-oriented framework for networked manufacturing coordination. *International Journal of Computer Integrated Manufacturing*. 2001; 14(6): 522-534.
- [34] Sherer SA. Critical Success Factors for Manufacturing Networks as Perceived by Network Coordinators. *Journal of Small Business Management*. 2003; 41(4): 325-345.
- [35] Lin HW, Nagalingam SV, Chiu M, Lin GCI. Development of a Web-based Three-tier Decision Support System for Virtual Enterprises, Flexible Automation and Intelligent manufacturing. FAIM2004. Toronto, Canada. 2004.
- [36] Tomkins C. Interdependencies, trust and information in relationships, alliances and networks. *Accounting, Organizations and Society*. 2001; 26: 161-191.
- [37] Palakshappa N, Gordon ME. Collaborative business Relationships Helping firms to acquire skills and economies to prosper. *Journal of Small Business and Enterprise Development*. 2007; 14(2): 264-279.
- [38] Vallespir B, Kleinhans S. Positioning a company in enterprise collaborations: vertical integration and make-or-buy decisions. *Production Planning & Control*. 2001; 12(5): 478-487.
- [39] Danilovic M. Bring your suppliers into your projects—Managing the design of work packages in product development. *Journal of Purchasing & Supply Management*. 2006; 12: 246-257.
- [40] Yam AYK, Chan MFS, Chung WWC. Networked enterprise: a case study of implementing an information network system for global product development. *Benchmarking: An International Journal*. 2007; 14(3): 369-386.
- [41] Shi Y, Gregory M. International manufacturing networks-to develop global competitive capabilities. *Journal of Operations Management*. 1998; 16: 195-214.
- [42] Evan JR, Lindsay WM. *Managing for Quality and Performance Excellence*. 7th Ed. Thomson South-Western. USA. 2008.
- [43] Technology Partnerz. Enterprise Relationship Management Overview, viewed 1 June 2009, <<http://www.technologypartnerz.com/eng/erm.asp>>. (2008),
- [44] Timings R. *Basic Manufacturing*, 3rd edition. Newnes. An imprint of Elsevier. Burlington. MA. 2004.
- [45] Poler R, Hernandez JE, Mula J, Lario FC. Collaborative forecasting in networked manufacturing enterprises. *Journal of Manufacturing Technology Management*. 2008; 19(4): 514-528.
- [46] Courtney JF. Decision making and knowledge management in inquiring organizations: toward a new decision-making paradigm for DSS. *Decision Support Systems*. 2001; 31: 17-38.
- [47] Lee WB, Lau HCW. Multi-agent modelling of dispersed manufacturing networks, *Expert Systems with Applications*. 1999; 16: 297-306.
- [48] Lin HW. Development of a Global Decision Support System towards Collaborative Manufacturing and Virtual Manufacturing. PhD Thesis. University of South Australia. Australia. 2008.

Simulation of Partial Discharge Induced Electromagnetic Wave in Power Transformer

Nhet Ra,^a Tomohiro Kawashima,^{a*} Naohiro Hozumi,^a Yoshinobu Murakami,^a Umar Khayam,^b Suwarno,^b

^aDepartement of Electrical and Electronic Information Engineering, Toyohashi University of Technology, Email: n169202@edu.tut.ac.jp

^bSchool of Electrical Engineering and Information, Bandung Institute of Technology, Bandung. Email: suwarno@stei.itb.ac.id

Abstract

This paper describes the numerical simulation of partial discharge (PD) in oil-filled power transformer using FDTD method (Finite Difference Time Domain). We investigate the effects of oil insulation medium and internal structures on the propagation of electromagnetic signal emitted from the partial discharge source. In this study, partial discharge is modeled as the Gaussian Pulse (pulse's width 1 ns). To observe the electromagnetic intensity and also the voltage distribution, three sensors are employed. The magnitude, frequency, and attenuation of the EM wave without internal structures and with internal structures are compared. The Results show that the EM wave intensity is attenuated while propagating through the oil insulation, iron-core, and windings. And the time arrival of each signal is different due to its distance from the PD source. The simulation results in both cases show that the first dominance frequency occurs in 1 GHz of frequency. However, the frequency spectrum of simulation with internal structures has resonance frequencies in the low region from 80 MHz to 300 MHz of frequency. These resonance frequencies occur because the windings are considered to be a loop antenna.

Keywords: Electromagnetic wave (EMW); FDTD approach; Ultra High Frequency (UHF)

1. Introduction

Power transformer is one of the most important elements in power transmission and distribution systems. During the operation, the threat such as lightning strikes, switching transient, and short-circuit, can lead to the immediate failure, especially for the aged transformer. When the insulation is degraded, it cannot withstand such events. The insulation degradation of partial discharge is frequently linked to partial discharge [1, 2].

The occurrence of partial discharge is accompanied by some energy such as impulse current, heat light radiation, electromagnetic wave, and mechanical wave [3, 4]. Various methods have been proposed for detecting partial discharge by mean of the energy released from partial discharge. The convention method, specified in the IEC 60270 standard, is extensively used to detect the impulse current induced by partial discharge [5]. The integration of the discharge current over time through the detecting impedance is the apparent charge corresponding to the partial discharge. The

insulation assessment can also be done by chemical method. A chemical test such as High-Performance Liquid Chromatography (HPLC) and Dissolved Gas Analysis (DGA) are employed to detect the gasses and components produced due to the breakdown of voids. Since partial discharge accompanied by an acoustic wave and an electromagnetic wave, a newly developed sensor such as an acoustic sensor, and UHF sensor are usually been employed for PD detection and finding the location of the defects [6-12].

However, it is very difficult for UHF antenna to locate the defects when partial discharge occurs and propagates through complex structures and the insulation medium of the transformer [13-15]. Therefore, it is necessary to examine the effects of transformer components such as windings, pressboard and iron core on EM wave propagation. In addition, the reliability enhancement of the diagnosis, such as PD location identification and increase the detection sensitivity, it is strongly required to understand the propagation properties of the EM waves induced by PD occurring inside the transformer.

From this point of view, we proposed to investigate the insulation diagnostics technique for oil-filled transformer using the UHF methods through numerical simulation using finite difference time domain (FDTD) method.

*Corresponding author. Tel.: +81-903-425-481

Address: 1-1 Hibarigaoka, Tempaku
Toyohashi, Aichi, JAPAN 441-8580

2. Finite Difference Time Domain Method (FDTD)

2.1. FDTD Formula

The finite difference time domain method (FDTD) has been widely used for solving electromagnetic field problems [16]. This technique was proposed by Kane Yee in 1996, specifically for solving Maxwell's equation and curl equation.

The idea of solving the electromagnetic field using Finite Difference Time Domain (FDTD) is a leapfrog manner in which the electric field is computed for given instant time, then the magnetic field is obtained in the next instant time, and the process is repeated over and over again. The finite difference technique is based on approximations which permit replacing differential equations by finite difference equations. These finite difference approximations are algebraic in form and they relate the value of the dependent variable at a point in the solution region to the values at some neighboring points. The basic steps involved are:

- Dividing the solution region into a grid of nodes: The commonly used grid patterns are rectangular, skew, triangular and circular grid
- Approximating the given differential equation by its finite difference equivalent that relates the dependent variable at a point in the solution region to its values at the neighboring points
- Solving the difference equations subject to the prescribed boundary and initial conditions.

2.2. Yee's FDTD algorithm

Maxwell's equations in an isotropic medium [16] are:

$$\nabla \times \vec{E} = -\mu \frac{\partial \vec{H}}{\partial t} \tag{1}$$

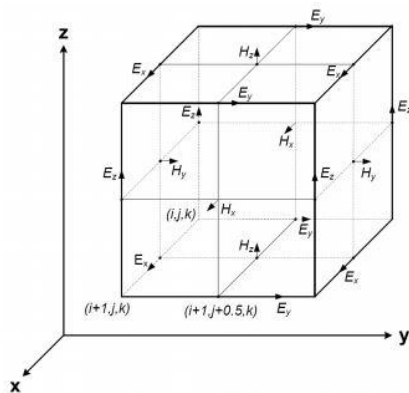


Figure 1. Yee's grids for finite difference time domain. The electric 'E' and magnetic field 'H' [16].

$$\nabla \times \vec{H} = \sigma \vec{E} + \epsilon \frac{\partial \vec{E}}{\partial t} \tag{2}$$

where 'E' is the electric field (v/m), 'H' is the magnetic field (A/m), 'ε' is dielectric constant (F/m), 'μ' is the permeability (H/m) and 'σ' is the conductivity (S/m) of the medium. Yee's defined the object into small grids and the grid points in the solution region needed to be defined as a function of space and time. The electric 'E' and magnetic field 'H' of a unit cell is shown in Fig. 1.

2.3. Absorbing Boundary condition

Absorbing boundary conditions known as ABCs method has been widely used for the boundary condition. Absorbing boundary condition allows an ongoing electric field 'E' and magnetic field 'H' without reflected back to the problem space. The most efficient of ABCs circuit is a perfect matched layer (PML) [17]. If a wave is propagating in medium A and it strikes upon medium B, the amount of reflection is dictated by the intrinsic impedances of the two media, which is given by:

$$\Gamma = \frac{\eta_A - \eta_B}{\eta_A + \eta_B} \tag{3}$$

The impedances are determined by "ε" and "μ" of the two media:

$$\eta = \sqrt{\frac{\mu}{\epsilon}} \tag{4}$$

2.4. PD Pulse Modeling

A typical pulse can be numerically simulated by a Gaussian function as [18]:

$$i(t) = I_0 \exp \left[\frac{-(t-t_0)^2}{2\sigma^2} \right] \tag{5}$$

where I_0 is the amplitude to the time instant measured at the center of the pulse, σ is the characteristic waveform parameter which describes the current pulse width at half the maximum value, which for a PD pulse is equal to 2.36σ .

Table 1 shows the impulse current's properties of the PD pulse model. Fig. 3 shows the model of impulse current corresponded to the partial discharge. Fig. 4 shows the model of inverse fast furrier transforms (IFFT) of impulse current.

Table 1. Impulse current's propagation

Parameters	Formula	Value
Sigma	$= (4 \times f_{max})^2$	1.6×10^{19}
Time	$T_0(s)$	0 (s)
	$T_a(s)$	20×10^{-9} (s)

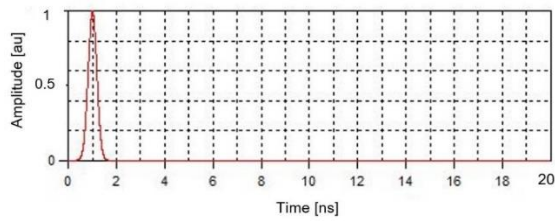


Figure 2. Model of impulse current corresponded to the partial discharge.

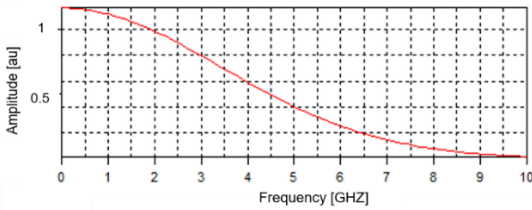


Figure 3. Model of inverse fast Fourier transform IFFT of impulse current

3. Simulation Model

Figure 4 shows the cut-view of the simplified three-phase transformer using Magna TDM (CTC: Magna version 8.0). The model consists of transformer tank, iron core, windings, and oil insulation medium. The dimension of the transformer tank is 2000 mm × 4000 mm × 2400 mm. The model has 3 windings with the 400 mm outer radius and 200mm inner radius each. These windings were wrapped around the iron.

In this study, we placed a partial discharge source (PD) on the surface of the transformer windings. The electromagnetic wave induced from the discharge point is propagated past through the oil insulation and internal structures of the power transformer. Finally, the electric field due to the partial discharge is observed at three different points.

The finite difference time domain (FDTD) is used to compute the electric field and voltage distribution due to the partial discharge. The mesh x, y, z sized was selected as 2 mm, 2 mm, 2 mm, respective. The simulation was performed without internal structures and with internal structures filled with oil insulation medium (the oil relativity permittivity $\epsilon_r=2.2$).

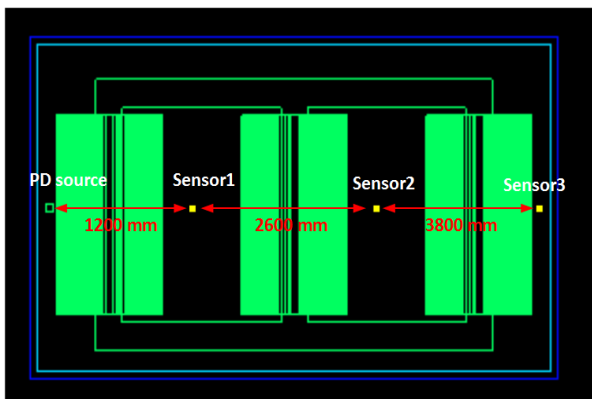


Figure 4. The model of a transformer with internal structures (oil insulation, core, and windings) for FDTD simulation

4. Simulation Results

The electric field intensity and voltage distribution in the x, y, z directions due to the partial discharge were detected. The results from this study is separated into two sections, simulation without internal structures and with internal structures as follow:

4.1. Electric Field intensity

- Simulation results without internal structures

Figures 5, 6 and 7 show the x, y, z component of the electric field intensity of the electric field of sensor 1, sensor 2, and sensor 3 without internal structures. The electric field intensity in the x-direction and z-direction are slightly different in magnitude. However, in the y-direction the magnitude is high due the y direction is used as the propagation of EMW. The electric field intensity detected by sensor 1 is higher compared to sensor 2 and 3.

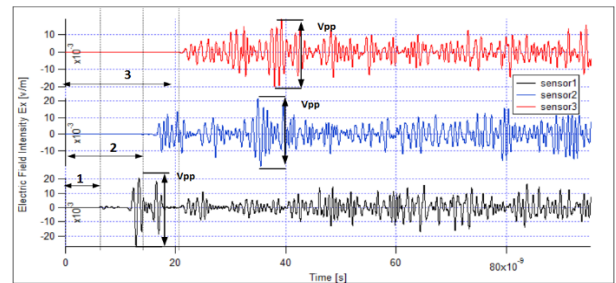


Figure 5. Simulation result of EMW in x-direction of power transformer without internal structure

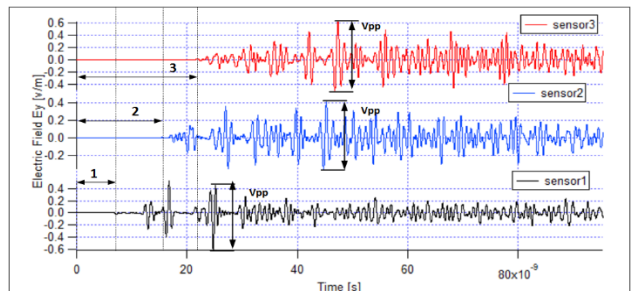


Figure 6. Simulation result of EMW in y-direction of power transformer without internal structure

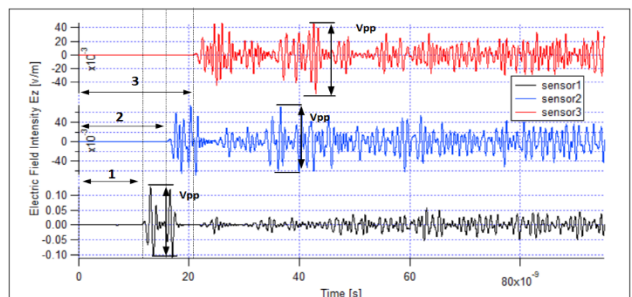


Figure 7. Simulation result of EMW in z-direction of power transformer without internal structure

In addition, the signal obtained from sensor 1 is shorter than sensor 2 and sensor 2 is shorter sensor 3 respectively.

• Simulation Results With internal structures

Figures 8, 9 and 10 show the x, y, z component of the electric field intensity of the electric field of sensor 1, sensor 2, and sensor 3 with internal structures. The peak to peak point is delayed due to the internal structures of the transformer. The electric field intensity in the x-direction and z-direction are slightly different in magnitude. However, on the y-direction the magnitude is high due the y direction is used as the propagation of EMW. The electric filed intensity detected by sensor 1 is higher compared to sensor 2, and 3. In addition, the signal derived from sensor 1 is shorter than sensor 2 and sensor 2 is shorter sensor 3 respectively.

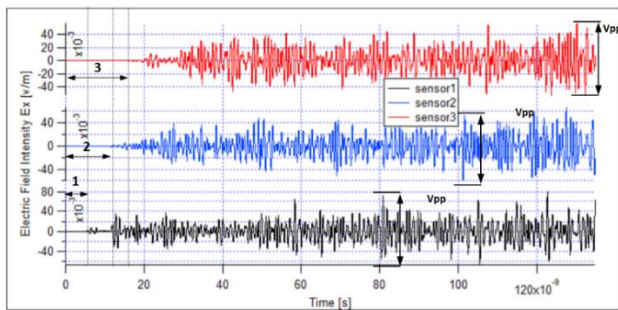


Figure 8. Simulation results of EMW in x-direction of power transformer with internal structure

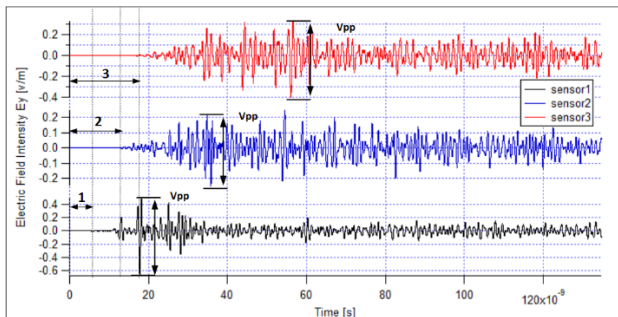


Figure 9. Simulation result of EMW in y-direction of power transformer with windings and core

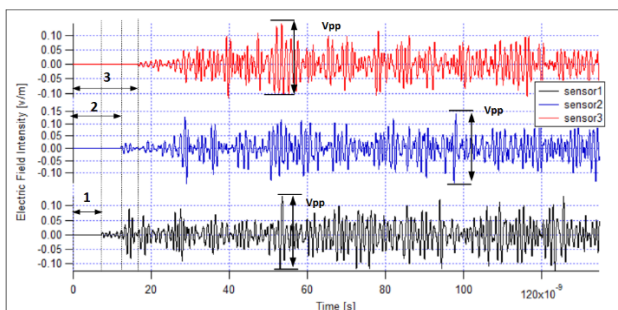


Figure 10. Simulation result of EMW in z-direction of power transformer with internal structure

4.2. Voltage Distribution

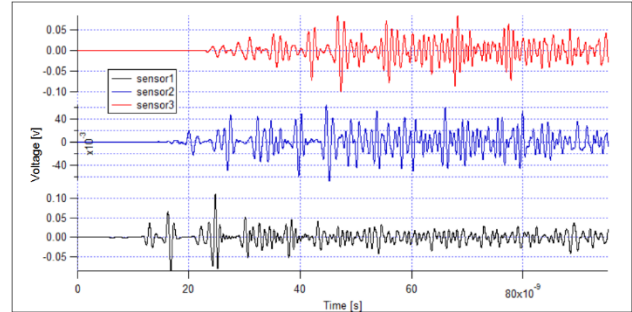


Figure 11. Simulation result of voltage distribution of power transformer without internal structures

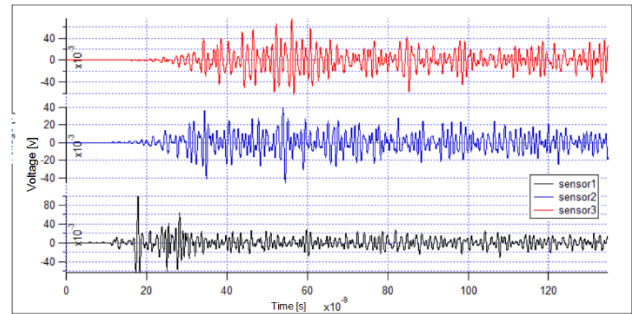


Figure 12. Simulation result of voltage distribution of power transformer with internal structures

Figures 11 and 12 shows the voltage distribution obtained from PD source, sensor 1, 2, and 3 with the peak amplitude -1, 0.09, -0.05, 0.07 V respectively. The voltages derived from each sensor are slightly different in magnitude. However, the time difference to detect the PD signal is different.

5. Analysis and Discussion

It is evident from Figs. 13, 14 and 15 that frequency components around 1 GHz have maximal and the resonance distinctly occurs in the low-frequency region at 80, 160 and 240 MHz. The resonance frequencies can be explained as follows.

The resonance is calculated by the existence of the windings. Namely, the windings work as a loop antenna. In the simulation model, the windings radius is = 0.4 m. When the windings are considered to be a loop-antenna, the resonance frequency f_r , is calculated using Eq. 6, respectively.

$$f_r = \frac{3.0 \times 10^8}{2\pi r \sqrt{\epsilon_r}} \quad (6)$$

The resonance frequency of 80.47 MHz derived from equation agrees well with that of 80 MHz obtained from the FDTD simulation. Accordingly, it is indicated that the frequencies 160, 240 MHz and so on are attributed to the

secondary and ternary resonance frequency of the windings looked like a loop antenna.

Moreover, the FFT spectrum without the windings exhibits no such resonance peaks in the low-frequency region, while it has a similar spectrum intensity around 1 GHz of the high-frequency region compared with the result without the windings.

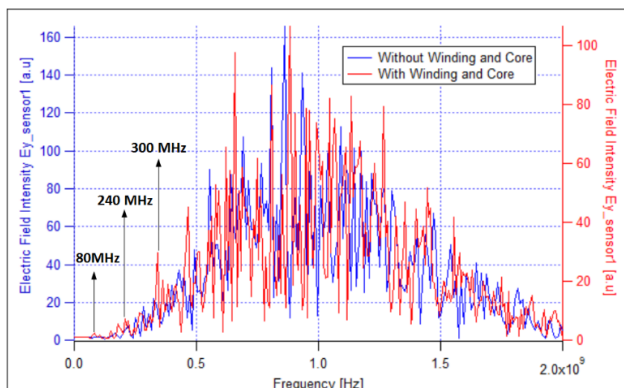


Figure 13. Simulation result of EMW frequency spectrum of power transformer detected by sensor 1

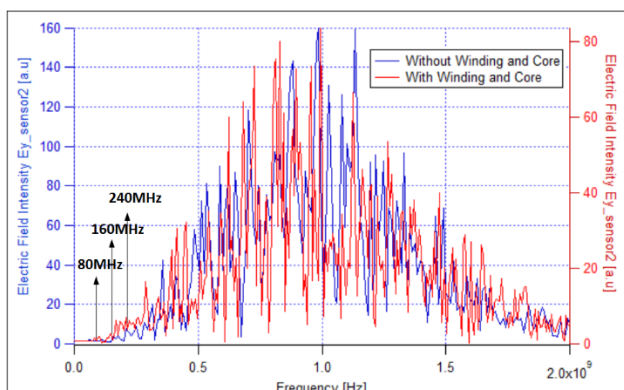


Figure 14. Simulation result of EMW frequency spectrum of power transformer by sensor 2

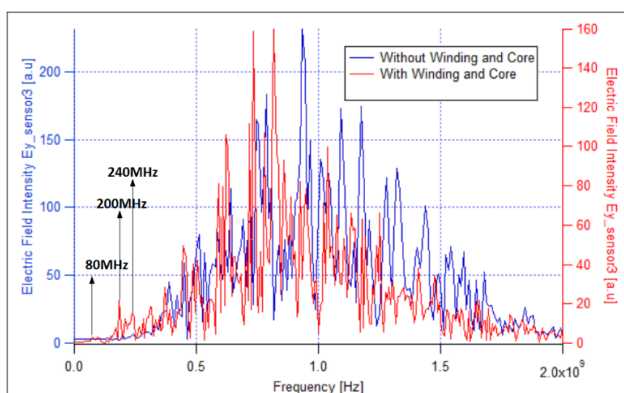


Figure 15. Simulation result of EMW frequency spectrum of power transformer detected by sensor 3

6. Conclusion

We investigated the effects of oil insulation medium and internal structures on the propagation of electromagnetic signal emitted from the partial discharge source. The Result showed that the EM wave intensity attenuated while propagating through the oil insulation, iron-core, and windings. And the time arrival of each signal was different due to its distances from the PD source. The first dominance frequency of the simulation without internal structures and with internal structures (oil insulation, windings, and core) occurred in 1 GHz of frequency. However, frequency spectrum of simulation with internal structures (oil insulation, windings, and core) had a resonance frequency in the low region from 80 MHz to 300 MHz of frequency. This resonance frequencies occurred because the windings of the transformer acted as a loop antenna.

Acknowledgements

The authors would like to acknowledge to AUN-SEED/Net Program for their funding support to make this research done.

References

- [1] S. V. Kulkarni, S.A. Khapade, "Transformer Engineering Design and practice". Indian Institute of Technology, Bombay Mumbai, India, 2004, pp. 389-409.
- [2] Suwarno, "Partial Discharge in high voltage insulations" in High Voltage diagnosis, Bandung, penerbit, 2010, pp.4-39.
- [3] H. Masayuki, K. Masahiro, "Recent Progress in Diagnosis of Transformers using Non-Conventional Partial Discharge Measurements," IEEE International Conference on Condition Monitoring and Diagnosis 23-27 September 2012, Bali, Indonesia.
- [4] IEC 61000-4-20 Electromagnetic Compatibility (EMC)- Part 4: Testing and Measurement techniques. Section 20: Emission and Immunity Testing in Transverse Electromagnetic (TEM) Waveguides. International Electrotechnical Commission Geneva, Switzerland, Draft 2 CD 61000-4-20, 2001.
- [5] IEC 60270, "High Voltage Test Techniques-Partial Discharge measurement," IEC, 2000-2012.
- [6] P. G. Reddy, K. Prasanta, "Detection and Analysis of Partial Discharge using Ultra High Frequency Sensor" International Conference on Magnetics, Machines & Drives, 24-26 July 2014, Kottayam, India.
- [7] M. Zanjani, A. Akabari, H.R. N. Shirdel, "Investigating Partial Discharge UHF Electromagnetic Waves Propagation in Transformers Using FDTD Technique and 3D Simulation," IEEE International Conference on Condition Monitoring and Diagnosis 23-27 September 2012, Bali, Indonesia
- [8] C. Sebastian, T. Stefan, "Location of PD Sources in Power Transformers by UHF and Acoustic Measurements," IEEE International Conference on Dielectric and Electrical Insulation, December 2012— Vol. 19, Issue. 6, pp.1934-1940
- [9] M. D. Judd, L. Yang, I.B.B. Hunter, "Partial Discharge Monitoring for Power Transformers Using UHF Sensors Part 2: Field Experience," IEEE Electrical Insulation Magazine, IEEE, June 2005— Vol. 3, Issue. 3, pp.5-13.
- [10] D. H. Froula, S. H. Glenzer, N. C. Luhmann, Jr., and J. Sheffield, *Plasma Scattering of Electromagnetic Radiation*, 2nd ed., Elsevier, 2001.

- [11] Martin D. Judd, Li Yang, Ian B. B. Hunter, "Partial Discharge Monitoring for Power Transformers Using UHF Sensors Part 2: Field Experience", IEEE Electrical Insulation Magazine, May/June 2005 — Vol. 21, No. 3
- [12] M. D. Judd, G. P. Cleary, C. J. Bennoch, Pearson, and J.S Pearson, and T. Breckenridge, "Power transformer monitoring using UHF sensors: site trials; Electrical Insulation", Conference Record of the IEEE International Symposium on Electrical Insulation, Boston, USA, pp, 145 – 149, 2002.
- [13] Z. Xu, C. Yonghong, M. Yongpeng, W. Kai, N. Yuhan, "The propagation characteristics of UHF partial discharge in power transformers with complex windings structure," 2012 Annual Report Conference on Electrical Insulation and Dielectric Phenomena (CEIDP). Montreal, QC, Canada, Tech. Report. 13174840, 14-17 Oct. 2012.
- [14] M. Joko., UHF Bowtie Antenna Modeling and Enhancement as GAS Insulated Substation (GIS) Partial Discharge (PD) Sensor, M. S. thesis, Bandung Institute of Technology, 2013.
- [15] A. TAFLOVE. "*Computational Electrodynamics: The Finite-Difference Time-Domain Method*" 3rd ed., Boston, London, 2005, pp. 229-267.
- [16] K. S. Yee., Numerical solution of Initial Boundary Value Problems Involving Maxell's Equations in Isotropic Media, In IEEE Transaction on Antenna and Propagation, vol. 14.No.3, May 1996,pp.302-307.
- [17] J. P. Berenger, "Three-Dimensional Perfectly Matched Layer for the Absorption of Electromagnetic Waves", Journal of Computational Physics, September 1996— Vol. 127, Issue. 2, pp.363-379.
- [18] W. Li, S. Su and L. Zhou, "The Deduction of Partial Discharge Pulse Current from Its Radiating UHF Signal," IEEE Power Engineering Conference, IPEC, pp. 193-198, Jan. 2005.

Transmission Scheduling Method for Delivery of Large-Sized Data Object based on Delay Constrained Request over Scheduled Transportation Vehicles

Shigeru Kashihara*

Graduate School of Information Science, Nara Institute of Science and Technology. Email:shigeru@is.naist.jp

Abstract

The paper proposes two transmission scheduling methods to deliver large-sized data object based on delay constrained request over scheduled transportation vehicles. Scheduled transportation vehicles like buses and rails have the potential to provide data communication for delay-tolerant large data object based on delay-/disruption-tolerant network (DTN) concept as a part of the Internet. However, since the operation of vehicles follows the timetable, even if the vehicles carry users' data objects, they may not always deliver the objects to their destination within their requested delay. As one of the approaches, to satisfy the delivery with delay requests, our previous paper presented the design of data offloading to public transportation vehicles. In the model, if a data port accepts data objects from users in a first-come, first-served (FCFS) schedule, the system cannot guarantee to deliver data objects within requested delay. In this paper, as the first step under the design, we propose two transmission scheduling methods for uploading data at a data port. Simulation evaluations demonstrate that the proposed methods significantly improve the successful data delivery compared with FCFS.

Keywords: Data delivery; delay-tolerant data objects; DTN; large-sized data objects; scheduled transportation vehicles; transmission scheduling method

1. Introduction

With the widespread use of advanced functionality and high-performance smartphones, a smartphone has become the primary communication device for an end user. The user deploys diverse applications on the smartphone, producing and storing text, photos, and videos. In particular, the multimedia file size is sharply increasing as users demand higher resolution photos and videos ever. For instance, a photo of more than 5 MB is not uncommon, while a 10-minute video clip requires about 2 GB. Also, other applications for backup, business use, and so on, will create more large data. Current smartphones have relatively large storage, inviting users to create a more significant amount of data objects. At the same time, personal, business, and backup applications require that the delivery of these data objects be completed within defined time constraints to share, upload, and download these data objects in accordance to the circumstance.

Presently, a smartphone can send and receive relatively large data objects of a few photos through public Wi-Fi and

4G networks. However, high transmission of data files like many high-resolution photos, videos, and backup data is not feasible on public Wi-Fi or LTE, because of communication quality changes due to a density of users or the signal environment. Also, as the amount of data per month depends on the data plan, a user like a tourist wants to save money as much as possible by reducing the data communication. On the other, public Wi-Fi (e.g., coffee shops, malls, airports) have limited coverage and cannot support ubiquitous user mobility. Compared with Wi-Fi, 4G provides broader area access and may be the best technology to support extended user mobility. However, the communication speed of a 4G is still slow and is prone to congestion. For instance, Cisco reports that the average global mobile connection speed in 2016 was 6.8 Mbps [1]. That means that it would take about 39 minutes to complete the transmission of a 2 GB file in an ideal environment where communication quality does not change. Furthermore, a user who relies on a smartphone as a primary communication device may want to conserve its battery power for future use. A long session would also severely degrade the other cell users' throughput. As a result, the smartphones will consume more battery for the long communication. These limitations of the current (and future) wireless infrastructure motivate our research to find

*Corresponding author. Tel.: +81-743072-5213
8916-5 Takayama, Ikoma, Nara, Japan, 630-0192

effective alternatives for the delivery of large-sized data objects within a user's desired delay.

As illustrated in Fig. 1, to deliver a large data object within a user's desired delay, our previous paper considered a data delivery approach over a regularly scheduled vehicle [2]. Examples include buses and rails, among others. References [3, 4] reported that a similar approach that relies on the use of "data mule" carriers to extend the Internet connectivity in a rural area. We believe that the "data mule" concept can be leveraged to support delay-constrained transport of large-sized data objects via public transportation facilities.

To deliver large data objects, we envisage the system, depicted in Fig. 1, where a user drops a large data object off into a data port at a bus stop. Current trends indicate that smartphones will eventually equip with a proximity wireless transfer technology such as Transfer Jet [5] and WiGig [6]. It is capable of forwarding large data objects in a shorter time. We assume that a user would transfer their large object to the data port via one of the above technologies. Then, a bus picks the data up from the data port and carries the forwarded data to a bus terminal. At the bus terminal, the vehicle offloads the data to the Internet through a high-speed connection like an optical fiber cable.

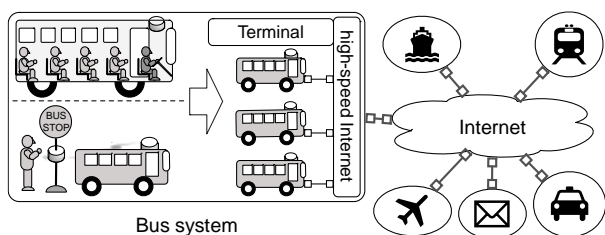


Figure 1. Data delivery over public transportation systems

To meet the user's specified deadline, we can estimate the time to deliver a large data object to its destination by utilizing the transportation service's timetable. However, since a vehicle's pick-up time follows the transportation system schedule, all data in the data port may not always be possible to be picked up within the stoppage time at a station. In this paper, we propose delay constrained large data object delivery using a scheduled public transportation system and introduce transmission scheduling algorithms for the data port. Note that as the first step for the study, this paper here focuses on uploading data flow because downloading flow requires a more complicated approach based on user's location information after solving the problems for uploading data. We first describe a communication approach for a bus system as an instance of the scheduled transportation system. We then show that the transportation system cannot deliver the required performance if the data port has no appropriate transmission-scheduling algorithm; that is if it operates in a first-come, first-served (FCFS) schedule. We propose two effective transmission scheduling methods and demonstrate through simulation experiments that the methods meet the desired constraints.

2. Communication approach with scheduled transportation vehicles

The section starts by describing how a scheduled transportation system can be exploited for delay constrained large data object delivery. Section 2.1 first describes the communication approach in the system, and Section 2.2 then analyzes the system performance considering data object size and user delay constraints as system parameters.

2.1. Communication approach and ideal transmission performance

Throughout this paper, we use a bus system as an example, but this concept is readily applicable to other transportation systems. Fig. 2 shows the communication flow in the system. We assume that a smartphone has an interface for proximity wireless transfer technology such as Transfer Jet. Likewise, a data port and bus employ Wi-Fi (802.11n) and Transfer Jet interfaces. Transfer Jet is used for communication between a smartphone and facilities (a data port or a bus), while communication between a data port and a bus employs 802.11n. We assume further that both the bus and the data port have huge but finite data storage capacity.

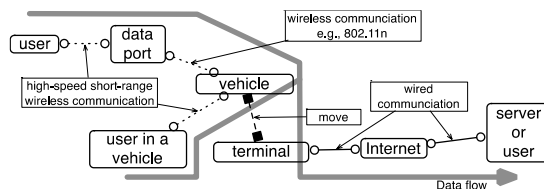


Figure 2. Communication flows over scheduled transportation vehicles

In our assumption, if an object size is relatively small or if the sending time via the current wireless network is tolerable for a user, a user may opt to send the data object through public Wi-Fi or 4G networks. Otherwise, a user tries to send the data object via the bus system. Besides, a user that boards a bus may upload the data object via Transfer Jet from his or her seat. As shown in Fig. 3, with the Transfer Jet's effective maximum throughput of 375 Mb/s [5], a user can send a large data object in a relatively short time. Also, since the connection distance of Transfer Jet is a few centimeters, the communication quality is expected to be very reliable against any multi-path fading and shadowing. On the other hand, if a user does not board a bus, a user drops a data object off at a nearby bus stop into a data port by using Transfer Jet. A bus picks up data from the data port via 802.11n. Once the data object is in the bus storage system, the bus carries the data to the bus terminal. After reaching the bus terminal, the bus then offloads all data objects to the Internet through a high-speed connection such as an optical fiber cable.

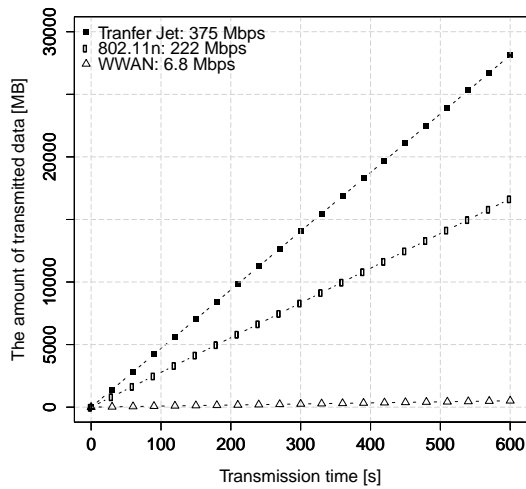


Figure 3. The amount of transmitted data over transmission time

Our primary emphasis is measuring the transmission performance for data objects in a data port at one bus stop since the overall transmission performance practically depends on data transfers from a data port to the bus. Although data objects uploaded by passengers from within the bus will eventually be delivered to a bus terminal, data objects that are picked up from the data port are restricted by the bus stoppage time at a bus station, according to a transit timetable. In other words, the transmission between a data port and a bus is the bottleneck in this system.

We first consider the ideal transmission performance. The effective transmission speed of Transfer Jet and 802.11n are here assumed to be 375 Mb/s [5] and 222 Mb/s [7], respectively. The amount of data from passengers per day is defined as alpha MB, while the amount of data from a data port per day is calculated as follows:

$$\text{The amount of data from a data port at one bus stop in a day (MB)} = (\text{Effective transmission throughput from a data port to a bus (Mb/s)} * \text{Stoppage time at a bus stop (s)} * \text{the number of buses in a day}) / 8.$$

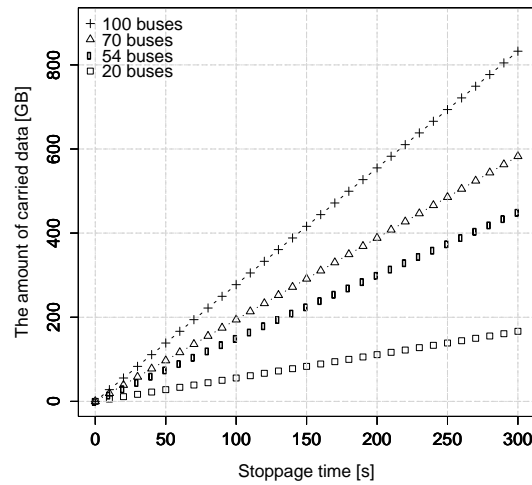
The throughput during service operation is calculated as follows:

$$\text{Throughput during service operation (Mb/s)} = ((\text{The amount of data from a data port in a day (MB)} + \alpha \text{ (MB)}) * 8 / \text{Operation time (s)}).$$

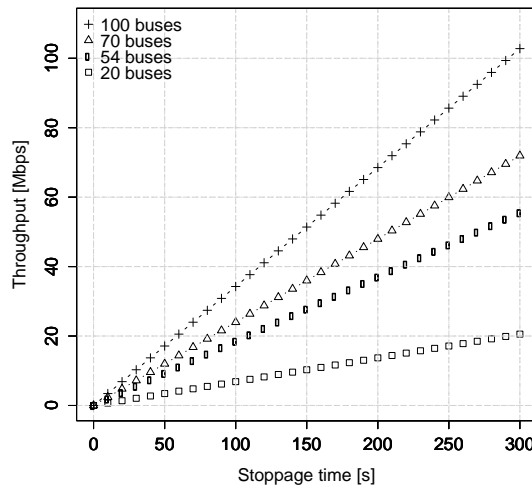
Thus, the transmission performance highly depends on stoppage time at a bus stop and the number of buses in a day.

Fig. 4 shows the ideal transmission performance for data objects in a data port. Fig. 4(a) shows the amount of carried data in a data port in a day, while Fig. 4(b) shows the throughput during service operation from 6:00 to 0:00. Each bus arrives at every 20 minutes, i.e., 54 buses per day and the stoppage time is 120 seconds. Thus, the ideal amount of carried data from the data port per day is approximately

179,820 MB/day with an effective throughput of 22.2 Mb/s. Since the results depend only on data objects in a data port at one bus stop, the system has higher performance if the data objects from passengers are included. Moreover, if a bus system has ten bus stops, the effective total throughput of the whole bus system is more than 222 Mb/s. Therefore, a scheduled transportation system has the potential for transporting large data objects.



(a) The amount of carried data



(b) Throughput

Figure 4. Ideal data transmission performance at one bus stop

2.2. Transmission performance under constraints of user's desired delay

This section provides simulation results for the above system under the user's delay constraint. Note that we here focus only on the transmission performance for data objects placed at a data port.

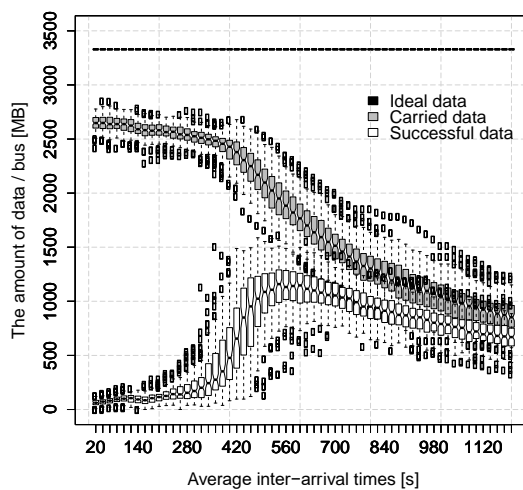
Table 1 shows the simulation parameters under an assumption. We assume that user arrival at a bus stop follow a Poisson distribution, while data size and user desired delay

for each data object are uniformly distributed. If a data object size is small, a user may choose to send the data via Wi-Fi or 4G. Otherwise, a user would be better off sending the large data object via the bus system. When a user arrives at a data port, a user is assumed to leave without sending the data object if another user is forwarding data at the data port. Otherwise, the user tries to forward the data object to the data port via Transfer Jet.

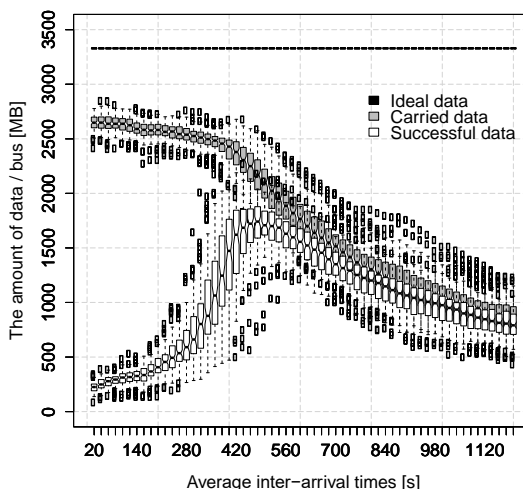
Table 1. Simulation Parameters

Parameters	Values
Average inter-arrival time (Poisson distribution)	From 20 to 1,200 sec
Data size (Uniform distribution)	Min: 1 MB, Max: 2,000 MB
User's requested delay (Uniform distribution)	Min: 3,600 sec Max: 7,200 sec, 14,400 sec
Throughput of Transfer Jet (From user to data port)	375 Mbps
Throughput of 802.11n (From data port to bus)	222 Mbps
Operation time	18 hours
Bus arrival interval	1,200 sec
Number of buses per day	54 buses
Stoppage time	120 sec

In our simulation experiments, the average inter-arrival time, the data size, and the user's desired delay are variable parameters. The average inter-arrival time varies between 20 and 1,200 seconds. The data size, uniformly distributed from 1 to 2,000 MB, represents the different sized data created by each user. The user's desired delay is assumed to be uniformly distributed between a minimum value (3,600 seconds) and a maximum value (7,200 or 14,400 seconds). The operation time for the bus system is from 6:00 a.m. to 12:00 a.m. with buses arriving every 20 minutes, for a total of 54 buses per day. The simulation analyzes only one bus stop since our focus is on the transmission performance of data objects uploaded from a data port. At a bus stop, the bus picks up data from the data port via 802.11n during stoppage time of two minutes. Without accounting for desired delays, the data port forwards data objects to the bus on the FCFS basis. Besides, data objects are not segmented. After leaving the bus stop, the bus transits to the bus terminal in about 50 minutes. Upon reaching the bus terminal, the bus assumes to offload all carried data objects to the Internet within 10 minutes.



(a) Max. of user desired delay: 7,200 sec



(b) Max of user desired delay: 14,400 sec

Figure 5. The amount of ideal data, carried data, and successful data per bus over average inter-arrival times under consideration of user's desired delay

Figure 5 shows the amounts of ideal data, carried data, and successful data per bus under consideration of a user's desired delay. The ideal data object volume is defined as follows. The amounts of data objects picked-up within a bus stoppage time is its maximum allowance, and all the picked-up data objects are entirely delivered within the user's desired delays. Then, the amount of carried data and successful data are defined as the amount of data carried by bus and the amount of data delivered within user's desired delay for the carried data, respectively.

Figure 5(a) displays transmission performance with a maximum value of 7,200 sec for a user's desired delay, while Fig. 5(b) displays results for 14,400 sec. Under the above assumptions, the amount of ideal data per bus is 3,330 MB. Since a data object is kept intact and not divided, if forwarding the head-of-line object in the data port does not complete within the stoppage time, another attempt will be required with the next bus. In other words, even if the bus has a small data file, which can be picked up within the

stoppage time, behind the head data in a data port, the bus cannot pick up other objects because of the inherent head-of-line blocking in FCFS. Furthermore, an object that is carried by bus under the FCFS discipline above is not guaranteed to be delivered within its desired delay. The rate of successful data per carried data may increase under a lower average inter-arrival time, yet, there are no assurances that all the data objects will be delivered within a user's desired delay. This is because a bus may carry data objects, which is going to be expired or is already expired, by FCFS under no consideration of a user's desired delay. From the graphs in Fig. 5, we also observe that the smaller maximum user's desired delay degrades the amount of successful data. Therefore, a data transmission scheduling algorithm in a data port is necessary to improve the transmission performance of a public transportation system.

3. Transmission scheduling method for data port

This section proposes two scheduling methods for the transmission from a data port to a bus. The objective is to improve the amount of data delivered within the user desired delay. We first discuss the design of a data port and then elaborate on each transmission scheduling method.

3.1. Design of data port

A data port estimates delivery time to show a user whether an object will be delivered within the user's desired delay. As illustrated in Fig. 6, a data port displays the estimated delivery time of the data object based on the object size from the smartphone and the current storage contents of the data port. As described in Section 2.1, the transmission between a data port and a bus is the bottleneck in this system. So, to improve the transmission performance, the data port should accept only data objects that will be delivered within the user delay threshold. Also, the user decides whether or not to send the data object from the estimated delivery time displayed. When a data-port cannot accept a data object, it suggests the current shortest delivery time for a user and the user decides whether or not send the data object.

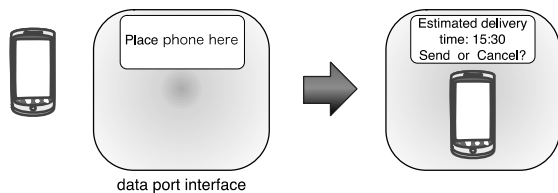
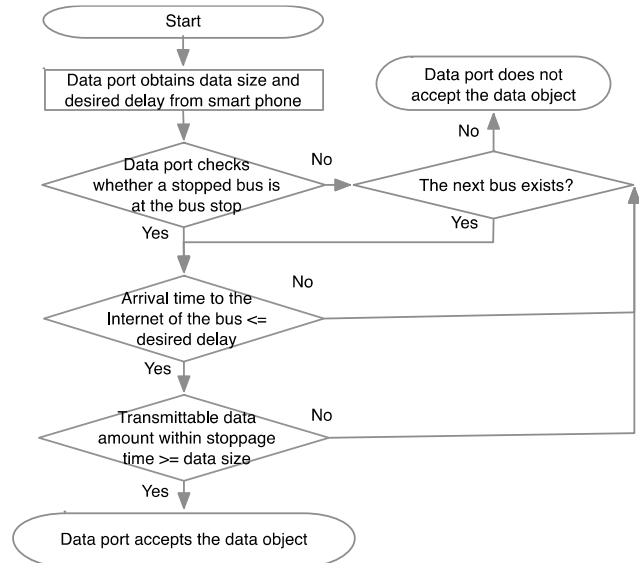


Figure 6. Example of interactive data port interface

To improve the transmission performance, a data port needs to schedule the transfer of data objects to buses according to the objects data sizes and users desired delay. So, the following sections introduce two scheduling methods.

3.2. Forward-packing transmission scheduling method (FPTS)

We first introduce a forward-packing transmission scheduling method (FPTS). Fig. 7 shows the flowchart of FPTS. When a smartphone is placed on the data port interface, the data port obtains the data size and the user's desired delay of the data object from the smartphone.



Bus #	transmittable data amount within stoppage time	arrival time to the Internet
1		
2		
3		
:		
the last bus		

Figure 7. Forward-packing transmission scheduling method (FPTS)

The data port then examines a bus that can deliver the data object within the delay. First, it checks the status of buses. If a bus is currently at the bus stop, the data port estimates the possibility of delivery within the delay and the transmission time to transfer the data object to a bus. If both are acceptable, the data port receives the data object from the smartphone.

If no bus is present or the data object cannot be delivered within the delay, the data port checks the scheduled time for the following buses in turn. In the process, the data port compares the delivery time to the Internet for the bus with the user's desired delay. If the delivery time to the Internet is larger than the user's desired delay, the data port checks the following buses iteratively, provided that the scheduled time does not exceed the user's desired delay. On the other hand, if the delivery time to the Internet is smaller than the user desired delay, the data port then checks whether the bus can pick up the data object within the stoppage time, i.e., transmittable data amount within stoppage time. If the bus has enough time, the data object is scheduled for that bus.

Otherwise, the data port checks iteratively whether the following buses will have enough time to deliver the data object within the user’s desired delay. Therefore, FPTS packs the data object with a bus that can deliver it within the user’s delay constraint, according to the bus arrival order.

3.3. Backward-packing transmission scheduling method (BPTS)

Similar to FPTS, the backward-packing transmission scheduling method (BPTS) also works according to data size and desired delay, but schedules data objects for a bus towards the upper bound of the user's desired delay. That is, BPTS examines a bus in turn from the last bus that can deliver the data object within the delay.

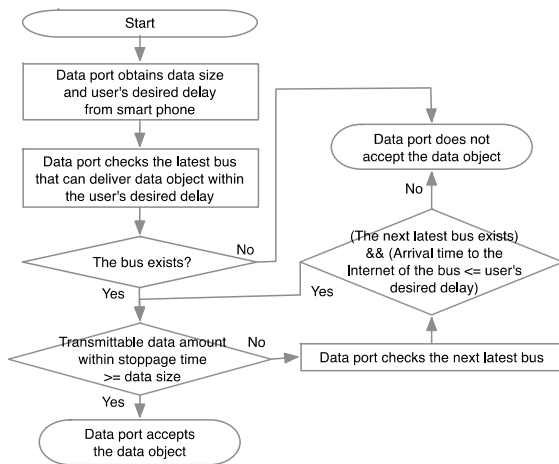


Figure 8. Backward-packing transmission scheduling method (BPTS)

BPTS works as depicted in Fig. 8. After obtaining the data size and desired delay from a smartphone, a data port checks the last bus that can deliver the data object within the desired delay. If a bus does not exist, the data port does not accept the data object. If a bus exists, the data port then checks whether the bus has enough time to pick up the data object (i.e., the transmittable data amount within stoppage time). If the bus has enough time, the data port accepts the data object. Otherwise, the data port considers the previous bus iteratively and compares the delivery time to the Internet for the bus with the user’s desired delay. If conditions are satisfied, the data port checks if there is enough time to pick up on the bus again. Otherwise, the data port does not accept the data object.

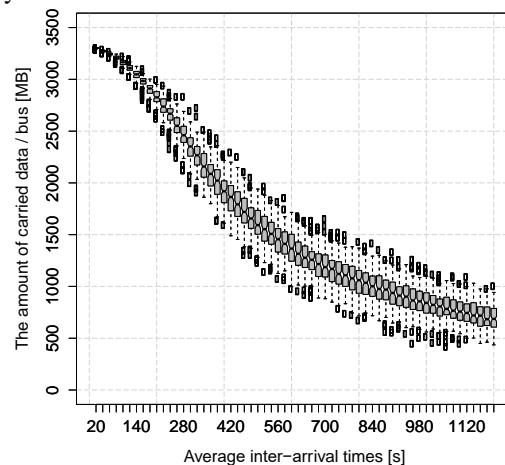
4. Performance evaluation

This section describes the performance evaluation and the discussion of the proposed method. Section 4.1 shows the transmission performance of the two scheduling methods compared with that of FCFS presented in Section 2. Section 4.2 then discusses remaining issues toward applying our methods to a real environment.

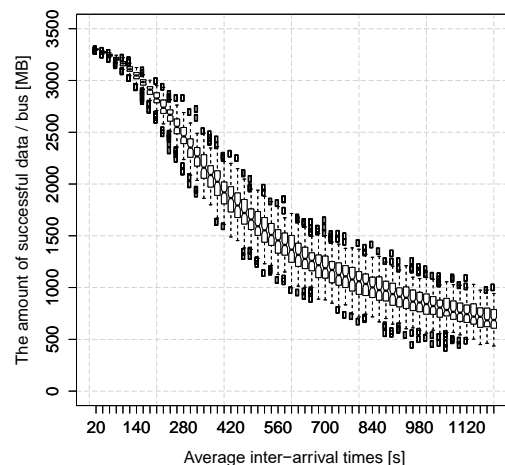
4.1. Simulation results

The section evaluates the transmission performance of FCFS, FPTS, and BPTS via simulation experiments. As previously mentioned in Section 2.2, our emphasis is on the performance of single data port, using the assumptions and parameters listed in Section 2.2. Note that the maximum user’s desired delay is set to 7,200 sec.

Figures 9 and 10 plot the amount of carried and successful data per bus for FPTS and BPTS, respectively. Figs. 9(a) and 10(a) show the amount of carried data by a bus, while Figs. 9 (b) and 10 (b) show the amount of successful data in the carried data. From the graphs, we observe that a bus completely delivers data objects within the user’s desired delay in both FPTS and BPTS. However, in comparison with FCFS (see Fig. 5 (b)), the amount of carried data for FPTS and BPTS decreases because FPTS and BPTS selectively accept data objects according to data size and user's desired delay.

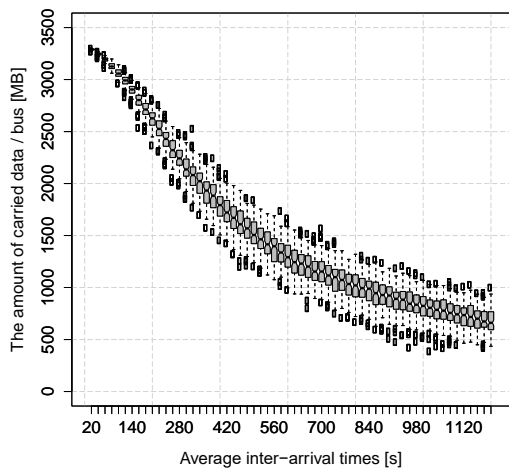


(a) Carried data for FPTS

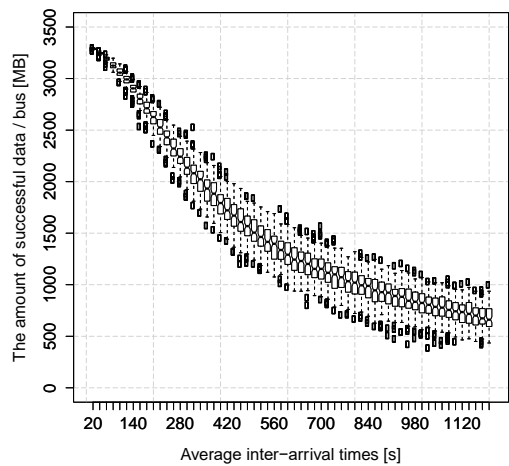


(b) Successful data for FPTS

Figure 9. The amount of carried and successful data per bus for FPTS



(a) Carried data for BPTS



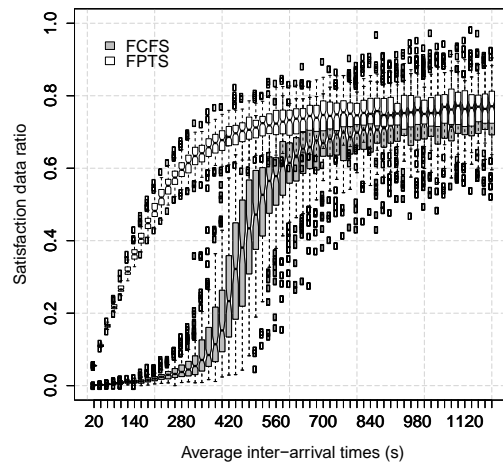
(b) Successful data for BPTS

Figure 10. The amount of carried and successful data per bus for BPTS

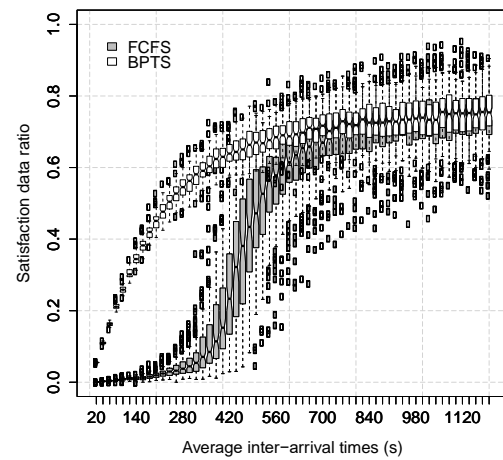
Figure 11 shows the satisfaction data ratio for the three scheduling algorithms. The satisfaction data ratio is defined as the fraction of successful data objects for all large data objects from users who do not board a bus. All large data objects include two kinds of data objects: one is data objects stored in the data port, and the other is data objects not stored in the data port. Figure 11(a) plots the satisfaction data ratio of FCFS and FPTS, whereas Fig. 11(b) plots that of FCFS and BPTS. Compared with FCFS, both FPTS and BPTS sharply improve the satisfaction data ratio, especially in high average inter-arrival times. However, some of the bus data transport capacity may remain unused because a data object remains un-fragmented. On the other hand, in the case that the average inter-arrival times are long, all algorithms have nearly identical results, and none of them fills the transmission capacity because of the scarcity of data objects that transmit to a bus.

We also note that the satisfaction data ratio of FPTS performs slightly better than BPTS because BPTS schedules a data object from the last possible bus within a user's desired delay. Therefore, BPTS may result in capacity underutilization since earlier buses may have enough space. Besides, since BPTS operates based on the last bus service

within the user's desired delay, there is a possibility that the satisfaction data ratio of BPTS may be damaged when an unprecedented bus delay occurs.



(a) FCFS vs. FPTS



(b) FCFS vs. BPTS

Figure 11. The satisfaction data ratio (the amount of successful data / the amount of all data)

4.2. Discussion

We also describe some remaining issues regarding delay constraints of large-sized data object delivery on a scheduled transportation system. First, the above simulation results show that our data port-to-bus transmission schedule sharply improves the performance of the scheduled bus system under no random bus delays beyond the bus system's ideal schedule. To analyze real-life transportation systems, we need to include realistic and random bus delays as the next step. Also, in regards to average inter-arrival time, data size and desired delay, more rigorous analyses are needed to identify these distributions and their parameters.

Second, to more improve the utilization of a bus transport capacity, a data object should be subdivided into smaller segments, with the added capability of tracking the divided data and reconstructing the original data object at a bus terminal or a user destination site. Moreover, different

fragments may be placed on different buses, and; store and forwarding across buses could be considered, to meet different delay requirements.

Because of its simplicity, our approach differs from traditional Delay-/Disruption-Tolerant Networks (DTN) based on the bundle paradigm [8]. If data fragmentation (over multiple buses and routes) and bus switching were introduced, new communication protocols and policies would be required to guarantee end-to-end communication. In essence, as a difference from traditional DTN carries, to improve the transmission performance, our approach shifts to processing at the data port site close to users like edge computing.

5. Related Work

The concept of “data mule” has been proposed to extend the Internet connectivity in a rural area [4], [9]. At first, such a data mule, however, focused only on carrying data without considering desired delays. After that, researchers have attempted to apply the concept to public transportation systems in a city, to alleviate the congestion of mobile networks.

In [10], the authors explored how messages could be carried over aerial carriers and showed performance measures of delivery probability, delay, and hop counts. Their results provide a starting point for future research. Also, [3], [11–18] study data delivery over a bus network, similar to our research, but focuses on routing methods. As far as we know, there is not any known research on transmission scheduling method on a data port to meet user-specified delay constraints for large data object delivery over public transportations systems.

References [19, 20] show experimental results for data offloading via Wi-Fi. In reference [20], authors measured the throughput of 3G network and Wi-Fi network between Carnegie Mellon University and business district through walking and driving. The results showed that as for instantaneous throughput, Wi-Fi network is faster than the 3G network, while the average downloading throughput of the 3G network is faster than that of Wi-Fi network. On the other hand, in uploading throughput, Wi-Fi network is superior to the 3G network for instantaneous and average throughput because the uploading throughput of the 3G network is slow. In reference [19], authors measured the communication throughput of the 3G network and Wi-Fi network through driving in three cities, Amherst, Seattle, San Francisco. The measurement results showed that 3G network provides higher throughput in downloading and uploading than Wi-Fi network. From their results, we can see that users can obtain higher throughput when users use 3G network during movement, or when users use Wi-Fi network during staying.

To efficiently improve data offloading, references [19, 21] have studied data offloading for delay tolerant data. Reference [19] proposed a data offloading method that a

smart mobile device sends/receives data within user’s tolerant delay by using Wi-Fi as much as possible. The method makes a threshold for delay tolerance, and considers data size and expected throughput in Wi-Fi area where a user will visit. If a user cannot offload all data within the desired delay through Wi-Fi networks, a user can use the 3G network to complete to send/receive data within the delay. In reference [21], authors measured Wi-Fi connectivity for about 100 iPhone users in Seoul, Korea. Based on the results, they then evaluated the efficiency of data offloading to Wi-Fi networks when user offload delay acceptable data to Wi-Fi networks, through simulation experiments. From the simulation results, in the case that 6 hours delay is acceptable, the efficiency of the data offloading rose up to 87.5 %. The authors, however, note that the results depend on the communicable area of Wi-Fi network and user’s mobility. Also, reference [22] proposed a data offloading method that a smart mobile device offloads data to another device by a Store-Carry-Forward routing, like DTN. As described above, data offloading that considers acceptable delay for users and applications is becoming a new trend.

Some studies [23, 24] proposed data offloading methods that consider power saving on smart mobile devices. In reference [24], authors investigated how the scanning of Wi-Fi APs impact to smart mobile device’s battery. They describe that the data offloading method that considers the scanning intervals is necessary. Reference [23] also showed that the scanning AP impacts to battery on a smart mobile device. From the results, we may save battery when the scanning interval is prolonged. However, since it may be late to find next Wi-Fi network, the connection period during movement may be reduced. Therefore, to efficiently offload data to Wi-Fi networks, AP scanning interval and battery consumption should be considered. Also, to efficiently make a connection to Wi-Fi networks, reference [25] proposed a connectivity forecast. The method forecasts Wi-Fi networks that a user will visit based on the information of user’s daily movement. Although various approaches have been studied for data offloading to Wi-Fi networks so far, it is essential to building a lot of Wi-Fi networks to improve the data offloading. Besides, as increasing APs, various issues such as deployment and radio interference are arising.

As described above, to utilize scheduled transportation vehicles as a part of the communication network in order to alleviate the congestion of the mobile network, many approaches have been proposed. Most of them focus on the routing method based on DTN. On the other hand, in this paper, to meet the users’ delay requirement for large data objects, we proposed the transmission scheduling algorithms that can deliver them as much as possible within delay requirements. As the next step, to realize the communication network over scheduled transportation vehicles, these existing work is expected to be combined organically.

6. Conclusion

This paper proposes a data delivery scheme that uses a public transportation system to deliver delay constrained large-sized data objects. We demonstrate that scheduled transportation vehicles have the potential to become an effective means for such data delivery service. We prove that, if the input data port has no transmission scheduling capability, in the case of high user demands, most of the data objects miss their deadlines. To efficiently exploit a public transportation system as a part of the delivery network, we proposed two transmission scheduling algorithms and have demonstrated via simulation that the fraction of objects delivered within a user's defined deadline significantly increases.

As mentioned in Section 4, our future work includes more rigorous analytic modeling and a system prototype implementation to study the feasibility of the public transportation-based delivery further. Although this paper focuses on measuring data uploads, download traffic may be of interest as well. For example, a user might request to deliver a data object to a data port at a location of interest. To accommodate download capabilities, we need to extend our investigation in this paper, to design and analyze the performance of a system supporting download traffic as well as upload traffic. A further opportunity for performance enhancement (with increasing complexity) is the introduction of message fragmentation in smartphones, a data port, and buses.

References

- [1] Cisco, "Cisco Visual Networking Index: Global Mobile Data Traffic Forecast Update, 2016–2021 White Paper." 2017.
- [2] S. Kashiwara, M. Y. Sanadidi, and M. Gerla, "Mobile, Personal Data Offloading to Public Transport Vehicles," in *The Sixth International Conference on Mobile Computing and Ubiquitous Networking (ICMU 2012)*, 2012, pp. 142–147.
- [3] I. Komnios and E. Kalogeiton, "A DTN-based architecture for public transport networks," *Ann. Telecommun. - Ann. des télécommunications*, vol. 70, no. 11, pp. 523–542, 2015.
- [4] M. Demmer and K. Fall, "DTLSR: Delay Tolerant Routing for Developing Regions," in *Proceedings of the 2007 Workshop on Networked Systems for Developing Regions*, 2007, p. 5:1--5:6.
- [5] "Transfer Jet." [Online]. Available: <https://www.transferjet.org/index.html>.
- [6] "WiGig." [Online]. Available: <https://www.wi-fi.org/discover-wi-fi/wi-fi-certified-wigig>.
- [7] Aerohive Networks Inc., "The Network Impact of 802.11n." Aerohive Networks Inc., 2010.
- [8] L. Torgerson *et al.*, "Delay-Tolerant Networking Architecture," no. 4838. RFC Editor, 2007.
- [9] A. Pentland, R. Fletcher, and A. Hasson, "DakNet: rethinking connectivity in developing nations," *Computer (Long Beach, Calif.)*, vol. 37, no. 1, pp. 78–83, 2004.
- [10] A. Keränen and J. Ott, "DTN over Aerial Carriers," in *Proceedings of the 4th ACM Workshop on Challenged Networks*, 2009, pp. 67–76.
- [11] F. R. Segundo, E. Silveira e Silva, and J.-M. Farines, "A DTN routing strategy based on neural networks for urban bus transportation system," *J. Netw. Comput. Appl.*, vol. 64, pp. 216–228, Apr. 2016.
- [12] T. Pögel, "Optimized DTN-Routing for Urban Public Transport Systems," in *17th GIITG Conference on Communication in Distributed Systems (KIVS 2011)*, 2011, vol. 17, pp. 227–232.
- [13] S. Ahmed and S. S. Kanhere, "Cluster-based Forwarding in Delay Tolerant Public Transport Networks," in *32nd IEEE Conference on Local Computer Networks (LCN 2007)*, 2007, pp. 625–634.
- [14] S. Jiang, J. Ferreira, and M. C. González, "Clustering daily patterns of human activities in the city," *Data Min. Knowl. Discov.*, vol. 25, no. 3, pp. 478–510, 2012.
- [15] S. Gaito, D. Maggiorini, C. Quadri, and G. P. Rossi, "On the Impact of a Road-Side Infrastructure for a DTN Deployed on a Public Transportation System," in *NETWORKING 2012*, 2012, pp. 265–276.
- [16] H. Yao, D. Zeng, H. Huang, S. Guo, A. Barnawi, and I. Stojmenovic, "Opportunistic Offloading of Deadline-Constrained Bulk Cellular Traffic in Vehicular DTNs," *IEEE Trans. Comput.*, vol. 64, no. 12, pp. 3515–3527, 2015.
- [17] S. Gaito, D. Maggiorini, G. P. Rossi, and A. Sala, "Bus switched networks: An ad hoc mobile platform enabling urban-wide communications," *Ad Hoc Networks*, vol. 10, no. 6, pp. 931–945, Aug. 2012.
- [18] M. Doering, T. Pögel, and L. Wolf, "DTN routing in urban public transport systems," *5th ACM Work. Challenged Networks, CHANTS '10*, pp. 55–62, 2010.
- [19] A. Balasubramanian, R. Mahajan, and A. Venkataramani, "Augmenting Mobile 3G Using WiFi," in *Proceedings of the 8th International Conference on Mobile Systems, Applications, and Services*, 2010, pp. 209–222.
- [20] R. Gass and C. Diot, "An Experimental Performance Comparison of 3G and Wi-Fi BT - Passive and Active Measurement," 2010, pp. 71–80.
- [21] K. Lee, J. Lee, Y. Yi, I. Rhee, and S. Chong, "Mobile Data Offloading: How Much Can WiFi Deliver?," *IEEE/ACM Trans. Netw.*, vol. 21, no. 2, pp. 536–550, 2013.
- [22] B. Han, P. Hui, V. S. A. Kumar, M. V. Marathe, G. Pei, and A. Srinivasan, "Cellular Traffic Offloading Through Opportunistic Communications: A Case Study," in *Proceedings of the 5th ACM Workshop on Challenged Networks*, 2010, pp. 31–38.
- [23] M.-R. Ra, J. Paek, A. B. Sharma, R. Govindan, M. H. Krieger, and M. J. Neely, "Energy-delay Tradeoffs in Smartphone Applications," in *Proceedings of the 8th International Conference on Mobile Systems, Applications, and Services*, 2010, pp. 255–270.
- [24] B. Han, P. Hui, and A. Srinivasan, "Mobile Data Offloading in Metropolitan Area Networks," *SIGMOBILE Mob. Comput. Commun. Rev.*, vol. 14, no. 4, pp. 28–30, 2010.
- [25] A. J. Nicholson and B. D. Noble, "BreadCrumbs: Forecasting Mobile Connectivity," in *Proceedings of the 14th ACM International Conference on Mobile Computing and Networking*, 2008, pp. 46–57.

Support Vector Machine Method to Reduce The Execution Time of Vehicle Plate Recognition System

Muh Ismail,^{a*} Indrabayu,^b Intan Sari Areni,^c

^aGraduated Student of Electrical Engineering Department, Engineering Faculty, Hasanuddin University, Makassar. Email:imuh77@gmail.com

^bDepartment of Informatics, Engineering Faculty, Hasanuddin University, Makassar. Email:indrabayu@unhas.ac.id

^cDepartment of Electrical Engineering, Engineering Faculty, Hasanuddin University, Makassar. Email:intan@unhas.ac.id

Abstract

This research aims to create a vehicle plate detection and recognition system with Cascade Classifier, Support Vector Machine (SVM) and Optical Character Recognition (OCR). Cascade Classifier with Local Binary Patterns (LBP) descriptor is used to detect the car licence plate (Coarse Location). SVM is used to reduce plate candidate detection error and the execution time. Optical Character Recognition (OCR) is used to recognize the characters in plates. The system test is performed using 19 video data of moving vehicles at night and rain conditions. Each video has a duration of 30 seconds and contains 4-10 cars per video. The testing results show reduction of the execution time of vehicle plate recognition system which reached 60% with the average accuracy of plate recognition 61.94%.

Keywords: Cascade classifier; license plate recognition; optical character recognition; support vector machine; video processing

1. Introduction

Research on plate detection or plate recognition become an interesting topic and has been widely practiced in the last two decades that is part of the field of intelligent transportation systems. Some utilization of vehicle license recognition are in parking applications, traffic monitoring, and vehicle traffic controlling [1, 2].

Although vehicle plates are very easy to be recognized by humans, they leave a problem or challenge if applied in a computer system, especially in rain and night conditions [3]. The ones that are still a challenge in various studies start from plate detection, detection image enhancement, and plate character recognition [4].

The research that has been done by Xiao-Hua in 2014 about vehicle plate recognition combining two methods of Pulse Couple Neural Networks (PCNN) and Template Matching (TM). In this study, PCNN is applied to segment a gray image that contains the plates and character extraction of the detected plates while TM is used for character recognition. However, plate recognition under irregular lighting became an obstacle in this study [5].

In 2015, Bunay et al also study about the recognition of vehicle plates that proposed hybrid techniques with Neural Network (NN) and TM methods. Recognition accuracy resulted from this study reached 100%. The data were taken in normal light conditions [6].

Animesh et al. have also studied plate recognition with complex backgrounds using the Morphological Approach and TM methods. The plate studied consists of two lines, where the first line contains texts and the second line includes numbers. This study has a recognition accuracy of 88.8%. However this research is still focused on the recognition of static images and one vehicle object [7].

The present research focuses on minimizing execution time on the system to detect and recognize moving vehicle plates at night and rain conditions. The Support Vector Machine (SVM) method is added to the classification process to reduce the execution time.

This paper is organized as follows: the following section describes literature review. Section 3 is proposed method which describes the algorithm of the vehicle plate coarse location detection, plate candidate preprocessing, vehicle plate precise location detection, and the plate candidate recognition. Section 4 provides results and discussions. Finally, the conclusions and further research are described in Section 5.

*Corresponding author. Tel.: +62-812-4420-9266
Jalan Poros Malino km. 6, Bontomarannu
Gowa, Sulawesi Selatan, Indonesia, 92171

2. Literature Review

2.1. Local Binary Pattern

Local Binary Pattern (LBP) is a binary code describes local texture patterns. It is built with a boundary environment with gray values from its center [8]. An example of LBP computing at 3x3 pixels is shown in Fig. 1. The basic version of LBP uses the center pixel value as a threshold for 3x3 neighbor pixels. The threshold operation creates a binary pattern that represents the texture characteristics. The equation for the basic version of LBP is shown in Eq. 1 [9]:

$$LBP(x_c, y_c) = \sum_{n=0}^7 2^n g(I_n - I(x_c, y_c)) \quad (1)$$

$LBP(x_c, y_c)$ is LBP value in the centre pixel (x_c, y_c) . And then, I_n and $I(x_c, y_c)$ are the neighbor pixel values and the center of each pixel. Index n is an index of neighbour pixels. The function $g(x) = 0$ if $x < 0$ and $g(x) = 1$ if $x \geq 0$.

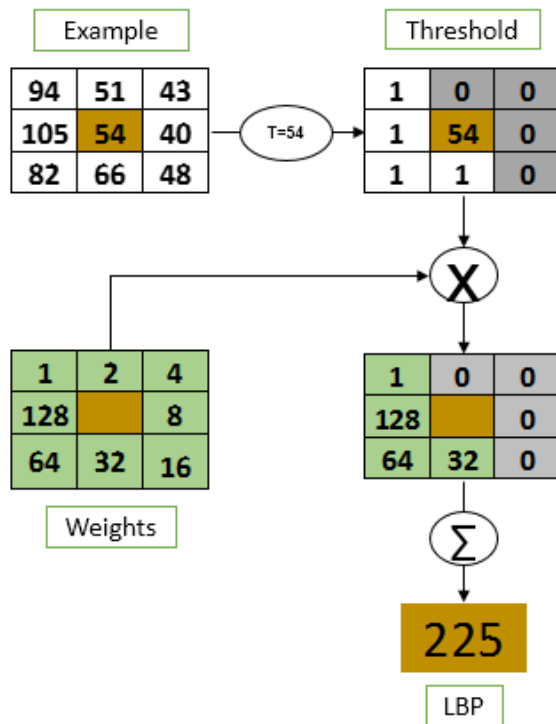


Figure 1. LBP Pixels Counting Process

In Fig. 1, the value 54 as a central pixel is selected to be a threshold. The neighbor pixel value becomes 0 if the value is less than 54. Meanwhile, the neighbor pixel value becomes 1 if the pixel value is greater than or equal to 54. Then the LBP value is obtained through the result of scalar multiplication between binary matrix (threshold) and weight. Therefore, the LBP value of the 3x3 matrix in Fig. 2 assigned $1 + 32 + 64 + 128$ or equal to 225.

2.2. Normalization

Normalization is the process of scaling attribute values or variables of a data so that values can be in a certain range. The result of normalization data (y_{ij}) is calculated based on the following Eq. 2.

$$y_{ij} = \frac{x_{ij}}{\sqrt{\sum(x_{ij}^2)}} \quad (2)$$

where:

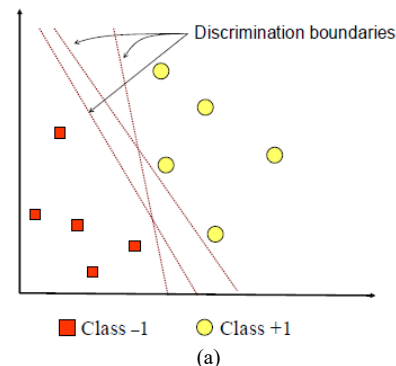
- x = data
- i = row index
- j = column index

2.3. Support Vector Machine

Support Vector Machine (SVM) is a prediction technique that can be used for cases classification and regression. SVM uses linear basic classifier principles, but has been developed to work on nonlinear problems by incorporating kernel concepts in high-dimensional workspaces. The basic idea of this technique is to find the best hyperplane by maximizing the hyperplane margin that serves as a separator of two data classes in the input space. Hyperplane with maximal margin will give better generalization on the classification method, so the result is more accurate [10].

Figure 2 shows an illustration of the SVM method in maximizing hyperplane boundaries [11]. Various alternative lines of discrimination (discrimination boundaries) are shown in Fig. 2(a), in which some patterns are members of two classes namely +1 and -1. Patterns belonging to class -1 are symbolized in red (box), while the pattern in class +1, symbolized by yellow (circle). The classification problem can be solved by finding a hyperplane that separates the two groups.

The best separator hyperplane between the two classes can be found by measuring the hyperplane's margins and searching for the maximum point. Margin is the distance between the hyperplane and the nearest pattern of each class. The closest pattern of the hyperplane is called support vector. The solid line in Fig. 2(b) shows the best hyperplane, which is located right in the middle of the two classes while the red and yellow dots that are in the black circle is the support vector.



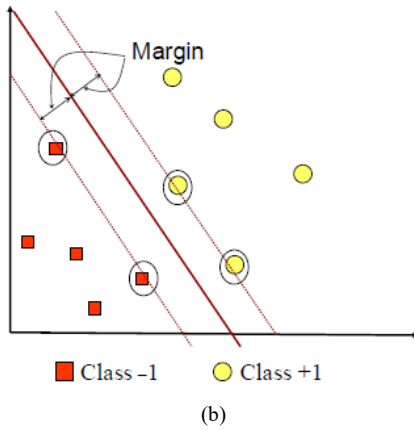


Figure 2. Finding Best Hyperplane Process
a. Alternative Hyperplane; b. Best Hyperplane

Suppose there are data denoted as x_i :

$$x_i \in \mathbb{R}^D, i = 1, 2, \dots, N \quad (3)$$

where N is the number of data with the positive class which is denoted as +1 and the negative class which is denoted as -1. Then each data and class label is denoted as [12]:

$$y_i \in \{-1, +1\} \quad (4)$$

It is further assumed that both classes can be perfectly separated by the hyperplane defined as [13]:

$$f(x) = w \cdot x + b \quad (5)$$

so the obtained equation is:

$$\begin{aligned} [(w \cdot x_i) + b] &\geq 1 \text{ for } y_i = +1 \\ [(w \cdot x_i) + b] &\leq -1 \text{ for } y_i = -1 \end{aligned} \quad (6)$$

with x_i = training dataset $i = 1, 2, \dots, n$ and y_i = class label of x_i .

Hyperplane is best obtained by searching for a hyperplane located in the middle of two class dividing areas. The best position is equal to maximizing the margin or distance between the hyperplane and the nearest object. The best hyperplane determination can be formulated into Quadratic Programming (QP) Problem that minimizes [13]:

$$\frac{\|w\|^2}{2} \quad (7)$$

provided that $y_i(w \cdot x_i + b) \geq 1, i = 1, 2, 3, \dots, n$.

The solution for optimization is solved by using the Lagrange function as follows [14]:

$$L(w, b, \alpha) = \frac{1}{2} \|w\|^2 - \sum_{i=1}^n \alpha_i \{y_i [(w \cdot x_i) + b] - 1\} \quad (8)$$

with α_i = multiplier Lagrange function and $i = 1, 2, \dots, n$.

The optimal value can be calculated by maximizing L against α_i , and minimizing L against w and b as the case of dual problems [15]:

$$\max_{\alpha} W(\alpha) = \max_{\alpha} (\min_{w, b} L(w, b, \alpha)) \quad (9)$$

The minimum value of the Lagrange function is given by [16]:

$$\begin{aligned} \frac{\partial L}{\partial b} = 0 &\Rightarrow \sum_{i=1}^n \alpha_i y_i = 0 \\ \frac{\partial L}{\partial w} = 0 &\Rightarrow w = \sum_{i=1}^n \alpha_i x_i y_i \end{aligned} \quad (10)$$

To simplify, the Eq. 10 must be transformed into the Lagrange Multiplier function itself, thus becoming [13]:

$$L(w, b, \alpha) = \frac{1}{2} w^T w - \sum_{i=1}^n \alpha_i y_i (w^T \cdot x_i) - b \sum_{i=1}^n \alpha_i y_i + \sum_{i=1}^n \alpha_i \quad (11)$$

become [17]:

$$L_d = \sum_{i=1}^n \alpha_i - \frac{1}{2} \sum_{i=1}^n \sum_{j=1}^n \alpha_i \alpha_j y_i y_j x_i^T \cdot x_j \quad (12)$$

and obtained dual problems:

with limits,

$$\alpha \geq 0, i = 1, 2, \dots, n \text{ dan } \sum_{i=1}^n \alpha_i y_i = 0 \quad (13)$$

The training data with $\alpha \geq 0$ which lies in hyperplane called support vector. The training data which is not located on the hyperplane has $\alpha_i = 0$.

Not all data can be separated linearly. However, SVM can also work on nonlinear data by applying the kernel approach to the initial data set data feature. The kernel function used to map the initial dimension (lower dimension) of the data is set to a new dimension (relatively higher dimension). So the data is mapped to a higher dimension to find the hyperplane. Suppose there is data on the input space denoted as [12]:

$$\{\{x_i \in \mathbb{R}^D\}\} \quad (14)$$

where D is the data dimension. It must be mapped to a new dimension of higher definition space (feature space) defined as:

$$\{\{x'_i \in \mathbb{R}^Q\}\} \quad (15)$$

The method used is kernel method in which a data x is mapped by the function $\phi: x \rightarrow \phi(x)$ [19]. This sorting is done while maintaining the data characteristics. For example, if there are two data whose distance is closer to the input space then the feature space space must also be adjacent and vice versa. Thus, the two classes can be separated linearly by a hyperplane [12]. So:

$$\phi : \mathbb{R}^D \rightarrow \mathbb{R}^Q, D < Q \quad (16)$$

Furthermore, the same training process as Linear SVM. The learning process in SVM in finding support vector points depends only on the dot product of both vectors (x_i) and (x_j) which have been transformed to feature space, i.e. $\phi(x_i) \cdot \phi(x_j)$. The dot product value of these two vectors can be calculated indirectly, i.e. without knowing the transformation function ϕ . This technique is called the kernel trick, which is counting the dot product of two vectors in the feature space by using the two vector components in the input space formulated as follows [12]:

$$K(x_i, x_j) = \phi(x_i) \cdot \phi(x_j) \quad (17)$$

To perform non-linear classification on SVM against data testing x , then formulated as follows:

$$\begin{aligned} f(\phi(x)) &= w \cdot \phi(x) + b \\ &= \sum_{i=1, x_i \in SV}^N \alpha_i y_i \phi(x) \cdot \phi(x_i) + b \\ &= \sum_{i=1, x_i \in SV}^N \alpha_i y_i K(x, x_i) + b \end{aligned} \quad (18)$$

where Support Vector (SV) is a subset of training data with a non-negative α . So classification of two classes can be done if $f(\phi(x)) < 0$, then class 1 and if $f(\phi(x)) > 0$, then the class is +1.

2.4. Optical Character Recognition

Optical Character Recognition (OCR) is a computer technology that can recognize characters in letters and numbers, whether from a printer (printer or typewriter) or from handwriting.

To use OCR, RGB image has to be converted into a binary image called thresholding process. The threshold value becomes very influential, where pixels that have values below the threshold become black, and pixels that have values above the threshold become white. However, many of the images encountered have rather large contrast ranges. In this case, a more sophisticated method for thresholding is required to get suitable results [18].

To get better character recognition results, an image enhancement process is required before performing OCR. One of the methods that can be used is Top Hat Transform.

3. Proposed Method

The system stages proposed in this study are shown in Fig. 3.

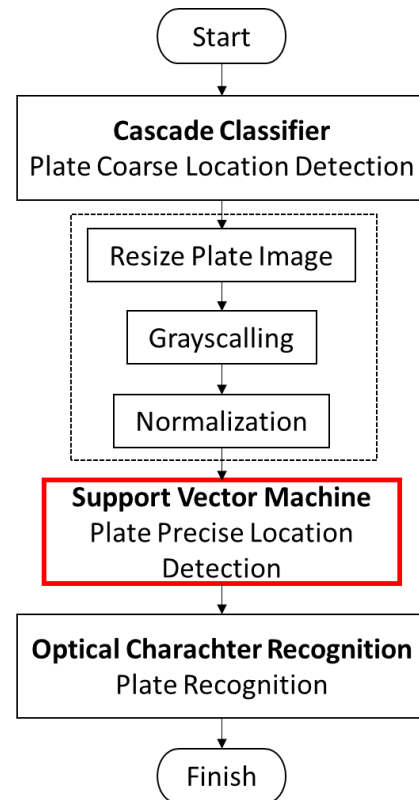


Figure 3. Flowchart of the proposed recognition system

3.1. Vehicle Plate Coarse Location Detection

The formation of the plate detection model proposed in this research uses the cascade classifier method because it has the advantage of being able to detect objects that have different sizes and be able to identify multi-objects. Then the descriptor used is LBP which is useful to describe the features of the image feature. LBP is defined as an invariant grayscale texture size, derived from the general definition of texture in the surrounding area. The plate coarse location detection training process in this study is shown in Fig. 4.

The training process of detection of plate candidates using two data, namely 1700 positive data frame and 3400 negative data as seen in Fig. 5. Parameters used are False Alarm Rate with value 0.2 and Number Stages for LBP set 20 to maximize training.

Based on the results of the analysis on the training process, obtained the size of the bounding box for the vehicle plate that has a wide range between 45 px – 70 px and long range between 150 px – 250 px. So all the detection results of plate candidate sized beyond the bounding box size are removed. Fig. 6 shows the bounding box results of the plate candidates detected by LBP. While, Fig. 7 shows the effect of cutting the bounding box of the plate candidate that has been recognized.

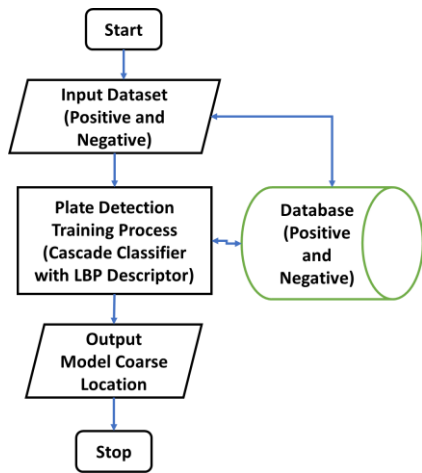
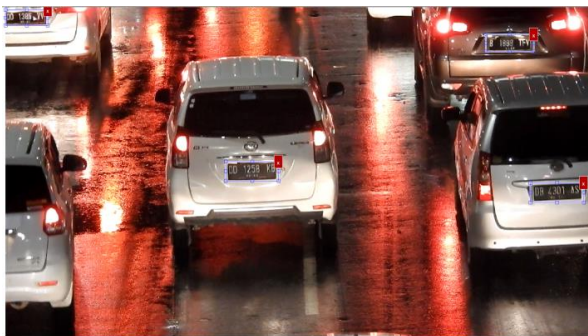


Figure 4. Plate Coarse Location Detection Training Process with LBP



(a)



(b)

Figure 5. LBP Training Data
(a) Positive Sample; (b) Negative Sample

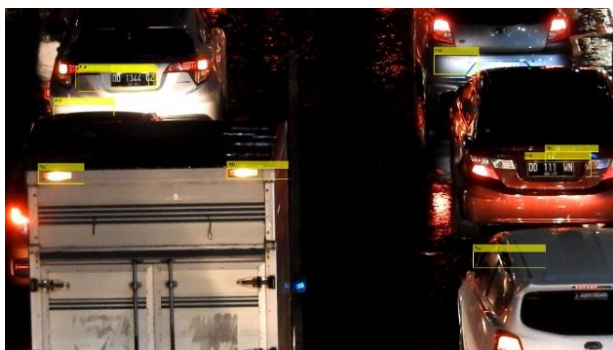


Figure 6. Bounding box Results example of the Plate Candidates Detected by LBP

There are many plate candidates detected incorrectly in Fig. 6. SVM method is added in the classification process to solve the problem. In addition, the plate candidate in Fig. 7 have different size, so it is necessary through the preprocessing process.

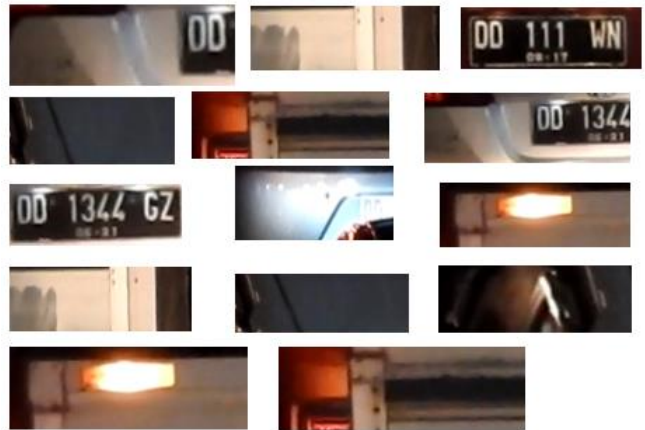


Figure 7. The example of plate candidate detected by LBP

3.2. Plate Candidate Preprocessing

Preprocessing the image of the plate candidate is required before performing the classification process using the SVM method. The first part, image conversion to grayscale. The second part, resizing the image become 14 x 42 px. This process is done to uniform all plate candidate matrices. The third part, normalization for scaling the value of each data. The recommended value of each plate candidate lies within the range of different values. After normalization, all features will be within the same value range [10]. So normalization is done by using Eq. 2 which produces all features within the same range of values.

3.3. Vehicle Plate Precise Location Detection

Detection of vehicle plates in a precise location in the research is a classification process using SVM method shown in Fig. 8.

In this study, the training data used were 300 plate images and 300 non-plate images that shown in Fig. 9.

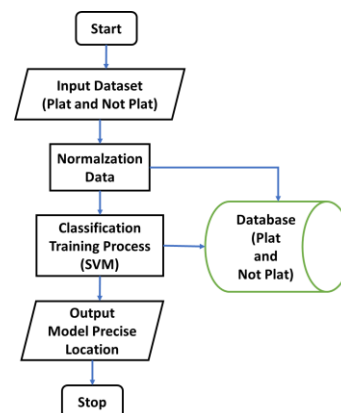


Figure 8. Plate Precise Location Detection Training Process with SVM

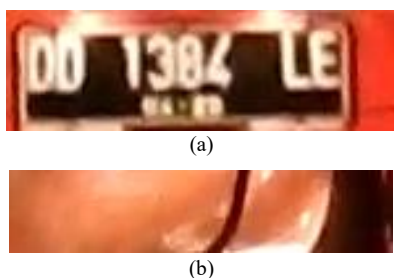


Figure 9. SVM Training Data
a. Plate; b. Non-Plate

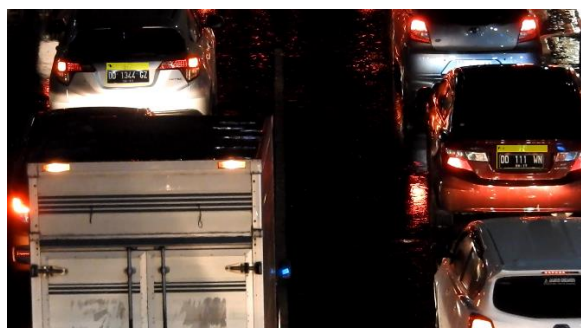


Figure 10. Detection results example using SVM

After SVM training, the training result model is used for a precise location detection testing process using video data whose results are shown in Fig. 10, where SVM succeeded in reducing the error of false plate candidate detection compared to the result of plate candidate detection with LBP shown in Fig. 6.

3.4. Plate Candidate Recognition

After the Precise Location detection process, then the next plate candidate goes into the recognition process using the method of Optical Character Recognition (OCR) with the addition of image enhancement method that is Top-Hat Transform to improve the results of recognition accuracy. The plate recognition training process with OCR is shown in Fig. 11.

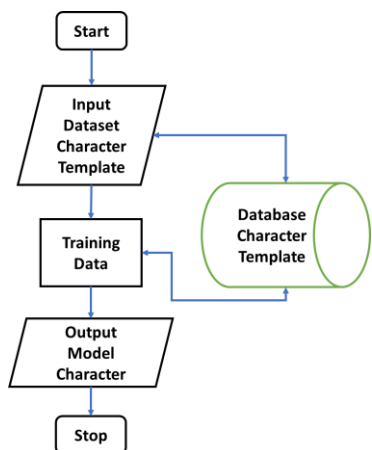


Figure 11. Plate Recognition Training Process with OCR

3.5. System Performance Validation

The performance of the plate recognition system using video data is shown in Fig. 12. The system performance to be measured in this study focuses on system execution time. Because the speed of the system in the process of recognition becomes very important, system validation is done by comparing execution time between recognition system using precise location detection process using SVM and recognition system without precise location detection process.

4. Results and Discussion

Testing the vehicle plate recognition system on moving vehicle at night and rain conditions using 19 videos with a duration of 30 seconds and includes 4-10 vehicles per video. This research has got average the accuracy of plate recognition of 61.94%.

Comparison of execution time with and without SVM in the classification process is shown in Table 1. The table shows that the average of execution time with SVM can reduce the average execution time of system testing process around 60% (=628 seconds).

The large magnitude of the plate candidate detection error in the process with the cascade classifier descriptor LBP method makes the recognition system takes a very long time. Because the detected plate candidates is detected correctly (plates) and those identified incorrectly (non-plates) all go into the plate recognition stage so that it still takes a lot of time for preprocessing before it is recognized. While, SVM be able to reduce the number of plate candidates is processed into recognition system so that the execution time becomes faster.

Table 1. Comparison of Execution Time

Video	Execution Time (second)	
	With SVM	Without SVM
1	383	923
2	364	1031
3	394	1208
4	360	1197
5	402	902
6	498	1258
7	471	1229
8	452	1067
9	330	1309
10	328	1120
11	402	1194
12	468	1112
13	415	1140
14	365	890

15	568	1244
16	311	927
17	429	664
18	495	798
19	379	528
Average	411	1039

5. Conclusion

The moving vehicle plate recognition system at night and rain conditions have its challenges because the system should have a fast execution time to ease the development of the system into real time. This research succeeded in reducing the execution time of system testing on video data by adding SVM classification process for plate candidates and not plates from average 1039 seconds to 411 seconds (= 60%).

For further research, the execution time of the system should be reduced again, and the accuracy of plate recognition also needs to be improved. Image enhancement method is one of the alternatives to enhance the image quality of plate candidates before being recognized.

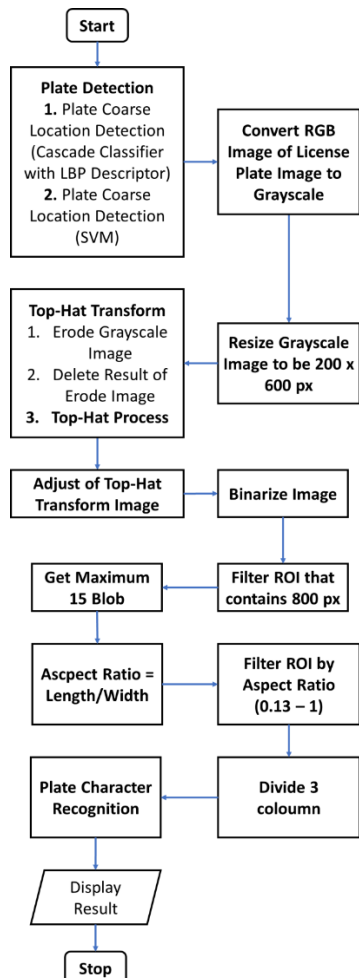


Figure 12. Plate Recognition System Validation Process in Data Video

References

- [1] Y. Yuan, W. Zou, Y. Zhao, X. Wang, X. Hu, and N. Komodakis, "A Robust and Efficient Approach to License Plate Detection," *IEEE Trans. Image Process.*, vol. 26, no. 3, pp. 1102–1114, Mar 2017.
- [2] A. Choudhury and A. Negi, "A new zone based algorithm for detection of license plate from Indian vehicle," in *2016 Fourth International Conference on Parallel, Distributed and Grid Computing (PDGC)*, 2016, page. 370–374.
- [3] N. H. Barnouti, M. A. S. Naser, and S. S. M. Al-Dabbagh, "Automatic Iraqi license plate recognition system using back propagation neural network (BPNN)," in *2017 Annual Conference on New Trends in Information Communications Technology Applications (NTICT)*, 2017, page. 105–110.
- [4] A. Elbamby, E. E. Hemayed, D. Helal, and M. Rehan, "Real-time automatic multi-style license plate detection in videos," in *2016 12th International Computer Engineering Conference (ICENCO)*, 2016, page. 148–153.
- [5] X. h Wang, J. j Yu, Z. h Miao, and Y. Song, "License plate recognition based on pulse coupled neural networks and template matching," in *Proceedings of the 33rd Chinese Control Conference*, 2014, page. 5086–5090.
- [6] B. B. Kumar, M. Bansal, and P. Verma, "Designing of Licensed Number Plate Recognition system using hybrid technique from neural network template matching," in *2015 International Conference on Computing, Communication and Security (ICCCS)*, 2015, page. 1–6.
- [7] A. C. Roy, M. K. Hossen, dan D. Nag, "License plate detection and character recognition system for commercial vehicles based on morphological approach and template matching," in *2016 3rd International Conference on Electrical Engineering and Information Communication Technology (ICEEICT)*, 2016, page. 1–6.
- [8] T. Ahonen, A. Hadid, and M. Pietikainen, "Face Description with Local Binary Patterns: Application to Face Recognition," *IEEE Trans. Pattern Anal. Mach. Intell.*, vol. 28, no. 12, hal. 2037–2041, Des 2006.
- [9] E. Prakasa, "Texture Feature Extraction by Using Local Binary Pattern," *J. INKOM*, vol. 9, no. 2, pp. 45, Mei 2016.
- [10] EkoPrasetyo, *Digital image processing and application using Matlab*. Yogyakarta: Andi, 2011. [Indonesian]
- [11] A. S. Nugroho, A. B. Witarto, and D. Handoko. *Support Vector Machine, Theory and Its Application in Bioinformatics*. Public Lecture IlmuKomputer.Com. 2003.[Indonesian]
- [12] Anonim, "Support Vector Machine (SVM) Java | Contoh Program," 2013.
- [13] B. Santosa, *Data Mining Data Utilization Techniques for Business Purposes*. Yogyakarta: Graha Ilmu, 2007. [Indonesian]
- [14] C. Cortes dan V. Vapnik, "Support-vector networks," *Mach. Learn.*, vol. 20, no. 3, pp. 273–297, Sep 1995.
- [15] S. R. Gunn, "Support Vector Machines for Classification and Regression," University of Southampton, Southampton, 1998.
- [16] Octaviani and P. Anna, "Application of Support Vector Machine Classification Method (SVM) on Primary School Accreditation Data (SD) In Magelang District," Faculty of Science and Mathematics, Diponegoro University, Semarang, 2014. [Indonesian]
- [17] T. Hastie, R. Tibshirani, and J. H. Friedman, *The elements of statistical learning: data mining, inference, and prediction*, 2nd ed. New York, NY: Springer, 2009.
- [18] L. Eikvil, *OCR - Optical Character Recognition*. Norsk Regnesentral, 1993.
- [19] H. Santoso, "Analysis and Prediction on Student Behavior of Diploma to Continue Study to Undergraduate Degree Using Decision Tree Technique and Support Vector Machine," University of North Sumatera, Medan, 2012. [Indonesian]

Partial Discharge Signal Denoising by Discrete Wavelet Transformation

Trinurkalid Sumarwoto,^{a*} Arief Basuki,^b Umar Khayam,^c Naohiro Hozumi,^d

^aSchool of Electrical Engineering and Informatics, Institut Teknologi Bandung. Email: trinurkalid@students.itb.ac.id

^bSchool of Electrical Engineering and Informatics, Institut Teknologi Bandung. Email: arief_basuki@students.itb.ac.id

^cSchool of Electrical Engineering and Informatics, Institut Teknologi Bandung. Email: umar@hv.ee.itb.ac.id

^dElectrical and Electronic Information Engineering, Toyohashi University of Technology. Email: hozumi@ee.tut.ac.jp

Abstract

There are several techniques to eliminate noise on signals such as signal analysis in time zone, frequency area and short time Fourier Transform. As we know, frequency and time domain analysis are the basic methodologies in signal processing. In the partial discharge signal, the signal analysis can be realized in the time domain or in the frequency domain. When the signal is processed in the frequency domain, the time domain information becomes lost. To overcome these weaknesses, wavelet transformation is developed which can provide information in time and frequency domain. Wavelet transforms have been applied in various fields for signal processing in recent years. In this paper, a study of wavelet transformation was done to reduce noise from partial discharge signals obtained from previous experiment.

Keywords: Noise; partial discharge; threshold; wavelet

1. Introduction

According to IEC 60270 standard, partial discharge (PD) is a local electrification phenomenon that partially connecting the insulation between the conductors and occurs either on the surface of the conductor or in the insulation (void). This can occur in a conductor (conductor) in a short time, either at close range or at a great distance [1].

Many methods have been developed to detect PD signal. In the PD measurement, noise may arise from various sources that reduce the quality of measured data, consequently, the result signal is different to the PD signal. Fortunately, the noise may be removed. The technique for removing noise from PD signals can be realized in the time domain or in the frequency domain. PD and noise may be seen in different frequency characteristics [2]. However, when the signal is processed in the frequency domain, the time domain information becomes lost. To overcome these weaknesses, wavelet transformation is developed which can provide information in time and frequency domain. Wavelet transform (WT) has become a new and excellent tool for signal processing in recent years and has been successfully applied to various fields and applications [3].

In this paper, a wavelet transformation is used to minimize noise contained inside PD signals which is obtained through previous experiment. The signal is already in the form of csv file from measurement through oscilloscope. The process of PD wavelet transformation is made using a matrix laboratory (MATLAB) program [4]. The method used in reducing PD signal noise in this study using wavelet transformation. The output of this application is a display of original PD signal that has not been filtered using wavelet, noise signal and signal that has been filtered through wavelet. In addition to measuring the level of noise, it also shows the value of Signal to Noise Ratio (SNR) to facilitate the analysis of wavelet transform (noise reduction) that has been done by the application.

2. Signal Denoising Process

2.1. Partial Discharge (DP)

Partial discharge occurs when the electric field inside the void exceeds the penetrating power of the gas in the void. When the AC voltage is given gradually then at a certain voltage value the partial discharge will begin to occur, this voltage is called the inception voltage (V_i). Where an inception voltage is the minimum voltage required for partial discharge to occur. When the voltage is raised and reaches

*Corresponding author. Tel.:+81-90-266-05739

Toyohashi University of Technology

1-1 Hibiya-aoka, Tempaku-cho. aichi. 441-8580, Japan

the spark voltage, there will be no discharge until the initial avalanche electron begins to emerge partial discharge [5]. These electrons can arise due to the difference in the electric field in an area (electrons 1 in Fig. 1).

The electron avalanche

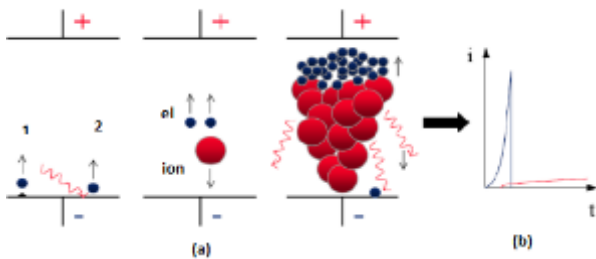


Figure 1. Discharge Process (a) avalanche electron and (b) discharge current [5]

2.2. Wavelet Transformation

Wavelet Transformation is a transformation that can provide resolution of frequency and time in the same time as well. There are two types of wavelet transformation, namely: *Continu Wavelet Transform (CWT)* and *Discrete Wavelet Transform (DWT)*, as follows :

2.2.1. Continue Wavelet Transform (CWT)

CWT works by calculating the convolution of a signal with a modulation window at any time with each desired scale. Modulation windows that have this flexible scale are called wavelets or wavelet base functions [9].

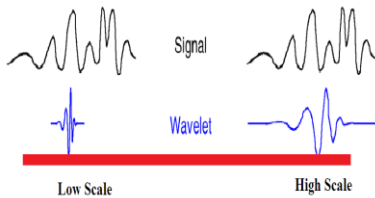
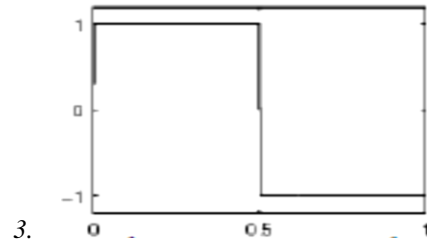


Figure 2. High-low scale relation with frequency [12]

In Fig. 2, we know that for low scale, wavelet signal undergoes compression and corresponds to higher frequencies. As for high-scale, the changes are roughly and slowly.

2.2.2. Daubhecies Wavelet

DWT is one of the wavelet transformation that represent signals in the time and frequency domain. The advantages of this DWT, easy to implement and efficient in terms of computing time. DWT is used to calculate the wavelet coefficients on all possible scales. DWT also generates enormous amount of data. Generally, the DWT process as follows : decomposition, filtering, downsampling and reconstruction [13].



4. Figure 3. Haar Wavelet

2.3. Coiflet Wavelet

2.3.1. Haar Wavelet

Haar Wavelet is the eldest and simplest wavelet. *Haar Wavelet Haar* is the same as *Db1 Wavelet* (1st orde Daubechies) with the Haar Wavelet filter length is being 2. [4, 12].

2.3.2. Daubhecies Wavelet

Daubhecies wavelet has a simple name, *Db.*, and for *N* orde is written with *DbN*. The Daubechies Wavelet Order is *N = 1* or Haar, *N = 2, ..., N = 45*. Wavelet daubechies filter length is $2N$ [4, 12]. We can see the Daubhecies wavelet in Fig. 6.

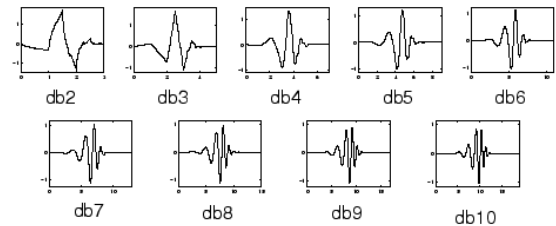


Figure 4. Wavelet Daubhecies

2.3.3. Coiflet Wavelet

Wavelet Coiflet has a short name *Coif*, and for the order *N* is written with *CoifN*. The length of the Coiflet Wavelet filter is $6N$ [4, 12]. For its figure as attached below.

2.3.4. Symlet Wavelet

Wavelet Symlet has a sym short name, for the order *N* written with *SymN*. Wavelet Symlet has the order $N = 2, ..., 45$. The filter length for Wavelet Symlet is $2N$ [4, 12].

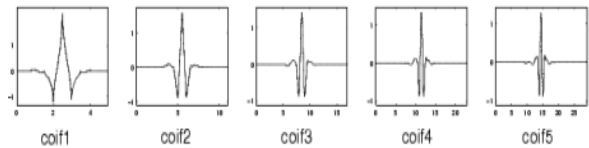


Figure 5. Wavelet Coiflet

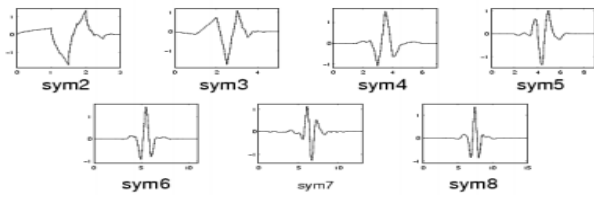


Figure 6. Symlet Wavelet

In this paper, we will use four types of wavelets namely, haar, daubhechies, symlet and coiflet. Although the haar is 1st Daubhechies type and Symlet-Daubhechies are having the same length, we want to know form and SNR its signal.

Another purpose is the use of wavelets with the type of symlet and coiflet because this wavelet type has a different filter length so it can see which wavelet transformation is better, particularly for noise reduction.

4.1. Thresholding [10]

Threshold is a process that make zero for existing values within a predefined threshold value. Thresholding can be done globally where a threshold value is applied to all level of scale of the wavelet transform, or each scale level has its own threshold value. There are two threshold functions used in this task, as follow:

2.4.1 Hard Treshold

Hard threshold has an equation as follows :

$$\delta_{\lambda}^H = \begin{cases} x & \text{if } |x| > \lambda \\ 0 & \text{if } |x| \leq \lambda \end{cases} \quad (1)$$

In the hard threshold there is a discontinuity in the threshold function so that the value of x which has been mentioned before, above the threshold is not touched. At hard threshold only coefficients with absolute values below the threshold value are affected and the coefficients are replaced by zero whereas other than fixed.

2.4.2 Soft Treshold

$$\delta_{\lambda}^H = \begin{cases} x & \text{if } x > \lambda \\ 0 & \text{if } |x| \leq \lambda \\ x + \lambda & \text{if } x < \lambda \end{cases} \quad (2)$$

with λ is threshold parameter.

The function of soft threshold is continue since x value is above threshold. The use of soft threshold comes from the principle that noise affects the whole wavelet coefficient. At the soft threshold, all coefficients undergo a modification process. Coefficients with absolute values above the threshold value will be reduced in value whereas the other coefficients will be zero.

4.2. Signal to Noise Ratio (SNR)

Signal to Ratio (SNR) is a measure in determining the quality of a signal disturbed by noise. In other words SNR shows the comparison between the power of the original signal (information) with the noise. Here is the formula used in SNR calculation on this task [11]:

$$SNR_{dB} = 20 \log \frac{V_s}{V_n} \quad (3)$$

With SNR_{dB} (Signal Derau Ratio in Decibel unit), V_s (Signal Voltage), and V_n (Noise Voltage).

5. Measurement Method

5.1. Partial Discharge (PD) Measurement System

Partial discharge measurement system that is used base on IEC 60270 standard. This detection method uses the recommended series of tests.

The main equipment which is used in Fig. 7: Voltage source 220 V, transformer step-up 220V/100kV, limiter resistor 6100 Ω , Coupling Capacitor 100 pF, Divider capacitor 68 nF and Detecting impedance 50 Ω . The discharges occurring in the sample are detected using the detection circuit High Frequency Current Transformer (HFCT), RC detector and Loop Antenna shown in fig. 7.

PD measurement result is given by oscilloscope that connect to Personal computer (PC). The PC is used to record and store test data in the form of images and CSV files. The test data is taken using Freeware software.

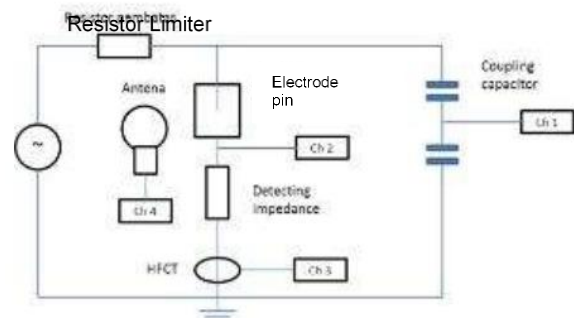


Figure 7. PD Measurement scheme [5]

After the PD data in CSV format has come out, it usually contain noise which cause difficult to make an analyze, the next step was denoising process by wavelet transformation.

5.2. Wavelet Design

This application was created using Graphical User Interface (GUI) Matrix Laboratory software (MATLAB) R2016a [1, 12]. The application which has been made, can reduce noise on the partial discharge signal by using the wavelet transform technique by passing signals on two different filter bands, then performing sub-sampling

operation, then the signal is modified, and the last signal will be reconstructed.

In this program, to different output with one another and make it easy determining better one, it give SNR value before and after signal process. Figure 8 is the overall programming flowchart of this application :

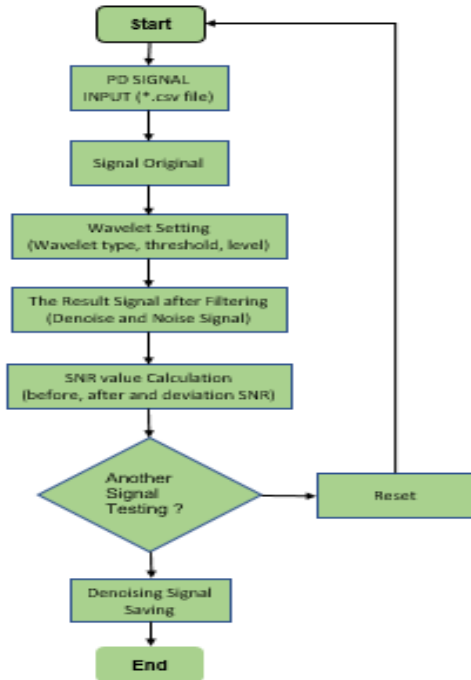


Figure 8. Programming Flowchart

3.3. Process Analysis for Wavelet Design

The first step is scaling. Volt/div is the value for each box on the oscilloscope in the vertical position. For each box on the oscilloscope will be written as many as 25 points in the CSV file. Therefore the y-axis value for each point on the CSV needs to be multiplied by the value of volt/div divided by 25.

The next process is wavelet transformation process of PD signal with threshold parameters. There are 2 types of threshold used, namely soft and hard threshold. Uncorrect election of thresholding will result in less than maximum gain or noise generated.

After the process of selecting the type of threshold, the next process is selecting the type of wavelet process. There are four types of wavelets used in this task, haar, daubhecies, symlet and coiflet. For haar type, daubhecies type (db1,db2,db3,db4,db5,db6,db7,db8,db9,db10), the symlet type (sym2, sym3, sym4, sym5, sym6, sym7, sym8) and coiflet (coif1, coif2, coif3, coif4, coif5).

The fourth process is the selection of wavelet transformation levels consisting of levels 1 through 6. After that we do denoising process. The noise signal itself is the difference between the original signal and signal after the wavelet process. Another important step is calculating the SNR value. It compares SNR before and after the wavelet transformation process.

The final step is storing the result by the *.CSV form. Furthermore, this file can be used for judgment system or SNR evaluation. After analyzing one data, to make it easier to display other data, it can be done reset all values and display from previous data.

4. Result and Discussion

Consisting of application usage procedures, application testing, analysis through SNR values and graphical visualization of PD signals from practice results using a combination of three parameters (threshold, level and wavelet type). Because if it can be done, all combination of three parameters have 144 data, then in this report 144 data will be sampling for graphical visualization. For SNR value, it will be shown all number 144 data.

4.1. Result [13]

The test is done by simulating the combination of three wavelet parameters and comparing them visually and through the SNR value. The three wavelet parameters are: threshold, wavelet type and wavelet level.

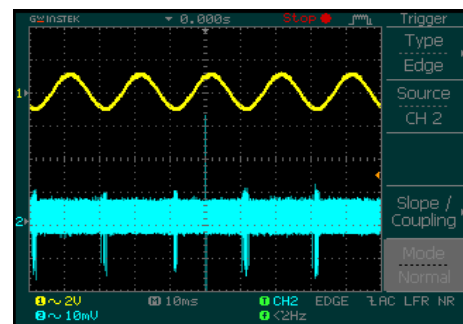


Figure 9. Positive PDIV on HFCT

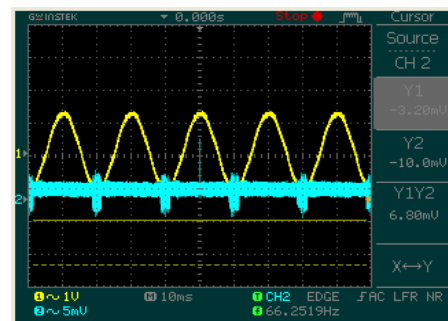


Figure 10. Positive PDIV on RC Detector

As a signal testing material, it will be used a partial discharge test signal by using the High Frequency Current Transformer (HFCT) and RC Detector [13]. The selection of this test signal at the time of partial discharge inception positive voltage (PDIV positive) as shown in Figs. 9 and 10.

The result of simulation test of partial discharge signal can be seen for HFCT processing signal with Hard Threshold, Level 6 and Coif5 wavelet type as shown Fig. 11 below:

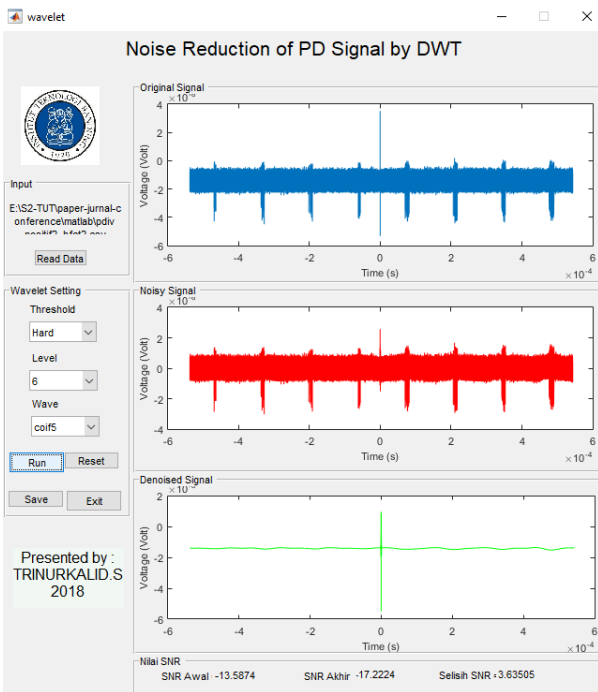


Figure 11. HFCT Denoising Signal Hard Threshold, level 6, coif5 wavelet type

For HFCT processing signal with Soft Threshold, Level 1 and Coif5 wavelet type as shown Fig. 12 below:

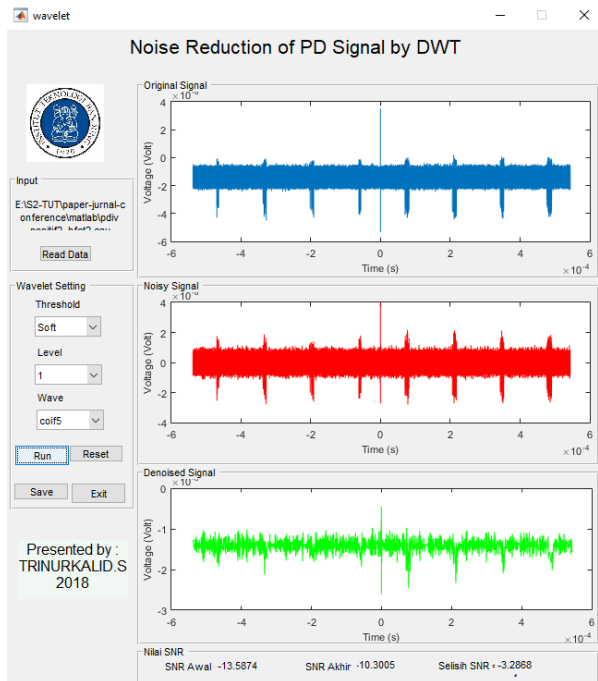


Figure 12. RC Detector Denoising Signal Hard Threshold, level 1, coif5 wavelet type

For HFCT processing signal with Soft Threshold, Level 6 and Coif5 wavelet type as shown Fig. 13 below:



Figure 13. HFCT Denoising Signal Soft Threshold, level 6, coif5 wavelet type

By Fig. 11, we can see original signal, noisy signal and denoised signal with the result of first, last and SNR deviation are -13.5874 dB, -17.2224 dB and 3.63505 dB. For Fig. 12, the result of denoising signal is -13.5874 dB, -10.3005 dB and -3.2868 dB. For Fig. 13, we could see the SNR value before, after and deviation : -13.5874 dB, -6.51924 dB and -7.0681 Db.

For RC detector processing signal with Hard Threshold, Level 6 and Coif5 wavelet type as shown Fig. 14 below:

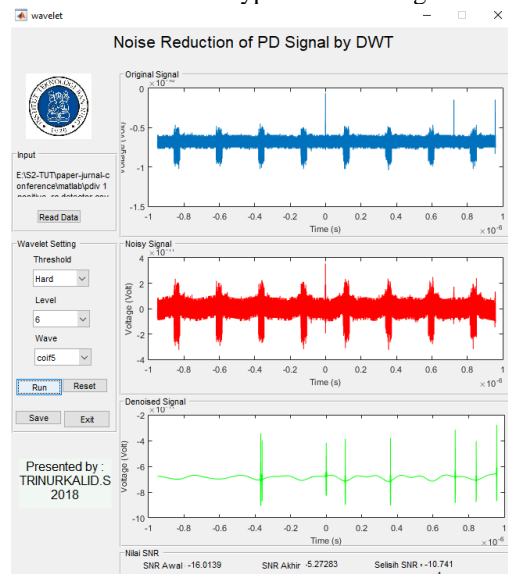


Figure 14. RC Detector Denoising Signal Hard Threshold, level 6, coif5 wavelet type

For RC detector processing signal with Soft Threshold, Level 1 and Coif5 wavelet type as shown Fig. 15 below:

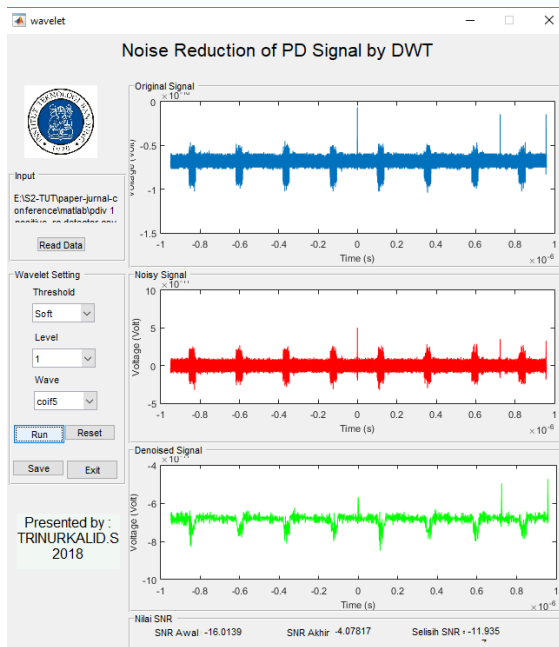


Figure 15. RC Detector Denoising Signal Hard Threshold, level 1, coif5 wavelet type

For RC detector processing signal with Soft Threshold, Level 6 and Coif5 wavelet type as shown Fig. 16 below:

By Fig. 14, like the result of HFCT, SNR in RC detector measurement give SNR as follow: -16.0139 dB, -5.27283 dB and -10.741 dB. If we change the threshold become soft and level become 1, as like Fig. 15, the SNR will be: -16.0139 dB, -4.07817 dB and -11.935 dB.

Same as Fig. 15 but we change level to 6, the SNR become: -16.0139 dB, -19.9331 dB and -35.947 Db as shown in Fig. 16.

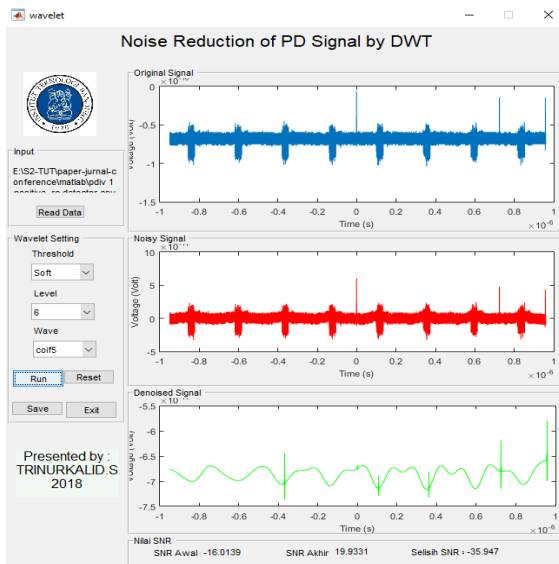


Figure 16. RC Detector Denoising Signal Soft Threshold, level 6, coif5 wavelet type

4.2. Discussion

From Figs. 11-13, the wavelet transformation simulation test result, threshold: hard; level: change; and wavelet type: coiflet5, we can get the following result:

Table 1. Test Result; type:coif5, threshold:hard

Threshold	Level	Wavelet	SNR		
			before	after	Diff
Hard	1	Coif5	-13.587	-14.1579	0.5705
	2			-17.9043	17.9043
	3			-17.698	17.688
	4			-17.601	17.601
	5			-15.5385	15.5385
	6			-15.4951	15.4951

Table 2. Test result; type:coif5, threshold:soft

Threshold	Level	Wavelet	SNR		
			before	after	Diff
Hard	1	Coif5	-13.587	-10.3005	-3.2869
	2			-10.4317	10.4317
	3			-9.13318	9.13318
	4			-8.36113	8.36113
	5			-7.14755	7.14755
	6			-6.51924	6.51924

From the results shown in Tables 1, it can be concluded that in the same wavelet type and threshold, generally, the higher the level of decomposition the better the value will be got. This can be seen from the increasing value of SNR after denoised and the smaller the difference.

Now, if we change the threshold to soft threshold like Figs. 12 and 13, we will see almost the same result like table-1 but in more higher in final result after denoising process. The higher the decomposition level, the higher SNR will be got and the lower difference SNR will produced.

If we compare between Table 1 and 2 with the same level, it implies that the soft threshold give better result than hard threshold because it is cleared from Table 1 and 2, the SNR of soft threshold more higher than hard threshold SNR and also, by comparing the noised signal between Figs. 14 and 16 or Figs. 11 and 13, the amplitude signal of soft threshold more smaller than hard threshold so that soft threshold could eliminate the noise quite well.

Below the tabel summary for all wavelet parameter combination, Table 3 for HFCT and Table 4 for RD detector.

Table 3. HFCT of wavelet parameter combination

Threshold	Level	Wavelet type		Result SNR (dB)	
		Highest	Lowest	Highest	Lowest
Hard	1	coif1	haar	-13.8665	-19.2227
	2	db6	db2	-15.8936	-19.0412
	3	db6	haar	-15.7129	-19.0143
	4	db5	haar	-16.5404	-19.0315
	5	db6	haar	-15.5385	-19.3231
	6	db6	coif1	-15.4951	-19.9518
Soft	1	db8	sym7	-9.89927	-12.8173
	2	coif3	db5	-10.3567	-12.063
	3	db4	db5	-8.82599	-10.5901
	4	db4	db5	-7.58862	-10.0539
	5	db4	db5	-6.54698	-9.3563
	6	db4	db5	-6.51924	-9.49774

Table 4. RC detector of wavelet parameter combination

Threshold	Level	Wavelet type		Result SNR (dB)	
		Highest	Lowest	Highest	Lowest
Hard	1	sym6	db6	-6.20452	-11.6479
	2	sym6	db6	-2.83113	-10.9276
	3	sym6	db6	-2.03524	-10.721
	4	sym6	sym7	-1.31779	-10.6421
	5	sym6	db6	-1.20826	-10.6117
	6	sym6	db6	-1.21057	-10.852
Soft	1	haar	sym3	-0.82448	-6.6141
	2	haar	db2	2.30468	-1.46216
	3	coif4	db2	6.85471	2.11982
	4	sym8	sym2	14.8486	3.23104
	5	sym4	sym2	20.7808	3.7416
	6	sym6	db2	31.8172	1.87374

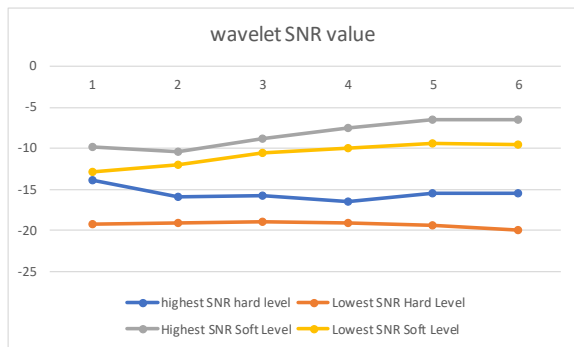


Figure 17. Comparison of HFCT SNR values

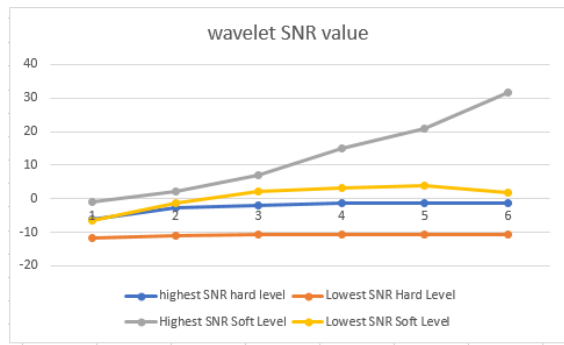


Figure 18. Comparison of RC detector SNR values

By Table 3 and 4, it can be seen that SNR signal increases inline with its level, for soft mode more better than hard mode. The highest SNR value, for table-3, at level 6 with wavelet Daubhecies-4 type, for soft threshold = -6.51924 dB and wavelet Daubhecies-6, for hard threshold = -15.4951 dB and for Table 4, with symlet-6 type for soft threshold = 31.8172 dB and hard threshold = -15.4951 dB This indicates that in soft mode there is more noise reduction than hard.

By Figs. 17 and 18, it can be seen visually that at each increase of wavelet level, more noise will be eliminated. This could be happened, because soft threshold is more sensitive than hard threshold. The soft threshold uses three equations to denoise the partial discharge signal, but the hard threshold only use two equations [4].

5. Conclusion

It is usually not easy to analyze partial discharge signal directly because noise comes from various sources that can reduce the quality of data received, consequently, the result signal which is obtained did not equal to the expectation. By the wavelet system, the noise could be reduced significantly.

In this system soft threshold mode is better than hard threshold mode for reduction noise and the higher level parameter was used in same level, the better signal can be analyzed for next pace. It happened because the soft threshold uses three equations to denoise the partial discharge signal, but the hard threshold only use two equations.

6. Acknowledgements

We acknowledge PLN for the financial support during study and research stay of Trinurkalid Sumarwoto in High Current and Voltage Laboratory, Bandung Institute of Technology, Bandung, Indonesia.

References

- [1] IEC 60270,2000, "Hight Voltage Test Technique - Partial discharge measurement"
- [2] Xiteng Liu, "A New Approach to Time-Frequency Analysis". IEEE Data Compression Conference, pp. 540, 2010.
- [3] Vidya H. A, V. Krishnan and Mallikarjunappa K, "A Wavelet Transform Technique for De-noising Partial Discharge Signals", IEEE Int. Conf. nn Condition Monitoring and Diagnosis, Beijing, China, April 21-24, 2008.
- [4] Tria Kasnalestari, " Wavelet Transformation Application For Denoising Sinyal Partial Discharge", Bandung Institute of Technology, 2016
- [5] Suwarno, "Diagnosis of High Voltage Equipments", ITB Press, 2010.
- [6] Emeraldi Primas, " Engineering and Implementation of Impedance Adjustment Circuit For Partial Discharge Measurement In Frequency Range To One Giga Hertz" Thesis of Postgraduate Program, High Voltage Engineering, STEI, ITB, Bandung, 2013.
- [7] Umar Khayam, "Partial Discharge Experiment Module." High Voltage Laboratory of ITB, 2014.
- [8] Ibrahim Alhanif, " Preparation of Partial Discharge Detection and Measurement ", Thesis of Postgraduate Program, High Voltage Eneengineering, STEI, ITB, Bandung, 2015.
- [9] Rendi Pradila, 2013, *Introduction of Wavelet*, term paper seismology resume, Brawijaya University.
- [10] Alok Kumar P., "Analysis of Partial Discharge Signals Using Digital Signal Processing Techniques", Natonal Institute of Technology Rourkla, 2012.
- [11] Hilton Mota, "Paritial Discharge Signal ProcessingUsing Wavelet", Univesulde Federal de Sao Joao del Rei, Bazil 2010..
- [12] Swastiti Vinana Sari, Achmad Hidayatno, Abdul Syakur, "Wavelet Transformation Application To Eliminate Noise On Partial Partitition Signals", Electrical Engineering, Diponegoro University , Semarang, Indonesia, 2008.
- [13] Group 8, "Modul II-Partial Discharge", Laboratory Report, High Voltage Laboratory, STIE-ITB, 2016

Development of The Structure and Construction of Seaweed Farmer's Residence in Bantaeng Regency

Pratiwi Mushar,^{a,*} Victor Sampebulu,^b

^aLaboratory of Material, Structure and Building Construction, Architecture Department, Engineering Faculty, Hasanuddin University.
Email: pratiwimushar@unhas.ac.id

^bLaboratory of Material, Structure and Building Construction, Architecture Department, Engineering Faculty, Hasanuddin University.
Email: victorsampebulu@unhas.ac.id

Abstract

Seaweed farmer is one of the biggest livelihoods of the society in Bantaeng Regency. The problems of seaweed farmer's residence in Bantaeng city (case study) are as follows: First, the excessive utilization of the residence so the hierarchy of the space is not clear. Second, utilizing the structure or construction of the residence as a place of goods storage and as a place for clothes drying simultaneously that can affect the building structure security. Third, the addition of space on the residence without a good planning on the structure and construction of the residence. Fourth, the spatial function for seaweed processing activities built in residential area and inside the residence itself so seaweed industry processing developed in dense, slum, without sanitation and unfit for habitation. The purpose of the research is to analyze the structure and construction of seaweed farmer's residence in Bantaeng Regency from the viewpoints of its spatial organization and function. The data were obtained by the direct survey and field observation where the interview is conducted by using questionnaire. The society aspiration data were obtained by using Focus Group Discussion (FGD) approach. Technical analysis is conducted by using qualitative description. The result of the analysis shows that (1) The space in the growing and developing residence is influenced by some seaweed farmer's activity and that spatial development influences the structure and construction development of stilt house buildings that are structured or overlapping each other. The construction development is conducted independently by the owner of the residence without appropriate or standard basic constructions. (2) The concept of the structure and development of farmer's residence maintains the construction system of Bugis-Makassar stilt house but the procurement of spatial organization is needed by the seaweed farmer.

Keywords: Construction; seaweed farmer; seaweed farmer's residential; structure

1. Introduction

Seaweed farming is one of the biggest livelihoods of the society in Bantaeng Regency. The problems of seaweed farmer's residence in Bantaeng city (chosen as a target of case study) are summarized as follows:

- The excessive utilization of the residence makes the hierarchy of the spatial unclear.
- The structure or construction of the residence is utilized simultaneously as a place of goods storage and as a place for clothes drying, and this affects security of the building structures. (Figs.1 and 2)
- The addition of space is made to the residence without a good planning in terms of the structure and construction of the residence. (Fig.3)

- The spatial function for seaweed processing is built in residential areas and even in the residence itself, so the seaweed processing is made in dense and slum environment without sanitation and unfit for habitation. (Fig. 4)



Figure 1. Illustration of utilizing the structure or construction of the residence as a place of goods storage and as a place for clothes drying

*Corresponding author. Tel.: +6281355084736
Jalan Perintis Kemerdekaan 4 Lr. 5 No.2
Makassar, Indonesia, 90245



Figure 2. Illustration of the spatial function for seaweed processing activities built in residential areas and in the residence



Figure 3. Illustration of the addition of space to the residence without a good planning on the structure and construction of the residence



Figure 4. Illustration of the insecure residence construction in Letta village because of the live/dead loads and aged wood material.

The purpose of the research is to analyze the problems of structure and construction of seaweed farmer's residence from the viewpoints of its spatial organization and function. Bantaeng Regency is chosen as a survey area.

The present research refers to a series of previously conducted researches, which are the study on the location development principles of productive residence and processing of community-based seaweed (case study: Watershed of Bantaeng Regency) by Wunas [1] in 2014 and the study on prototypes of productive energy-efficient residence and model of residential area with seaweed processing industry (case study: river bank of Bantaeng Regency) by Wunas et al [2] in 2016. Specifically, it can be emphasized that this research is beneficial to seaweed farmers for them to have safer and more functional residence. Other researches by Wunas [3-7] are referred for more information, and references [8-11] are also useful for general information in methodology and conceptual ideas.

2. Methodology

The research was conducted in Bantaeng Regency, specifically in the coastal area of Calendu, Letta village, and Bantaeng sub-district. Data collection was done by direct survey (Table 1). The field observation of seaweed farmer residences was measured in detail and documented, and direct interview was made with seaweed farmer. The society aspiration data were obtained by using Focus Group Discussion (FGD) approach. Data analysis methods used in the research were qualitative descriptive and comparative.



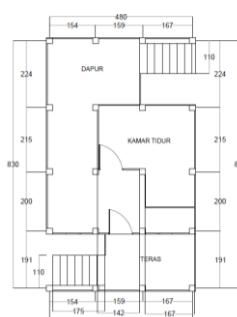

3. Result and Discussion

3.1. Analysis of Design, Structure, and Construction of Seaweed Farmer's Residence Reviewed from Its Spatial Organization and Function in Bantaeng Regency.

3.1.1. Roof construction

The roofs that are used is a saddle and a shield roofs with the construction of simple wooden trestle similar to roof construction in the traditional Bugis-Makassar house. Zinc is used as a roof covering material. (Fig. 5)

Table 1. Residence Plan Types of Seaweed Farmer's Residence

<p>RESIDENCE PLAN TYPE 1 (stilt floor) The upper floor in a stilt house is a residential area without being mingled by the seaweed farmer activities.</p> 	 <p>The farmers developed their stilt houses on by utilizing the house basement become residential and seaweed processing functions</p>
<p>RESIDENCE PLAN TYPE 2 (stilt floor) The upper floor is used only for residential activities such as receiving guests, cooking, relaxing, sleeping, etc.</p> 	 <p>The entire area of the stilt house basement is used as a binding area of seaweed seeds</p>

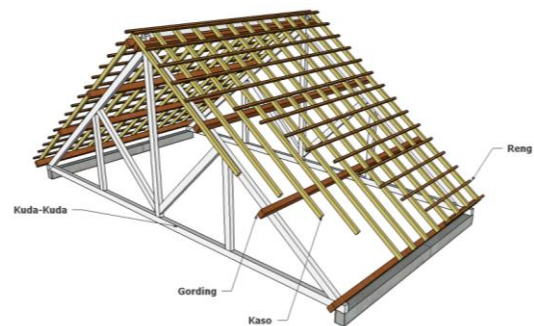


Figure 5. A saddle shape roof can provide an effective wind circulation system when ventilated.

3.1.2. Wall-floor construction

a. Floor (Figs. 6 and 7)

The wall material made of plank is constructed with the tongue and groove construction and the partition material of the room is using plywood.

Construction of skeletal frame wall has several advantages:

- Saving $\pm 50\%$ of wood building materials.
- Higher stability against buckling.
- High stability to horizontal force by wallcoverings such as multiplex or diagonal wooden plank.

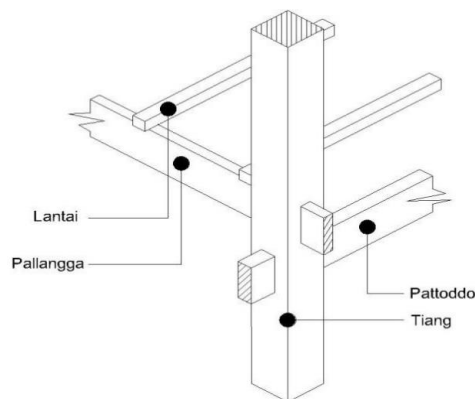
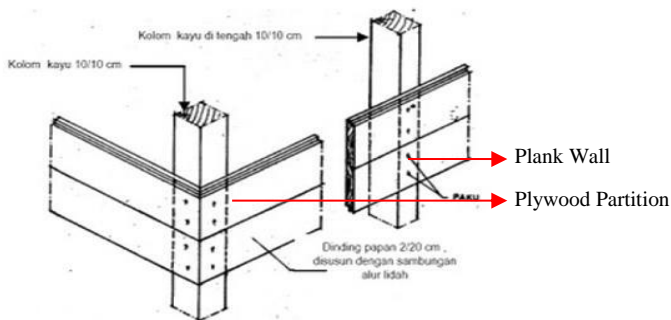
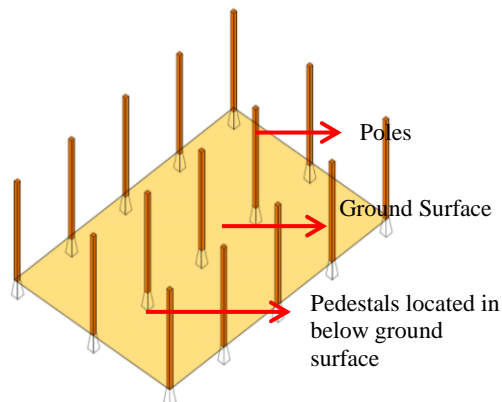


Figure 7. Floor construction in seaweed farmer's residence



Figure 6. Construction and wall material in seaweed farmer's residence



b. Wall

The floor construction of stilt house is supported/carried by the longitudinal beams or *pallangga*, then distribute the force to the main beam or *pattoddo*.

Floor beams are the lowest wooden construction as a floor support or as a support beam, which is usually made of 1st grade wood that is resistant to termites.

Preservation of low-grade wood does not guarantee resistance to termites. Painting the surrounding floor beams can pose a danger of decay because of all the pores on wood are closed.

c. House Basement Construction

The house basement consists of several poles that serve as a trestle and tied by a transverse beam (*pattoddo*) and tied by a longitudinal beam (*pallangga*). (Fig. 8)



Figure 8. Basement Construction in seaweed farmer's residence

The foundation that is used is a pedestal system. The foundation of the house basement. The poles were made by wood material.

3.2. Spatial Organization

Spatial organization functions to understand how the relation between space is created. (Figs.9 and 10)

With the need of existing standard space, the spatial planning and organizing can be made by conduct zoning, grouping, and circulation studies.

<Function of Spatial Organization>

- Making the house more compact
- The house circulation becomes comfortable

- Space relate to each other is well connected.
- The house appearance becomes more interesting.
- Manufacturing cost can be more efficient

Based on the description in Table 2, the space created is not fully functionalized or utilized by the residents. Living room is very rarely used as well as the terrace because the socialization of seaweed farmer society there is very strong that the interaction between people or individuals with each other happens outside the residence only.

Table 2. Spatial and zone organizations of seaweed farmer's residence

SHAPE	Space organization before development	Zone	Space organization after development	Zone	
Type 1					
Roof	Not functioned	-	Attic warehouse	In service	
Main structure	Terrace	Public	Terrace	Public	
	Living room	Semi public	Living room	Semi public	
	Family room	Private	Family room	Private	
	Bedroom	Private	Bedroom	Private	
	Kitchen	In service	Warehouse	Private	
Basement	Livestock space	Semi private	Bathroom	Private	
	Water disposal	In service	Kitchen	In service	
	Courtyards		In service	Toilet	In service
				Well	In service
				Parking lot	Semi private
				Cage	In service
				Fishing equipment warehouse	In service
		Courtyards	In service		
Type 2					
Roof	Not functioned		Not functioned		
Main structure	Terrace	Public	Terrace	Public	
	Living room	Semi public	Living room	Semi public	
	Family room	Private	Family room	Private	
	Bedroom	Private	Bedroom	Private	
	Kitchen	In service	Warehouse	In service	
Basement	Livestock space	Semi private	Seaweed tying space	Semi private	
	Water disposal	In service		(probably used by family/relatives)	



Figure 9. Living room is rarely functioned and filled with furniture that is quite heavy and disproportionate with the space so that it affects the construction of floors (planks) which are sag.



Figure 10. Terrace is used for a short break and place to work

Toilet still less calculated in the spatial planning by the residents. Even the toilet is placed separately from the building. But some houses have built the toilet under a building that has been built permanently.

Construction of residence reviewed from special organization and function is summarized in Table. 3.

3.3. Analysis of Residence Structure

Stilt houses have a number of advantages such as:

- Anti Flood
- Safe against wild animals
- Larger Yard
- Resist to Earthquake
- Strong Traditional
- Unique Shape
- Cooler Interior

The disadvantages of the stilt house are that the houses require funds and architecture to make it and the stilt houses require a certain material and slightly different from ordinary house in general. Also, the stilt houses take a fairly long time on the construction process.

3.3.1. Residence type

The design of seaweed farmer's residence in Bantaeng Regency is dominated by traditional stilt house of South Sulawesi (Bugis-Makassar) (Fig. 11). It can be seen from the structure and construction of the houses which consists of:

- a. Roof Design (Top)

Top Benua or a triangular house head characterized by tropical buildings in the eastern part of Indonesia. Traditionally, the roof functioned as a place to store crops.
- b. Body Design (Middle)

Middle Benua or a rectangular house body that functions as a place to perform daily activities of the residents
- c. Basement Design (Bottom)

Bottom Benua or the house basement. It is described as the foot of the house and serves as a place to rest and socialize with neighbors.



Figure 11. The design of Bugis Makassar stilt house dominated the design of seaweed farmer's residence in Bantaeng Regency

3.3.2. Dimension

Generally, the width of the stilt house is $\pm 45m^2-90m^2$, with dimensions of type $\pm 5m \times 9m$, and type $\pm 10m \times 9m$. The type of space located on the stilt floor is a terrace that functions as a semi-public living room, bedroom, and kitchen. Service facilities such as laundry room and toilet are located outside of the stilt building. Multiple of building module (length between pole to pole) is 2 meters. The pole dimension is dominated by size of 25cm x 25cm. (Fig.12)



Figure 12. Illustration of stilt house poles

3.3.3. Building material

Building materials are any materials used for construction purposes. Many natural materials, such as clay, sand, wood and stones, even twigs and leaves have been used to build buildings. Aside from natural ingredients, artificial products are widely used and some of them are less synthetic. Manufacture of building materials is established in many countries and the use of such materials is usually divided into certain specialized trades, such as carpentry, piping, roofing and insulation work. These references relate to human habitation and structures including houses.

- a. Roof Material (Fig. 13)

Roofing material used in stilt house is dominated by zinc. Construction of trestle is made of wooden beams. While the ceiling material only use tarpaulin to reduce the heat effect from the zinc.



Figure 13 Materials in the roof

- b. Wall Material (Fig. 14)

The wall used in the stilt house is a combination of planks and plywood as partitions. While in the basement wall, some have used a brick in combination with plywood as a space divider.



Figure 14. Materials in the wall





- c. Floor and Basement Material (Fig. 15)






The stilt house basement has been built due to the increasing need for space. It is influenced by the growing number of residents of the house or the desire of residents to have a wider space such as kitchens and bedrooms.

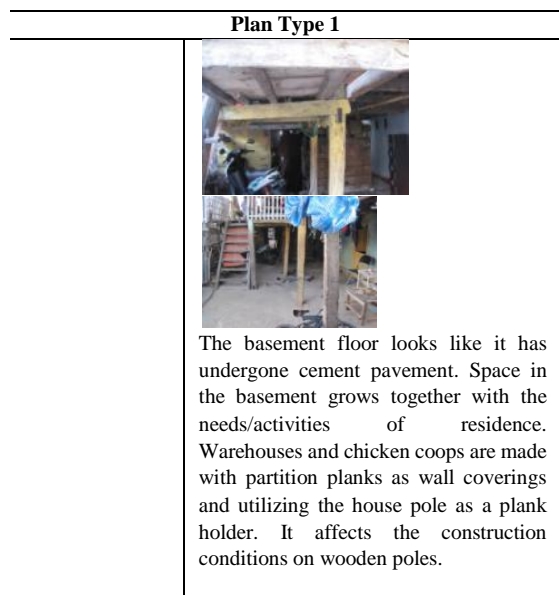


Figure 15. Materials in floor and basement

Table 3 Construction of residence reviewed from spatial organization and function

Plan Type 1	
Top (Roof)	<p>Storage Place</p>  <p>it can be seen the structure / construction of the roof of the house (trestle) used by the residents as a storage space of goods by adding another construction (wood) and attached it with straps on the trestle to sustain or to store goods. It is done without consideration of the roof construction safety.</p>
Middle (Stilt Floor)	<p>teracce/<i>lego-lego</i>, living room, bed room, family room, and warehouse.</p>  <p>Teracce/<i>lego-lego</i> is generally used for gathering or receiving guests, but almost all houses in this area utilize the terrace as a working area of seaweed farmers. Changes in the function of this space does not affect the building construction.</p>  <p>The main access to the residence (Only one access)</p>  <p>Living room is made but the furniture used in it is not too functioned.</p>

Plan Type 1	
	  <p>Family room is used for watching, sleeping, and receiving guests. The space is separated without a divider. However, it is safe in terms of building construction..</p>  <p>Wardrobe became the divider to create a new space behind the divider which is a warehouse. It can be at risk on the floor construction in accepting an unaccounted / considered load..</p>
Bottom (House Basement)	<p>The basement space in the house is built / functioned permanently (massive). The space consists of: bedroom, kitchen, cage/warehouse, vehicle parking place (motorcycle).</p>   <p>The kitchen is made in the basement and it can be accessed from above or bottom. There is no link between the construction of the stilt buildings with massive buildings so that massive buildings in the basement is growing without planning a circulation.</p>



3.3 Development Concept of Structure and Construction of Seaweed Farmer's in Bantaeng Regency

The design of seaweed farmer's residence in Bantaeng Regency is developed based on the society needs and activities. Residence development is conducted independently by the residents without basic knowledge of building security and safety. Based on the above analysis, development concept of the structure and construction of seaweed farmer's residence is proposed as follows (Fig. 16):

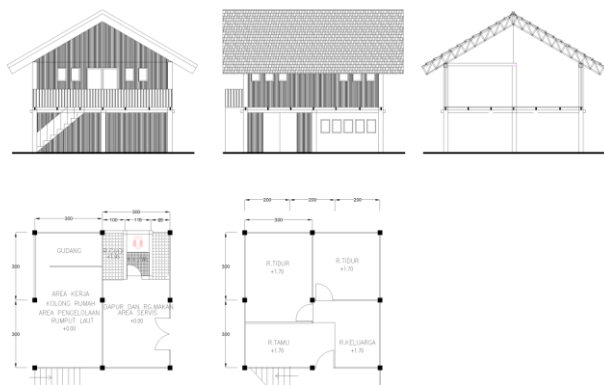


Figure 16. Illustration of development concept of structure and construction of seaweed farmer stilt house reviewed by spatial organization and function

4. Conclusion

There have been tendencies in seaweed farming residence that additional space is extended without structural and functional consideration in the residence and this unfavorable extension has influenced negatively on some seaweed farmer activities and quality of life. For improving such working and living situations, survey was made to measure the structure of seaweed farmers' stilt houses and to study spatial organization and building materials. Based on such collected data, analysis was made to improve the current problems, and the concept of structure and construction was proposed for a new type of seaweed farmer's house. It is hoped that the new concept of the structure and construction for seaweed farmer's stilt house with basement can improve both efficiency of the work and quality of farmer's life. Particularly, the addition of space with mezzanine concept to create a space on the roof may create a storage place of goods and mini warehouse.

References

- [1]. Wunas, dkk. 2014. *Prinsip-prinsip pengembangan lokasi perumahan produktif dan industri pengolahan rumput laut berbasis komunitas (kasus DAS Kabupaten Bantaeng)*. Unhas, penelitian hibah kompetensi.
- [2]. Venny Veronica Natalia, Wunas, Shirly. 2016. *Housing development: sign and symptoms in middle city of Indonesia*. ELSEVIER, *Procedia: Social and behavioral sciences*, 227(2016)278-285, akses *Science Direct*.
- [3]. Wunas, dkk, 2013. *Pengembangan sentra produksi rumput laut melalui dukungan jaringan transportasi di Kabupaten Bantaeng*, kerjasama Litbang perhubungan.
- [4]. Wunas, S. 2013. *Model perluasan bangunan swadaya sebagai pendukung fungsi hunian dan usaha berbasis ramah lingkungan*, dipresentasikan dalam seminar Nasional temu ilmiah IPLBI.
- [5]. Wunas, S. 2013. *Housing on waterfront landuse conflict in City of Kolaka*. On Seminar international architecture in urbanize maritime culture.
- [6]. Wunas, and Veronica. 2013. *Traditional sailing and local economic development in rural area of Sulawesi Island*. Seminar Internasional of FSTPT Solo.
- [7]. Wunas, S. 2008. *Pengembangan perumahan swadaya di wilayah pesisir Sulawesi Selatan (Kasus Kabupaten Takalar)*, kerjasama Kemenpera.
- [8]. Frick Heinz. 2006. *Seri Eko-Arsitektur 2, Arsitektur Ekologis, Konsep arsitektur ekologis di iklim tropis, penghijauan kota dan kota ekologis, serta energy terbarukan*. Kanisius Soegijapranata University Press.
- [9]. Isfa sastrawati. 2009. *Pengembangan rumah panggung swadaya tahan bencana melalui pemberdayaan masyarakat di kawasan pesisir sulawesi selatan*. Penelitian hibah kompetitif penelitian sesuai prioritas nasional (Hibah Penelitian Strategis Nasional).
- [10]. Turner, J.F.C. 1976. *Housing By People, Towards autonomy in buiding environments*, Marion Boyars London.
- [11]. Van Lengen Johan, The Barefoot Architect. *A Handbook for Green Building*. Shelter Publications. Bolinas, California. USA.

The Effect of Air Distribution System towards Indoor Air Quality (Case Study: Auditorium of Phinisi Tower)

Yetti Yuniati Ishak,^{a*} Baharuddin Hamzah,^b Rosady Mulyadi,^c

^aDepartment of Architecture, Engineering Faculty, Hasanuddin University. Email: yettiyuniati@gmail.com

^bDepartment of Architecture, Engineering Faculty, Hasanuddin University. Email: baharsyah@unhas.ac.id

^cDepartment of Architecture, Engineering Faculty, Hasanuddin University. Email: rosadyd51rm@gmail.com

Abstract

This research aims to analyze the type of air distribution system in auditorium, the effect on air quality in the room, as well as the design of appropriate air distribution systems for the auditorium to improve air quality. This study used quantitative methods, by measuring the CO₂ gas concentration, air temperature and humidity in room, using the HT-2000 data logger. The measurements were conducted when the room is empty and when the room is occupied. After that, the analysis and simulation were done by using ANSYS-Fluent software. Displacement ventilation distribution system was designed by calculating the total amount of cooling load, the required air flow rate, the air supply temperature, and the return air temperature. The analysis result showed that the mixing ventilation distribution system in the auditorium could not resolve air quality in the room. Based on that results when the room is inhabited, it was known that the lowest and highest value for CO₂ concentration level was 973 ppm and 1993 ppm; for air temperature of 20.5°C and 28.6°C; while the room air humidity of 49% and 71%. The displacement ventilation distribution system was designed to overcome the air quality problem in the chamber by air temperature setting was 24°C, the air supply velocity coming from the diffuser was 0.25 m/s, the total surface area of the diffuser was 20.7 m², and the flow pattern of moving air from the bottom to top of the room.

Keywords: Ansys Fluent, carbondioxide, displacement ventilation, mixing ventilation

1. Introduction

Auditorium is one of the rooms in Phinisi Tower, Makassar City. This room can accommodate up to 472 visitors. The intensity of the auditorium usage is quite high, therefore, the comfortableness factor of auditorium users is one of the important things to be noted. The condition of this room with no less visitors, got the auditorium in air pollution problems. Carbondioxide (CO₂) gas accumulation can occur as a result of the visitors respiration's process when the activity takes place in the room. Hence, the auditorium requires special treat in order to obtain a good air quality. Because unlike the other rooms, opening windows for fresh air intake can't be able to get. In addition, air quality is also closely related to the health of users / visitors.

Sufficient air quality in the auditorium can actually be obtained through a good air distribution system within a large area, especially in the visitor area, to reduce the of pollutants in the form of CO₂ gas.

Therefore, research on the air distribution system and its effect on air quality levels in the auditorium, it is important to be held. This is done in order to obtain a solution in the form of design of air distribution system in the appropriate space for auditorium. The design of air distribution system is expected to be able to supply a fresh air with a comfortable level of air flow, while reducing or avoiding CO₂ gas, especially in the area of the audiences. The design of the air distribution system is also ultimately expected to be an input to the future auditorium development plan.

This research on thermal comfort analysis and indoor air quality (IAQ) in theater space using mechanical ventilation, has also been done by Kavgic M., et al. [1]. The objectives of the study were to analyze indoor air quality levels and thermal comfort in the theater, and to identify improvements that could be made. The parameter indicators in this study are Predicted Mean Vote (PMV) Index, Percentage People of Dissatisfied (PPD) Index, Draft Rrate Index, Mean Age of Air (AGE) and Ventilation Effectiveness (Ev). Based on the results of monitoring and evaluation, most of the environmental parameters within the theatrical building under study are within the thermal

*Corresponding author. Tel.: +62-813-402-00293

*Sipil Raya Ruko No. 11 Antang
Makassar, Indonesia, 90235*

comfort and IAQ standards. However, there are some things that need attention such as: the energy consumption for large circulation, therefore the operation of CO₂ control system for ventilation system can be mixed in the existing system.

The research on distribution systems utilizing mechanical ventilation and its effect on thermal amenities, has been done by Fong, M.L., et al. [2]. The purpose of this study is to determine the model of ventilation design that is able to create a neutral temperature and can achieve thermal comfort with optimal energy efficiency. The dependent variable found on this research is thermal comfort in the classroom, while the independent variable is a model of ventilation design. Parameter indicators in this study are Predicted Mean Vote (PMV) Index, relative humidity (RH), temperature, and air change per hour (ACH). The results of this study indicated that for a classroom with a capacity of 42 people, Stratum ventilation can provide satisfactory results at the thermal comfort level with the highest energy savings compared to other types of mechanical ventilation. After that was displacement ventilation and the last was mixing ventilation.

2. Research objectives

- To analyze the type of air distribution system contained in the auditorium of the Phinisi Tower.
- To evaluate the effect of the air distribution system in the auditorium towards the air quality level in the room.
- To design air distribution system in auditorium which can provide air flow in a comfortable space while simultaneously reducing/avoiding the buildup of indoor CO₂ gas especially in audience area.

3. Research method

3.1. Location and time of study

The research location was located in the auditorium, precisely on the 3rd and 4th floors of Phinisi Tower, Universitas Negeri Makassar, located in Jalan Andi Pangeran Pettarani, Makassar City. The time of research from collecting to data processing were done for 3 months, started from September to November 2017.

3.2. Data source

Indoor Air Quality (IAQ) is the condition of indoor air content that can affect occupant health and comfort [3]. According to ASHRAE the maximum limit of indoor CO₂ gas should not pass 1,000 ppm to achieve comfortable room state [4].

In general, air distribution system is divided into 2 types, namely: (1) Mixing Ventilation; an air distribution system where fresh air is supplied in such a way that the entire air volume in the chamber is fully mixed [5]; and (2) Displacement Ventilation; an air distribution system by

supplying fresh air into the room at low speed and also usually at low altitudes [5].

According to SNI 03-6572-2001 [6], to maintain comfortable conditions, the air velocity that falls on the head should not be greater than 0.25 m/s and preferably less than 0.15 m/s.

In addition to secondary data in the form of information derived from various literatures, primary data collection is also obtained from the results of direct measurement at the study sites, including:

- Auditorium room dimension, as well as stage placement and audience seats.
- Airflow rate
- Air temperature
- Humidity
- Level of concentration of CO₂ gas

3.3. Research design

The method used in this research is quantitative research method. On its application, research is done through several stages. The first stage is the dimension of the auditorium room dimension including: dimension as well as the placement of the stage and audience seats, the number and the inlet placement, the outlet and the point of light, and the measurement of temperature and movement of air originating directly from the source, from inlet and outlet.

The second stage, is a measurement of CO₂ gas concentration level, air temperature and humidity when the room is empty, without any activity taking place in it. At this stage the measurements were made at six predetermined sets of times, (1) when the HVAC element such as the inlet, outlet and the lamp is not turned on at all; and (2) after the inlet, the outlet and the lights were turned on and the room had been idle for ± 1 hour. This was done to determine the level of air quality when the auditorium is empty, before and after the inlet, outlet and room lights are turned on.

The third stage, is a measurement of CO₂ gas concentration level, air temperature and humidity when the activity takes place in the auditorium at six predetermined points. Due to the limited number of equipment available, the data collection is done 2 times in 2 different activities. In the first activity, the measurements of CO₂, air temperature and humidity concentration levels were performed at 3 point measurements in 3 groups of audience seats located in the front row (point A, B, and C). Furthermore, in the second activity, the measurements of CO₂, air temperature and humidity concentration levels were performed at 3 point measurements in 3 groups of audience seats located in the back row (D, E, and F measurements).

After the measurement done, next step is to make the simulation based on the data of the primary data collection that had been done. Simulation using mixing ventilation method that is suitable with existing auditorium condition.

After that, design the distribution system of displacement ventilation through calculation and simulate the result of the calculation.

The process of data analysis was done by analyzing the measurement result of the existing distribution system (mixing ventilation) with the result of displacement ventilation design and the standard used.

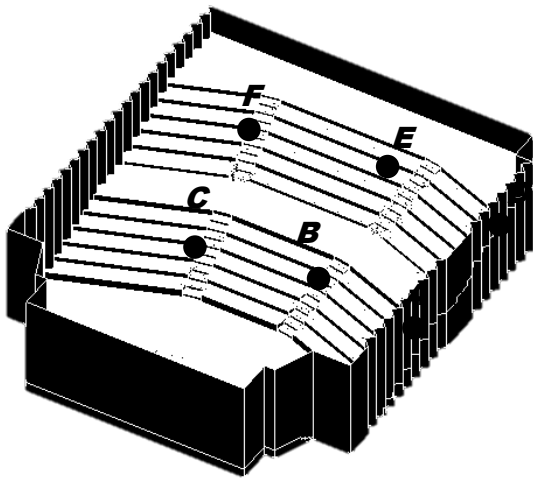


Figure 1. Position of measurement points in auditorium

4. Data analysis method

Analysis of data used was correlational analysis which was trying to find a relationship or influence between several variables.

- To determine the type of air distribution system used in the auditorium, the analysis process is carried out by comparing the measurements of the CO₂ gas concentration level, air temperature and humidity when the room is empty, without occupants and no activity taking place in it. The measurements made before and after the inlet, the outlet and the light were turned on; then summarized, analyzed and compared with the characteristics of mixing ventilation distribution system.
- To know the level of air quality in the auditorium, measurements of CO₂ gas concentration, air temperature and humidity level during the auditorium activity. The results of these measurements were then summarized and analyzed and then compared with the standards, so it was known whether the current air distribution system can meet the air quality required by visitors within the auditorium.
- To obtain the design of the displacement ventilation distribution system, calculations were made to the total amount of cooling loads, the required air flow rate, the air supply temperature, and the air-return temperature. The results of these calculations are then analyzed to obtain the dimensions, number of diffuser points, and room temperature required and in accordance with the standards of comfort.

5. Research result

5.1. The analyze of air distribution system used in the auditorium

Identification of air distribution system was done by measuring CO₂, air temperature and humidity in twice, namely: (1) when inlet, outlet and lamps were not turned on; and (2) the inlet, the outlet and the lights were turned on, then the room was silenced for 1 hour.

The results of data collection at this stage can be seen as the following table.

Table 1. The measurement's result of CO₂ gas concentration level, air temperature and humidity in auditorium, before and after the inlet, the outlet and the light were turned on

Measurement points	CO ₂ Concentration level (ppm)		Temperature (°C)		Humidity (%)	
	Before	After	Before	After	Before	After
A	537	461	31.1	26.7	64.0	63.0
B	551	463	32.0	26.7	64.0	63.0
C	573	459	30.7	27.3	63.9	63.0
D	509	462	31.9	27.4	64.3	63.3
E	508	460	31.8	27.4	64.3	63.2
F	513	463	31.6	26.7	64.2	63.0
Range	65	4	1.3	0.7	0.4	0.3

From the table above, it can be seen that when the HVAC element especially diffuser and exhaust has not been turned on, the value of CO₂, air temperature, and humidity contained in the six measuring points tend to vary greatly. This can be seen from the range of values that occur between the maximum value and the minimum value with the condition of the same room. For indoor CO₂, the value range reaches 65 points; for indoor air temperature reached 1.3 points; while for air humidity reaches 0.4 points.

Conversely, after the HVAC elements, especially the diffuser and the exhaust were turned on, the variation of that value becomes smaller. CO₂, temperature and humidity levels tend to be evenly distributed at each measuring point in the auditorium.

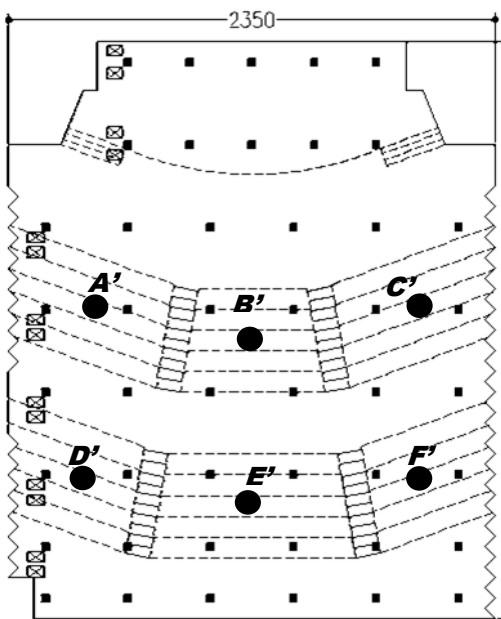
In addition to the above measurements, data retrieval of temperature and air velocity originating from the air supply source (supply air) and also at the point of exit of air from the room (return air), also done. This data will be input when performing computerized simulations.

The measurements made on the inlet and outlet contained in the auditorium are: for inlet, the temperature and velocity of the airflow contained at that point is 20°C and 2.7m/s; while for the outlet, the temperature and velocity of the airflow at that point are 22°C and 1.6m/s. The temperature and velocity of the airflow were considered constant at all inlet and outlet points, since the ventilation system used is a mechanical.

5.2. Air quality level in auditorium

To determine the level of air quality during the activity in the auditorium, measurements of CO₂ levels, temperature and humidity of the room in the six-point group of audience seats in the auditorium. However, due to the limited equipment, the data collection was done in 2 different activities.

The first activity was held on the first Sunday of November, 2017. The number of visitors during the activity took place around 370 people (filled space ± 80%). The activity lasted for 2.5 hours from 09.30 WITA until 12.00 WITA. The data were collected at 3 points of measurement for the group of chairs located at the front of the room, at points A', B', and C'. Recording of the measurement results was done every 5 minutes during the activity.



Keterangan :
 ● Measurement points
 ⊗ Outlet/Exhaust points
 ■ Inlet/Diffuser points

Figure 2. Position of measurement points, inlet points and outlet points during the activity took place in auditorium

The second activity was held on the second Sunday of November, 2017. The number of visitors in this activity is about 280 people (the room is filled ± 60%). The activity lasted for 3 hours from 09.20 WITA until 12.20 WITA. There was a break time in the middle of the activity that is at 9:50 am until 10:15 am, where visitors were directed out of the room to take a break and enjoy a snack. The data were collected at 3 point measurements for the group of chairs located at the back of the room, at point D', E', and F'. Recording of the measurement results was done every 5 minutes during the activity.

5.2.1. Analysis of the results of CO₂ gas concentration level measurements during activities in the auditorium

The following two figures (Figs. 3 and 4) show that average levels of CO₂ are above the threshold permitted by ASHRAE.

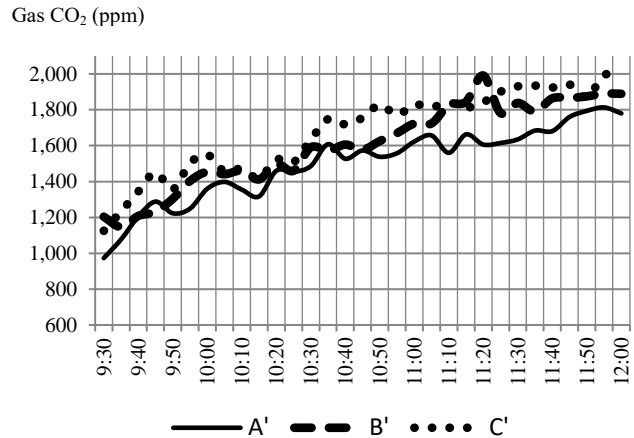


Figure 3. The measurement result of CO₂ gas concentration level at points A', B' dan C' during the first activity took place in auditorium

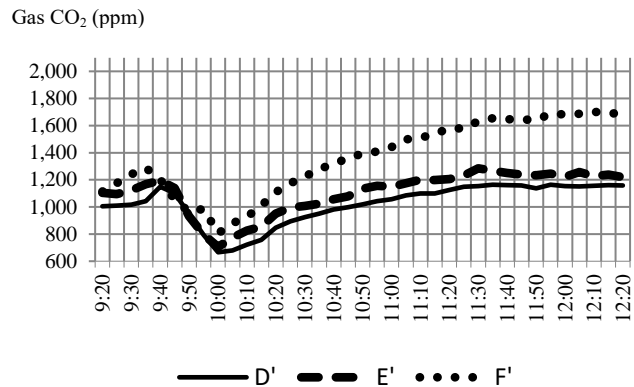


Figure 4. The measurement result of CO₂ gas concentration level at points D', E' dan F' during the second activity took place in auditorium

The maximum value of CO₂ in a room should not exceed 1000ppm in order to get a good quality air. However, if the results of the six points measurements were compared, it will be seen that at the measuring point A' and the mean D' point have a concentration level of CO₂ gas below the point B' and the measuring point E'. The concentration level of CO₂ gas at point B' and point E' is below the measuring point C' and point F'. The difference that occurs can be caused by the position of the measuring point to the location of the exhaust that was only found on one side of the room (Fig. 2). In first activity and for the bench group located in the front, the measuring point A' which was closest to the exhaust, has a concentration level CO₂ gas is the lowest compared to 2 other measuring points; after that followed by point B' which is in the center of the room; and point C' which is farthest from the exhaust position, has the highest level of CO₂ concentration. Similarly to activity II, for the bench group located at the

back. The measurement point D' which is closest to the exhaust, has the lowest concentration of CO₂ gas than the other 2 points; after that followed by point E' which is in the center of the room; and point F' which is farthest away from the exhaust position, has the highest level of CO₂ concentration.

Table 2. The measurement result of CO₂ gas concentration level during activities in auditorium

Measurement points	CO ₂ CONCENTRATION (PPM)				Mean
	Min	Time	Max	Time	
ACTIVITY I					
A'	973	9.30 am	1813	11.55 am	1501
B'	1147	9.35 am	1991	11.20 am	1605
C'	1125	9.30 am	1993	11.55 am	1678
ACTIVITY II					
D'	848	10.20 am	1164	11.55 am	1075
E'	951	10.20 am	1285	11.30 am	1164
F'	1054	9.45 am	1702	12.10 am	1447

There are many things that can affect the level of CO₂ concentration in the room, such as the number of visitors who are around the measuring point. At the time of activity, visitors are free to choose their own seats in the auditorium, so that the spread of visitors in the auditorium is uneven. In addition, visitor activity also influences the variation of CO₂ gas concentration value at each measuring point. Visitor activity as long as the activities within the auditorium are quite diverse; there are visitors who just sit quietly and silently, there are busy talking with a group of other friends, sometimes there are also visitors who come out of the room, some are back again but some are not. Auditor doors are sometimes open and close because the activities of visitors who come out and enter the room also affect the level of CO₂ concentration in the room. The CO₂ gas concentration value will drop in several points when the door of the room is open, and will go back up when the door of the room is closed. It is shown in Fig. 3. But in general it can be concluded that: (1) the longer the activity is running, the CO₂ gas concentration level in the auditorium will also be higher; (2) other than that the seat position against the exhaust also determine the value of CO₂ gas concentration. The further away the seat from the exhaust the higher the CO₂ gas concentration in that place. Compared to the exhaust, the inlet / diffuser in the auditorium did not appear to have a significant effect on the variation in the value of the measurement results. This is because the number of diffuser / inlet placed on the ceiling is quite large (there are 46 point diffuser / inlet) and located spread in the room.

Temperature (°C)

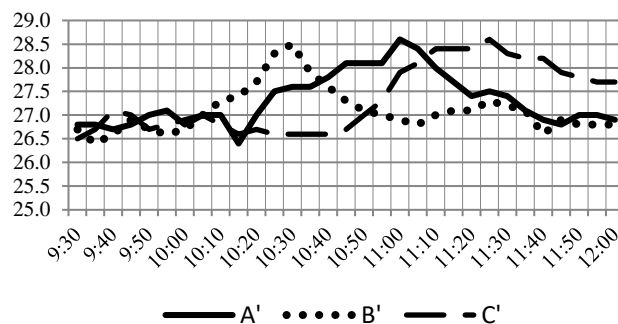


Figure 5. The measurement result of air temperature at points A', B' dan C' during the first activity took place in auditorium

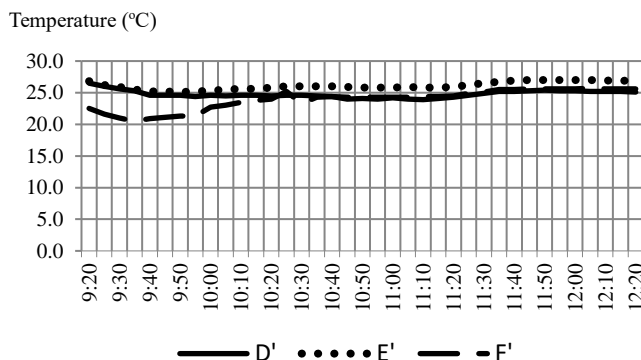


Figure 6. The measurement result of air temperature at points D', E' dan F' during the second activity took place in auditorium

5.2.2. Analysis of the results of temperature measurements during activities in the auditorium

As shown in Table 1, when the room is empty but the diffuser/inlet, exhaust and lights are turned on in the room; then the temperature will be uniformly mixed in the room with a variation of the value of 0.7°C (less than 1°C) in the six measuring points. But at the time of the activity in the auditorium, there are many things that can affect the value of the temperature in the room.

In the first event, the event that took place in the auditorium was the opening ceremony of "Gebyar Aktivitas Fisika" held by students of the Faculty of Mathematics and Natural Sciences UNM. The event took place quite attractively, in the form of dances, choirs, parodies and poetry readings. It was very different when the second activity took place inside the hall. This second activity was an international seminar held by the Language Center. The event took place quietly and seriously. Activities are quite attractive take place only at the opening ceremony that was at the beginning of the activity. After the opening ceremony, the room was vacated briefly from 9:50 am to 10:15 am, where visitors were directed outdoors to enjoy snacks and take a break. After that the seminar activity continued with the activity of the audience more quiet and serious than at the first activity took place. This is what influences the variation of the temperature value in the first

activity, which is very different from the measurement result in the second activity

Table 3. The measurement result of air temperature during activities in auditorium

Measurement points	Temperature (°C)				Mean
	Min	Time	Max	Time	
Activity I					
A'	26.4	10.15 am	28.6	11.00 am	27.3
B'	26.4	9.35 am	28.5	10.30 am	27.1
C'	26.5	9.30 am	28.6	11.25 am	27.3
Activity II					
D'	23.9	11.10 am	26.5	9.20 am	24.8
E'	25.2	9.40-9.45 am	27.0	11.45-12.05 am	26.2
F'	20.5	9.35 am	25.7	12.05 am	24.2

In addition to visitor activity, the total visitors are also affected the value of temperature. This is proven in the results of temperature measurements taken during the second activity. At the beginning of the event, at the measuring point F', the audience seats around the measuring point tend to be empty. This causes the lowest temperature level to be at point F' and occurs at the beginning of the activity (Table 3). After the re-activity took place inside the auditorium at 10.15 am, the D' and F' group chairs only drew the first and second rows of the group of occupied seats. Another case was in the seat group E', where the seat visitors almost full. This causes the temperature value at the measured point E' to be higher than the value of temperature at point D' and the measuring point F'. Unlike the case of the first activity. The density of the audience is almost the same in the three groups of seats. So even if there is a variation in the temperature value during the activity (Fig. 5), but if it is averaged, it will be known that the temperature values of the three measuring points (A', B', and C') are almost identical. This can be seen in the average value of room temperature measurements contained in Table 3.

5.2.3. Analysis of the results of humidity measurements during activities in the auditorium

From the following two figures, we can see that at point A' and point D', which is closest to the exhaust, has a constant humidity value compared to other points. The humidity levels at both points are also on average higher than other measuring points (Table 4). This shows that the role of exhaust in determining the humidity value at one particular measuring point is quite high. The closer to the exhaust the moisture value in the position tends to be more constant and higher. In contrast to the inlet, because of the number and position that spread evenly in the room, the effect on the humidity value is not very noticeable.

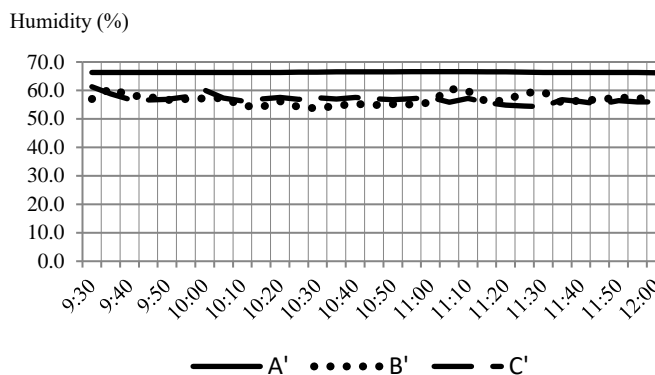


Figure 7. The measurement result of air humidity at points A', B' dan C' during the first activity took place in auditorium

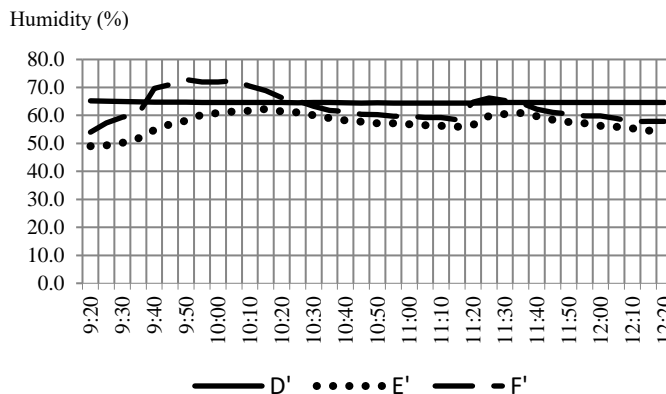


Figure 8. The measurement result of air humidity at points D', E' dan F' during the second activity took place in auditorium

In addition to the position toward the exhaust that is enough to determine the humidity level at a point of measurement, the number of visitors around the measuring point also contributes considerable influence. This can be seen in the result of measurement of humidity level at F' measurement point which is done on activity II. Before the break, the number of visitors seated in the F' seat group tends to be empty and the humidity level at that point is quite high. But after the break, the audience seats in the group filled up to 2 front row seats. This results in reduced moisture levels to 58.5%. The value variations occurs, can be caused by the mobility of visitors in the group of chairs.

Table 4. The measurement result of air humidity during activities in auditorium

Measurement points	Humidity (%)				Mean
	Min	Time	Max	Time	
Activity I					
A'	66.2	12.00 am	66.6	10.55-11.10 am	66.4
B'	53.7	10.30 am	60.7	9.35 am	56.7
C'	54.3	11.30 am	61.3	9.30 am	56.9
Activity II					
D'	64.4	10.45-11.20 am	65.2	9.20 am	64.6
E'	49.0	9.20 am	61.4	10.20 am	56.7
F'	54.0	9.20 am	71.0	9.45 am	61.4

5.2.4. The simulation results of the existing auditorium condition (mixing ventilation)

As previously described, the working principle of mixing ventilation is to supply air into the room at a sufficiently high speed, so that the air contained in the room can be mixed, so that air temperature and humidity tend to be the same in every corner of the room, and the buildup pollutants at a certain point can be avoided.

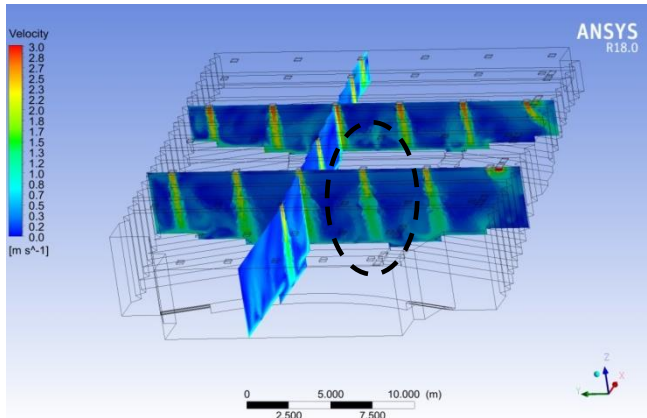


Figure 9. Simulation result of air velocity in auditorium

The same is also shown in the simulation of the existing conditions performed. As shown in Fig. 9, the air coming out of the diffuser (marked with dark circles), is supplied at a fairly high velocity, inducing the already existing air in the room resulting in a mixture of air.

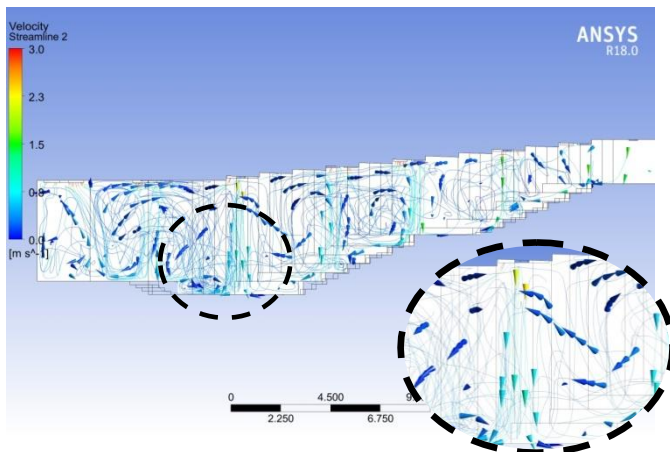


Figure 10. Hasil simulasi pola aliran udara dalam a auditorium

In the figure above, show the pattern of airflow that moves in all directions. This is in accordance with the working principle of mixing ventilation which aims to mix all air contained in the room. In the same picture is also seen air moving down from the diffuser with high speed. It is marked with a yellowish-colored arrow and pointed down (see the black circle in Fig. 10).

5.3. Design of Displacement Ventilation Distribution System

The following design procedures for displacement ventilation are based on ASHRAE's research on the 949 project by Chen, Glicksman, Yuan, Hu and Yang in 1999 and on the scheme of procedures made by Chen and Glicksman in 2003 (Price Engineer's HVAC Handbook, 2016).

As is known, the auditorium has a capacity of 472 people with power generated by the occupants assumed at 75 watts per person. The expected temperature in the auditorium in accordance with SNI 6390: 2011 standard is 24°C. The auditorium floor area is 612.5m² and the volume of the room is 2,189,7m³. The auditorium utilizes 2 LCD projector units with assumed power of 60 Watts per unit, while for laptops it is assumed to be 40 Watt. For lighting, the power used is assumed to be 25 W/m². Heat and density in the auditorium is assumed to be 1,007 kJ / (kgK) and 1.2 kg/m³.

- Step 1: Determine the total amount of cooling load.

$$\begin{aligned}
 q_t &= q_{oe} + q_l + q_{ex} \\
 q_{oe} &= (472 \times 75 \text{ W}) + 2 (60) \text{ W} + 40 \text{ W} \\
 &= 35.560 \text{ W.} \\
 q_l &= 25 \text{ W/m}^2 \times 612,5 \text{ m}^2 = 15.312,5 \text{ W.} \\
 q_{ex} &= 0 \text{ W} \\
 q_t &= 50.872,5 \text{ W.}
 \end{aligned}
 \tag{1}$$

Total cooling load for the auditorium is 50,872.5 Watt.

- Step 2: Determine the airflow rate in the auditorium

$$\begin{aligned}
 Q_{DV} &= \frac{0.295 q_{oe} + 0.132 q_l + 0.185 q_{ex}}{\rho c_p \Delta t_{hf}} \\
 Q_{DV} &= \frac{0.295 (35.560) + 0.132 (15.312,5) + 0}{(1,2) (1,007) (2)} \\
 &= 5.176,87 \text{ L/s}
 \end{aligned}
 \tag{2}$$

- Step 3: Determine the rate of fresh air flow in the auditorium

$$\begin{aligned}
 Q_{oz} &= \frac{R_p P_z + R_a A_z}{E_z} \\
 Q_{oz} &= \frac{2,5 (472) + 0,3 (612,5)}{1,2} \\
 Q_{oz} &= 1.136,45 \text{ L/s}
 \end{aligned}
 \tag{3}$$

The total volume of air supply is the maximum value between Q_{DV} and Q_{oz}.

$$Q_s = \max [Q_{DV} , Q_{oz}] = 5.176,87 \text{ L/s}$$

- Step 4: Determine the temperature of the air supply

$$t_s = t_{sp} - \Delta t_{hf} - \frac{A_z q_t}{2,456 Q_s^2 + 1,08 A Q_s} \quad (4)$$

$$t_s = 24 - 2 - \frac{612,5 (50872,5)}{0,584 (5176,87)^2 + 1,208 (612,5) (5176,87)}$$

$$t_s = 20,4 \text{ } ^\circ\text{C}$$

- Step 5: Determine the air temperature back

$$t_e = t_s + \frac{q_t}{1,208 (Q_s)} \quad (5)$$

$$t_e = 20,4 + \frac{50,872,5}{1,208 (5.176,87)}$$

$$t_e = 28,5 \text{ } ^\circ\text{C}$$

If a fresh air velocity corresponding to the comfort standard is 0.25 m/s, then for an air supply volume of 5176.87 L/s, it is necessary to have a diffuser with a surface area of 20.7 m² (1 L equivalent to 0.001 m³).

The selected diffuser type is a wall mounted diffuser because of its embedded position on the lower wall. This diffuser will not block the viewer's view of the stage, and is also freely placed anywhere; be it on the stage area or on the storied audience area.

With a surface dimension of 0.3 m x 0.6 m, the surface area for one diffuser unit is 0.18 m². Means the number of diffuser required is 115 units.

6. Conclusions

- Based on the analysis of the measurements taken when the room is empty, without visitors and without any activity in the room, we can know that the air distribution system in the auditorium is mixing ventilation, with the following considerations: (1) diffuser and exhaust placement which is at the top of the room; (2) air is supplied at high speed, ie 2.7 m/s; and (3) when the diffuser or exhaust is turned on, the level of CO₂, air temperature and humidity in the room become uniformly tended at every measured point.
- The effect of the air distribution system present in the auditorium on the indoor air quality level is not good enough. Mixing ventilation proved inadequate to overcome air quality problems within the auditorium. The concentration of CO₂ gas during the activity can reach 1993 ppm, well above the maximum threshold set by ASHRAE, which is 1000 ppm. Air quality is closely related to the health and comfort of visitors. High levels of CO₂ gas concentration can adversely affect visitors' health and comfort. This shows that the selection of the type of air distribution system used in the auditorium, has a considerable influence on the air quality level contained in the space.

- Air distribution system in the auditorium can provide air flow in a comfortable space and simultaneously avoiding the buildup of CO₂ gas is a displacement ventilation system, with an indoor air temperature setting of 24°C, the air supply velocity coming from the diffuser is 0.25 m/s, the total surface area of the diffuser is 20.7 m², and the airflow pattern is likely to move upwards.

Based on the results of this research, it is recommended: (1) Utilizing the detector level CO₂ gas concentration especially for the closed room. This is done to determine the level of indoor air quality so that action can be taken if the level of air quality in the room has passed the maximum threshold set by ASHRAE, which is 1000 ppm; (2) Reorganize the number and placement of the exhaust contained in the auditorium. This needs to be done to obtain better air quality for audience within the auditorium. Based on the results of the measurements taken during the activities in the auditorium, there was a significant influence between the number and the placement of exhaust on air quality in space. It can also be a concern as well as material for further research; (3) There needs to be coordination between the auditorium management and the event committee on the duration of activities that can take place in the auditorium. Based on the results of research that has been done, it is known that there is a considerable influence between the duration of activities that take place on air quality in space. The longer the activity takes place in the auditorium, the level of CO₂ gas concentration also increased. Hence, it is consider that a break time is needed. This is useful in addition to visitors to be able to break, also for air quality in the room. Diffuser and exhaust can work to remove the heat and pollutant to the maximum when the room is emptied, so that air quality can be back to normal when the activity resumed.

References

- [1] Kavgić M., Mumović D., Stevanović Z., Young A. (2007), Analysis of Thermal Comfort and Indoor Air Quality In A Mechanically Ventilated Theatre.
- [2] Fong M. L., Lin Z.; Fong K. F., Chow T. T., Yao T. (2010). Evaluation of thermal comfort conditions in a classroom with three ventilation methods, Hongkong, City University of Hongkong.
- [3] Satwiko, Prasasto(2009), Fisika Bangunan , Yogyakarta
- [4] ASHRAE, (2002), Indoor Air Quality : A Guide to Understanding ASHRAE Standard 62-2001.
- [5] Price Engineer's HVAC Handbook (2016), Engineering Guide Displacement Ventilation.
- [6] SNI 03-6572-2001, Tata Cara Perancangan Sistem Ventilasi dan Pengkondisian Udara pada Bangunan Gedung.

Deformation Analysis of Self-Expanding Stent Considering Plaque and a New Expanding Mechanism

Katsuhiko Sasaki,^{a*} Yukiko Tomooka,^b Ryo Takeda,^c Achmad Syaifudin^d

^aDepartment of Mechanical Engineering, Faculty of Engineering, Hokkaido University. Email: katsu@eng.hokudai.ac.jp

^bDepartment of Mechanical Engineering, Faculty of Engineering, Hokkaido University. Email: yukikotomooka@frontier.hokudai.ac.jp

^cDepartment of Mechanical Engineering, Faculty of Engineering, Hokkaido University. Email: r.takeda@eng.hokudai.ac.jp

^dDepartment of Mechanical Engineering, Institut Teknologi Sepuluh Nopember. Email: saifudin@me.its.ac.id

Abstract

In this research, effects of material properties of stent materials, such as nitinol and ferrous alloy, on a self-expanding stent are studied by the stent deployment simulations using finite element method (FEM). Stent, vessel, and plaque are modeled by using AutoCAD. The model is imported to a finite element analysis software Ansys 15.0 and the deployment analysis of the stent is carried out. In addition, two methods of the unsheathing of the self-expanding stent are studied: (1) a conventional method where a stent comes out from one end of the sheath and (2) a new method in which a stent comes out from the center of the sheath. Also, both the area stenosis ratio and Dog-Boning are discussed referring the simulations conducted in the paper.

Keywords: FEM; nonlinear deformation; plague; SMA; stent

1. Introduction

Recently, the number of deaths caused by the blood vessel related disease, such as heart diseases, is increasing in Japan. Atherosclerosis is one of the most serious and common form of vascular diseases [1]. A vascular stent is a small mesh tube used to open narrow or blocked arteries and restore blood flow. Stents are classified two types: one of them is a balloon-expanding stent and the other a self-expanding stent. The balloon-expanding stent uses the plastic deformation of the stent material caused by the balloon expansion, while the self-expanding stent uses the super-elastic deformation of the stent material such as the shape memory alloy. The self-expanding stents have an advantage to be able to recover even after complete flattening or radial crushing due to the pseudo-elasticity of shape-memory alloy (SMA). Thus, the self-expanding stents are suitable for superficial locations, such as the carotid and femoral arteries. On the other hand, the self-expanding stents represent the lower radial expansion force and are largely affected by the recoil force of artery than the balloon-expanding stents [2, 3].

As for the balloon-expanding stents, there are some studies indicating that the balloon expanding stents use the high strength material which gives important advantages to them. For example, the cobalt-based alloy, which has the higher strength than stainless steels, allows thinner struts to maintain the radial strength [4]. The thin-strut stents tend to have the smaller radius than the thick-strut stents, therefore the high strength material makes it easier to reach distally [4]. In addition, recent clinical reports suggest that strut thinness may affect the restenosis rates [5-7]. Kastrati and Pache et.al demonstrated that the implantation of the thin-strut stents is associated with a significant reduction of the risk for restenosis compared with the thick-strut stents implantation [6, 7].

So far, Ni-Ti alloy has been widely used for the self-expanding stent materials. Recently, a high strength ferrous polycrystalline shape-memory alloys (SMA), which have superelastic strain range of more than 13%, have been developed [8]. However, the effects of these advanced materials, which have the higher strength and the extremely high superelasticity, on both the stent functions and stenting have not been verified yet. Finite element method (FEM) has an advantage to investigate the mechanical behavior of stenting. Since inappropriate stenting (e.g., overexpansion and insufficient expansion) results in the undesirable clinical events such as neointimal hyperplasia, restenosis,

*Corresponding author. Tel.: +81-(0)11-706-6414
Kita 13, Nishi 8, Kita-ku
Sapporo, Hokkaido, Japan, 060-8628

thrombosis, and so on, it is important to understand the mechanical behavior of the stenting [9]. There have been some FEM analyses simulating the self-expanding stent placement into stenosed artery [10, 11].

Delivery systems for the self-expanding stents consist of a series of sheaths, catheters and guidewires. The self-expanding stents are manufactured in the expanded shape and then compressed and restrained in a delivery system [12]. Haller et al. suggested the importance of delivery technique in determining vessel wall apposition of the Enterprise self-expanding intracranial stent [13]. However, few analyses concerning the effect of delivery systems, especially unsheathing methods, of self-expanding stents on stent deployments have been conducted.

In this paper, the effect of material properties of the stent materials (i.e., nitinol and ferrous alloy) on the stenting was studied by stent deployment simulations using FEM. Stent, vessel, and plaque were modeled by using AutoCAD. The model was imported to a finite element analysis software Ansys 15.0. In addition, two methods of the unsheathing were studied: (1) the conventional method where a stent comes out from one end of the sheath and (2) a new method in which a stent comes out from the center of the sheath.

2. Analysis Method

2.1. Stent Geometry, FEM Model, and Delivery System

In this analysis, simulations of the self-expanding stent implantation to carotid artery with concentric plaque were carried out. Two kinds of stent materials and delivery systems were considered and the outcomes of the stent deployment were compared.

A stent, outer sheath, plaque and artery models were built by using AutoCAD and Inventor. Figure 1 shows the stent geometry used for this analysis. The stent model was generated as expanded state referring to the Palmaz stent released by Johnson and Johnson. The 3D stent model was generated by the following steps:

- 1) 2D geometry of the expanded state of stent was drawn by using AutoCAD.
 - 2) 2D stent geometry was embossed to a cylinder and the cylinder was subtracted afterwards by using Inventor.
- FEM models used for this analysis are shown in Fig. 2.

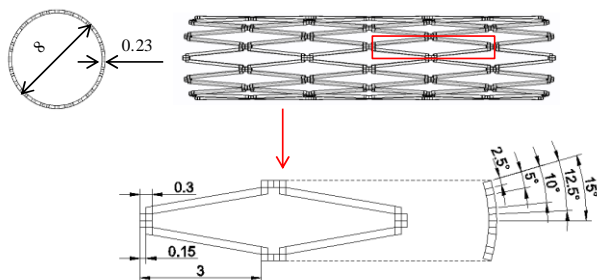


Figure 1. Stent geometry.

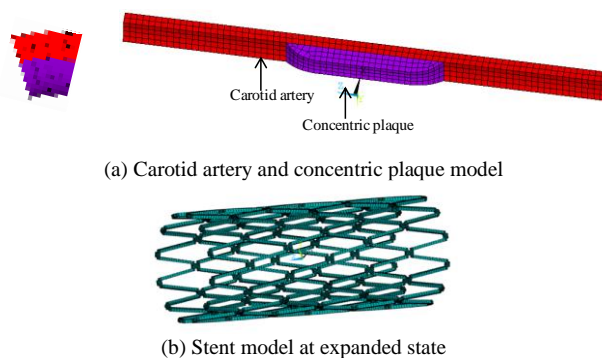


Figure 2. FEM model

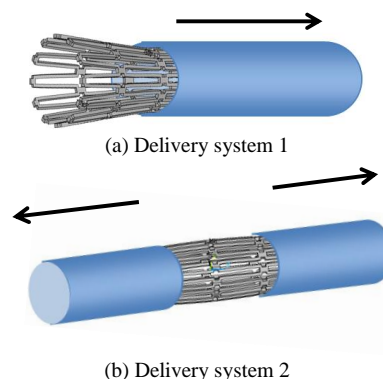


Figure 3. FEM model

In this analysis, the plaque distribution was assumed to be concentric. Thus, the thickness of the plaque is constant in the circumferential direction. The plaque thickness is 1mm at the thickest part and the length 9.8mm, respectively. Artery was assumed to be a cylinder and the inner diameter, thickness, and length of the model are 6mm, 0.7mm, and 30mm, respectively. Since the unit cell of the stent is 30 degrees in the circumferential direction and the plaque distribution was assumed to be concentric, 30 degrees models in the circumferential direction were employed. An outer sheath was modeled as a rigid cylindrical surface, which has 19.8mm in length.

To consider the effects of the delivery systems, two methods of the unsheathing were studied as shown in Figs. 3(a) and 3(b): (1) the conventional method where a stent comes out from one end of the sheath and (2) a new method in which the stent comes out from the center of the sheath.

2.2. Material Properties

The material model used for the self-expanding stents was the super-elastic model available in Ansys 15.0. Figure 4 and Table 1 show the material parameters of the super-elastic materials. One of the most common self-expanding stents material Ni-Ti alloy and newly developed ferrous alloy, which has the higher strength and a larger super-elastic strain, were used for the stent materials. Table 2

summarizes the values of each parameter used in this analysis.

Mooney-Rivlin model given by Eq. (1) was used to demonstrate the hyper-elastic behavior of both the artery and plaque.

$$W = C_{10} (I_1 - 3) + C_{01} (I_2 - 3) + C_{20} (I_1 - 3)^2 + C_{11} (I_1 - 3)(I_2 - 3) + C_{30} (I_1 - 3)^3 \quad (1)$$

where I_1 , I_2 and I_3 are the strain invariants, and C_{ij} are Mooney-Rivlin parameters. Mooney-Rivlin parameters used in this paper are shown in Table 3. Outer sheath was assumed to be a rigid surface model with negligible thickness.

Figure 5 shows the fitting of the stress strain curve of the ferrous alloy using the material parameters shown in Table 1. Fig. 6 shows the comparison of the stress strain curves of Ni-Ti with the ferrous alloys.

Figure 7 shows the stress strain curves of artery and plaques obtained by Mooney-Rivlin model with the material parameter shown in Table 3. Two types of plaque were chosen: one is stronger than artery (Calcified plaque) and the other softer the artery (Cellular plaque).

2.3. Boundary Conditions

The cylindrical coordinate system was applied for the analysis conducted here. Therefore, x axis, y axis, and z axis show radial, circumferential, and longitudinal directions, respectively. Since 1/12 model in circumferential direction was used, both the circumferential ends of all the models were constrained in y direction. Moreover, both the longitudinal ends of vessel were constrained in all directions. Also, the stent models were restrained in z direction at the center. This analysis can be divided into 2 steps, the crimping process and the expansion process as shown in the below in details. To avoid rigid motion of both the vessel and the plaque, all the nodes of these models were constrained in the crimping process and the constraint was deleted in the expansion process.

Table 1. Stent material parameters [1, 10]

	σ_s^{AS} (MPa)	σ_f^{AS} (MPa)	σ_s^{SA} (MPa)	σ_f^{SA} (MPa)	ϵ_L	α
Ni-Ti	346	365	83	57	0.063	0.09
Ferrous alloy	719	941	265	113	0.175	0

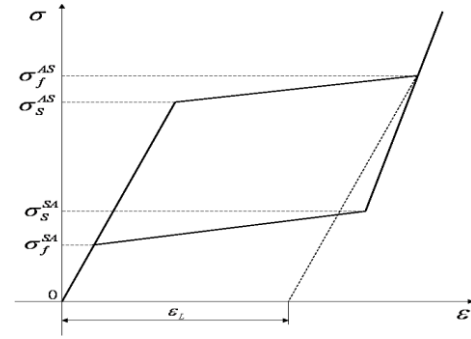


Figure 4. Material parameters for superelastic materials

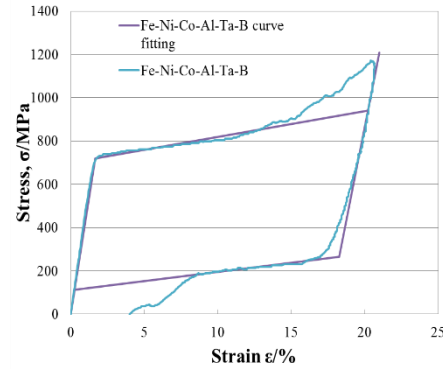


Figure 5. Stress-Strain curve fitting of the ferrous alloy

2.4. Contact Conditions, and Death and Birth of Elements

The contact definitions are important for the stent deployment analysis since the interactions of the stent with sheath or balloon and artery are one of the most important factors of the stenting process. Two surface-surface contact conditions are applied between the stent and sheath, and the vessel and stent, respectively. Between the stent and vessel, the node-surface contact was also defined since not only the stent's surface but also the stent's edge contact to the vessel wall.

Table 2. Stent material parameters [8, 10].

Component	Stent	Plaque	Vessel
Material	NI-Ti alloy Ferrous alloy	Calcified Cellular	Carotid
Yong's modulus [GPa]	60 43.8	2.19×10^{-3}	1.75×10^{-3}
Poison's ratio	0.33	0.495	0.495
Material model		Mooney Rivlin	Mooney Rivlin

Table 3. Mooney-Rivlin Parameters [15, 16].

	C_{10} [kPa]	C_{01} [kPa]	C_{11} [kPa]	C_{20} [kPa]	C_{30} [kPa]
Artery	18.9	2.75	85.7	590.4	0
Calcified	-496	506	1.19×10^3	3.64×10^3	4.74×10^3
Cellular	-803	832	1.15×10^3		

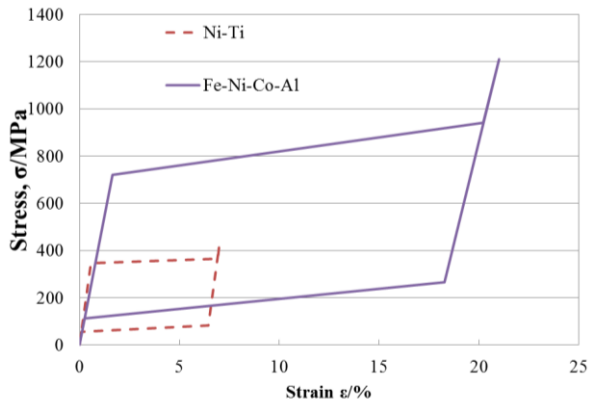


Figure 6. Stress-Strain curve of the stent materials.

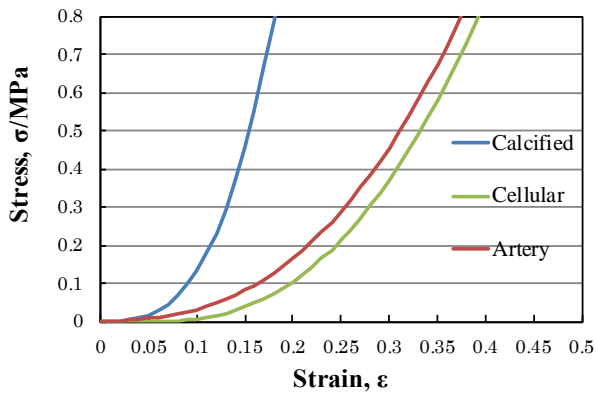
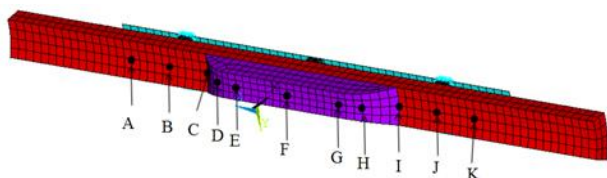
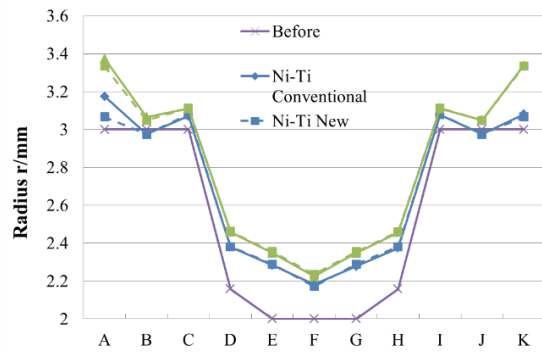


Figure 7. Stress-strain curve obtained from Mooney-Rivlin parameters.

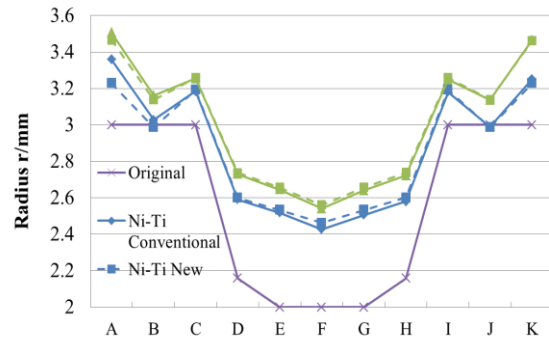
In this analysis the “element birth and death” command was introduced to activate and deactivate the elements during the calculation. Since the diameter of self-expanding stents at the expanded state should be slightly larger than that of the vessel to open up and support artery wall, the diameter of vessel was modeled smaller than that of the stent in the beginning of the simulation. Thus, both the vessel and plaque models had to be deactivated to crimp the stent until its diameter reaches smaller than the vascular lumen diameter. Therefore, all the elements of both the plaque and vessel models were deactivated by using the element death command to prevent the contact of stent to both the vessel and plaque. In addition, the contacts between the stent and vessel or plaque do not occur in this process, then all the contact elements were also deactivated. In the stent expansion process, all the elements including the contact elements were activated by using the element birth command to consider the interactions of the stent with both the artery and plaque models.



(a) Measuring points on the inner surface of the vessel wall

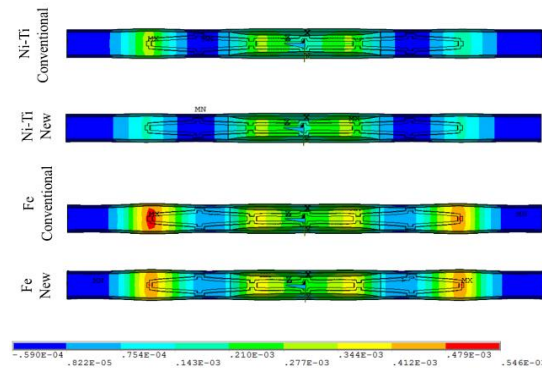


(b) Radii at each point on the vessel wall with calcified plaque after stent deployment

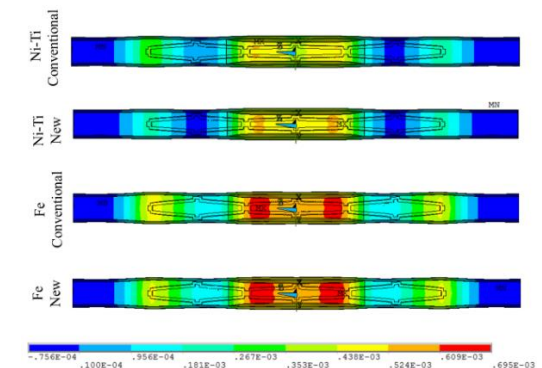


(c) Radii at each point on the vessel wall with cellular plaque after stent deployment

Figure 8. Radii of stent after expansion.



(a) Calcified plaque model



(b) Cellular plaque model

Figure 9. Radial displacement distribution after stent deployment.

3. Results and Discussions

3.1. Radial Displacement

Figure 8 shows the radii at each measuring point shown in Fig. 8(a) after the self-expanding stent placement. Fig. 8(b) shows the radius of the vessel wall with the calcified plaque after each stent deployment. Fig. 8(c) shows the radius of the vessel wall with cellular plaque after the stent deployment. The purple, blue, and green lines show the original radius, radius after Ni-Ti stent deployment, and radius after ferrous alloy stent deployment at each point on the vessel, respectively. The solid line shows the results using the conventional delivery system (delivery system 1), while the broken line shows the results using the new delivery system (delivery system 2). “Ni-Ti Conventional”, “Ni-Ti New”, “Fe Conventional” and “Fe New” on the figures in this section correspond to the results of “Ni-Ti alloy placement stent using the conventional delivery systems”, “Ni-Ti alloy stent placement using the new delivery system”, “Ferrous alloy placement stent using the conventional delivery systems” and “Ferrous alloy placement stent using the New delivery systems”, respectively.

Figure 8(b) shows that the radius of the vessel becomes larger by using the ferrous alloy stent than using the Ni-Ti stent due to the higher strength of ferrous alloy though the differences were small. There is not large difference in the radius between the delivery systems except for the radius at measuring point A, where the stent and artery initially contact. In case of the conventional delivery system, the radius at the point A, where both the stent and vessel wall initially contacts, becomes larger than that at point K, where both the stent and vessel contact at the end of stent deployment process for both the stent materials. On the other hand, in case of using the new delivery system, the radius at both the point A and K become almost same values. In other words, the amount of expansion of the initial contact area becomes larger than that of the last contact area. Since the regions around the distal points of the stent (i.e. point A and K) are on the vessel wall without plaque, the expansion of stent did not become large, whereas enough expansion to restore blood flow is required around the plaque lesion. The stents have the “dog-bone effect” that both the distal and proximal ends of stents tend to expand largely compared to the center of stents. This can cause the vascular injury which leads to the in-stent neointimal formation and restenosis afterward. Therefore, the uniform expansion of stents is desirable to decrease a risk of the vascular injury. Some studies have conducted to find out an optimum stent geometry to reduce dog-bone effect [14]. The results shown in Fig. 8 indicate that using the new delivery system may help decrease excess expansion of distal part of stents.

Figure 8(c) also describes the similar results as Fig. 8(b). Comparing Fig. 8(c) with Fig. 8 (b), the radius become larger at all measuring points. This is because the soft plaque was displaced easily by the stent comparing with the hard plaque.

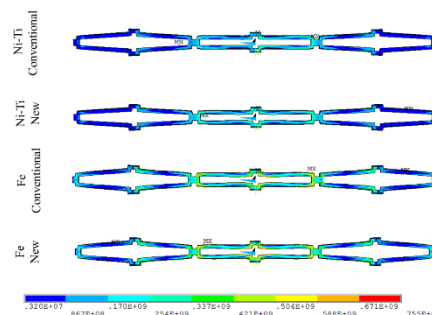
In addition, the radius at the center of plaque (point F) becomes smaller by using the new delivery system than that by using the conventional delivery system though the differences were small. Larger difference of the radius between two delivery systems was observed in case of the Ni-Ti stent placement compared to the ferrous alloy stent placement.

In case of the conventional delivery system, the stent was released from one distal part to the other distal part (from measuring point A to K shown in Fig. 8(a)). Fig. 9 shows the radial displacement distribution after stent deployment: Fig. 9(a) the results of hard plaque (i.e. calcified plaque) model and Fig. 9(b) the results of soft plaque model (i.e. cellular plaque).

Figures 9(a) and 9(b) also clearly show that, when the conventional delivery system was used, the radial displacement of vessel wall, where both the stent and vessel wall initially contact, become larger than that of the other end, where both the stent and vessel wall lastly contact. The vessel wall near the plaque ends were not displaced largely, while the end of the stent expanded largely and displaced vessel wall. The ferrous alloy stent displaced larger than that of the Ni-Ti stent in all region of the vessel wall. Though the large expansion of the plaque is desirable, the ferrous alloy stents also displaced the vessel wall where the plaque does not exist largely. One of the reasons of the excess expansion at the end of the stent might be the stent geometry. By using other stent geometry which decreases the dog-bone effect with ferrous alloy stent, the larger expansion of the plaque lesion and the adequate expansion of the normal artery may be expected.

3.2. von Mises Stress

Figure 10(a) shows the von Mises stress on the stent after the stent placement to the hard plaque and Figure 10(b) that after the stent placement to the soft plaque. The maximal von Mises stress values induced on the stents are shown in Fig. 11. Figure 11(a) shows the calcified plaque and Figure 11(b) the cellular plaque, respectively.



(a) Calcified plaque model

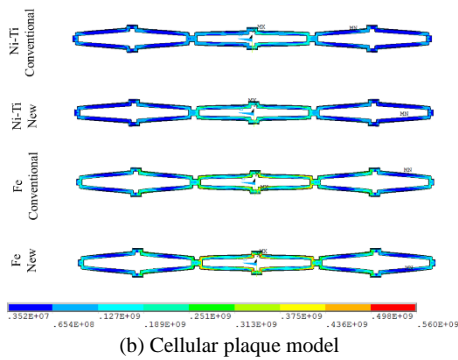
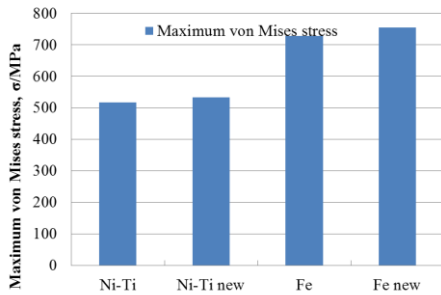
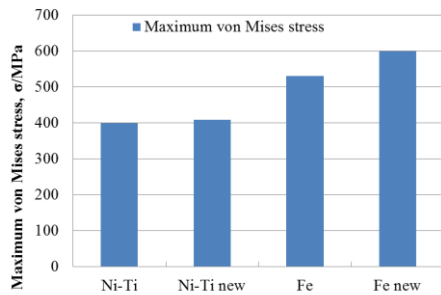


Figure 10. von Mises stress distribution



(a) Calcified plaque model



(b) Cellular plaque model

Figure 11. Maximum von Mises stress value induced on stents.

Figures 10 and 11 indicate that the higher von Mises stress was observed on the ferrous alloy stent than the Ni-Ti stent because of the different stress-strain relation of them. For all the delivery systems and stent materials, the stress concentrations were observed around the links of stents. The von Mises stress distributions on the stent were similar in all analyses.

The von Mises stress distributions on the plaque are shown in Fig. 12. Figure 12(a) shows the calcified plaque and Figure 12(b) the cellular plaque, respectively. The maximal values of the von Mises stress induced on the plaques are shown in Fig. 13. Fig. 12 shows that the von Mises stress value induced on the plaque becomes higher in case of the ferrous alloy stent deployment since the ferrous alloy stent has the higher strength and the larger self-expands than the Ni-Ti stent. The stress concentration was observed on the plaque where stent's circumferential edges contact plaque in the ferrous alloy stent deployment analyses. It is

also found out from Fig. 13 that the stress values induced on the plaque were lower in the soft plaque than that of the hard plaque. The stress distributions of both the soft and hard plaque were similar.

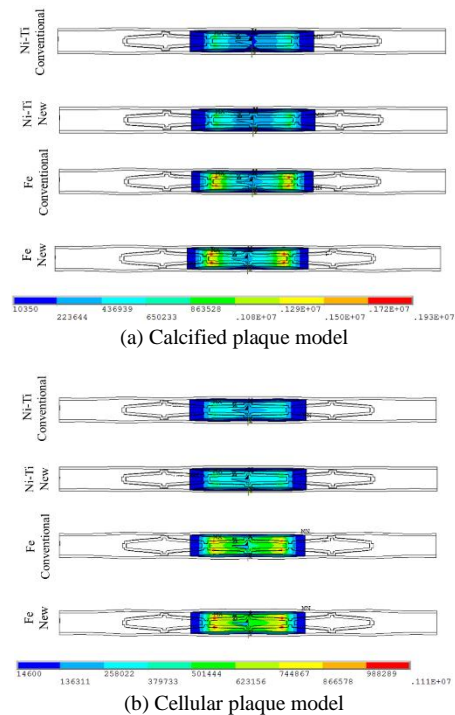
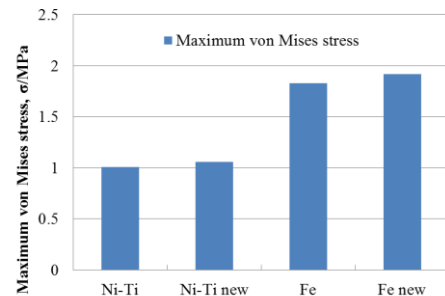
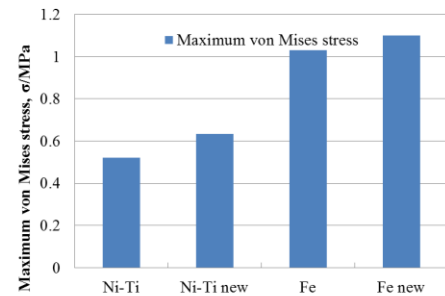


Figure 12. von Mises stress distribution



(a) Calcified plaque model



(b) Cellular plaque model

Figure 13. Maximum von Mises stress value induced on stents.

The von Mises stress distributions on the vessel wall are shown in Fig. 14. Figure 14(a) shows the calcified plaque

and Figure 14(b) the cellular plaque, respectively. The maximal von Mises stress values induced on the vessel walls are shown in Fig. 15. Figs. 14(a) and 14(b) show that the stress values induced on the vessel wall with the soft plaque was higher than that on the vessel wall with the hard plaque. From these results, it can be seen that the hard plaque absorbs the higher expanding load of the stent than the soft plaque. Therefore, the effect on the vessel wall with the hard plaque becomes lower. In addition, it can be found out that the stress concentrations on the distal ends of the vessel wall can be minimized by using the new delivery system. According to the results of the tensile tests of the human carotid artery, the initial failure begins around 0.2MPa and the ultimate failure occurs around 1.0MPa though the value varies from patients and clinical stages [17]. In this simulation, all the von Mises stress values induced on the vessel wall was lower than 0.2MPa. The highest value of 0.179MPa was observed by the ferrous alloy stent deployment with the conventional delivery system to the vessel with hard plaque. By using the new delivery system, the value decreased to 0.135MPa with keeping the amount of expansion of the plaque lesion. This indicates the effectiveness of using the new delivery system to reduce risks of the vascular injury by the stent deployments.

Figure 15(a) shows that maximal von Mises stress values induced on the vessel wall becomes smaller by using the new delivery system. However, the value was higher by using the new delivery system in case of the stent placement to the cellular plaque as shown in Fig. 15(b). This is due to the different location of the maximal von Mises stress. In case of the calcified plaque shown in Fig. 14(a), the maximal von Mises stress was induced on the end of the vessel wall because the hard plaque absorbed the higher stress. In case of the cellular plaque shown in Fig. 14(b), the maximal value was observed on the vessel wall under plaque. It is clarified that the larger stent expansion occurs at the initial contact area between the stent and vessel wall comparing with the area where the stent and vessel wall contact in the end. Therefore, the new delivery system has an advantage to reduce the stress at the end of the vessel.

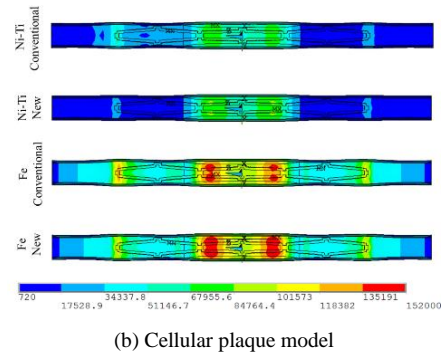
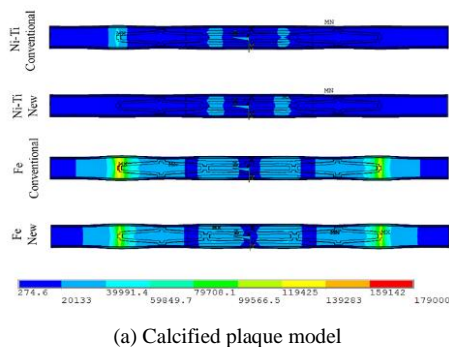


Figure 14. von Mises stress distribution on vessel wall after stent deployment

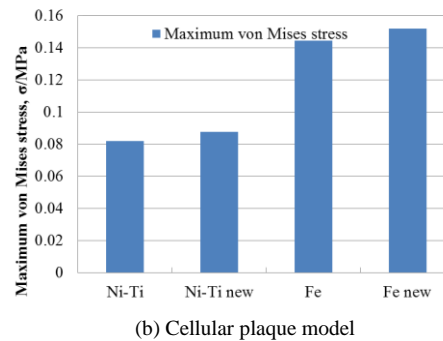
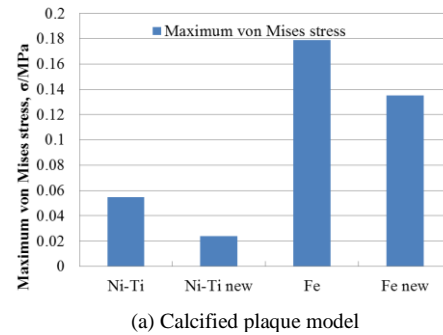


Figure 15. Maximum von Mises stress value induced on vessel walls

3.3. Area Stenosis Ratio and Dog-Boning

The area stenosis ratio is used to measure the severity of the stenosis. It is clinically used to measure the severity of narrowing of the blood vessel. Area stenosis ratio is defined by Eq. (2), where the cross-sectional area of the healthy blood vessel and that of the narrow blood vessel are denoted D and A , respectively. The area stenosis ratio changes are described in Fig. 16.

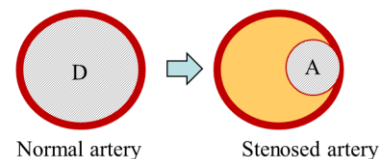


Figure 16. Definition of area stenosis ratio.

The stenosis ratio was calculated from the area of the narrowest part of the vessel (i.e. central cross-sectional areas of the lumen).

$$\text{Area stenosis ration} = (D-A)/D \times 100 [\%] \quad (2)$$

The dog-boning is a phenomenon that the both stent's proximal and distal ends expand excessively like a dog bone shape. Though this phenomenon works to fix a stent to the vessel wall, ideally stent should be fixed to a vessel wall by pressure between full surface of stents and vessel wall [18]. In addition, the stent's edges with the dog-boning phenomenon becomes causes of the vascular injury which may lead to restenosis. Therefore, the dog-boning value should be minimized. The degree of the dog-boning can be defined by the Eq. (3).

$$\text{Dog-boning} = \frac{R_{POI}^{expanded} - R_{central}^{expanded}}{R_{central}^{load}} \quad (3)$$

where, $R_{POI}^{expanded}$ and $R_{central}^{expanded}$ are the radius at the point of interest (POI) and the central radius after the stent expansion, respectively. The dog-boning values were measured on the POI shown in Fig. 17. Dog-boning values on POI are summarized in the Tables 4(a) and (b). Table 4(a) shows the result of the calcified plaque model and Table 4(b) that of cellular plaque model.

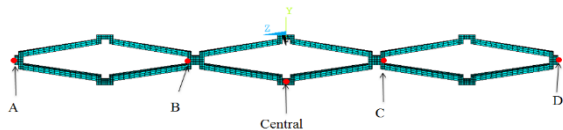


Figure 17. Points of interest

Table 4. Dog-boning on each measuring point
(a) Calcified plaque model.

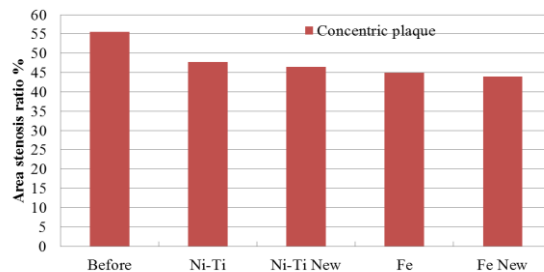
POI	Ni-Ti [%]	Ni-Ti new [%]	Fe [%]	Fe new [%]
A	53.6	44.8	59.8	57.0
B	9.05	7.46	11.6	11.2
C	8.24	7.45	11.6	11.2
D	47.4	44.8	58.0	57.0

(b) Cellular plaque model.

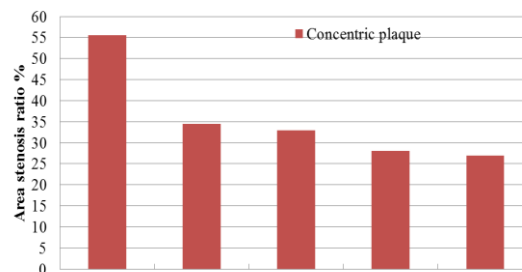
POI	Ni-Ti [%]	Ni-Ti new[%]	Fe [%]	Fe new [%]
A	39.4	31.9	38.8	36.0
B	7.47	5.82	8.52	7.91
C	6.58	5.82	8.23	7.93
D	34.9	31.9	37.2	35.9

Figure 18 shows the relationship between the area stenosis ratio and the stent types. It can be seen that the area stenosis ratio becomes smaller by using the ferrous alloy stent than the Ni-Ti alloy stent. The area stenosis ratio becomes the smallest by placing the ferrous alloy stent with the new delivery system. The new delivery system has an advantage to reduce the area stenosis ratio compared with the conventional delivery system. This is because the new delivery system allows the larger expansion at the center of

the stent, while the distal and proximal expansion are relatively larger by using the conventional delivery system. Similar tendency was observed in both the calcified plaque model and the cellular plaque model.



(a) Calcified plaque model



(b) Cellular plaque model

Figure 18. Area stenosis ratio after stent deployment

Some guidelines for the carotid artery stenting indicate that about 80% of the reference diameter is the recommended amount of expansion by stent. Reference diameter is measured at the internal carotid artery in the distal side of the plaque lesion in practice. In case of this analysis, the blood vessel was assumed to be a cylinder thus the diameter is constant. When the reference diameter is simplified as the diameter of the cylindrical blood vessel, approximately 36% of the area stenosis ratio would be the desired value after the stent expansion. The area stenosis ratio remained the high value even after the stent deployment in the calcified plaque model. On the other hand, the area stenosis ratio becomes acceptable level in case of the cellular plaque model. These differences between the calcified plaque model and the cellular place model were caused by their different stiffness. Since the calcified plaque is harder than the cellular plaque, the expansion by the stent was not enough in this analysis. In this analysis, the plaque and vessel wall were assumed to be mono layer though there are actually some layers and compositions. Therefore, using further detailed modeling of the plaque and vessel into analysis may improve the reality of the simulation.

Table 4 shows that the dog-boning values becomes lower by using the new delivery system compared with the conventional delivery system in both the stent materials (Ni-Ti alloy and ferrous alloy stents) and both the plaque compositions (calcified plaque and cellular plaque). In addition, the difference of the dog-boning values between the distal and proximal ends (POI A and D) was minimized

by using the new delivery system. These results show the effectiveness of the new delivery system on minimizing both the dog-boning values and the dog-boning value's difference between the distal and proximal ends. In the analysis using the calcified plaque model, the dog-boning values were higher with the ferrous alloy stent than that with the Ni-Ti alloy stent. This maybe because the ferrous alloy has the higher strength than the Ni-Ti alloy, therefore, the ferrous alloy stent expands largely on the vessel wall at the distal and proximal ends of the stent than the Ni-Ti stent. However, since the calcified plaque is harder than the vessel wall, the stent expansion might be restrained to a certain extent.

4. Conclusions

In this study, stenting using the two types of the stent materials (i.e. Ni-Ti alloy and ferrous alloy) and delivery systems are compared based on the simulations conducted by FEM analysis. As a result, the following conclusions were obtained.

- (1) The ferrous alloy stent has the larger expansion than the Ni-Ti stent irrespective of the plaque distribution and composition.
- (2) The ferrous alloy stent placement leads to the higher von Mises stress on the plaque and the vessel wall.
- (3) The ferrous alloy stent increases the area stenosis ratio more than the Ni-Ti stent in both the concentric and the eccentric plaque analyses.
- (4) The higher dog-boning value was observed in case of the ferrous alloy stent placement.
- (5) The new delivery system has an advantage to reduce the excessive expansion at the distal and proximal ends of the stents.
- (6) The new delivery system reduces the area stenosis ratio in all the results compared with the conventional delivery system.
- (7) The new delivery system reduces the dog-boning value irrespective of the stent material, plaque composition, and plaque distribution.

References

[1] Ministry of Health, Labour and Welfare, Vital Statistic 2015.
[2] Duerig TW, Wholey M. A comparison of balloon- and self-expanding stents. *Minim Invasive Ther Allied Technol* 2002;11:173-178.

[3] Grenacher L, Rohde S, Gänger E, Deutsch J, Kauffmann GW, Richter GM. In vitro comparison of self-expanding versus balloon-expandable stents in a human ex vivo model. *Cardiovasc. Intervent. Radiol* 2006;29:249-254.
[4] Medtronic, Advantages of Cobalt Alloy for Coronary Stents 2003.
[5] Briguori C, Sarais C, Pagnotta P, Liistro F, Montorfano M, Chieffo A, Sgura F, Corvaja N, Albiero R, Stankovic G, Toutoutzas C, Bonizzoni E, Mario CD, Colombo A. In-stent restenosis in small coronary arteries: Impact of strut thickness. *J. Am. Coll. Cardiol* 2002;40:403-409.
[6] Kastrati A, Mehilli J, Dirschinger J, Dotzer F, Schühlen H, Neumann FJ, Fleckenstein M, Pfafferoth C, Seyfarth M, Schömig A. Intracoronary stenting and angiographic results: strut thickness effect on restenosis outcome (ISAR-STEREO) trial. *Circulation* 2001;103:2816-2821.
[7] Pache J, Kastrati A, Mehilli J, Schühlen H, Dotzer F, Hausleiter J, Fleckenstein M, Neumann FJ, Sattelberger U, Schmitt C, Müller M, Dirschinger J, Schömig A. Intracoronary stenting and angiographic results: strut thickness effect on restenosis outcome (ISAR-STEREO-2) trial. *J. Am. Coll. Cardiol* 2003;41:1283-1288.
[8] Tanaka Y, Himuro Y, Kainuma R, Sutou Y, Omori T, Ishida K. Ferrous Polycrystalline Shape-Memory Alloy Showing Huge Superelasticity. *Science* 2010;327:1488-1490.
[9] Russo RJ, Silva PD, Yeager M. Coronary artery overexpansion increases neointimal hyperplasia after stent placement in a porcine model. *Heart* 2007;93:1609-1615.
[10] Wu W, Qi M, Liu XP, Yang DZ, Wang WQ. Delivery and release of nitinol stent in carotid artery and their interactions: A finite element analysis. *J. Biomech* 2007;40:3034-3040.
[11] Lally, C, Dolan F, and Prendergast PJ. Cardiovascular stent design and vessel stresses: a finite element analysis. *J. Biomech* 2005;38:1574-1581.
[12] Stoeckel D, Bonsignore C, Duda S. A survey of stent designs. *Minim. Invasive Ther. Allied Technol* 2002;11:137-147.
[13] Heller RS, Malek AM. Delivery technique plays an important role in determining vessel wall apposition of the Enterprise self-expanding intracranial stent. *J. NeuroInterventional Surg* 2011;3:340-343.
[14] Lim D, Cho S, Park W, Kristensson A, Ko J, Alhassani ST, Kim H. Suggestion of Potential Stent Design Parameters to Reduce Restenosis Risk driven by Foreshortening or Dogboning due to Non-uniform Balloon-Stent Expansion. *Ann. Biomed. Eng* 2008;36:1118-29.
[15] Prendergast PJ, Lally C, Daly S, Reid AJ, Lee TC, Quinn D, Dolan F. Analysis of prolapse in cardiovascular stents: a constitutive equation for vascular tissue and finite-element modelling. *J. Biomech. Eng* 2003;125:692-699.
[16] Pericevic I, Lally C, Toner D, Kelly DJ. The influence of plaque composition on underlying arterial wall stress during stent expansion: the case for lesion-specific stents. *Med. Eng. Phys* 2009;31:428-433.
[17] Stemper BD, Yoganandan N, and Pintar FA. Methodology to study intimal failure mechanics in human internal carotid arteries. *J. Biomech* 2005;38:2491-2496.
[18] Yoshida S. Effect of Distal Stiffness against Dog-Boning. *Comput. Mech. Conf* 2014;2014:155-156.

Comparative Study on Search Performance between GA and PSO for Stacking Optimization of Laminated Plates

Michio Innami^{a*}, Yoshihiro Narita^b

^aDepartment of Production Electronics and Information System Technology, Hokkaido Polytechnic College. Email:innami@hokkaido-pc.ac.jp
^bC-BEST, Center of Technology, Faculty of Engineering, University of Hasanuddin. Email: ynarita@eng.hokudai.ac.jp

Abstract

This paper deals with the optimization problem to maximize the vibration performance of laminated composite plates by properly tailoring the fiber orientation angles in the layers. The optimization is performed by using two metaheuristic methods, Genetic Algorithm (GA) and Particle Swarm Optimization (PSO), and comparison is made to evaluate differences in search performance of the two methods. Test problems are set for the evaluation of maximizing the fundamental frequencies, and some parameters are properly tuned for efficient solution search. From the numerical experiments, it turned out that the search using PSO indicates faster convergence and better solutions than GA scheme under assumption of search domain in real number.

Keywords: Genetic algorithm; laminated composite plate; metaheuristic optimization; particle swarm optimization; vibration

1. Introduction

Thin structural elements made of long-fiber reinforced composite material are used widely in aerospace, automotive, marine and civil engineering applications because they may be designed to be economic in the long run due to having low mass and achieving high stiffness and strength. For such a wide range of applications, various structural models such as the analytical or numerical finite element (FE) models may be combined with optimization procedures to achieve the best design.

In the engineering optimization, there are a variety of optimization techniques, ranging from mathematical programming approaches [1] to metaheuristic approaches [2]. A class of the mathematical programming includes well-accepted gradient-based methods, simplex algorithm for linear programming (LP), quadratic programming, dynamic programming, branch/bound method and etc. In the past few decades, however, the metaheuristic methods are more often used, such as Genetic Algorithm (GA) originally proposed by Holland [3] in 1975. Then GA was first applied to structural design in the late 1980's by Goldberg [4]. More recently, other types of nature-inspired methods have been

developed, and one of the promising ones is Particle Swarm Optimization (PSO) [5-7].

The reason for increasing use of metaheuristics is mostly due to the advantages that they are simple to code and use and can provide optimum or nearly optimum solutions without falling into local solutions. The drawback is the long computation time, but the recent development of computational technology compensates the situation.

In this paper, stacking sequence problem is under consideration, where the objective function, in this case fundamental frequency, is maximized by searching the optimum fiber orientation angles in all the layers of symmetrically laminated rectangular plates. From metaheuristics, two representative methods are chosen, namely, Genetic Algorithm (GA) and Particle Swarm Optimization (PSO), and comparisons are made to evaluate the difference in search performance between the two methods. The bench mark problem is given for the evaluation of maximizing the fundamental frequencies, and the design of experiments (DoE) is used to make some search parameters being properly tuned. In the numerical experiments, it found out that the search by using PSO has shown the faster converged solutions than GA solution.

*Corresponding author. Tel.: +81-134-62-3553
3-190 Zenibako, Otaru, Japan, 047-0292

2. Metaheuristics and overview

2.1. Basic concept of GA

Genetic algorithm (GA) is one of metaheuristics that are generally inspired by the process of natural selection in nature. It is within the larger class of evolutionary algorithms (EA). GA is usually used to generate nearly optimum solutions to the engineering search problem by the help of bio-inspired operators such as selection, crossover and mutation [4], and it became popular optimization approach in the past few decades. After the first works by Holland in the 1970s, he authored a book [3], and he and his co-workers have established a basic framework in GA.

In GA, a population of individuals is improved toward better solutions, where each individual is given a set of properties (genotype) to be changed and/or mutated. It is a usual practice to represent it in binary strings of 0 and 1. The process for improvement starts from with the first generation whose members (individuals) are randomly generated. The values of fitness in all individuals are evaluated and are taken usually from the value of the objective function in the optimization. The individuals with higher fitness are selected stochastically by, for example, a roulette rule. A new generation of candidate solutions is adapted in the iteration. The iterative process is terminated based on prescribed condition, in such ways as a maximum number of generations is produced or a satisfactory fitness level is reached in the population.

The essence of GA consists in repetitive application of the selection of parents for mating and applying crossover and mutation. Particularly, the crossover and mutation are known as the most important genetic operators, and their probabilities are GA parameters needed to be tuned, called as the mutation probability and crossover probability. The population size for reasonable settings that depend on the problem being worked on.

2.2. Basic concept of PSO

As GA is a method inspired by principle observed in nature, a particle swarm optimization (PSO) is also one of metaheuristics and belongs to a class of evolutionary algorithm [4]. The advantages of PSO include no requirement for the gradient information in the problem and capability of searching a large space of feasible solutions. Just like GA, PSO is a numerical method to optimize in iterative process by improving individual solutions with respect to a given measure of quality. So, it requires a population of candidate solutions to be moved in the search-space, but there is no notion like cross-over, mutation and mating of parents and that generation changes from parents to children.

The iteration process is repeated by simple mathematical formula by using the particle's position and velocity vectors. A new position is decided by adding three vectors, an inertia vector of a particle (difference of the present and past

position vectors), a vector heading to the best position of an individual particle, and a vector heading to the global best among the population. Coefficients are multiplied to each vector and tuned as input parameters.

PSO was first originated by Kennedy, Eberhart and Shi [6] and was designed to simulated social behaviors of the movement in a flock of birds and school of fish. Kennedy and Eberhart published a book [7] to describe many theoretical aspects in PSO and swarm intelligence. Extensive surveys of PSO applications were made by Poli [8, 9]. Recently, a comprehensive review on theoretical and experimental works on PSO was published by Bonyadi and Michalewicz [10].

To summarize, algorithm of PSO is to have a swarm (population) of particles (feasible solutions) and the particles are moved following the formula in the search-space according to a few simple formulae. When improved positions are being discovered, these will then come to guide the next movements of the swarm. The process is repeated until a satisfactory solution will eventually be discovered, although the convergence is not guaranteed in strict mathematical sense.

2.3. Overview of literature on plate stacking optimization

For optimization of mechanical behaviors in laminated composite plates, the pioneering studies of Bert [11, 12], in which the fiber-orientation angles (design variables) that maximize the fundamental frequency (objective function) of laminated plates were sought. Since these early studies, a variety of approaches have been used to identify the lay-ups that maximize the frequencies and buckling loads of laminated plates. In the early days, metaheuristic methods and supporting computational environment were not available, lamination parameters coupled with mathematical programming were used by Fukunaga and others [13]. Zhao and Narita [14] used the complex method (extension of simplex method) for the problem. Todoroki and Haftka [15] used GA with repair strategy. The progress of design and optimization on composites was summarized in a textbook [16] in 1999.

In the years of 2000's, GA and metaheuristic approaches have evolved, and Todoroki and his co-workers have published some papers [17-19]. Narita has also presented a number of related papers [20-22] by developing a layerwise optimization method, where the physics-oriented behaviors are utilized in the solution process.

More recently in the 2010's, significant progress has been observed by using GA and PSO, or even GA-PSO combined method, to solve the stacking sequence problem. Le-Manh and Lee [23] dealt with stacking sequence optimization for the maximum strength of laminated composite plates using GA. Ehsani and Rezaeepazhand [24] solved the same optimization of laminated composite grid plates for maximum buckling load using GA. Ho-Huu and others [25] optimized laminated composite plates for maximizing buckling load using improved differential evolution.

Schaedler and Almeida [26] optimized maximum buckling load by harmony search algorithm. In 2017, Herath and others [27] used GA to optimized structural strength and laminate optimization of self-twisting composite hydrofoils. Vosoughi and co-workers [28, 29] presented a mixed finite element and improved GA for maximizing buckling load of stiffened laminated composite plates. These authors also made academic efforts to combine different ideas and presented maximized buckling load by using FE-GAs-PSO, a combined approach.

For comparison of GA and PSO, Zhou and others conducted a comparative study of improved GA and PSO in solving multiple traveling salesmen problem [30]. Modification from a simple GA was made by Pathan and others [31] by GA for optimizing the damping response of composite laminates. Javidrad and his colleagues [32] combined PSO with a simulated annealing (SA), and named as a hybrid PSO-SA method. Akmar and others [33] summarized recent progress in probabilistic multi-scale optimization of hybrid laminated composites. As overviewed on the applications of GA, PSO and heuristic methods above, a large number of studies are made on applications of GA and PSO to the stacking sequence problem of laminated composite plates. The comparison studies of search performance between GA and PSO have not been carried out enough, and therefore in the present paper, the research on clarifying the difference in performance will be made for the purpose.

3. Problem description for stacking sequence optimization of laminated composite plates

Consider a laminated plate composed of orthotropic laminas as shown in Fig. 1. The stress-strain equations in the k -th layer can be written as

$$\begin{Bmatrix} \sigma_x \\ \sigma_y \\ \tau_{xy} \end{Bmatrix}^{(k)} = \begin{bmatrix} \bar{Q}_{11} & \bar{Q}_{12} & \bar{Q}_{16} \\ \bar{Q}_{12} & \bar{Q}_{22} & \bar{Q}_{26} \\ \bar{Q}_{16} & \bar{Q}_{26} & \bar{Q}_{66} \end{bmatrix}^{(k)} \begin{Bmatrix} \varepsilon_x \\ \varepsilon_y \\ \gamma_{xy} \end{Bmatrix} \quad (1)$$

where $\bar{Q}_{ij}^{(k)}$ ($i, j = 1, 2$ and 6) are the elastic constraints of the k -th layer. The $\bar{Q}_{ij}^{(k)}$ are determined by the coordinate transformation of the Hooke's law for orthotropic plate $Q_{ij}^{(k)}$ ($i, j = 1, 2$ and 6) given by

$$\begin{aligned} Q_{11} &= E_L / (1 - \nu_{LT}\nu_{TL}), \quad Q_{22} = E_T / (1 - \nu_{LT}\nu_{TL}), \\ Q_{12} &= \nu_{TL}Q_{11} = \nu_{LT}Q_{22} \quad \text{and} \quad Q_{66} = G_{LT} \end{aligned} \quad (2)$$

where E_L and E_T are the moduli of elasticity in the L and T directions, respectively, G_{LT} is the shear modulus, and ν_{LT} and ν_{TL} are the Poisson ratios, as shown in Fig. 1.

The maximum strain energy U_{\max} and kinetic energy T_{\max} are derived as

$$U = \frac{1}{2} \int \int_A \{\kappa\}^T [D] \{\kappa\} dA \quad (3)$$

$$T = \frac{1}{2} \rho \int \int_A \left\{ \frac{\partial W}{\partial t} \right\}^2 dA \quad (4)$$

where $\{\kappa\}$ is curvature vectors defened by

$$\{\kappa\} = \left\{ -\frac{\partial^2 W}{\partial x^2} \quad -\frac{\partial^2 W}{\partial y^2} \quad -\frac{\partial^2 W}{\partial x \partial y} \right\}^T \quad (5)$$

$[D]$ is the bending stiffness matrix, A is area of the plate, ρ is material density of CFRP, h is thickness of plate, and W is bending deflection function. To simplify the analysis, the normalized co-ordinate system $O-\xi\eta$ ($-1 \leq \xi, \eta \leq 1$) is defined in equation

$$\xi = \frac{2x}{a}, \quad \eta = \frac{2y}{b} \quad \text{and} \quad \Omega = \omega a^2 \sqrt{\frac{\rho}{D_0}} \quad (6)$$

where ξ and η are dimensionless coordinates, Ω is dimensionless frequency parameter, ω is the angular frequency, and D_0 is reference plate stiffness represented by

$$D_0 = \frac{E_T h^3}{12(1 - \nu_{LT}\nu_{TL})} \quad (7)$$

Then, the deflection is expressed by

$$W(\xi, \eta, t) = \sum_{m=0}^{M-1} \sum_{n=0}^{N-1} A_{mn} X_m(\xi) Y_n(\eta) \sin \omega t \quad (8)$$

with

$$\begin{aligned} X_m(\xi) &= \xi^m (\xi + 1)^{bc1} (\xi - 1)^{bc2} \\ Y_n(\eta) &= \eta^n (\eta + 1)^{bc3} (\eta - 1)^{bc4} \end{aligned} \quad (9)$$

where A_{mn} is unknown coefficients and $X_m(\xi)$ and $Y_n(\eta)$ are the displacement functions which satisfy at least the kinetic boundary conditions on the edge. The bci ($i = 1, 2, 3$ and 4) is the boundary index which is used to satisfy the boundary conditions on each edge, and they are defined [34] as

$$bci, bc2, bc3, bc4 = \begin{cases} 0 & \text{(free)} \\ 1 & \text{(simple support)} \\ 2 & \text{(clamp)} \end{cases} \quad (10)$$

The stationary value is obtained by

$$\frac{\partial (U_{\max} - T_{\max})}{\partial A_{mn}} = 0 \quad (mn = 0, 1, 2, \dots, (M-1)) \quad (11)$$

The result of the minimization process Eq. (11) yields frequency equation in terms of unknown coefficient A_{mn} as

$$|[K]-\Omega^2[M]|=0 \tag{12}$$

where $[K]$ is the total stiffness matrix and $[M]$ is the total mass matrix. Solving this eigenvalue equation gives the non-dimensional frequency parameter Ω to be optimized.

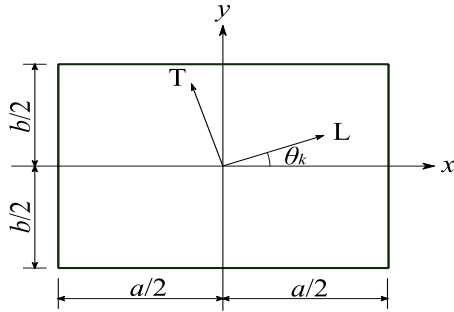


Figure 1. Laminated composite rectangular plate and coordinates

4. Numerical experiments by GA and PSO

4.1. Problem setting

This study employs GA and PSO for searching nearly optimal solutions. The design variables, *i.e.*, the fiber orientation angles of laminas are treated as continuous values. An 8-layer symmetric CFRP laminated plate shown in Fig. 1 is analyzed. The dimensions and material constants are as follows:

$$a = b = 150\text{mm}, h = 15\text{mm}$$

(Note that the frequency parameter is normalized with h , and the value of a/h does not affect it)

$$E_L = 138\text{GPa}, E_T = 8.96\text{GPa}, G_{LT} = 7.1\text{GPa}$$

$$\nu_{LT} = 0.3, \rho = 1578\text{kg/m}^3$$

This study tries to find the fiber orientation angles of the laminas that composes the plate, which make the fundamental natural frequency maximum.

The boundary conditions are assumed as CSFF, SSSS, CCFF, CSSS, where the sequence of four characters stands for the type of constraint on the left, lower, right, and upper edge, starting from the left edge. The letters F, S, and C denote Free, Simply supported, and Clamped, respectively.

4.2. GA

Continuous values are to be stored in the genes on a chromosome. Roulette wheel selection is adopted. Linear scaling is applied so that the selection might be operated effectively. It scales the fitness values using the following equations

$$f_s = af + b$$

$$a = \frac{(c-1)f_{\text{avg}}}{f_{\text{max}} - f_{\text{avg}}}, \quad b = \frac{f_{\text{avg}}(f_{\text{max}} - cf_{\text{avg}})}{f_{\text{max}} - f_{\text{avg}}} \tag{13}$$

where f_{max} and f_{avg} are the maximum and average values of the original function, respectively. In this study, the constant c is set to 2. The elite strategy is also applied. This study adopts two-point crossover and mutation operators.

4.3. PSO

The position and velocity vectors of each particle in a swarm are defined as follows.

$$\mathbf{v}_i^{k+1} = w\mathbf{v}_i^k + c_1r_1(\mathbf{pbest}_i - \mathbf{x}_i^k) + c_2r_2(\mathbf{gbest} - \mathbf{x}_i^k) \tag{14}$$

$$\mathbf{x}_i^{k+1} = \mathbf{x}_i^k + \mathbf{v}_i^{k+1}$$

where \mathbf{x}_i^k and \mathbf{v}_i^k are n -dimensional position and velocity vectors of particle i at the k -th generation, respectively. \mathbf{pbest}_i and \mathbf{gbest} are the position vectors where the objective function took the best value so far in the track of particle i , and of the whole particles, respectively. w , c_1 , and c_2 are constants, r_1 , and r_2 are uniform random numbers between 0 and 1.

5. Parameter setting

The parameters of GA and PSO should be selected properly. This study employs DoE approach for determining them [35]. In both GA and PSO, four factors are chosen, then 4 levels are set for each of them. Normally there are 4^4 combinations of parameters. However with DoE approach, the number of experiments can be extremely reduced. The experiments for determining the parameters are planned to be executed according to the orthogonal array $L_{16}(4^4)$ as shown in Table 1. It requires 16 types of experiments.

Table 1. Orthogonal array $L_{16}(4^4)$

Experiment	Level			
	A	B	C	D
1	1	1	1	1
2	1	2	2	2
3	1	3	3	3
4	1	4	4	4
5	2	1	2	3
6	2	2	1	4
7	2	3	4	1
8	2	4	3	2
9	3	1	3	4
10	3	2	4	3
11	3	3	1	2
12	3	4	2	1
13	4	1	4	2
14	4	2	3	1
15	4	3	2	4
16	4	4	1	3

5.1. Parameters of GA

Population size, elite count, crossover rate, and mutation rate are defined as factors of DoE. Table 2 shows the factors and their levels. The maximum number of generations are chosen as the products of the population size and itself might be equal among all the levels.

5.2. Parameters of PSO

Population size, w , c_1 , and c_2 are defined as factors of DoE. The factors and their levels are shown in Table 3. The maximum number of generations are chosen as the products of the population size might be equal among all the levels, same as the case of GA.

6. Experimental results

In accordance with the experimental plan in Table 1, every experiment was conducted 3 times. Tables 4 and 5 present the fundamental frequencies derived from above trials by GA and PSO, respectively. Figures 2 and 3 show the values with each factor level. Consequently, the parameters of GA and PSO were selected as shown in Table 6 and 7, respectively. The maximum number of generation is extended to 500 in both cases.

Table 2. Factors and their levels of GA parameters

Factor	Level			
	1	2	3	4
A Population size	20	40	80	160
Max. generation	200	100	50	25
B Elite count	1	3	5	10
C Crossover rate	0.3	0.5	0.7	0.9
D Mutation rate	0.01	0.03	0.05	0.10

Table 3. Factors and their levels of PSO parameters

Factor	Level			
	1	2	3	4
A Population size	20	40	80	160
Max. generation	200	100	50	25
B w	0.3	.05	0.7	0.9
C c_1	1.0	1.5	2.0	2.5
D c_2	1.0	1.5	2.0	2.5

With above parameters, the search experiments were carried out 3 times by each method. The calculation was executed under Java environment 1.8.0 using a laptop (Core 2 Duo, T9300, 2.50GHz, 4GB RAM, Windows 10 64-bit).

The results are shown in Table 8. “Converged” means the point when Ω_1 reaches the final value.

The transition of Ω_1 in every trial is shown in Figs. 4-7. It turns out that the calculation time per generation is almost same between GA and PSO, although the final Ω_1 values are slightly better derived from PSO than from GA. Furthermore the search with PSO converges faster than those of GA. The results indicate that the calculation is sufficient at least up to 40th generation. In contrast, with GA, the generation considered sufficient for convergence cannot be estimated within 500th generation.

7. Conclusions

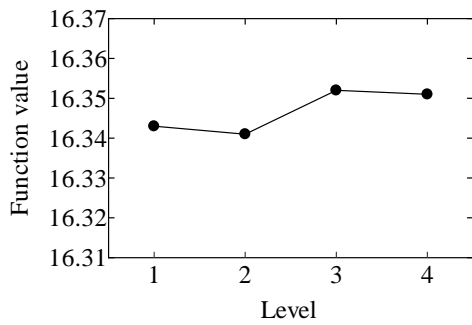
Search performance for optimizing the natural frequencies of fundamental mode was compared between GA with PSO. Appropriate parameters of GA and PSO were selected by DoE approach. It revealed the performance with PSO is better than with GA. In maximization, higher values of Ω_1 were obtained by using PSO. Moreover, the results showed that all the solutions are converged until at least 40th generation.

References

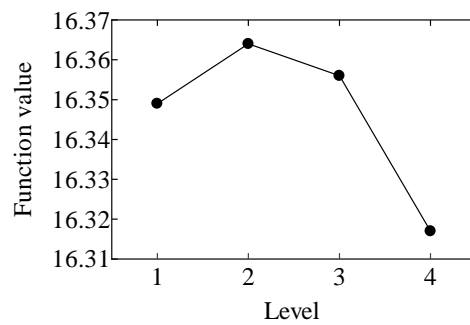
- [1] R.T. Haftka, Z. Gürdal, Elements of Structural Optimization (Solid Mechanics and Its Applications, Springer, 1991.
- [2] K.L. Du, M.N.S. Swamy, Search and Optimization by Metaheuristics: Techniques and Algorithms Inspired by Nature, Birkhaeuser, 2016.
- [3] J.H. Holland, Adaptation in Natural and Artificial Systems: An Introductory Analysis with Applications to Biology, Control, and Artificial Intelligence, A Bradford Book, 1975 & 1992.
- [4] D.E. Goldberg, Genetic Algorithms in Search, Optimization, and Machine Learning, Addison-Wesley Professional, 1989.
- [5] A. E. Olsson, Particle Swarm Optimization: Theory, Techniques and Applications, Nova Science Pub Inc., 2011.
- [6] J. Kennedy, R. Eberhart, Particle Swarm Optimization, Proceedings of IEEE International Conference on Neural Networks. IV., 1995, pp.1942–1948.
- [7] J. Kennedy, R.C. Eberhart, Swarm Intelligence. Morgan Kaufmann, 2001.
- [8] R. Poli, An analysis of publications on particle swarm optimisation applications, Technical Report CSM-469. Department of Computer Science, University of Essex, UK, 2007.
- [9] R. Poli, Analysis of the publications on the applications of particle swarm optimization, Journal of Artificial Evolution and Applications, 2008, pp.1–10.
- [10] M.R. Bonyadi, Z. Michalewicz, Z., Particle swarm optimization for single objective continuous space problems: a review. Evolutionary Computation, 25, 2017, pp. 1–54.
- [11] C.W. Bert, Optimal design of a composite material plate to maximize its fundamental frequency, Journal of Sound & Vibration, 50, 1977, pp.229–237.
- [12] C.W. Bert, Design of clamped composite material plates to maximize fundamental frequency, Journal of Mechanical Design, 1978, pp.274–278.
- [13] H. Fukunaga, H. Sekine, M. Sato, Optimal design of symmetrically laminated plates for the fundamental frequency, Journal of Sound & Vibration, 171, 1994, pp.219–229.
- [14] X. Zhao, Y. Narita, Maximization of fundamental frequency for generally laminated rectangular plates by the complex method, Transactions of JSME 63C, 1997, pp.364–370 (in Japanese).

Table 4. Experimental results (GA)

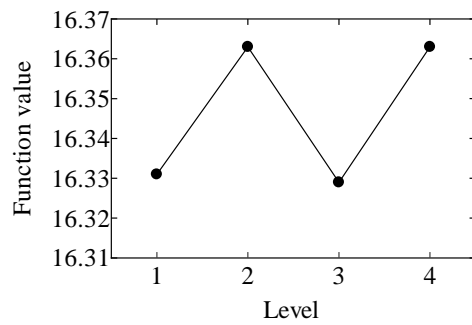
Experiment	Level				Results			
	A	B	C	D	Trial 1	Trial 2	Trial 3	Mean
1	1	1	1	1	16.363	16.292	16.340	16.332
2	1	2	2	2	16.359	16.361	16.388	16.369
3	1	3	3	3	16.389	16.295	16.327	16.337
4	1	4	4	4	16.371	16.349	16.285	16.335
5	2	1	2	3	16.342	16.376	16.379	16.366
6	2	2	1	4	16.316	16.359	16.357	16.344
7	2	3	4	1	16.401	16.412	16.330	16.381
8	2	4	3	2	16.319	16.242	16.259	16.273
9	3	1	3	4	16.371	16.298	16.315	16.328
10	3	2	4	3	16.406	16.355	16.339	16.367
11	3	3	1	2	16.319	16.366	16.366	16.350
12	3	4	2	1	16.353	16.369	16.363	16.362
13	4	1	4	2	16.394	16.335	16.384	16.371
14	4	2	3	1	16.396	16.371	16.360	16.376
15	4	3	2	4	16.333	16.385	16.352	16.357
16	4	4	1	3	16.278	16.325	16.295	16.299



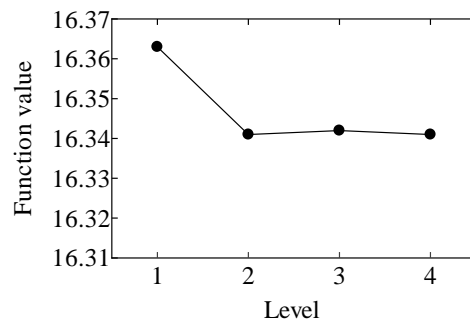
(d) Factor A



(c) Factor B



(b) Factor C



(a) Factor D

Figure 2. Main effects plot (GA)

Table 5. Experimental results (PSO)

Experiment	Level				Results			
	A	B	C	D	Trial 1	Trial 2	Trial 3	Mean
1	1	1	1	1	16.410	16.308	16.410	16.376
2	1	2	2	2	16.415	16.415	16.415	16.415
3	1	3	3	3	16.344	16.331	16.368	16.348
4	1	4	4	4	16.278	16.242	16.187	16.236
5	2	1	2	3	16.415	16.415	16.415	16.415
6	2	2	1	4	16.415	16.415	16.415	16.415
7	2	3	4	1	16.381	16.307	16.375	16.354
8	2	4	3	2	16.338	16.269	16.301	16.303
9	3	1	3	4	16.393	16.404	16.314	16.370
10	3	2	4	3	16.326	16.393	16.314	16.344
11	3	3	1	2	16.413	16.412	16.411	16.412
12	3	4	2	1	16.291	16.332	16.363	16.329
13	4	1	4	2	16.376	16.402	16.378	16.385
14	4	2	3	1	16.389	16.336	16.359	16.361
15	4	3	2	4	16.310	16.364	16.389	16.354
16	4	4	1	3	16.329	16.373	16.367	16.356

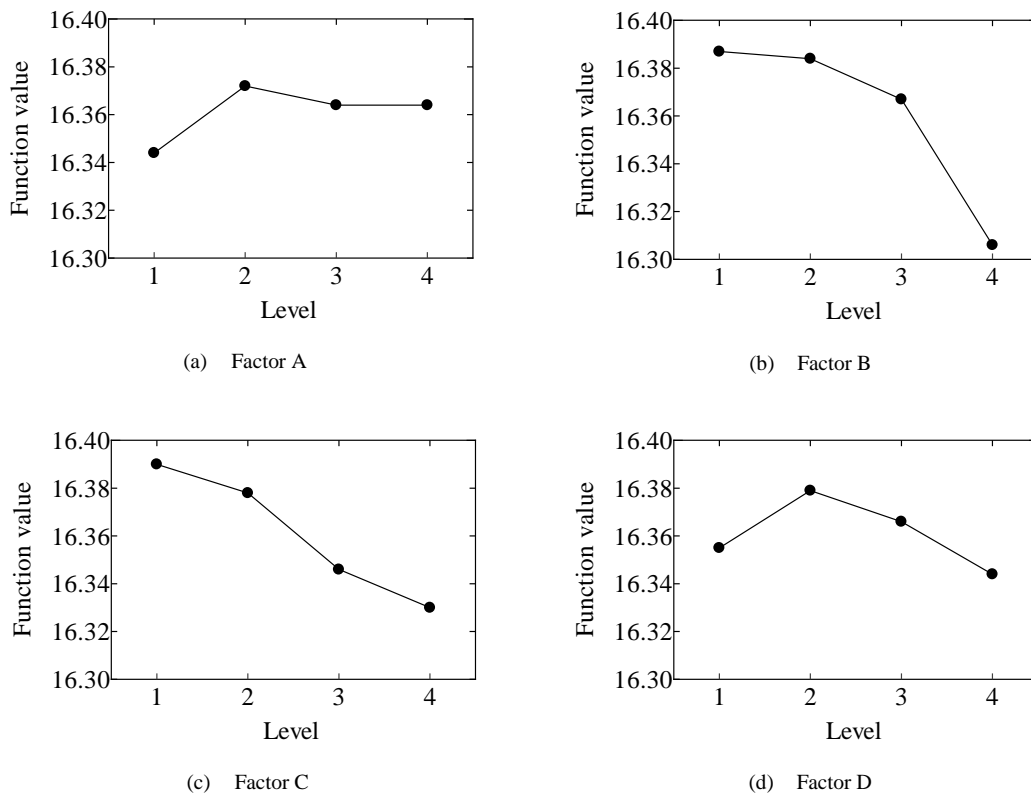


Figure 3. Main effects plot (PSO)

Table 6. Selected parameters of GA

Population Size	Maximum generation	Elite count	Crossover rate	Mutation rate
80	500	3	0.5	0.01

Table 7. Selected parameters of PSO

Population Size	Maximum generation	Elite count	Crossover rate	Mutation rate
80	500	3	0.5	0.01

Table 8. Maximized Ω_1 , stacking sequence, and elapsed time

(a) CSFF

	Trial	Final (500 th generation)			Converged			Stacking sequence		
		Ω_1	(Mean)	Time(s)	(Mean)	Generation	(Mean)		Time(s)	(Mean)
GA	1	16.399		16898		488		16494	[21.1/-45.4/ 18.7/-41.7]s	
	2	16.403	(16.401)	16261	(16367)	186	(260)	6079	(8671)	[22.6/-42.5/ 17.5/ 19.3]s
	3	16.402		15941		107		3439		[21.2/-45.9/ 20.3/ 5.6]s
PSO	1	16.410		16757		20		705		[21.9/-44.0/ 21.9/-44.0]s
	2	16.415	(16.413)	17236	(16877)	22	(20)	794	(722)	[21.5/-44.4/ 21.5/ 21.5]s
	3	16.415		16638		19		668		[21.5/-44.4/ 21.5/ 21.5]s

(b) SSSS

	Trial	Final (500 th generation)			Converged			Stacking sequence		
		Ω_1	(Mean)	Time(s)	(Mean)	Generation	(Mean)		Time(s)	(Mean)
GA	1	56.290		35198		379		26698		[-43.8/ 44.1/ 42.5/ 49.3]s
	2	56.224	(56.232)	35266	(35182)	61	(225)	4371	(15887)	[48.1/-43.9/-42.7/-50.5]s
	3	56.182		35083		236		16592		[45.4/-45.7/-40.4/-22.6]s
PSO	1	56.319		36084		34		2570		[-45.0/ 45.0/ 45.0/ 45.0]s
	2	56.319	(56.319)	35331	(35513)	37	(35)	2790	(2605)	[-45.0/ 45.0/ 45.0/ 45.0]s
	3	56.319		35125		34		2456		[45.0/-45.0/-45.0/-45.0]s

(c) CCFF

	Trial	Final (500 th generation)			Converged			Stacking sequence		
		Ω_1	(Mean)	Time(s)	(Mean)	Generation	(Mean)		Time(s)	(Mean)
GA	1	19.025		22510		18		850		[48.0/-45.5/ 43.3/ 2.3]s
	2	19.028	(19.028)	22756	(22489)	104	(192)	4773	(8583)	[45.3/-46.6/ 37.4/ -5.5]s
	3	19.032		22201		453		20125		[45.4/-45.8/ 44.5/-57.9]s
PSO	1	19.035		22789		15		729		[45.0/-45.0/ 45.0/-45.0]s
	2	19.028	(19.033)	22480	(22712)	12	(14)	586	(668)	[44.6/-44.4/ 44.6/ 90.0]s
	3	19.035		22868		14		688		[45.0/-45.0/ 45.0/-45.0]s

(d) CSSS

	Trial	Final (500 th generation)			Converged			Stacking sequence		
		Ω_1	(Mean)	Time(s)	(Mean)	Generation	(Mean)		Time(s)	(Mean)
GA	1	66.710		68529		364		49910		[-28.1/ 31.2/ 35.7/ 10.6]s
	2	66.709	(66.725)	66771	(67356)	483	(378)	64505	(50929)	[28.2/-30.0/-31.9/-48.8]s
	3	66.756		66767		286		38371		[-28.5/ 31.5/ 33.2/ 26.0]s
PSO	1	66.765		66917		21		2940		[27.7/-31.8/-31.8/-31.8]s
	2	66.765	(66.765)	68934	(68170)	20	(21)	2888	(2948)	[-27.7/ 31.8/ 31.8/ 31.8]s
	3	66.765		68659		21		3015		[-27.7/ 31.8/ 31.8/ 31.8]s

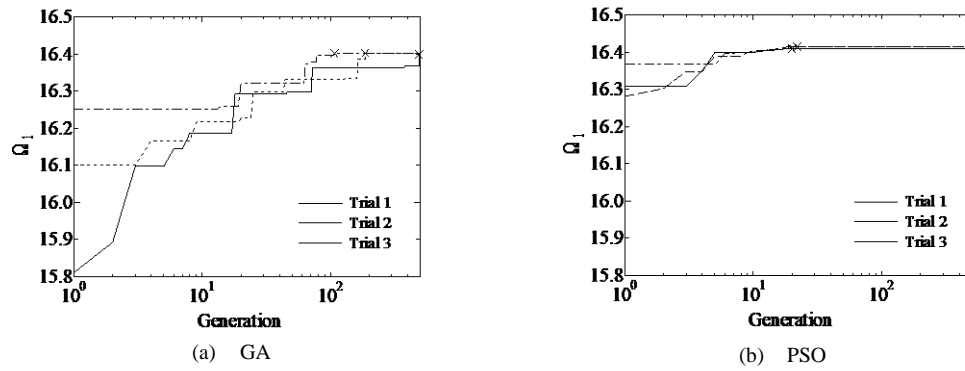


Figure 4. Transition of Ω_1 with generation for CSFF

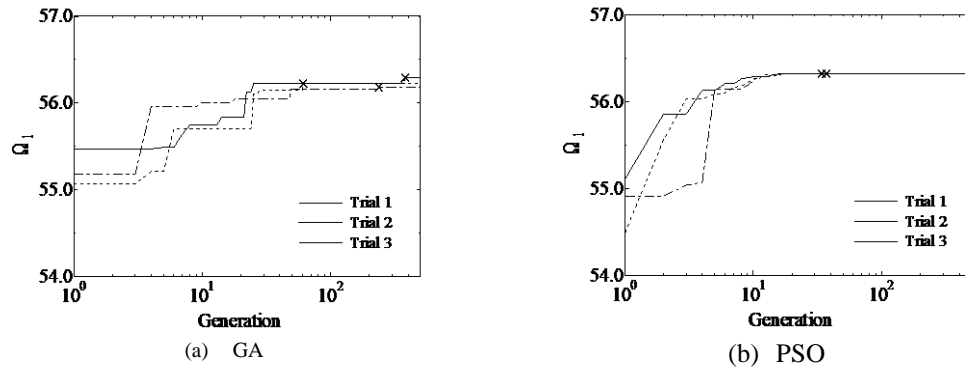


Figure 5. Transition of Ω_1 with generation for SSSS

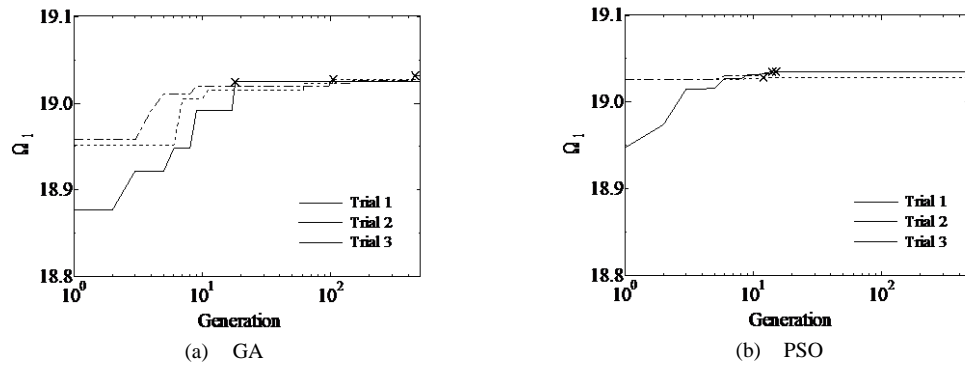


Figure 6. Transition of Ω_1 with generation for CCFE

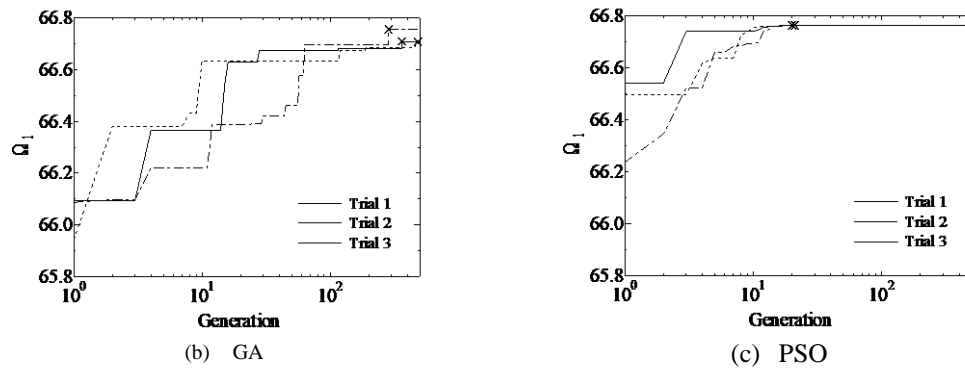


Figure 7. Transition of Ω_1 with generation for CSSS

- [15] A. Todoroki, R.T. Haftka, Stacking sequence optimization by a genetic algorithm with a new recessive gene like repair strategy, *Composites Part B*, 29, 1998, pp.277-285
- [16] Z. Gürdal, R.T. Haftka, P. Hajela, *Design and Optimization of Laminated Composite Materials*, Wiley-Interscience, 1999.
- [17] A. Todoroki, T. Ishikawa, Design of experiments for stacking sequence optimizations with genetic algorithm using response surface approximation, *Composite Structures*, 64, 2004, pp.349-357.
- [18] R. Matsuzaki, A. Todoroki, Stacking-sequence optimization using fractal branch-and-bound method for unsymmetrical laminates, *Composite Structures*, 78, 2007, pp.537-550.
- [19] A. Todoroki, M. Sekishiro, Stacking sequence optimization to maximize the buckling load of blade-stiffened panels with strength constraints using the iterative fractal branch and bound method, *Composites Part B*, 39, 2008, pp.842-850.
- [20] Y. Narita, Layerwise optimization for the maximum fundamental frequency of laminated composite plate, *Journal of Sound & Vibration*, 263, 2003, pp.1005-1016.
- [21] Y. Narita, G.J. Turvey, Maximizing the buckling loads of symmetrically laminated composite plates using a layerwise optimization approach, *Journal Mechanical Engineering Science*, 218, 2004, pp.681-691.
- [22] Y. Narita, Maximum frequency design of laminated plates with mixed boundary conditions, *International Journal of Solids & Structures*, 43, 2006, pp.4342-4356.
- [23] T. Le-Manh, J. Lee, Stacking sequence optimization for maximum strengths of laminated composite plates using genetic algorithm and isogeometric analysis, *Composite Structures*, 116, 2014, pp.357-363.
- [24] Ehsani, J. Rezaeepazhand, Stacking sequence optimization of laminated composite grid plates for maximum buckling load using genetic algorithm, *International Journal of Mechanical Sciences*, 119, 2016, pp.97-106.
- [25] V. Ho-Huu, T.D. Do-Thi, H. Dang-Trung, T. Vo-Duy, T. Nguyen-Thoi, Optimization of laminated composite plates for maximizing buckling load using improved differential evolution and smoothed finite element method, *Composite Structures*, 146, 2016, pp.132-147.
- [26] F. Schaedler, de Almeida, Stacking sequence optimization for maximum buckling load of composite plates using harmony search algorithm, *Composite Structures*, 143, 2016, pp.287-299.
- [27] M.T. Herath, B.G. Prusty, A.W. Phillips, N.S. John, Structural strength and laminate optimization of self-twisting composite hydrofoils using a Genetic Algorithm, *Composite Structures*, 176, 2017, pp.359-378.
- [28] A.R. Vosoughi, A. Darabi, N. Anjabin, U. Topal, A mixed finite element and improved genetic algorithm method for maximizing buckling load of stiffened laminated composite plates, *Aerospace Science and Technology*, 70, 2017, pp.378-387.
- [29] A.R. Vosoughi, A. Darabi, H. Dehghani, Forkhorji, Optimum stacking sequences of thick laminated composite plates for maximizing buckling load using FE-GAs-PSO, *Composite Structures*, 159, 2017, pp.361-367.
- [30] H. Zhou, M. Song, W. Pedrycz, A comparative study of improved GA and PSO in solving multiple traveling salesmen problem, *Applied Soft Computing*, 64, 2018, pp.564-580.
- [31] M.V. Pathan, S. Patsias, V.L. Tagariellia, A real-coded genetic algorithm for optimizing the damping response of composite laminates, *Computers & Structures*, 198, 2018, pp.51-60.
- [32] F. Javidrad, M. Nazari, H.R. Javidrad, Optimum stacking sequence design of laminates using a hybrid PSO-SA method, *Composite Structures*, 185, 2018, pp.607-618.
- [33] A.B.I. Akmar, O. Kramer, T. Rabczuk, Probabilistic multi-scale optimization of hybrid laminated composites, *Composite Structures*, 184, 2018, pp.1111-1125.
- [34] Y. Narita, Series and Ritz-type buckling analysis, in: G.J. Turvey, I.H. Marshall (Eds.), *Buckling and Postbuckling of Composite Plates*, Chapman & Hall, London, pp. 33–57 (Chapter 2), 1995.
- [35] Son D, Kazem A, Romeo M. Maximising Performance of Genetic Algorithm Solver in Matlab. *Engineering Letters*, 24; 2016. pp. 75-83.